University of Liverpool

Department of Building Science

THE RESPONSE OF STRUCTURES TO ACOUSTIC EXCITATION WITH SPECIAL REFERENCE TO THE SONIC BOOM

by

Roderick Reginald Hudson, B.Sc., Grad.Inst.P.

This thesis is submitted in accordance with the requirements of the University of Liverpool for the degree of Doctor in Philosophy.

July, 1969.

ACKNOWLEDGEMENT

I wish to acknowledge the constant encouragement and assistance given throughout my research by Dr. K.A. Mulholland and Mr. M.J. Crocker.

The work was supported by the Science Research Council.

SUMMARY

The research reported in this thesis is concerned with the response of mechanical structures to the excitation of acoustic fields. Both the vibration of the structure itself (sonic boom studies) and the secondary sound field which this vibration produces (transmission loss studies) are investigated.

In measuring the airborne transmission loss of a high loss partition an important limitation of the University's experimental suite was discovered. Attempts at an indirect measurement of transmission loss using vibration transducers illustrate a fallacious assumption of most transmission loss theories. These findings impose a considerable limitation upon the accelerometer method of transmission loss measurement.

The study of structural vibration was extended to sonic boom response. In particular the effects of a cavity behind a panel upon the panel's dynamic properties is studied both experimentally and theoretically. This model is comparable with a window-room system and so is of current interest in the evaluation of the possibility of sonic boom damage.

List of Contents

List of Contents

List of Contents

List of Contents

List of Contents — Page No.

List of Figures

Fig. No.

Fig. No.

List of Symbols

Symbol	Definition	Section in which first used
a	Panel length	5.5.1
A	Equivalent acoustical absorption area in "open window" units	2.3.1
A	Relative amplitude of second N-wave	4.7
A	Arbitrary constant	A5.1.4
b	Panel breadth	5.5.1
B	Total response amplitude due to two N-waves	4.7
B	Arbitrary constant	A5.1.4
c	Velocity of sound in air	3.2
c_s	Bending wave velocity	3.4.3
c_l	Longitudinal wave velocity	3.4.2
c_l'	Longitudinal wave velocity in a thin plate	3.4.2
C	Viscous damping coefficient of generalised system	4.2
C	Arbitrary constant	A5.1.4
D	Arbitrary constant	A5.1.4
e_{x1}	Panel strain in the x direction due to a unit generalised displacement in the first cavity-modified panel mode.	6.4.1
e_{x2}	As above	6.4.1
e_{y1}	As above	6.4.1
e_{y2}	As above	6.4.1
E	Sound energy density	2.3.1
E	Young's modulus of panel	3.3.3
E'	Complex Young's modulus	3.4.2
E_i	Energy density of incident sound field	3.2
E_I	Energy density of an average plane sound wave	3.2
f	Eigenfrequency of generalised system	4.3.6
f_c	Critical frequency of the panel	3.3.3

F	Ratio of panel to shim stiffness	A5.1.4
F_i	Sound energy flux incident on the panel	3.2
F_I	Energy flux of average sound wave	3.2
F_t	Transmitted energy flux	3.1
G(x,y)	Panel displacement	5.5.1
h	Panel thickness	3.3.3
h	Cavity depth	6.3.1
K	Stiffness constant of generalised system	4.2
K_1	Panel bending stiffness	3.4.2
K_2	Viscous damping constant	3.4.2
$\mathcal{L}$	Shim length	A5.1.4
L	Sound insulation. In chapter 2 see Table 2.1 for meaning of subscripts	
L	Panel length	A5.1.4
$L_{n,m}$	Generalised force acting on n,m^{th} panel mode	5.5.1
LTL	Limiting Transmission Loss of the suite	2.3.3
m	Surface density of test panel	3.2
m	Mode number in the y direction	5.5.1
m_1	Mass of the light accelerometer	3.3.1
m_2	Mass of the heavy accelerometer	3.3.1
M	Mass of the generalised system	4.2
n	Mode number in the x direction	5.5.1
N	Number of plane waves per steradian	3.2
p	Acoustic overpressure	3.3.2
p_a	Atmospheric pressure	6.3.1
p_o	Reference sound pressure level of 2×10^{-4} dyne/cm^2	3.3.2
p_o	Peak overpressure of sonic boom	4.3.1
p_o	Pressure amplitude of sine waves	5.5.2

p_1	Pressure of undisturbed medium	5.3.2
Δp	Overpressure of shock front	5.3.2
$q_{n,m}$	Generalised co-ordinate of n,mth in vacuo panel mode	5.5.1
$Q_1(Q_2)$	Generalised displacement of first (second) cavity-modified panel mode	6.4.1
r	Ratio of sonic boom's rise time to positive phase duration (excluding rise time)	4.4
R(w)	Ratio of 3,1 to 1,1 in vacuo modes contained in a cavity-modified panel mode	6.4.1
Rt	Reverberation time	2.3.3
s	Ratio of total to positive phase duration of a sonic boom	4.2
S	Geometrical area of test panel	2.3.1
SPL_1 (SPL_2)	Sound pressure level in transmission (reception) room	3.3.1
t	Time	
t'	Time measured from a displaced origin	4.7
$\overline{t}$	Time delay between two N-waves	4.7
T	Total transmission coefficient	2.3.1
T	Non-dimensionalised time	4.6
TL	Transmission loss. In Chapter 2 see Table 2.1 for meaning of subscripts	
TL_1	Transmission loss obtained by airborne measurement	3.3.1
TL_2	Transmission loss predicted by piston theory and experimental panel response	3.3.2
TL_3	Transmission loss using piston theory and mass law prediction of panel response	3.3.2
TL_M	Mass law prediction of transmission loss	3.3.2
T_p	Panel thickness	5.5.1
u	Sonic boom shock reflection factor	4.6

U_o	Peak velocity amplitude of the test panel	3.1
v	Bending wave velocity	A5.1.4
V	Room volume	2.3.1
V	Velocity of shock front	5.3.2
V_o	Experimental peak panel velocity corrected for panel-loading	3.3.1
V_1 (V_2)	Experimental peak panel velocity using the light (heavy) accelerometer	3.3.1
V_I	Velocity amplitude of an average plane wave	3.2
δ V	Reduction in cavity volume due to panel displacement	6.3.1
x	The difference between the measured signal and background electrical noise levels	2.3.1
X	Ratio of measured signal to noise powers	2.3.1
X_s	Displacement caused by a static force equal to the peak overpressure of the sonic boom	4.3.4
y	The difference between the measured and actual signal levels	2.3.1
Z	Impedance of panel	3.4.2
α	Reflection coefficient	2.4.2
α	Panel aspect ratio (a/b)	6.3.1
β	A function of α defined in Equation (6.19)	6.3.1
γ	Ratio of the principal specific heats of a gas	5.3.2
δ	Critical damping ratio	4.2
η	Loss factor	3.4.2
η	Ratio of acoustic to mechanical stiffness in the first in-vacuo panel mode	6.3.1
θ	Angle	3.2
θ_L	Limiting angle of incidence	3.2

K	Second moment of area	5.4.1
ξ	Panel displacement	3.4.2
ρ	Density of air	3.1
ρ_p	Density of panel material	3.3.3
σ	Poisson's ratio	3.4.2
σ	Dummy time variable	4.2
σ_x (y)	Strain in x, (y) direction	5.5.1
τ	Positive phase duration of sonic boom	4.1
τ'	(r + 1) . N-wave's positive phase duration inclusive of rise time	4.4.1
τ	Transmission coefficient per unit area of test panel	2.3.1
τ_{ML}	Mass law prediction of	3.2
τ_p	Piston theory prediction of	3.2
ϕ	Acoustic velocity potential	3.4.2
ϕ	Phase angle	4.7
ϕ	Phase angle	A5.1.4
$\phi_{n,m}$	Mode shape of n,mth in-vacuo panel mode	5.5.1
Φ	Mode shape of cavity-modified panel mode	6.4.1
ψ	Acoustic velocity potential	6.2.1
w	Angular frequency	
w_d	Damped angular frequency	4.2
$w_{n,m}$	Undamped angular resonant frequency of the n,mth in-vacuo panel mode	5.5.1
w_r	Resonant frequency	5.4.3
w_1 (w_2)	Cavity modified panel angular eigenfrequencies	6.4.1
Δw	Difference between the eigenfrequency of the shim-supported panel and that of an ideal simply-supported panel	A5.1.4

Δw	Half-power width of a resonance curve	5.4.3
	Non-dimensionalised frequency	4.6
	Ratio of cavity-modified panel eigenfrequency to in-vacuo fundamental eigenfrequency.	6.3.1

Super-script	Pertaining to:	Definition	Section
'	E_1, E_2, E_3,	Refer to experiments 1,2 and 3 respectively	2.3.2
''			
'''			
o	w, z_s, z_p	Unperturbed and first order perturbation results respectively	A5.1.4
1			

Subscript			
i		Incident	
r		reflected	3.4.2
t		transmitted	
o		peak amplitude of	
p	z	of the panel	A5.1.1
s		of the shim	
1		1st estimate	
2	x	2nd estimate	2.3.3
3		mean of above	
1		Transmission room	
2	T,E,A,V,Rt	reception room	2.3.1
3		instrument area.	

1.0 Introduction

1.1 The Measurement of Sound Transmission Loss

A great deal of effort has already been expended at Liverpool University into the investigation of various methods of transmission loss measurement (1.1), (1.2), (1.3). The University possesses a large transmission loss suite and the method of airborne measurement (1.1) remains (with slight modifications) the principal method of laboratory measurement. Utley (1.2), undertook a survey of alternative methods of measurement which are applicable in the field or the presence of flanking paths and Cummings (1.3), developed the transmission loss box for normal incidence measurements within the laboratory.

Chapter two is concerned with measuring the transmission loss of a cavity brick wall. As the brick wall had a much higher value of transmission loss than any panel previously measured in the suite the electronics employed had to be considerably modified. Also in view of the unusually high value of transmission loss the suite's external flanking transmission is investigated. Because of the doubtful reliability of airborne measurements of high values of transmission loss the accelerometer method of measurement is investigated in Chapter Three.

1.2 The Theory of Sound Transmission Loss of single panels

The simplest theory of sound transmission loss is the "mass law" (1.8) which assumes that the panel acts simply as a limp mass. Mulholland (1.1) has shown that this theory is equivalent to a more general theory

given by Lord Rayleigh (1.9) when the panel thickness becomes negligible compared with the acoustic wavelength. Cremer (1.10) has developed a theory which takes the panel stiffness into account and predicts the coincidence effect.

In Chapter three a theory similar to Cremer's is developed and the transmission loss and panel response which it predicts is compared with experiment. The need to be able to correctly predict the mechanical vibration caused by an acoustic excitation lead to an interest in the response of structures to the sonic boom.

1.3 Structural response to the Sonic Boom.

Because of Britain's involvement in the building of Concorde, the world's first supersonic transport aircraft, the problem of structural response to the sonic boom is currently of topical interest. The dangers of uncontrolled supersonic flight were aptly demonstrated a few years ago when a single bang due to a fighter aircraft resulted in $300,000 worth of damage to Ottawa Air Terminal (1.11). Because of the shape of their pressure time-history, sonic boom's are sometimes termed "N-waves" and in Chapter four their effects upon an ideal structure are calculated theoretically. The work reported in Chapter four was undertaken in conjunction with Mr. M.J. Crocker.

In order to study these effects experimentally a shock tube facility was developed. The experimental "N-wave" was made to impinge normally upon a rectangular simply supported steel plate whose strain was recorded together with the shock wave's pressure time-history.

These experiments are described in Chapter five.

1.4 The Panel Cavity problem

When a thin panel is backed by an acoustically stiff cavity, the panel's dynamic behaviour is affected. For a large plate glass window in front of a shallow room (e.g. a display window) the room's acoustic stiffness is comparable with the windows mechanical stiffness and so in order to calculate the window's sonic boom response, room effects must be considered.

A study of the panel-cavity problem is undertaken in Chapter six and a theory is developed which allows the cavity-modified panel response to be calculated for real window room and sonic boom parameters. This theory is compared with the results obtained from an experimental panel-cavity system.

2.0 The measurement of high transmission loss (The brick wall experiment)

2.1 Introduction

The sound insulation provided by a cavity brick wall in the field has been established by measurements carried out by the Building Research Station (2.1). This shows that the insulation varies in an approximately linear manner from 39 dB at 100 Hz to 66 dB at 3.2 kHz but there is also evidence both measured (2.2) and theoretical (2.3 - 2.6) that under special conditions the insulation provided by such a wall can exceed these values quite substantially. Moeller reported a measured insulation of 57 dB at 100 Hz to 80 dB at 400 Hz and the theoretical work of Mulholland et al shows that under diffuse field conditions a sound insulation curve ranging from 50 dB at 100 Hz to 128 dB at 4 kHz is possible. In order to provide further experimental evidence to substantiate these theoretical ideas it was decided to construct a double brick wall in the new Liverpool University transmission loss suite and attempt to measure the insulation provided.

Special experimental difficulties were encountered when attempting to measure transmission losses of the order of 100 dB with conventional rooms and apparatus. It was found necessary to modify the apparatus normally employed for transmission loss measurements and these modifications are described in Section 2.2. Further experiments were carried out to determine the amount of sound energy passing along airborne paths via the instrument area adjacent to the two rooms. This investigation, which justified the assumption that this external airborne flanking transmission of the suite was significantly less than the suite's internal transmission, is described in Section 2.3.

Section 2.4 is concerned with the brick wall experiments themselves. In Section 2.4.1 the actual experiments that were performed on various types of double and single brick walls are described and the results are investigated in Section 2.4.2. Finally, Section 2.5 summarises the conclusions that may be drawn from the whole of this chapter about both the experimental transmission loss properties of a single and double brick wall and also about the facilities of the new Liverpool University transmission loss suite.

In Table 2.1, the various measurements undertaken are listed for easy reference.

TABLE 2.1

N.B. An 'L' represents a sound insulation and a 'TL' is the transmission loss derived from it (where applicable).

L	TL_1	Transmission room to reception room with a double cement faced cavity brick wall in the window.
L_1		Transmission room to instrument area.
L_2		Reception room to laboratory.
L_3		Laboratory to reception room.
L_4	TL_4	As 'L' but without cement facing.
L_5		As 'L_4' but with one brick removed from reception room wall.
L_6		Transmission room to cavity.
L_7		Reception room to cavity.
L_8	TL_8	Transmission room to reception room with a single brick wall on the transmission room side of the window.
L_9	TL_9	As 'L_8' but with the wall on the reception room side of the window.
L_{10}	TL_2	Semi-empirical prediction of that between the transmission and reception rooms with a double cement faced cavity brick wall in the window.
L_{11}		As 'L_{10}' but allowing for the unequal insulation provided by the two leaves of the double brick wall.
TL_3		Multiple reflection theory for a cavity brick wall.
LTL		The limiting transmission loss that can be measured by the suite in view of the external flanking path.

2.2 Experimental method of measuring high values of transmission loss

The apparatus normally employed to measure the sound level difference during the course of transmission loss measurements is shown in Figure 2.1. The noise generation equipment was not modified and is, therefore, not shown on Figures 2.1 and 2.3. It has been described by previous authors (1.1 - 1.3). The sound level in the transmission room on one side of the sample is measured and then immediately a switch is thrown to connect a microphone in the reception room on the other side of the panel to the measuring instrument. This procedure reduces the possibility of experimental error due to variation in the sensitivity of apparatus. However, if the levels of the two signals differ by more than about 60 dB it is impossible to measure both signals with the same instrument set to the same sensitivity without either overloading the instrument with a signal from one channel or losing the signal from the other channel into the electrical background noise. This difficulty was overcome by providing extra microphone amplification for one channel and the apparatus used for this is shown in Figure 2.2. Each amplifier was set at a suitable sensitivity to receive the signal from one of the microphones and pass it to the selector switch at a level approximately equal to that of the other signal. By suitably attenuating the transmission room signal, it was thus possible to read both signals from the same instrument without overloading or noise level difficulties.

It was necessary to interrupt the transmission room channel with a supplementary microphone amplifier as well as the reception room channel because of the signal rectification and change from 11 core microphone cable to standard co-axial cable that occurs at an amplifier. The microphone selector switch had now to handle co-axial cables instead of 11 core

microphone cables and in order that the process remain fully automatic, a new selector switch driven by an astable multivibrator with a 4 second time constant was designed and built.

The method suffers now of course from the disadvantage that the two channels no longer have the same amplification and so a variation of the amplification of one with respect to the other after calibration with a pistonphone is recorded as a correction to be made to the measured transmission loss. Similarly if the difference between the sensitivities for different amplifier settings did not exactly correspond with the nominal values given by these settings, these discrepancies would again result in errors in the measured value of transmission loss. This error could, in theory, be reduced by dispensing with the twin amplifiers and introducing a passive attenuator in the transmission room microphone lead. However, due to the high accuracy specification of the Bruel and Kjaer equipment, it was found that such errors were small in comparison with those of the reverberant room method itself. Therefore, it was decided that the design and construction of a radiation shielded 11 core microphone cable interruptor with passive attenuators that did not introduce any noise or error into the system would not be justified.

Care had to be taken with calibration and frequency response and it was necessary to guard against losing the reception room signal into the ambient noise as the level fell off at higher and higher third octave frequency bands. Despite the double amplification, it was noted that if a complete transmission loss spectrum was to be obtained without altering the gain of an amplifier during an automatic run, the reception room signal dropped to within a few dB of the noise level at the highest frequency employed (4,000 Hz). It was noted that this persistently high noise

level at the high frequencies was mainly of electrical origin and did not vary with time. Use was made of this fact when the measured signal was less than 10 dB above the electrical noise level. If the measured signal is x dB above the noise level, it exceeds the actual signal by y dB where y is given by:-

$$y = x - 10 \log\left[\text{antilog}\left(\frac{x}{10}\right) - 1\right] \qquad \text{(A2.5)}$$

The derivation of the above formula together with a pre-calculated table for rapid application of the correction is given in Appendix 2.1. A typical result of employing this correction technique to the measured sound insulation between the transmission and reception rooms of a double cement faced cavity brick wall can be seen in Figure 2.3. As the electrical noise is frequency independent, its effect upon the reception room signal is similar to that produced by a high but frequency independent transmission loss as is usually associated with a thin panel air leak (assuming that the transmission room noise field is "perfectly white" and that the non-geometrical effects can be ignored (1.7)). Therefore, failure to correct for it produces the same sort of levelling of high frequency high transmission loss values as does a thin panel air leak which can be seen from the shape of Figure 2.3.

2.3 Investigation of an airborne flanking path

2.3.1 Introduction and theory

The other main problem that was considered was that of airborne flanking paths through the doors and walls of the measurement rooms via the instrument area adjacent to the two rooms. For accurate results it is necessary for the sound energy reaching the reception room through the panel to exceed that reaching the reception room via the instrument room.

The reason that this investigation was undertaken originated from the following subjective observations. With the double brick wall in the transmission loss suite window it was observed that the noise level inside the reception room resulting from the source in the transmission room was lower than the noise level in the surrounding laboratory. Furthermore, it was noted that if the reception room door was not properly closed the main influx of sound into the room was from this door as opposed to the brick wall under test and that when it was closed, the resonant field was barely audible. It, therefore, seems possible that a considerable proportion, if not the majority of the reception room's resonant field was caused by sound travelling along this flanking path. Assuming that the instrument area can be regarded as a resonant cavity, the situation is represented in Figure 2.4 where T is a total transmission coefficient between two rooms and the subscripts 1, 2, 3, refer to the transmission room, the reception room and the instrument area respectively. It is noted that in view of the high values of transmission loss under investigation and that $E_1 \gg E_3 \gg E_2$, reverse transmission effects have been ignored. For example, the sound power flowing from the transmission room to the reception room is assumed to be $E_1 \tau S$ whereas it should more

accurately be represented by $(E_1 - E_2)\ \tau\ S$. However, for values of transmission loss in excess of 15 dB such an assumption is justified (1.1, 1.4).

For the results to be meaningful, we require a signal in excess of the flanking sound, i.e.,

$$E_1\ \tau\ S \gg E_3\ T_{2,3} \tag{2.1}$$

If we define X as being the ratio of the power of the signal plus the flanking noise to that of the flanking noise, we have:-

$$X = \frac{\{E_1\ \tau\ S + E_3\ T_{2,3}\}}{E_3\ T_{2,3}} \tag{2.2}$$

But the total sound entering the reception room ($E_1\ \tau\ S + E_3\ T_{23}$) is equal to the power being absorbed by the walls of the reception room, i.e.,

$$E_1\ \tau\ S + E_3\ T_{2,3} = E_2\ A_2 \tag{2.3}$$

Combining Equations (2.2) and (2.3) we have:-

$$X = \frac{E_2\ A_2}{E_3\ T_{2,3}} \tag{2.4}$$

Similarly, the sound power entering the instrument area from the transmission room and reception room is equal to the power being absorbed by the walls of the instrument area, i.e.,

$$E_1\ T_{1,3} + E_2\ T_{2,3} = E_3\ A_3 \tag{2.5}$$

where A_3 includes the energy lost from the instrument area via T_{13} and T_{23}. If $T_{13} \approx T_{23}$ (which is a reasonable assumption in view of the fact that the transmission and reception rooms share almost identical construction) and $E_1 \gg E_2$ the second term on the left hand side of Equation (2.5) can be ignored whence:-

$$E_3 = \frac{E_1 \; T_{1,3}}{A_3} \tag{2.6}$$

Substituting Equation (2.6) into Equation (2.4):-

$$X = \frac{E_2 \; A_2}{\frac{E_1 \; T_{1,3}}{A_3} \; T_{2,3}} \tag{2.7}$$

Taking the logarithm to base 10 and then multiplying by 10 both sides of Equation (2.7) and defining:-

$$x = 10 \log(X) \tag{2.8}$$

as the number of dB by which the signal exceeds the noise we have:-

$$x = 10 \log\left\{\frac{1}{T_{1,3}}\right\} + 10 \log\left\{\frac{1}{T_{2,3}}\right\} + 10 \log(A_2 \; A_3) - 10 \log\left\{\frac{E_1}{E_2}\right\} \tag{2.9}$$

We define:-

$$10 \log\left\{\frac{E_1}{E_2}\right\} = L \tag{2.10}$$

which is the experimental sound insulation of the double brick wall under test (after correction for electrical noise as described in Section 2.2). In order to find T_{13} and T_{23} three subsidiary experiments were performed which provided two separate estimates of x.

2.3.2 Subsidiary Experiments

Experiment 1

A sound field of intensity E_1' was generated and measured in the transmission room and the resultant energy level in the instrument area E_3' was measured.

$$E_1' T_{1,3} = E_3' A_3$$

$$10 \log\left\{\frac{1}{T_{1,3}}\right\} = 10 \log\left\{\frac{1}{E_3' A_3}\right\} \qquad (2.11)$$

$$= L_1 - 10 \log(A_3) \qquad (2.12)$$

where L_1 is the sound insulation measured in Experiment 1.

Experiment 2

Similarly by generating and measuring a noise E_2'' in the reception room and measuring the resultant noise in the instrument area E_3'' we have:-

$$10 \log\left\{\frac{1}{T_{2,3}}\right\} = L_2 - 10 \log(A_3) \qquad (2.13)$$

where L_2 is the sound insulation measured in Experiment 2.

Experiment 3

A sound field of intensity E_3''' was generated and measured in the instrument area and the resultant energy level in the reception room E_2''' was measured. During the course of this experiment the experimentalist took refuge from the high noise level in the instrument area by siting himself and his recording instruments in the transmission room. As before, we have:-

$$10 \log\left\{\frac{1}{T_{2,3}}\right\} = L_3 - 10 \log(A_2) \qquad (2.14)$$

where L_3 is the sound insulation measured in Experiment 3.

2.3.3 Analysis of results and conclusions

Substituting Equations (2.10), (2.12) and (2.13) into the definition for x given in Equation (2.9) we have for a first experimental measurement of x which we call x_1 where:-

$$x_1 = \{L_1 - 10 \log(A_3)\} + \{L_2 - 10 \log(A_3)\}$$

$$+ 10 \log(A_2 A_3) - L$$

$$= L_1 + L_2 - L + 10 \log\left\{\frac{A_2}{A_3}\right\} \qquad (2.15)$$

In order to determine the ratio of the two absorption areas it was found necessary to measure the reverberation times of both the reception room and the instrument area. From elementary theory (1.5) it then follows that:-

$$\frac{A_2}{A_3} = \frac{V_2\ Rt_3}{V_3\ Rt_2} \qquad (2.16)$$

where Rt_2 and Rt_3 are the reverberation times of the reception room and instrument area respectively.

A second estimate of x which we call x_2 was found by substituting Equations (2.12) and (2.14) into Equation (2.9)

$$x_2 = \{L_1 - 10\log(A_3)\} + \{L_3 - 10\log(A_2)\}$$

$$+ 10\log(A_2\ A_3) - L$$

$$= L_1 + L_3 - L \qquad (2.17)$$

This second estimate of x does not require a knowledge of reverberation times. Furthermore, it can be intuitively understood as the sum of the transmission room to instrument area and instrument area to reception room sound insulations minus the direct transmission room to reception room insulation.

On Figure 2.5 the level L is plotted together with the values of x_1 and x_2 derived above. It can be seen that the two estimates of x are in reasonable agreement with each other. Although errors of 3 dB

or so are larger than those normally associated with the suite it must be remembered that the instrument area is not the perfect reverberant cavity upon which the above calculations are based. The instrument area is approximately L-shaped, has various other peculiarities of geometry, the distribution of absorbent is uncertain and the reverberation time is as low as 1.5 seconds.

We now make use of the arithmetic mean of x_1 and x_2 which we call x_3 to calculate the error in L due to this flanking path. If we regard the flanking sound as a "noise" x_3 dB below the noise plus signal in the reception room when L is being measured, it is possible to use the table in Appendix 2.1 to calculate the error (y dB) that this produces. Hence, we can calculate the insulation that would be measured if the error due to this flanking sound were not present. This corrected value of L is also plotted on Figure 2.5. It can be seen that this correction is not important except at high frequencies and even there does not exceed 1.5 dB. In the remaining sections of this chapter, whenever the insulation of the double cavity brick wall is quoted, it is this corrected value L to which we refer.

This calculation of x_1 and x_2 only takes into account airborne sound leakage through the instrument area. Other sources of sound leakage in the suite such as structure borne sound and air leaks around the window are not included. Direct evaluation of these would be a much more complicated process. However, the experiment does set an upper limit to the transmission loss that can be measured with the suite given by:-

$$LTL = L + x_3 \qquad (2.18)$$

This function is plotted in Figure 2.6 and represents an absolute limit to the values of sound insulation (which is usually within 3 dB of the transmission loss of the test panel) that can be measured by the suite.

The actual limit of the suite may well be less than this due to structure borne leakage and lie somewhere between L and LTL. The values of L quoted for the double cement faced brick wall may have more connection with the limit of the suite than the properties of the wall itself. To test whether or not this is the case, a further experiment in which a panel (or panels) of mass comparable to that of the brick wall would have to be added to it. If this produced no significant increase in the transmission loss L would represent the limit of the suite.

2.4 Brick wall experiments

2.4.1 Summary of the experiments performed

The brick wall that was used in the experiments consisted of two identical single brick walls separated by a 3.3 inch air gap. One was built into the transmission room window and the other into the reception room window as shown in Figure 2.7. Each wall was built of "Phorpres" $4\frac{1}{4}$" x $2\frac{1}{2}$" x $8\frac{5}{8}$" bricks manufactured by the London Brick Company and weighing 4lb 9oz. each. They were professionally laid using cement of specific gravity 1.75 ± 0.25 and in some of the experiments were faced with half an inch of this cement.

The experiments actually performed were as follows:-

a) The insulation between the transmission room and the reception room L_4 when the sound is generated in the transmission room and a double unsealed brick wall is in the window (Figure 2.7(a)).

b) As (a), only with a double cement faced brick wall L (Figure 2.7(b)).

c) A single brick was then carefully cut out of the reception room wall and a measurement similar to (a) and (b) was performed L_5 (Figure 2.7(c)).

d) A condenser microphone was lowered into the cavity through the hole in the reception room wall. The brick was then replaced and sealed with "plasticine". The insulation L_6 between the transmission room and the cavity resulting from sound being transmitted from the transmission room was then measured (Figure 2.7(d)).

e) The insulation L_7 between the reception room and the cavity resulting from sound being transmitted from the reception room was then measured (Figure 2.7(e)).

f) A small speaker was introduced into the cavity but was not sufficiently powerful to produce a measurable sound field in either the transmission or reception rooms. Consequently it was not possible to measure the equivalent of L_6 and L_7 in the reverse direction. However, the cavity field was sufficient to give an indication of the reverberation time of the cavity at frequencies greater than 800 Hz.

The cavity reverberation time was measured at 800, 1600, and 3150 Hz. At 800 and 3150 Hz, it was too short to be resolved by the level recorder and was consequently less than 0.05 sec. At 1600 Hz however, the reverberation time was 0.6 sec. This was probably due to standing waves in the cavity when the wavelength is equal to twice the wall separation. This corresponded to a frequency of 2 kHz at normal incidence and slightly lower frequencies at non-normal incidence, which fell within the octave band centred on 1.6 kHz. The reverberation time of the reception room was also measured.

g) Finally, the remainder of the reception room wall was knocked down to leave the single cement faced transmission room wall. The insulation L_8 between the transmission room and reception room resulting from transmission from the transmission room was then measured (Figure 2.7(f)).

2.4.2 Conclusions arising

As has already been indicated L_1 the measured transmission loss of the double cement faced cavity brick wall, might well be the result of leaking and flanking paths rather than the properties of an infinite wall. In order to investigate this possibility further, an attempt was made to relate the various measurements described in Section 2.4.1 to see if they were compatible. If it is assumed that the cavity between the walls can be regarded as resonant, we can obtain a theoretical prediction for L which we term L_{10} where:-

$$L_{10} = L_6 + L_8 + 3 \qquad (2.19)$$

This relationship can be understood as the sum of two sound insulations. The first L_6 is the insulation between the transmission room and the cavity and the second L_8 is that when sound incident on a single brick wall is received in the cavity. The 3 dB is added to L_{10} because of the proximity of the cavity microphone to the reception room wall. This causes a 3 dB increase in the sound pressure level over what it would have been if measured under homogeneous diffuse field conditions several wavelengths away from the reception room wall (assuming that the wall has an absorption coefficient less than 0.2) resulting in a consequent 3 dB increase in the "apparent transmission loss" of that wall (2.7).

The values of L_{10} calculated above are shown on Figure 2.8 together with L. It is noted that there is a wide discrepancy between L and L_{10} which requires some explanation. If L_{10} on Figure 2.8 is compared with LTL on Figure 2.6, it is seen that L_{10} is well above the capabilities of the suite and therefore, if L_{10} did, in fact, represent the transmission loss of the double brick wall, it could not possibly be measured. The reasoning behind the estimation of L_{10} assumes that the transmission loss of the remaining single brick wall on the transmission room side of the cavity is the same as the wall on the reception room side. This would be the case if the transmission loss were an intrinsic property of the brick wall but comparing the transmission into the cavity from either side L_6 and L_7 shown on Figure 2.9 this is apparently not so. In order to check that the discrepancy between these two results for L_6 and L_7 did not arise from faulty sealing of the brick that was replaced in the

reception room wall the measurement of L_7 was repeated. On a different day the cavity microphone and brick were replaced and the brick was re-sealed with "plasticine". A new measurement of L_7 was found by a different operator to differ from that previously obtained by less than 1 dB above 200 Hz. Therefore, it may be concluded that the two brick walls do not provide equal insulation. As they are identical in every other respect it was, therefore, concluded that the transmission between the cavity and the reception room was the result of flanking transmission.

It is possible to allow for the difference in insulation provided by the two walls and derive a second semi-empirical estimate L_{11} of the transmission loss of the double wall. If we consider sound travelling from the reception room into the cavity it has a drop in level of L_7. This sound in travelling from the cavity to the transmission room will suffer a further level drop of L8 dB if we assume reciprocity of sound transmission (ignoring the slight error due to the different volumes and absorption areas of the reception and transmission rooms). Assuming reciprocity once again the sum of L_5 and L_6 should (with the addition of 3 dB as in the previous case) provide a second semi-empirical estimate of L.

$$\therefore \quad L_{11} = L_7 + L_8 + 3 \qquad (2.20)$$

L_{11} is shown plotted on Figure 2.8 and is seen to be a better approximation to L than L_{10} calculated previously especially at the higher frequencies. However, it is still 10 dB or more in excess of L measured directly. From this we may conclude that the directly measured value of L not only differs from an ideal cavity brick wall in respect of the different insulation provided by each of its two leaves but there is also some error

caused by direct flanking transmission between the transmission and reception rooms. This flanking path does not make any contribution to the cavity sound field or there would have been no discrepancy between L and L_{11}. It is, therefore, a direct flanking path with an insulation such as to be insignificant when measuring a single wall but catastrophic for a double wall measurement.

In order that the results obtained so far in this chapter be compared with theory or the results of other experimentalists, it is necessary to convert the sound energy level differences that we have been discussing so far into transmission losses of the walls in question. This conversion, which relies upon a knowledge of the volume and reverberation time of the receiving room is dealt with by previous authors (1.1, 1.2, and 1.3). In Figure 2.10 the experimentally measured transmission loss of a single brick wall TL_8 (derived from L_8) is plotted together with the mass law prediction. It is noted that the experimental transmission loss is consistently 10 dB or so below the mass law prediction at all frequencies. It is indeed fortunate that the decision to knock the reception room wall down and leave the transmission one standing was taken. Otherwise the measurement of the transmission loss of a single brick wall would have been performed on the "leaky" reception room wall. Assuming that its transmission loss differed from that of the transmission room wall by the difference of L_6 and L_7 it is possible to hazard a prediction to what it might have been. Subtracting $(L_6 - L_7)$ from TL_8 we arrive at the very tentative prediction TL_9 of the transmission loss of a single brick wall mounted on the reception room side of the transmission cavity. The irregular behaviour of TL_9 which is shown on Figure 2.10 is evidence of the approximate nature of this estimate. Although the two main dips in TL_9

are separated by one octave, this is probably more fortuitious than the result of a standing wave interference effect.

On Figure 2.11, various predictions estimate the transmission loss of a double cement faced cavity brick wall. The directly measured transmission loss (TL_1 derived from L) is shown together with a semi-empirical value TL_2 derived from L_{10}. The purely theoretical predictions of simple mass law and multiple reflection theory (with reflection coefficient $\alpha = 0.9$) Reference 1.6, are also shown. It is found that the nearest approximation to TL_1 is the mass law which was calculated assuming a single panel of the combined mass which is obviously an unsatisfactory physical representation of the situation. A better estimation of the wall's ideal transmission is obtained from the semi-empirical value TL_2. Even this is not necessarily free from flanking effects and its value lies about 10 dB below that predicted by multiple reflection theory (TL_3).

The discrepancy between TL_1 and TL_2 raises the question first posed in Section 2.3.3 as to whether the wall construction itself was very relevant in the experimental results obtained for TL_1. In Figure 2.12, TL_1 is compared with the directly measured transmission loss of the double wall before it was faced with cement. The mass law predictions for both constructions are also shown. The general trend of the unsealed wall to register a consistently lower transmission loss would seem to indicate that although there is a lot of flanking sound, it appears from Figure 2.12, that the wall construction is still relevant to the amount of sound entering the reception room. However, this difference could possibly be due to a calibration error of the equipment.

2.5 Summary of conclusions

As described in Section 2.2, a method of measuring high transmission loss was developed. This method is now regularly employed in the routine measurement of high transmission loss panels. The value of the highest transmission loss that can be measured by the suite LTL (Figure 2.6) that was derived in Section 2.3 provides an upper limit to the capabilities of the suite. However, any transmission loss measured in the suite that is equal to or exceeds that measured for the double brick wall (TL_1 Figure 2.11) must be regarded with some suspicion.

The measured value of the transmission loss of a single brick wall (TL_8) is well within the most pessimistic view of the suite's capability (TL_1) and is, therefore, a valid result in so far as it is purely a function of the wall under test. The fact that it is 10 dB or so below the mass law value is no great surprise when one remembers that mass law ignores the transmission due to flexural waves. As explained in the next chapter, these waves are efficient radiators of sound above the critical frequency which, in the case of a brick wall, occurs at 160 Hz (2.9). On Figure 2.13, the value of transmission loss for a single brick wall TL_8 is compared with the results obtained by the Building Research Station (2.1). The two results are in remarkably good agreement especially when one bears in mind the fact that the Building Research Station results were the average of several field measurements which had a spread of about 5 dB.

There is, on the other hand, a great deal of doubt as to whether TL_1 represents the transmission loss of an ideal double brick wall where we define "ideal" as meaning a wall in which the wall to wall coupling is purely acoustic. Certainly the unequal insulation provided by the two

leaves represents a very serious deviation from the ideal (Figure 2.9). However, the semi-empirical prediction L_{11} which assumes that there is only acoustic wall to wall coupling allows for this inequality and still exceeds the directly measured insulation L by over 10 dB. We must, therefore, assume that the main sound transmission path relies upon mechanical coupling between the two leaves of the wall. However, before rejecting the results out of hand, one must consider the circumstances under which they were taken. The New Liverpool University Transmission Loss Suite was constructed in such a way as to keep sound leakage to a minimum. The manner in which this has been done has already been described (1.1, 1.2, and 1.3) and in very few functional buildings will such stringent precautions be taken. It is true that the basic construction of the suite relies largely upon that of its double brick wall construction for airborne sound insulation but that should not produce an unacceptably large error in the measurement of the test wall's transmission loss. The measured transmission loss TL_1 therefore, represents the best that one can hope to achieve from a practical wall. It is seen on Figure 2.14 that it is not substantially different from results obtained by the Building Research Station (2.1) which represent the average of 22 measurements in the field for both flats and houses. Also shown on Figure 2.14 are the experimental results obtained by Moeller (2.2) for the insulation afforded by a broadcasting studio wall. The results, however, are not directly comparable with the other two curves because the wall in question had a 12 inch airgap (apart from the results being for insulation as opposed to transmission loss). However, in view of the previous comments about mechanical coupling, the increase in insulation is probably more a

result of better vibration isolation employed in the broadcasting studio than being directly attributable to the wider airgap.

To conclude, it appears that an "ideal" cavity brick wall is unlikely to be obtained in practice and that such theories as multiple reflection theory (2.3) or the impedance matching of Beranek and Work (2.4), and (2.7) are largely academic in this particular case. The experimental result TL_1 is in good agreement with those of the Building Research Station but in order to have any success in making a theoretical prediction in reasonable agreement with experimental results it will be necessary to consider mechanical coupling between the two wall leaves and other flanking paths. Such a theory is being developed by Zaborov (2.8), (2.10) but for the present we must rely entirely upon empirical results.

3.0 The use of vibration transducers in the measurement of transmission loss

3.1 Introduction

In Chapter two the difficulties encountered when attempting to measure the transmission loss of a panel, by directly measuring the insulation it provides between two reverberant rooms, were discussed. In particular the difficulties and limitations due to flanking paths were considered. It is sometimes necessary to measure sound insulation in the presence of these flanking paths and it is often found in field measurements that the flanking path has a much lower insulation than the transmission path being considered (e.g., the transmission loss of a partition in a partially finished building). Consequently, a great deal of effort has already been expended in developing methods of transmission loss measurement in the presence of flanking paths (3.1). These rely upon correlation techniques (3.2), (3.3), (3.4), short pulse measurements (3.5), (3.6), measurement of sound pressure or particle velocity in close proximity to the test panel (3.7), or the use of vibration transducers (3.8), (1.2), (3.9). It is with the last of these various methods that this chapter is concerned.

In measurements with accelerometers it has previously been assumed that the surface of the test panel has a radiation efficiency of unity (3.8), (3.9). This is equivalent to assuming that the vibration of the panel is in phase at all points on the panel and consequently such an assumption where the energy flux transmitted by the panel is given by (3.10)

$$F_t = \frac{1}{2} \rho c U_o^2 \qquad (3.1)$$

(where U_o is the peak velocity amplitude of the panel from the accelerometer reading), has been termed "the piston theory". No justification for the piston theory can be put forward except for the fact that in certain circumstances it gives (3.8), (3.1), and has sometimes been wrongly claimed (3.9), to give correct results when calculating the transmission loss of the panel. The assumption that a panel radiates as a plane piston when reacting to a random incidence white noise field cannot be justified theoretically and thus the agreement between measured and predicted transmission loss using the theory is fortuitous.

Utley and Mulholland (3.9) when using accelerometers to measure the transmission loss of a single panel reported that there is a discrepancy of about 15 dB between the experimental value of the vibration amplitude of such panels and the value predicted theoretically from the mass law. Despite this discrepancy, the panels usually have a measured transmission loss close to mass law. It is also claimed (3.9), that by using the experimental panel velocity in a simple piston theory to predict the transmitted sound flux, a value of transmission loss is obtained which is in good agreement with both the mass law and airborne measurements (performed, according to BS.2750 with a slight modification (3.11)).

Thus it seems that we are faced with a discrepancy in the simple mass law and piston theories whereby a panel that has an airborne transmission loss in good agreement with mass law predictions has an experimental vibration amplitude that exceeds the mass law predictions by 15 dB; furthermore, when used in the simple piston theory this experimental vibration amplitude was claimed to predict a value of transmission

loss in good agreement with mass law and the airborne measurements. In order to investigate the above discrepancy and find the false link in the chain of argument, the preliminary calculations described in Section 3.2 were performed.

These calculations showed that if the value of vibration amplitude predicted by the mass law was substituted into the piston theory, the resultant calculated value of transmission loss exceeded the mass law by 3 dB. Thus, there appears to be no discrepancy between piston theory and mass law as a 3 dB or so error can be expected from a theory that fails to allow for the random-angle re-radiation of sound from the panel's surface. However, if this is the case, how can the experimental vibration amplitude exceed that predicted by mass law by 15 dB and yet still provide an approximately mass law value of transmission loss when substituted in the piston theory? In order to answer this question, the experiments of Section 3.3 were performed and the results are discussed, in detail, in Section 3.3.3. These results prompted an investigation into the theory of sound transmission and panel vibration which is described in Section 3.4. Finally, the conclusions arising from the whole of the chapter are summarised in Section 3.5.

3.2 The relation between simple piston theory and the mass law

In Reference (3.9) Equation 7 the velocity amplitude of a mass law panel due to a random incident field containing N plane waves per steradian, each with velocity amplitude V_I is given by:-

$$U_o^2 = \int_0^{\theta_2} \frac{2\pi N V_I^2 \cos^2\theta \sin\theta \, d\theta}{\left\{ 1 + \left(\frac{w.m \cos\theta}{2\rho c} \right)^2 \right\}} \qquad (3.2)$$

The sound energy flux incident on the panel from a random incidence field of energy density E_i is given by:

$$F_i = \frac{c}{4} E_i \tag{3.3}$$

where the total energy density E_i is related to that of one of the plane waves E_I by:

$$E_i = 4 \pi N E_I \tag{3.4}$$

Each of these plane waves has an energy flux F_I given by:

$$F_I = c E_I \tag{3.5}$$

also

$$F_I = \frac{1}{2} \rho c V_I^2 \tag{3.6}$$

combining Equations (3.3), (3.4), (3.5) and (3.6) we have for the incident flux:

$$F_i = \frac{1}{2} \pi N \rho c V_I^2 \tag{3.7}$$

Similarly combining Equations (3.1) and (3.2) we have for the transmitted flux:

$$F_t = \int_0^{\theta_L} \frac{\rho c \pi N V_I^2 \cos^2\theta \sin\theta \, d\theta}{\left\{ 1 + \left\{ \frac{w m \cos\theta}{2 \rho c} \right\}^2 \right\}} \tag{3.8}$$

Consequently, we have for the transmission coefficient:

$$\tau_p = \frac{F_t}{F_i} = \int_0^{\theta_L} \frac{2 \cos^2\theta \sin\theta \, d\theta}{\left\{ 1 + \left\{ \frac{w\, m \cos\theta}{2 \rho c} \right\}^2 \right\}} \qquad (3.9)$$

This expression is similar in appearance to the transmission coefficient predicted directly from the mass law:

$$\tau_{ML} = \frac{2}{\sin^2\theta_L} \int_0^{\theta_L} \frac{\cos\theta \sin\theta \, d\theta}{\left\{ 1 + \left\{ \frac{w\, m \cos\theta}{2 \rho c} \right\}^2 \right\}} \qquad (3.10)$$

except that τ_p has an extra $\cos\theta$ term in the numerator which leads to the 3 dB increase in transmission loss. The transmission loss resulting from these two values of transmission coefficient was calculated for a panel with surface density, $m = 0.2$ gm/cm^2 at a frequency of 1000 Hz. It was found that the transmission loss predicted by the piston theory was 21 dB and the value directly from mass law was 18 dB. The discrepancy of 3 dB or so can be attributed to the piston theory's assumption that all the sound is radiated normally.

Thus, we find that there is no theoretical discrepancy between piston theory and the mass law's assumptions concerning the panel's vibration amplitude. However, the discrepancy between this theoretical amplitude and that measured experimentally (3.9), suggested further experiments and a thorough investigation of the methods used to calculate transmission loss from experimental panel velocity.

3.3 The experiments performed

3.3.1 Details of experimental measurement

The experiments were all performed on a 7 ft 4 in by 5 ft 10 in quarter inch thick aluminium panel mounted in the aperture of Liverpool University's transmission loss suite. A white noise level of about 90 dB was produced in the transmission room in the usual way (1.1), (1.2), (1.3). The sound pressure level in the transmission room SPL_1 with respect to a reference level of 2×10^{-4} μbar $_{RMS}$ was measured using a Bruel and Kjaer microphone type 4131 in conjunction with a cathode follower type 2613 and a spectrometer type 2112 calibrated with a pistonphone type 4220. The microphone's indicated pressure level was further corrected for a random incidence field using Figure 1.17 of Reference (3.12). The results of several microphone positions were averaged and the sound pressure level in the reception room SPL_2 was measured in a similar manner. The need for such care (and specification of the exact method and equipment used) was because an absolute value of sound pressure was required in order to be compared with the panel's vibration amplitude; whereas usually in the sound transmission loss laboratory, the measured sound pressure level is compared with another measured sound pressure level and any calibration errors (apart from a small difference in the sensitivity of two microphones) are self compensating.

A light accelerometer type 4335, in conjunction with a preamplifier, type 1606, was used to measure the peak panel velocity U_o . The equipment was calibrated using a shaker table in which ball bearings vibrated audibly when the acceleration amplitude of the table reached 1 g

(1.2), (3.13). The panel velocity amplitude was then measured using a heavy accelerometer, type 4328, which required re-calibration of the pre-amplifier. The measured velocity amplitude was considerably less than the value obtained with the light accelerometer.

In order to be sure that this difference in the two measured velocity amplitudes was not due to a calibration error of the pre-amplifier, the whole experiment was repeated for both the light and heavy accelerometers. Thus, two values of panel velocity were obtained for each accelerometer, the discrepancy between the two values for a single accelerometer gave an estimate of the probable calibration error. The values of vibration amplitude and their errors are shown in Table 3.1.

TABLE 3.1

Panel velocity amplitude (U_o) at 4 kHz

	Light Accelero-meter.	Heavy Accelero-meter.	Mass-corrected value
U_o cm/sec	0.174	0.147	0.202
Error cm/sec	± 0.007	± 0.007	± 0.021

It is noted that the calibration errors are much less than the discrepancy between the values for the two accelerometers. It was, therefore, concluded that the discrepancy was due to the mass loading effect of the accelerometer upon the panel. A mass corrected value of panel velocity V_o , (3.9), was found using the formula:

$$V_o = \frac{(m_1 - m_2)\ V_1 V_2}{m_1 V_1 - m_2 V_2} \qquad (3.11)$$

where m_1, m_2, V_1, V_2, are the masses and velocities of the light and heavy accelerometers respectively. The results of this correction are shown in Table 3.1 and it is seen to increase the light accelerometer reading by about 15%.

However, if we apply the well known formula of error theory (3.14):

$$V_o(V_1,V_2) = \left\{\left(\frac{\partial V_o}{\partial V_1}\,\Delta V_1\right)^2 + \left(\frac{\partial V_o}{\partial V_2}\,\Delta V_2\right)^2\right\}^{\frac{1}{2}} \qquad (3.12)$$

to Equation (3.11) we obtain:

$$V_o = \frac{m_1 - m_2}{\{m_1 V_1 - m_2 V_2\}^2}\left\{(m_2 V_2^2\,\Delta V_1)^2 + (m_1 V_1^2\,\Delta V_2)^2\right\}^{\frac{1}{2}} \qquad (3.13)$$

The error in the mass corrected panel velocity calculated in this way is shown in Table 3.1 and is seen to represent an error of about 10%. Thus the error in applying the mass loading correction, although large (10%), (because of the subtraction of two experimental results) is less than the correction itself (15%) and, therefore, such a correction is justified. However, the above calculation illustrates the need for an accurate calibration of the accelerometers as any calibration error is multiplied threefold when the mass loading correction is applied to readings taken with the 13.42 gm. and 31.94 gm. accelerometers that were used in these experiments.

Since these experiments were performed, a less subjective method of accelerometer calibration has been introduced. The onset of ball bearing rattle (formerly detected audibly) at a peak shaker table acceleration of 1g is determined by observing the accelerometer output on an

A scale weighting network. The A scale weighting effectively suppresses (-30 dB) the 50 Hz oscillations of the shaker table but records the ball bearings' rattle thus causing a sudden increase in the meter reading at the onset of rattling. It is considered that if the experiments were to be repeated using this new method of calibration, the 10% error may be substantially reduced. However, this error is not sufficient to affect the conclusions of later sections.

The reverberation time of the reception room was measured and used in conjunction with SPL_1 and SPL_2 to calculate a value of airborne transmission loss according to BS.2750 (TL_1) which is shown plotted on Figure 3.1.

3.3.2 The piston theory calculation of transmission loss

From Equation (3.9) we have:

$$\tau_p = \frac{F_t}{F_i}$$

where, according to the piston theory F_t is given by:

$$F_t = \frac{1}{2} \rho c U_o^2 \qquad (3.1)$$

and from elementary diffuse field theory (3.15) F_i is given by:

$$F_i = \frac{c}{4} E_i \qquad (3.3)$$

but (3.10)

$$E_i = \frac{\overline{p^2}}{\rho c^2} \qquad (3.14)$$

and

$$\overline{p^2} = \overline{p_o^2} \times \text{antilog}(SPL_1/10) \qquad (3.15)$$

where p_o is the reference sound pressure level of 2×10^{-4} dyne/cm^2 RMS. Therefore, substituting Equations (3.1), (3.3), (3.14) and (3.15) into Equation (3.9) we have:

$$\tau_p = \frac{2 (\rho c)^2 U_o^2}{p_o^2 \, \text{antilog}(SPL_1/10)} \qquad (3.16)$$

The transmission loss value (TL_2), calculated by inserting the experimental values of U_o^2 and SPL_1 in Equation (3.16) is shown in Figure 3.1. A theoretical mass law value of U_o^2 was also calculated by substituting Equations (3.7), (3.3), (3.14) and (3.15) into Equation (3.2) which gives:

$$U_o^2 = \int_o^{\theta_1} \frac{\overline{p_o^2} \, \text{antilog}(SPL_1/10) \cos^2\theta \sin\theta \, d\theta}{(\rho c)^2 \left\{ 1 + \left\{ \frac{w m \cos\theta}{2 \rho c} \right\}^2 \right\}} \qquad (3.17)$$

and using the experimental value of SPL_1. It was noted that this vibration amplitude was appreciably less than the experimental one. This theoretical vibration amplitude was used in conjunction with Equation (3.16) to calculate another value of transmission loss (TL_3) which is shown on Figure 3.1. This curve shows the value of transmission loss that ought to be predicted by the piston theory if the measured vibration amplitude agrees with the amplitude predicted by the mass law. In order to reduce the possibility of human error, the calculation of TL_2 and TL_3 from the experimental and theoretical values of U_o utilised the same

computer program. A direct mass law calculation of transmission loss (TL_M) is also shown for comparison on Figure 3.1.

3.3.3 Discussion of results

Looking at Figure 3.1 it is at once seen that the value of predicted transmission loss using the mass law predicted vibration amplitude and the piston theory (TL_3) exceeds the value of transmission loss predicted by using the measured value of panel vibration amplitude and piston theory (TL_2) by about 15 dB throughout the frequency range. From this we can at once confirm the earlier findings of Utley and Mulholland (3.9), that the measured value of the panel vibration amplitude exceeds the theoretical value by 15 dB.

It also appears that at frequencies below 1 kHz, whereas the piston theory using a theoretical panel velocity overestimates the theoretical transmission loss by 4 dB or so ($TL_3 - TL_M$), it underestimates the experimental transmission loss by 7 dB or more when the experimental value of panel velocity is used ($TL_1 - TL_2$).

An even more striking discrepancy between the airborne measurement (TL_1) and the accelerometer curve (TL_2) is the pronounced dip in TL_1 at 2 kHz which is hardly noticeable in TL_2. This dip is due to the coincidence effect as the critical frequency of the panel is calculated from (3.16):

$$f_c = \frac{c^2}{1.8\ h} \left\{\frac{\rho_p}{E}\right\}^{\frac{1}{2}} \qquad (3.18)$$

to be 2,012 Hz where h, ρ_p and E are the thickness, density and Young's modulus of the panel.

If the coincidence effect was entirely due to a greater panel

response at the critical frequency, one would expect the greater panel velocity to register as a dip in TL_2. However, the accelerometer registers only a marginal drop in transmission loss. At frequencies greater than the critical frequency, the piston theory is in agreement with the airborne measurement of transmission loss. Because of this we may assume that the panel is only an efficient radiator at frequencies greater than f_c . This condition seems reasonable when one bears in mind that this condition requires that the panel's bending wavelength for a given frequency be longer than the corresponding acoustic wavelength. The panel's radiation efficiency calculated as the difference between TL_2 and TL_1 is shown on Figure 3.2.

As the reduction in transmission loss associated with the coincidence effect is caused as much by an increase in radiation efficiency as a measureable increase in panel vibration amplitude, care must be exercised when using the accelerometer (or indeed any other form of displacement or vibration transducer such as a non-contacting capacitive or inductive gauge) to measure transmission loss. If one can be certain that one is working above the critical frequency and that, therefore, the panel has an approximately unity radiation factor, the use of a simple piston theory appears to be justified. This explains the good results obtained by workers (3.1), when applying this theory to typical building structures which have a low critical frequency (e.g., for a 9 in. brick wall

f_c = 80 Hz (2.9))

However, in order to be able to calculate transmission loss of a panel in the field at frequencies in the region of, or lower than, the coincidence frequency, one requires a knowledge of the panel's radiation

efficiency. This can be found by measuring the transmission loss and vibration amplitude of a similar panel mounted in a transmission loss suite. This knowledge can be used in conjunction with the field panel's vibration amplitude to calculate the sound power passing through it. This can then be used to estimate the transmission loss of a composite structure of which the panel under investigation is the final re-radiating element (although error will be introduced because the panel will no longer have the same mode of vibration as when it was an independant leaf), or, alternatively, to find through which surface most of the sound power is entering a room.

3.4 The theory of panel vibration

3.4.1 Introduction

From the conclusions of the previous section, it is obvious that both the mass law and piston theory are inadequate descriptions of the sound transmission mechanism of a panel. Below coincidence, the mass law appears to predict the correct value of transmission loss but piston theory does not and above coincidence the situation is reversed. As the mass law theory implies a panel motion that should be in agreement with piston theory we may conclude that nowhere in the spectrum does the mass law theory correctly represent the physical facts of the situation. Consequently it was decided to study the theory of sound transmission loss and panel vibration and in particular to consider the effects of panel stiffness.

3.4.2 Development of the theory

With reference to Figure 3.3 for steady state conditions, we assume that the reflected and transmitted are plane waves with the same frequency as and hence bearing a constant phase relationship to the incident wave.

Let:- $$\phi_i = \phi_{i,o}\, e^{j w(t - \frac{x \cos\theta_i}{c} - \frac{y \sin\theta_i}{c})} \qquad (3.19)$$

$$\phi_r = \phi_{r,o}\, e^{j w(t + \frac{x \cos\theta_r}{c} - \frac{y \sin\theta_r}{c})} \qquad (3.20)$$

$$\phi_t = \phi_{t,o}\, e^{j w(t - \frac{x \cos\theta_t}{c} - \frac{y \sin\theta_t}{c})} \qquad (3.21)$$

where the phase relationships are included by allowing complex values of $\phi_{r,o}$ and $\phi_{t,o}$. If this phase relationship is to be the same at all parts of the panel, we must have:

$$\frac{\sin\theta_i}{c} = \frac{\sin\theta_r}{c} = \frac{\sin\theta_t}{c} \qquad (3.22)$$

which, for physically meaningful values of θ requires:

$$\theta_i = \theta_r = \theta_t \qquad (3.23)$$

As in the derivation of the mass law, we assume that there is no discontinuity in velocities normal to the panel, i.e.,

$$\phi_i \frac{j\,w\cos\theta_i}{c} - \phi_r \frac{j\,w\cos\theta_r}{c} = \dot{\xi} = \phi_t \frac{j\,w\cos\theta_t}{c} \qquad (3.24)$$

Substituting Equation (3.23) into Equation (3.24):

$$\phi_i - \phi_r = \phi_t \qquad (3.25)$$

Equation (3.24) also implies that the panel motion must have the same waveform as the incident wave, i.e.,

$$\xi = \xi_o e^{j\,w(t - \frac{y\sin\theta}{c})} \qquad (3.26)$$

The equation of motion for a bending wave in a thin plate is given by (3.16):

$$K_1 \frac{\partial^4 \xi}{\partial y^4} + m \frac{\partial^2 \xi}{\partial t^2} = \text{driving force} \qquad (3.27)$$

where the bending stiffness:

$$K_1 = \frac{m(h\, c_l')^2}{12} \tag{3.28}$$

c_l' being the longitudinal plate velocity. If c_l' is real the above system has no damping. It follows from a later discussion that a better agreement between theory and experiment can be obtained for non-zero damping. It was, therefore, decided to introduce an arbitrary viscous damping term K_2 into the equation of motion:

$$K_1 \frac{\partial^4 \xi}{\partial y^4} + K_2 \frac{\partial \xi}{\partial t} + m \frac{\partial^2 \xi}{\partial t^2} = \text{driving force} \tag{3.29}$$

As with the mass law the driving force must be due to the pressures acting on the panel, i.e.,

$$\text{driving force} = \rho_j w(\phi_i + \phi_r - \phi_t) \tag{3.30}$$

The assumptions of Equation (3.26) yield:

$$\frac{\partial^4 \xi}{\partial y^4} = \frac{w^4 \sin^4}{c^4} \xi \tag{3.31}$$

$$\frac{\partial \xi}{\partial t} = j w \xi \tag{3.32}$$

$$\frac{\partial^2 \xi}{\partial t^2} = - w^2 \xi \tag{3.33}$$

Substituting Equations (3.30) through (3.33) into Equation (3.39):

$$K_1 \frac{w^4 \sin^4\theta}{c^4} \xi + K_2 j w \xi - m w^2 \xi = \rho j w (\phi_i + \phi_r - \phi_t) \qquad (3.34)$$

Substituting Equation (3.25) into the R.H.S. of Equation (3.34), differentiating with respect to time and substituting for $\dot{\xi}$ from Equation (3.24):

$$\tau = \frac{\phi_t}{\phi_i} = \frac{1}{1 + \frac{\cos\theta}{2\rho c}\left\{ j w m + K_2 - \frac{j K_1 w^3 \sin^4\theta}{c^4} \right\}} \qquad (3.35)$$

which after substituting for K_1 from Equation (3.28), neglecting the first term in the denominator, and taking the case of zero damping ($K_2 = 0$), leads to an expression for transmission loss identical to one given by Cremer (3.17). Thus we have an English language derivation of this oft-quoted formula. However in the case of non-zero damping, the above expression differs from that given by Cremer (3.18),(3.16).

From Equation (3.35) by analogy with the mass law we have for the impedance of the panel:

$$Z = j \left\{ w m - \frac{m h^2 c_L^2 w^3 \sin^4\theta}{12 c^4} \right\} + K_2 \qquad (3.36)$$

whereas Cremer (3.16) gives the impedance of the panel as:

$$Z_{Cremer} = \frac{c_L^2 m h^2 w^3 \sin^4\theta}{12 c^4} + j \left\{ w m - \frac{c_L^2 m h^2 w^3 \sin^4\theta}{12 c^4} \right\} \qquad (3.37)$$

where η is the loss factor of the panel's complex Young's modulus

$$E' = E(1 + j\eta)$$

The difference between the two damping terms in Equations (3.36) and (3.37) results from the differing initial assumptions about the damping mechanism. Cremer assumed a complex Young's modulus which leads to frequency dependent hysteretic damping whereas the constant K_2 in Equation (3.29) represents viscous damping which is independent of frequency. Certainly for an infinite sheet the internal losses are best represented by hysteretic damping. However, for a practical panel the actual damping is orders of magnitude greater than that predicted by the internal loss factor of the panel material. Therefore, the main damping mechanism is not due to the panel's internal loss factor but is due to radiation damping and the imperfect reflection of bending waves at the panel boundaries. In view of the complicated and uncertain nature of the damping, it is difficult to say in what way, if any, it varies with frequency and so at this stage neither viscous nor hysteretic damping can be justified to the exclusion of the other. Therefore, the arbitrary decision to continue the investigation with viscous damping was taken.

FOOTNOTE:
Beranek (3.16) quotes Equation (3.37) with c_L (the longitudinal velocity $c_L = \sqrt{E/\rho}$) throughout as opposed to c'_L (the longitudinal plate velocity $c'_L = \sqrt{E/\rho\,(1-\sigma^2)}$ where σ is Poisson's ratio). However, from a study of Cremer's original paper (3.17) it is obvious that he intended the latter to be used.

From Equation (3.36) we can derive an expression for the transmission loss:

$$TL = 10 \log\left\{ \frac{\cos\theta}{2\rho c} \left\{ (1 + K_2)^2 + \left\{ w\,m - \frac{m\,h^2\,c_1'^2\,w^3\,\sin^4\theta}{12\,c^4} \right\}^2 \right\} \right\} \qquad (3.38)$$

The damping factor was adjusted until a best fit was obtained between the above theoretical transmission loss and that obtained experimentally (TL_1). Curves for zero damping and the best fit value (K_2 = 600 c.g.s. which corresponds to a critical frequency Q factor of 36) are shown along with TL_1 on Figure 3.4.

There is a discrepancy between the theoretical and experimental curves which is especially pronounced at 2 KHz. This is due to the fact that the points on the BS.2750 curve were measured using third octave band filters whereas the theoretical curve calculates the transmission loss at specific frequencies. This explains why the experimental curve "rounds off" such pronounced features as the sharp coincidence dip at 2 KHz. There is bound to be an error present in comparing the two curves in regions of rapidly varying transmission loss which may result in an incorrect value of K_2 being selected to give the best fit. It would be possible to calculate the theoretical transmission loss at several frequencies within a third octave band and perform a third octave analysis using a computer program developed by A. Cummings. However, it was not considered that such an investigation would justify the computer time required nor the time required to re-write the Dartmouth Algol program that had previously been used into KDF9 Algol in order to utilise the Cummings third octave program.

3.4.3 Discussion of the theory and its implications

Despite the discrepancy at the coincidence frequency itself this theory seems to be in remarkably good agreement with the airborne transmission loss (TL_1). However, if we are to take this theory at face value at frequencies in the region of 500 Hz the panel would have a mass law vibration amplitude and TL_2 of Figure 3.1 would agree with TL_3. This is clearly not the case and so like the mass law itself our theory, although it correctly predicts the transmission loss, underestimates the panel vibration amplitude by 15 dB or so.

The fault in the argument probably lies in the assumption of Equation (3.26) (which, presumably, was also made by Cremer) i.e., that the panel displacement assumes the same waveform as the incident radiation. As the panel's bending waves represent such a highly tuned oscillatory system (Q factor = 36) it seems probable that they would be excited and that the panel would, therefore, assume a waveform of the type:

$$\xi = \xi_o \, e^{j\,w(t - \frac{r}{c})} \qquad (3.39)$$

where c_s is the bending wave velocity (3.16):

$$c_s = (1.8\ h\ f\ c_l)^{\frac{1}{2}}$$

This, of course, assumes that the dimensions of the panel are large compared with its bending wavelength. If we consider a spatially infinite panel upon which a time infinite wave train of the form of Equation (3.19) is incident, we find that the correlation between the incident radiation (Equation (3.19)) and a panel deformation of the form of Equation (3.39) is zero. If, however, either the incident wave train or the panel dimensions are finite, then the correlation between the bending waves and

incident radiation is non-zero and so there will be some bending wave response.

Both these alternative conditions for bending wave response are satisfied in practice. The white noise consists of non-infinite wave trains and the panel dimensions are only a few wavelengths. The second of these conditions also causes a further complication to the panel wave-form. The reflections of the bending waves from the panel boundaries create the formation of standing waves. In order to study such effects, methods based on modal theories (such as statistical energy methods (3.19), (3.20), (3.21) and (3.22)), are needed.

If we accept that the panel has a wave form of the type given by Equation (3.39) it explains the low frequency discrepancy between TL_1 and TL_2. At such frequencies the bending waves are shorter than the corresponding acoustic waves which makes the panel a very inefficient radiator. At frequencies in the coincidence region Equations (3.39) and (3.26) become equivalent for certain specific angles of incidence which explains to some extent why the curves coalesce.

3.5 Conclusions

One of the purely experimental aspects of this work has been the confirmation of the previous findings of Utley and Mulholland (3.9) that the experimental panel velocity exceeds that predicted by mass law by 15 dB or so. From this it follows that, as there is no disagreement between piston theory and mass law, the experimental panel velocity cannot, as was claimed, be used in conjunction with piston theory to correctly predict the panel's transmission loss. Because of the dangers inherent in the indiscriminate use of this accepted method of transmission loss measurement (3.1), (3.8), (3.9), a letter was written to the Editor of the Journal of Sound and Vibration (3.23) summarising the limitations of the method.

The theory that was developed in Section 3.4 was able to predict the panel's transmission loss with great accuracy whilst being completely wrong in its prediction of panel velocity at sub-critical frequencies. We must, therefore, conclude that this theory, like the mass law itself, is giving the right answers for wrong reasons. The evidence and arguments of Section 3.4.3 suggest that in order to explain the true physical situation, we must abandon infinite panel theories.

Crocker and Price (3.22) simultaneously arrived at identical conclusions about the panel's radiation efficiency by studying the essentially modal theories of Lyon and Maidanik (3.19), (3.20), (3.21). In order to prevent a duplication of effort, it was decided not to attempt to develop a finite panel theory in view of the success that Crocker and Price were having when comparing their experimental results with the already existing theories based upon a statistical treatment of panel and room

modes. Consequently, the work of following chapters is concerned not with steady state conditions such as are encountered in the reverberant measurement of transmission loss, but with the response of structures to acoustic transients.

4.0 The theoretical response of an ideal structure to sonic booms

4.1 Introduction

A supersonic aircraft in flight produces a pressure disturbance on the ground which is commonly known as a sonic boom or bang. In the case of a supersonic transport flying at 70,000 ft. the sonic boom may be experienced in a corridor up to about 100 miles wide on the ground under the flight path of the aircraft. Two of the undesirable effects produced by the sonic boom are the annoyance it causes to people and the effect which it has upon buildings. In this thesis only the response of structures to sonic booms is considered.

Typical measured pressure-time histories (4.1) of sonic booms measured at ground level are shown in Figure (4.1) for small, medium and large aircraft flying at their cruising altitudes. The total durations (2τ) of the sonic booms shown are of the order 0.1, 0.2, and 0.3 seconds respectively, while the overpressure is about 2 to 3 lb/ft^2. The time histories in Figure (4.1) are seen to have the shape of a capital letter N. For this reason sonic booms are sometimes termed N-waves. Unless an aircraft flies supersonically at low altitude, it is unlikely that the pressure wave produced will be strong enough to cause fracture in any of the structural members of a building. However, if a building component such as a window has a built-in stress then on occasions when the sonic boom is magnified the extra stress induced by the boom can cause failure. Magnification of the sonic boom may be caused by reflection from the ground or walls, by acceleration or manoeuvring of the aircraft and by atmospheric focusing. Even if structural failure does not occur sonic booms will cause building members to vibrate and rattle

which is annoying and psychologically undesirable.

For these reasons it is necessary to understand how structures respong to N-waves and to know how the response of a structural member depends upon the structural and sonic boom parameters. With this knowledge it is possible to estimate the likelihood of damage to windows due to supersonic overflights and to make recommendations to minimise the response of structural members of buildings to sonic booms.

In this chapter a structural member is considered to be represented by a mass-spring-damper system and the sonic boom is represented by an idealised mathematical expression. The sonic boom and structural parameters are varied one at a time in order to find the dependence of the structural response upon the variations of each parameter.

Sonic booms are by no means repeatable and the pressure-time history depends upon several factors including location, atmospheric absorption and the speed, acceleration, rate of climb, size and weight of the aircraft. The three main types of sonic booms normally observed are shown in Figure (4.1). The "normal" N-wave is most often observed. However, as shown in Figure (4.1a) the positive phase duration is often not equal to the negative phase duration. The effect upon the structure of varying the ratio of the total duration to the positive phase duration is examined in Section 4.3. Sometimes, the sonic boom is "rounded" due to atmospheric absorption of the high frequency content of the N-wave (Figure (4.1b)). This effect which produces a finite rise time is examined in Section 4.4. Sonic booms are also observed with "peaks" (Figure 4.1c)). The peaks are often produced by reflection from the

ground or buildings. This effect is examined in Section 4.6. The effect of structural damping upon the response is examined in Section 4.5. Finally all these effects of variations in sonic booms are considered and a dynamic magnification factor curve (Figure (4.20)) is produced which may be used to predict possible damage to building components such as windows due to overflights of a super-sonic transport.

4.2 The Duhamel integral

Suppose that the damping in a structure is small so that intermodal coupling may be neglected, or else that the system can be idealised by an equivalent single degree of freedom system. Then in the first case, each mode, or in the second case, the equivalent system, may be represented by the simple mass-spring-damper system shown in Figure 4.2. The equation of motion for this system is:-

$$M\ddot{x}(t) + C\dot{x}(t) + Kx(t) = p(t) \qquad (4.1)$$

If the system is subjected to a force $p(\sigma)$ which varies with time σ, then provided that the initial displacement and velocity are zero, the displacement at time t during the excitation is (4.2), (4.3), (4.4), (4.5):-

$$x(t) = \frac{1}{M w_d} \int_{\sigma=0}^{t} p(\sigma)\, e^{\frac{-C}{2M}(t-\sigma)} \sin(w_d(t-\sigma))\, d\sigma \qquad (4.2)$$

where w_d is the damped angular resonance frequency which is given by:-

$$w_d^2 = w^2 - \left\{\frac{C}{2M}\right\}^2 = w^2(1-\delta^2) \qquad (4.3)$$

where w is the undamped angular resonance frequency given by $w^2 = K/M$ and δ is the critical damping ratio. Equation (4.2) is only valid if the damping is subcritical, $(C/2M)^2 < K/M$. If the excitation ends at time $s\tilde{\tau}$, then the displacement after excitation at time t (where $t > s\tilde{\tau}$), is given by Equation (4.2) with the upper limit of integration changed to $s\tilde{\tau}$.

4.3 The response to an asymmetrical N-wave

4.3.1 Introduction

The effect of a symmetric N wave upon a single degree of freedom system has recently been evaluated by several authors (4.5), (4.6), (4.7). Previous results given in the literature appear to have been incorrect (4.8), (4.9), or incomplete (4.10). However, in practice sonic booms are usually somewhat asymmetric (Figure (4.1a)). To account for this asymmetry the pulse length parameter s has been introduced (4.2), (4.11), (4.12), (4.13), (4.14).

Suppose a mass-spring system is subjected to an N-wave, the force-time history experienced by the system being (see inset to Figure 4.3):-

$$\left.\begin{aligned} p(\sigma) &= p_o(1 - \sigma/\tau), && (0<\sigma<s\tau), \\ p(\sigma) &= 0, && (-\infty<\sigma<0, \text{ and } s\tau<\sigma<\infty). \end{aligned}\right\} \quad (4.4)$$

For an undamped system $C \to 0$. The response of the system may be obtained by substituting Equations (4.4) into Equation (4.2). The response must be divided into two time regimes, the first during forced motion and the second during free motion.

4.3.2 The response during forced motion

For time $0 < t < s\tau$ from Equations (4.2) and (4.4), if the damping C is zero the displacement is:-

$$x(t) = \frac{1}{M w} \int_{\sigma=0}^{t} p_o \left(1 - \sigma/\tau \right) \sin(w(t - \sigma)) \, d\sigma \qquad (4.5)$$

$$x(t) = \frac{p_o}{M w^2} \left\{ 1 - \frac{t}{\tau} - \cos(w t) + \frac{1}{w \tau} \sin(w t) \right\} \qquad (4.6)$$

4.3.3 The response during free motion

For time $s\ \tau < t < \infty$ from Equations (4.2) and (4.4), if the damping C is zero the displacement is:-

$$x(t) = \frac{1}{M w} \int_{\sigma=0}^{s\tau} p_o \left(1 - \sigma/\tau \right) \sin(w(t - \sigma)) \, d\sigma \qquad (4.7)$$

$$x(t) = \frac{p_o}{M w^2} \left\{ \left(1 - s \right) \cos(w(s\tau - t)) - \frac{\sin(w(s\tau - t))}{w \tau} - \cos(w t) + \frac{\sin(w t)}{w \tau} \right\} \qquad (4.8)$$

4.3.4 Dynamic magnifaction factor during excitation

The displacement, X_s, due to a static force p_o is given by Equation (4.1) with $\ddot{x}(t) = \dot{x}(t) = 0$, thus $X_s = p_o / K$. However $K = Mw^2$ and thus $X_s = p_o / (Mw^2)$. Thus from Equation (4.6) the normalised displacement during excitation is:-

$$\frac{x(t)}{X_s} = 1 - \frac{t}{\tau} - \cos wt + \frac{1}{w\tau} \sin wt \qquad (4.9)$$

The times at which maxima or minima of the displacement occur are obtained by differentiating Equation (4.9) with respect to time and equating the result to zero. The maximum values of the displacement will occur at the times:-

$$t = \frac{2}{w} \tan^{-1}(w\tau) \qquad (4.10)$$

The minima of the normalised displacement will occur at times:-

$$t = 2n\pi/w \qquad (n = 1, 2, 3 \ldots.) \qquad (4.11)$$

Since Equations (4.10) and (4.11) must also satisfy the relation $t < s\tau$ it is seen from Equation (4.11) that there can be no minimum for $s\tau < 2\pi/w$.

The maximum value of the normalised displacement is given by substituting Equation (4.10) into Equation (4.9) and using half angle formulae (4.5):-

$$\frac{Xmax}{X_s} = 2\left[1 - \frac{\tan^{-1}(w\tau)}{w\tau}\right] \qquad (4.12)$$

It follows from Equation (4.10) that there is a maximum during forced motion provided $\tan^{-1}(w\tau) < (s/2)w\tau$. Thus for $s > 2$ there must always be a maximum during forced motion. This is easily

understood qualitatively if one considers the N wave as two separate impulses. For $s \geqslant 2$ the negative impulse is at least as great as the positive one. The positive impulse initially creates a positive displacement which sets up negative restoring forces. Therefore, the total negative impulse (second part of N-wave plus restoring forces) is greater than the positive one. Thus by the end of the N wave the oscillator will have acquired a negative velocity after a positive displacement which explains why there must always be a true positive maximum of the displacement. For $s < 2$ there will be no maximum during forced motion for $w\tau$ less than some limiting value.

The minimum value of the normalised displacement is found by substituting Equation (4.11) into Equation (4.9) and choosing the largest value of n which satisfies the relation $s\tau \geqslant 2n\pi/w$:-

$$\frac{X_{min}}{X_s} = -2n\pi/(w\tau) \qquad (4.13)$$

The dynamic magnification factor may be defined as the greatest maximum or minimum of normalised displacement for any value of non-dimensionalised frequency $f\tau$. The dynamic magnification factor is so named because it represents the ratio of the dynamic to static displacement of the system.

4.3.5 Dynamic magnification factor after excitation

From Equation (4.8) the normalised displacement is:-

$$\frac{x(t)}{X_s} = (1 - s)\cos(w(s\tau - t)) - \frac{\sin(w(s\tau - t))}{w\tau} - \cos(w\,t) + \frac{\sin(w\,t)}{w\tau} \qquad (4.14)$$

Maxima or minima of the displacement occur when $\frac{\dot{x}(t)}{X_s} = 0$ that is for times:-

$$t_{max,min} = \frac{1}{w} \tan^{-1}\left\{\frac{(1 - s)\sin(ws\tau) - \frac{\cos(ws\tau)}{w\tau} + \frac{1}{w\tau}}{(1 - s)\cos(ws\tau) + \frac{\sin(ws\tau)}{w\tau} - 1}\right\} \quad (4.15)$$

Substitution of Equation (4.15) into Equation (4.14) gives the maximum or minimum value of the normalised displacement after excitation; this calculation was conducted using a digital computer. Equations (4.12) and (4.13) were evaluated by hand.

4.3.6 Discussion

Plots of the dynamic magnification factor against non-dimensionalised frequency $f\tau$ are given in Figures (4.3), (4.4), (4.5) and (4.6) for several representative values of s.

It is observed that as s is increased the frequencies at which the large free response peaks occur are decreased. Increasing s also has the effect that these peaks grow in magnitude and emerge further above the curve for the greatest maximum of displacement during forced motion which is independent of s (providing $s > 1$). Fortunately, in practice, there is not a great variation in s and it is usually found that $1.6 < s < 2.2$ and for most sonic booms $s \approx 2.0$.

For a symmetric N-wave $s = 2$ and Equation (4.15) gives the solution:-

$$t_{max,min} = \tau + n\pi/w ,$$

provided $\tan w\tau \neq w\tau$.

It can be shown (4.5), that the second equation gives the values of $w\tau$ at which there is zero free motion, that is at which nulls occur. This equation is satisfied by:-

$$w\tau \approx \left(n + \frac{1}{2} \right)\pi \qquad n = 1, 2, 3, \ldots.$$

and this solution becomes progressively better as n is increased. For values of s other than 2.0 the nulls disappear although there is still a minimum of free response at certain values of w

4.4 The response to an N-wave with a finite rise-time

Suppose an undamped mass-spring system is subjected to an N-wave with a finite rise time and decay. Such an idealised N-wave (see the inset to Figure 4.7) is a good approximation to measured sonic booms (see Figure 1(b)). Using the notation of the inset to Figure 7, the force-time history of such an N-wave (for $r_1 = r_2 = r$) is:-

$$\left.\begin{aligned} p &= 0 , \quad (-\infty < \sigma < 0 , t_3 < \sigma < \infty) , \\ p &= p_o(\sigma/(r\tau)) , \quad (0 < \sigma < t_1) , \\ p &= p_o(r + 1 - \sigma/\tau) , \quad (t_1 < \sigma < t_2) , \\ p &= p_o(1 - s)\left\{\frac{(2\,r + s)\tau - \sigma}{r\,\tau}\right\} , \quad (t_2 < \sigma < t_3) , \end{aligned}\right\} \quad (4.16)$$

where $t_1 = r_1\tau$, $t_2 = (r_1 + s)\tau$ and $t_3 = (r_1 + r_2 + s)\tau$

The response must be divided into four time regimes and using a Duhamel integral approach similar to that presented in Section (4.3) the normalised displacement may be shown to be:-

$$\frac{x(t)}{X_s} = \frac{t}{r\tau} - \frac{\sin(wt)}{w\,r\,\tau} \quad \text{when} \quad 0 \leqslant t \leqslant r\tau \qquad (4.17)$$

$$\frac{x(t)}{X_s} = 1 + r - \frac{\sin(wt)}{w\,r\,\tau} - (1 + r)\,\frac{\sin(w(r\tau - t))}{w\,r\,\tau} - \frac{t}{\tau}$$

$$\text{when} \quad r\tau \leqslant t \leqslant (s + r)\tau \qquad (4.18)$$

$$\frac{x(t)}{X_s} = \frac{t - 2\tau(r+1)}{r\tau} + \frac{(r+1)\sin(w((r+2)\tau - t))}{w\,r\,\tau} - \frac{(r+1)\sin(w(r\tau - t))}{w\,r\,\tau} - \frac{\sin(wt)}{w\,r\,\tau}$$

when $(s + r)\tau \leq t \leq (s + 2r)\tau$, (4.19)

$$\frac{x(t)}{X_s} = (r+1)\frac{\sin(w((r+2)\tau - t)) - \sin(w(r\tau - t))}{w\,r\,\tau} - \frac{\sin(w(2(r+1)\tau - t)) + \sin(wt)}{w\,r\,\tau}$$

when $(s + 2r)\tau \leq t \leq \infty$. (4.20)

The dynamic magnification factor was calculated for forced motion (Equations (4.17), (4.18) and (4.19)) and for free motion (Equation (4.20)) using a digital computer program. The program calculated the displacement time history for different values of the parameters r and w and also selected the dynamic magnification factors. Typical results are given in Figures (4.7), (4.8), (4.9) and (4.10).

It is seen that the dynamic magnification factor is plotted against $f\tau'$. This non-dimensionalisation ensures that the positive impulse imparted by the N wave as r is varied remains constant. As the rise time ratio r is increased it is seen that the peak in the response during free motion which occurs at $f\tau' \approx 0.5$ increases, while the successive peaks decrease in magnitude. When r = 1.0 the dynamic magnification factor curve begins to look similar to that for a complete cycle sine pulse forcing function (see Figure 4.4 and 4.5, Reference 15). The maximum dynamic magnification factor for the sine pulse is 3.25 at $f\tau \approx 0.5$. This magnification factor is larger than the value of 2.68 produced for an N wave with r = 1.0 (Figure 4.9) because the impulse for the sine pulse is greater. Since the response is impulse dependent (10) up to values of $f\tau$ of about 0.5, it might be expected that the ratio of these maximum dynamic magnification factors be very nearly equal to the ratio of the positive impulses for these two forcing functions. This does indeed prove to be the case, since the ratio of impulses is 1.27:1 and the ratio of maximum dynamic magnification factors is 1.22:1.

4.5 The effect of viscous damping

Suppose the damped mass-spring system (shown in Figure 4.2) is subjected to an N-wave (whose force-time history is given by Equations (4.4)).

4.5.1 Forced response

During excitation, $0 < t < s\tau$ the displacement is given by integrating Equation (4.2) from $\sigma = 0$ to $\sigma = t$ where $p(\sigma)$ is given by the first half of Equations (4.4). Thus the normalised displacement may be shown to be (14):-

$$\frac{x(t)}{X_s} = 1 - \frac{t}{\tau} + \frac{2}{w\tau} - e^{-w\delta t}\left\{\left\{1 + \frac{2\delta}{w\tau}\right\}\cos(w_d\tau) + \left\{w\delta\tau + \left\{\frac{(w\delta)^2 - w_d^2}{w^2}\right\}\frac{\sin(w_d t)}{w_d\tau}\right\}\right\} \quad (4.21)$$

4.5.2 Free response

Similarly after excitation, $s\tau < t < \infty$, the displacement is given by integrating Equation (4.2) from $\sigma = 0$ to $\sigma = s$ where $p(\sigma)$ is again given by the first of Equations (4.4). The normalised displacement is (14):

$$\frac{x(t)}{X_s} = e^{-w\delta t}\left\{\left\{\left\{\tau(s-1)w\delta - \frac{(w\delta)^2 - w_d^2}{w^2}\right\}\frac{\sin\{w_d(s\tau - t)\}}{w_d\tau}\right.\right.$$

$$+ \left\{(1-s) + \frac{\delta}{w\tau}\right\}\cos\{w_d(s\tau - t)\}\Big\}\Big\} e^{w\delta s\tau}$$

$$- \left\{\left\{1 + \frac{2\delta}{w\tau}\right\}\cos\{w_d t\}\right.$$

$$\left.\left. + \left\{w\delta\tau + \frac{(w\delta)^2 - w_d^2}{w^2}\right\}\frac{\sin\{w_d t\}}{w_d\tau}\right\}\right\} \qquad (4.22)$$

From Equation (4.3) the undamped frequency $w = w_d/(1-\delta^2)^{\frac{1}{2}}$. Thus making this substitution in Equations (4.21) and (4.22), the normalised displacement may be expressed in terms of $w_d\tau$ and thus of $f_d\tau$. The dynamic magnification factor was calculated for forced and free vibration using a numerical digital computer program for a symmetric N-wave. The program calculated the response time history for different values of the damping ratio δ and selected the dynamic magnification factors as the parameter $f_d\tau$ was varied. A typical time history is given in Figure (4.11). Typical dynamic magnification factor plots are given in Figures (4.12), (4.13), (4.14) and (4.15).

The greatest true maxima or minima are plotted against $f_d\tau$ during forced motion, but during free motion the greatest absolute value of the normalised displacement is plotted. It is seen that damping has the effect of reducing the free motion considerably, especially as $f_d\tau$ is increased. However, the greatest maximum during forced motion is not as much reduced as δ is increased and the free motion at higher values

of $f_d \tau$ falls further below the forced motion curve. The damping also has the effect of smoothing out the nulls and peaks during free motion. However, the nulls and peaks still occur at the same values of $f_d \tau$ as for a symmetric N wave (see Figure (4.4)).

4.6 The response to an N-wave with shock reflections

When a sonic boom is reflected by the ground or by the wall of a building shock reflections will occur. Typical measured N-waves with reflections are shown in Figure (4.1c). A suitable mathematical representation for the force-time history of such a pulse is given by Equations (4.23) (see Figure 10 of Reference 2 or the inset to Figure 4.16). Using the notation of the inset to Figure 4.16, the force-time history of this idealised pulse is:-

$$
\left.
\begin{aligned}
p &= 0, && (-\infty < \sigma \leq 0, \quad (2+u)\tilde{\tau} < \sigma < \infty) \\
p &= p_o \left\{ 1 - \frac{\sigma(1+u)}{2u\tilde{\tau}} \right\}, && (0 < \sigma < u\tilde{\tau}) \\
p &= \tfrac{1}{2} p_o \left\{ 1 - \frac{\sigma}{\tilde{\tau}} \right\}, && (0 < \sigma < 2\tilde{\tau}) \\
p &= \tfrac{1}{2} p_o \left\{ 1 - \frac{\sigma - 2\tilde{\tau}}{u\tilde{\tau}} \right\}, && (2\tilde{\tau} < \sigma < (2+u)\tilde{\tau})
\end{aligned}
\right\} \quad (4.23)
$$

Suppose an undamped mass-spring system is subjected to a shock pulse with a pressure-time history given by Equations (4.23). Again as in Section 4.4, the response must be divided into four time regimes. Using a Duhamel integral approach similar to that presented in Section 4.3 the normalised displacement may be shown to be:-

$$
\frac{x(t)}{X_s} = 1 - \left\{\frac{1+u}{2u}\right\} T - \cos(\Omega T) + \left\{\frac{1+u}{2u}\right\} \frac{\sin(\Omega T)}{\Omega}
$$

when $0 < T < u$ (4.24)

$$\frac{x(t)}{X_s} = \frac{1}{2}\left\{ 1 - T + \frac{1}{\Omega u}\sin(\Omega(u - T)) - 2\cos(\Omega T) + \left\{\frac{1+u}{u}\right\}\frac{\sin(\Omega T)}{\Omega}\right\}$$

when $u \leqslant T \leqslant 2$ (4.25)

$$\frac{x(t)}{X_s} = \frac{1}{2}\left\{ 1 + \frac{(2-T)}{u} + \frac{1}{\Omega u}\sin(\Omega(u - T)) - 2\cos(\Omega T) + \left\{\frac{1+u}{u}\right\}\frac{\sin(\Omega T)}{\Omega} - 2\cos(\Omega(2-T)) - \left\{\frac{1-u}{u}\right\}\frac{\sin(\Omega(2-T))}{\Omega}\right\}$$

when $2 \leqslant T \leqslant 2 + u$ (4.26)

$$\frac{x(t)}{X_s} = \frac{1}{2}\left\{ \frac{1}{\Omega u}\sin(\Omega(2+u-T)) + \frac{1}{\Omega u}\sin(\Omega(u-T)) - 2\cos(\Omega T) + \left\{\frac{1+u}{u}\right\}\frac{\sin(\Omega T)}{\Omega} - 2\cos(\Omega(2-T)) - \left\{\frac{1-u}{u}\right\}\frac{\sin(\Omega(2-T))}{\Omega}\right\}$$

when $2 + u \leqslant T \leqslant \infty$ (4.27)

where $T = \frac{t}{\tilde{\zeta}}$ and $\Omega = w\tilde{\zeta}$

The dynamic magnification factor was calculated for forced motion (Equations (4.24), (4.25) and (4.26)) and for free motion (Equation (4.27)) using a digital computer program. The program calculated the displacement-time history for different values of the parameters u and $w\tau$ and selected dynamic magnification factors. Typical results for the reflection shock pulse ratio u = 0.1, 0.2 and 0.3 are given in Figures (4.16), (4.17) and (4.18) respectively. Figure (4.19) shows a comparison of the envelopes for curves with increasing values of u.

It is observed that as the reflection shock pulse ratio is increased both the forced and free motion dynamic magnification factors increase although the effect is greater for increasing $f\tau$. One very interesting feature is that the nulls which were observed for free motion for a symmetric N-wave (see Figure 4.4) are still virtually retained independant of the value of u. The reason for this is that the force-time history (Equations (4.23)) may be regarded as an N-wave with the addition of two triangular pulses separated in time by 2

Since the equation of motion is a linear differential equation, the response to these separate pulses may be found by superposition. However, there will be nulls in the free motion due to the N-wave when $f\tau \approx (2n + 1)/4$ (n = 1, 2, 3 .....), (see Section 4.3.6 or Reference (5)). However, there will also be zero free motion due to the repeated triangular pulses when $2\tau = (2n - 1) / (2f)$ or $f\tau = (2n - 1)/4$, (n = 1, 2, 3 ....). Since the values of $f\tau$ are not quite identical for the N-wave and the repeated triangular pulses, absolute nulls will not be produced. Also since $f\tau \approx (2n + 1)/4$ becomes a better solution as n increases, the nulls will become more

nearly absolute as $f\tau$ increases. Both these facts are confirmed by Figures (4.16), (4.17), (4.18) and (4.19).

4.7 Repeated N Waves

In some cases it is found that more than one N-wave is experienced at a point in space. This may be due to a variety of reasons. The first N wave may travel direct while the second is reflected from the ground. Acceleration of the aircraft can also cause two N waves. A window in a building may also experience a sonic boom directly on its outside face and then on its inside face a sonic boom which is delayed and diffracted through an opening such as a doorway.

These sonic booms may be separated or they may overlap. The analysis for the response of a simple system to repeated N waves proves complex since there are four time regimes for the overlapping case and four for the non-overlapping case.

For the case of the free motion, the results are very simple and tractable. It may be shown that the displacement due to each shock pulse during free motion may be expressed as a sine wave.

Let the free response due to the first shock pulse be:-

$$\frac{x(t)}{X_s} = \sin (wt'). \qquad (4.28)$$

Then the free motion displacement due to the second shock pulse is:-

$$\frac{x(t)}{X_s} = A \sin \left(w (t' - \bar{t}) \right) , \qquad (4.29)$$

where t' is the time measured from a displaced origin, $\bar{t}$ is the time difference between the pulses and A is the relative magnitude of the second pulse. Thus the total free motion displacement is (summing Equations (4.28) and (4.29)):-

$$\frac{x(t)}{X_s} = B \sin (wt' - \phi) \quad , \tag{4.30}$$

where $B = \sqrt{1 + A^2 + 2A \times \cos (w\bar{t})}$, (4.31)

and $$\tan \phi = \frac{A \sin w\bar{t}}{1 + \cos w\bar{t}} \tag{4.32}$$

when $A = +1$, $B = 2$, for $w\bar{t} = 0, 2\pi, 4\pi, \ldots$ and $B = 0$ for $w\bar{t} = \pi, 3\pi, 5\pi, \ldots$. Thus as one might expect the dynamic magnification factor for two N-waves can be increased by a value up to twice that for a single N-wave.

The results for forced motion are more complicated although somewhat similar results are found. Again the dynamic magnification factor can be increased to twice the value for a single N-wave.

4.8 Discussion and conclusions

Building components will be subjected to a variety of N-wave shapes during overflights of a supersonic transport (see Figure (4.1)). It is thus desirable to determine an upper limit to the dynamic magnification factor curve against non-dimensionalised frequency $f\tau$ which will encompass the effects of these sonic boom variations. Such a curve, Figure (4.20), was produced by studying Figures (4.6), (4.10) and (4.15). It is seen that increasing the values of s, r and u tends to produce higher dynamic magnification factors and to cause some shift in the non-dimensionalised frequency $f\tau$ at which peak responses occur. However, increasing values of structural damping δ cause a marked decrease in response particularly for free motion as $f\tau$ increases. Thus it was necessary to choose upper values of s, r and u and a representative value of δ before Figure (4.20) could be drawn. With the supersonic transport and with windows particularly in mind, these upper values where chosen to be $s = 2.2$, $r = 0.5$, and $u = 0.2$. A representative value of $\delta = 0.02$ was chosen for the critical damping ratio for a window.

It is seen that the envelope given in Figure (4.20) rises to a maximum value of 2.5 at $f\tau = 0.5$ and then at high values of $f\tau$ assumes a value of 2.0. The assumption is made that increases in the dynamic magnification factor at higher values of $f\tau$ due to the values of s, r, and u chosen, are reduced by the damping so that an asymptotic value of the dynamic magnification factor of 2.0 is reached at high values of $f\tau$

Figure (4.20) should be useful in a study of the possibility of damage to windows and other building structural members due to overflights by a supersonic transport. It is foreseen that the curve in Figure (4.20)

is dependent upon the maximum values of s, r, and u chosen and the assumed value of δ . However, it is also seen that the resultant curve is not too sensitive to small changes in the values of these parameters. In order that these results be more freely available they have been published in detail (4.14) and provide an aid to the calculation of sonic boom response that has already been requested, used and acknowledged (4.16).

One interesting result shown in Figures (4.11), (4.12), (4.13), (4.14), and (4.15) is that increasing structural damping causes a considerable reduction in response in all regimes with the exception of the first maximum during forced motion. It would seem very worthwhile if the internal damping ratio of a window could be raised possibly by the use of a different support. This should at the very least reduce the free vibration considerably, hence reducing the psychologically bad effect of rattling or vibration of a window when it is excited by a sonic boom.

5.0 The Experimental investigation of the response of a structure to Acoustic transients. (The Shock Tube)

5.1 Introduction

In order to verify whether or not the Duhamel Integral technique of the previous chapter could accurately predict the response time history of an actual structure to an acoustic transient, it was decided to perform a series of experiments making use of a shock tube. The experiments of Crocker (5.1), (5.2), (5.3), showed that if a small explosive charge is detonated at the open end of a metal tube of square cross-section, the resultant pressure time history contains two shock waves and is almost identical (except for time and pressure scaling factors) to the time history of the sonic boom. Although there are more predictable and, therefore, reliable methods of generating experimental N waves (5.4), the "Blunderbuss" facility requires a great deal of precision engineering, compressors and diaphragm bursting mechanisms which make it a very costly piece of equipment. However, the simple shock tube that was used in these experiments consisted of a steel tube from stock, driven by a commercially available firework, and consequently, was remarkably inexpensive in comparison.

The aim of the experiments was to use this simple tube to produce an N wave which would then impinge normally upon a simply supported steel panel. The N-wave pressure time history was recorded by photographing the oscilloscope trace of a microphone's output. The resultant panel response was recorded in a similar manner using strain gauges. The detailed description of the tube's construction and instrumentation is given in Section 5.2. and the success in producing satisfactory N waves in Section 5.3.

In Section 5.4 the design and construction of the test panel's simple support is described. In order to have any success whatsoever in predicting the panel response, it is necessary that the supports provide a known set of boundary conditions. Of the various possible theoretical boundary conditions possible, clamped-clamped, and simply supported are the two most likely to be achieved experimentally and, therefore, met in practice. In order that the plate represent a window as nearly as possible, a simply supported panel was chosen for the analysis as that most closely corresponding to the boundary conditions of a real window. At first thought it appears that the clamped-clamped boundary conditions are easier to achieve experimentally. It is true that a clamped-clamped panel is easier to construct. However, due to thermal expansion an experimental clamped-clamped panel can experience a surface tension which produces membrane effects in the panel's response. Worse still, it can experience a surface compression which produces "oil-canning". Therefore an experimentally clamped panel may not be mathematically, what it appears to be. Finally not only is a simple support a better representation of a window and unlikely to be affected by spurious effects such as oil-canning, it is also simpler to analyse mathematically. This is not of great importance in this chapter where the straightforward panel response and strain are calculated, but is important in obtaining a solution to the panel-cavity problem of the following chapter.

In Section 5.5 the multi-mode response (and strain) of the panel is calculated using Duhamel technique and compared with the experimental values in order to see whether better agreement can be obtained than was obtained by previous authors. On Figure 9 of Reference (5.3) the theoretical and measured time histories bear little correlation to one

another. By eliminating "oil-canning", the higher modes excited by grazing incidence and the difference between the experimental and theoretical physical conditions, it is hoped that this may be improved. In view of the findings of Section 5.2.3 concerning the triggering of the oscilloscope, even the previous claim that "the first measured strain maximum is overestimated by only 13%" (5.3), requires thorough investigation.

In Section 5.6 the findings of the chapter are summarised and in particular from the results of Section 5.5 whether or not the assumption of the following chapter, that a two-mode analysis can effectively represent the physical situation, can be justified.

5.2 Construction and instrumentation of the shock tube

5.2.1 Construction

Basically the tube consisted of a 10 inch square steel tube with quarter inch walls which was purchased from stock. As the tube weighed 33 pounds per foot it was cut into manageable sections and mounted on castors as shown in Figure 5.4. The first section to section join was by means of two flanges bolted together and sealed with a rubber gasket. The other joints contained no vibration bridge and were sealed with waterproof sticking plaster (from the inside where possible) in order that the inner surface remain flush. It was necessary not to have a vibration bridge between the tube and the tail-piece in order that flexural waves in the tube excited by the explosion should not directly excite the test panel. However, even when the test panel excitation was purely acoustic the flexural waves produced undesirable secondary acoustic waves as described in Section 5.3.3. The end plate which contained the simply supported test panel was bolted to the flange of the tail piece and sealed with a second rubber gasket. The general lay-out of the tube and its associated instrumentation is shown in Figure 5.1. At a later date a damping compound described in Section 5.3 was added which changed the appearance of the tube.

5.2.2 Instrumentation - General considerations

In selecting the instruments to be employed with the shock tube, and in particular the microphone, one was largely working in the dark in

so far as the exact magnitude and form of the signal was uncertain. Once these factors are known it is possible to exercise discretionary choice in selecting the most suitable instruments, but in order to discover these factors, the instruments have to be employed and purchased. There was no alternative but to assume that the results would be similar to those obtained by Crocker (5.1), (5.2), (5.3), and hope that an American "Cherry-bomb" was comparable in explosive power to a British "Mighty Demon" etc. It was assumed that the peak overpressure would be about 4 p.s.i. and that the positive phase duration τ would be about 3 milliseconds.

With the aid of reference (5.5) it was then a simple matter to calculate the frequency range that the instruments required in order to record the N-wave with the minimum of distortion. For $\tau \approx 3$ milliseconds, in order that the error in the measurement of τ be 1% or less the transducer's lower cut-off frequency should be 2 Hz. Similarly in order that the error in the measurement of peak overpressure be 1% or less the transducer's upper cut-off frequency should be 200 kHz. Therefore, the instrumentation requires the surprisingly large frequency range of 2 Hz to 200 kHz in order to adequately record the N-wave.

5.2.3 Pressure measurements

Although the original experiments of Crocker had used a "Photocon" microphone it was considered desirable that Bruel and Kjaer equipment be used if at all possible in order that it be compatible with the existing amplifiers etc. It was found that a Bruel and Kjaer quarter inch condenser microphone, Type No.4136, when used in conjunction with the usual cathode

follower, Type 2615, did not have a sufficiently wide frequency range. However, the new preamplifier, Model 2618 (which at the time was still in the final stages of development which caused considerable delays) has a frequency range of exactly 2 Hz to 200 kHz and so appears admirably suited for the job in that respect. However, the quarter inch condenser microphone becomes non-linear at 180 dB (4.16 peak p.s.i.) and damages at 184 dB (6.59 peak p.s.i.). In view of the fact that the shock tube had almost twice the cross-sectional area of Crocker's it was considered unlikely that these pressures be encountered and so the above microphone and preamplifier were purchased and employed.

The microphone had its protective cover removed and was mounted in a bush which was flush fitting in the back plate (Figure 5.6) alongside the test panel (Figure 5.3). The preamplifier (which was rigidly attached to the microphone) is shown in Figure 5.3. The pressure signal then passed from the preamplifier to a Bruel and Kjaer microphone amplifier, Type No.2603, and then to an E.M.I. oscilloscope, Type No.WM16. The resultant trace was photographed using a Telford, Type A.513, camera with "Polaroid" film. The oscilloscope was in a single-shot mode and a time exposure was used. A block diagram of the equipment is shown on Figure 5.5.

Although with the single-shot, time exposure technique it was not necessary to trigger the camera shutter, it was still necessary to trigger the oscilloscope time base itself. It was decided to employ a second microphone to trigger the oscilloscope externally before the shock wave reached the quarter inch microphone. This would provide a complete trace of the pressure time history including the rise of the first shock front. It was feared that unless this first shock was observed (which required that the initial part of the trace be undisturbed) by use of the external trigger, some unknown portion of the trace would be lost.

If the signal triggers itself internally the first part of the trace to be observed is the N-wave's steady decline.

In order to see whether these fears were justified or not the following subsidiary experiments were performed. Ideally it would have been preferable to photograph pressure time histories with the oscilloscope on internal and external trigger and compare the two photographs. Unfortunately, the waveform produced by the fireworks was not consistent enough for this approach to be very meaningful. However, it was found that a highly reproducible waveform could be obtained by tapping the test panel and observing the resultant strain (see Section 5.2.4). With practice it was found that with a free-running time base a very consistent initial peak strain could be obtained (Figure 5.7(a)). When the time base was set to internal trigger however only the tail-end of the decay was observed (Figure 5.7(b)). Photographs of the form of Figure 5.7(a) and Figure 5.7(b) were found to be highly reproducible and without there being any conscious change in the "tapping level" it was possible to produce an "(a)" followed by a "(b)" then an "(a)" and a "(b)" again. Hence by using the internal trigger a great deal of the signal is lost and so all the measurements were taken using the external trigger.

The reason why so much of the signal was lost in the time between the internal trigger signal being received and the time base actually firing was probably due to a fault in the oscilloscope being used. However, even when using a reliable oscilloscope some signal is lost when used in the internal trigger mode. This is apparent from a study of Figure 8 of Reference (5.3). The oscilloscope was on internal trigger when this photograph was taken, the time base was assumed to have fired when the N-wave reached the first microphone. As one would expect from the microphone separation of 9 inches, the signal from the second microphone is about $\frac{3}{4}$ of a millisecond behind that from the first, as can easily

be seen by observing the position of the second shock. That being the case one would expect that if the time base fired when the first shock reached the first microphone, the signal from the second microphone ought to have an initial $\frac{3}{4}$ of a millisecond of undisturbed trace. This is not found to be the case and so the first shock must have reached the second microphone before the time base fired. Therefore the trace from the first microphone has lost at least $\frac{3}{4}$ of a millisecond if not more. This failure to record the whole of the incident N-wave therefore, throws the previous experimental observations (5.1), (5.2), (5.3), into doubt.

The oscilloscope amplifiers were not properly calibrated and so it was difficult to obtain an absolute value of acoustic pressure from the oscilloscope trace. To minimise the possibility of error which may arise from the non-specification sensitivity of the microphone, preamplifier, amplifier or oscilloscope a pistonphone calibration of the whole system was undertaken. The oscilloscope trace resulting from the microphone being coupled to the 124 dB pistonphone was too small to be observed with the overall sensitivity set to record an explosive's pressure time history. However, if the sensitivity of the microphone amplifier was increased by 40 dB the pistonphone waveform was now equivalent to a signal of 164 dB at the original sensitivity and provided a measurable trace. A single-shot photograph of such a trace was taken and used to calibrate both the overpressure and the time-base (from a knowledge of the pistonphone frequency measured by a digital frequency counter) of the oscilloscope.

5.2.4 Strain Measurements

Although it is unlikely that the strain time history vary as rapidly as that of the pressure producing it (in order to do so it would require a mass-less panel) it was decided not to pre-judge the situation too much by employing a strain measurement system which imposed a serious frequency limitation. It is found, as was expected, that the panel response and strain, can be adequately described by the first few modes of the panel, which fall within a somewhat limited frequency band. However, if the measuring system employed had only been capable of measuring frequencies within this band the above conclusion could hardly be justified.

Because of the difficulties usually encountered when using non-contacting displacement gauges, and the ease with which the theoretical predictions of modal panel displacement can be converted into strain for comparison with experiment, it was decided to employ strain gauges to measure the panel response. A rosette of two orthogonal foil strain gauges, Kyowa KF2 D1 was cemented to the centre of the test panel, as shown in Figure (5.2), using EP18 cement in order to measure strain along the panel's major and minor axes (x and y directions). As it was only dynamic strain with which we were concerned the gauges were not temperature compensated.

The gauge was used in conjunction with a "Peekel" bridge and amplifier unit type GRL 1. which was used in the $\frac{1}{4}$ bridge mode. The unit had a frequency response of D.C. to somewhere between 120 kHz and 400 kHz depending on the sensitivity. The strain gauge amplifier output was recorded on the second trace of the oscilloscope which was triggered together with the first (it being a single gun scope in the switched mode)

by the external trigger microphone. In order to calibrate the strain the strain gauge amplifier had a position in which, when correctly calibrated by adjusting a potentiometer it gave a D.C. signal of 10 volts (measured on an "AVO"). This voltage when fed onto the oscilloscope's second trace gave it a deflection equivalent to that which would be obtained from a f.s.d. (of the amplifier) strain. Hence it was not necessary to make any assumption about the oscilloscope amplifier sensitivity but merely to compare the strain trace deflection with that produced by the calibrating D.C. signal, multiply this ratio by the strain gauge amplifier's f.s.d. and make a slight correction for the gauge factor in order to obtain an absolute value of strain for comparison with the theory of Section 5.5 and the following chapter.

5.3 Experimental Waveforms and the Result of Tube Damping

5.3.1 General Observations

Initially it was hoped that by exploding a common firework in the open end of the tube N-waves similar to those obtained by Crocker, (5.1), (5.2), (5.3), would result. However, this shortly proved not to be the case as the photograph of Figure (5.23) shows there to be no stern shock and a very ill-defined negative phase. This was a normal incidence shock wave, the microphone being mounted in the end plate. The peak overpressure was 4.2×10^4 c.g.s. (0.625 lb/ft^2) and the positive phase duration was 1.5 milliseconds, This waveform was by no means reproducible in shape or intensity. The positive "hump" before the bow shock was not always present and sometimes there were many secondary waves following the initial wave.

As Crocker's N-waves were obtained for grazing incidence the microphone was fitted in the side wall of the shock tube and the photographs of Figure 5.24 were obtained. Figure (5.24(a)) was a good example of a "clean" waveform whereas Figure (5.24(b)) illustrates the variations that may occur. In Figure (5.24(a)) the waveform has a negative phase but this has about half the pressure amplitude of the positive phase. The negative phase intensity of 0.15 lb/ft^2 had not been sufficient to create the piling of a stern shock. In Appendix A5.2 it is calculated that a wave starting with the shape of Figure (5.24(a)) and negative pressure amplitude of 0.45 lb/ft^2 would form a stern shock in the shock tube. Obviously Figure (5.24(a)) has already experienced some shock piling and so in order that a stern shock form within the 29 ft. of tube available a negative pressure amplitude of 0.6 lb/ft^2 would be required. With this in mind the firework manufacturers were asked to produce an explosive charge of approximately this pressure amplitude.

The charges supplied were detonated electrically which took some of the athletics out of the photographic procedure. The charges were detonated by a foot operated switch which allowed the operator two free hands to protect his ears. The waveform produced for normal incidence is shown in Figure (5.25). Although the pressure amplitude was 1.3 lb/ft^2 the almost complete lack of negative phase prevented the formation of a stern shock.

The results obtained from a second more powerful electrically detonated charge are shown in Figure 5.26. The positive pressure amplitude was increased only marginally to 1.4 lb/ft^2 and a large proportion of the extra energy available appears in the form of secondary waves.

A third type of electrically detonated charge which was claimed to be even more powerful was found to produce a pressure amplitude of 1.2 lb/ft^2. Their variability is illustrated by Figures (5.27(a)) and (5.27(b)) which are photographs of two of the charges detonated within a minute of each other. However, they do not vary as much as the firework waveforms as illustrated by Figure (5.28).

In view of the unpredictable nature of the explosives used and the small negative phase of their waveforms it was decided to accept the waveforms as they were rather than continue in the search for an ideal N-wave. If the experimental response and strain of a panel to an arbitrary acoustic transient, (which is what this and the following chapter are primarily concerned with), can be predicted by a theory, the same theory can presumably be used with confidence in predicting the response to an ideal N-wave. This obviously precludes the use of closed form solutions for the theoretical panel response and requires Duhamel integral technique using a numerical analysis of the pressure waveform.

5.3.2 Calculation of the shock velocity

With the oscilloscope on a slow timebase it is possible to observe a second shock wave as shown on Figure (5.29). It is presumed that this second disturbance is due to reflection of the shock wave when it returns to the open end of the tube. It is observed that the pressure of the reflected wave is "reversed" as one would expect from open-ended reflection. Furthermore, if one uses the time delay of the second wave and assumes the above explanation of open end reflection one can calculate the wave's propagation velocity as being 1140 ± 30 ft/sec. As this is approximately equal to the velocity of sound in air the interpretation of Figure (5.29) was correct the measured waveforms being beyond doubt purely acoustic (as opposed to tube vibration) phenomona.

Furthermore, using Equation (5.1) extracted from Reference 5.11 Equation (19.59) (derived from the Rankine Hugoniot equations), we have for the velocity of a shock front V of overpressure Δp travelling into an undisturbed medium of pressure p_1 :-

$$V = c \left[1 + \left(\frac{\gamma + 1}{2}\right) \frac{\Delta p}{p_1} \right]^{\frac{1}{2}} \qquad (5.1)$$

For $\Delta p = 1.3$ lb/ft^2 , $p_1 = 14.7$ lb/ft^2, $\gamma = 1.4$, and taking the velocity of an infinitesimal sound wave (c) from Reference (5.12) we have:-

$$V = 1124 \times 1.04 = 1170 \text{ ft/sec.}$$

which is in reasonable agreement with the experimental value.

5.3.3 The effect of tube damping

Many of the experimental waveforms were complicated by secondary waves such as those on the upper traces of Figures (5.30) and (5.31). These waves were due partly to discontinuities in the tube's internal geometry, and partly to the tube "ringing" and exciting secondary acoustic waves. The tube discontinuities were eliminated as much as possible by removing firework debris from the tube at frequent intervals, and also by sealing the airgap between different tube sections as smoothly as possible with waterproof "elastoplast" (internally where accessible).

The first attempt at tube damping was to drape felt over the tube but this did not meet with much success as the photographs of Figures (5.30) and (5.31) were taken with the felt in place. Eventually the tube was covered with a layer of "Aqua-Plas", a commercially available damping compound. It is difficult to assess the effectiveness of this treatment quantitatively because of the non-reproducibility of the results but in general, it seemed to provide a substantial reduction of the secondary waves. However, these secondary waves were not completely eliminated and unlike Crocker's results (5.3) there is no region in the pressure time history that can truly be called "free response".

5.4 The Design and Construction of a Simple Support

5.4.1 Theoretical Considerations

A simple support is defined as being the type of support provided by an ideal pair of knife edges situated at the extremities of the panel.

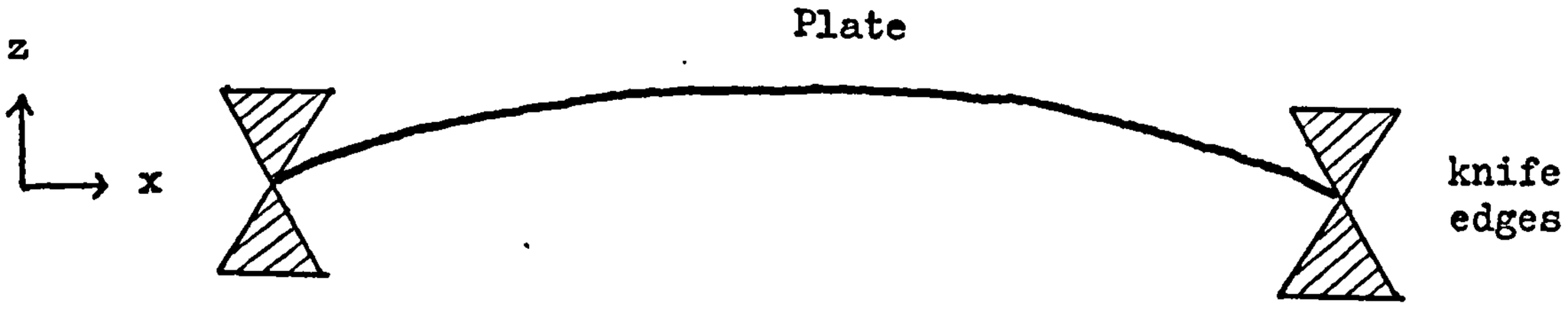

AN IDEAL SIMPLE SUPPORT

These supports prevent lateral (z) displacement but allow the panel to pivot freely with no bending moment at the panel extremities. Mathematically this is equivalent to:-

$$z = \frac{\partial^2 z}{\partial x^2} = 0 \quad \text{at } x = x_1 \text{ and } x_2 \qquad (5.2)$$

In order to achieve this condition experimentally a knife-edge type of support is unlikely to be successful, for several reasons. In the above diagram the panel is assumed to be infinitely thin whereas a panel of finite thickness would experience a bending moment between the grip of the opposing knife edges. A single knife edge may be used to overcome this in the civil engineering type of problem where gravity ensures that the support reaction is always upwards but this is obviously

not applicable for an acoustic problem with a vertically mounted plate. It is also unlikely that the knife edge support could give an airtight seal, which is essential in the following chapter, without resorting to some form of gasket or sealing compound that would produce undesirably high damping. Therefore, it was decided to try to achieve the simple support conditions expressed in Equations(5.2) by mounting the panel on thin shims in the (z) plane that would provide negligible bending moment but resist edge displacement. In Appendix A5 the effect upon a panel of such shim supports is studied mathematically and compared with some experimental results obtained by Parrott. The conclusions of this Appendix influenced the design of the actual constructions employed.

5.4.2 The actual constructions employed

Before the theoretical investigations of Appendix 5A1, the experimental support shown in Figure 5.8 was constructed. Figure 5.9 shows the decay of strain in this construction after the panel had been excited by a shock wave. Although the decay is not that of a pure sine wave there is an obvious fundamental frequency present which, upon measurement, is found to be 270 Hz compared with a theoretical value of 515 Hz for a perfect simply supported panel. This discrepancy was attributed to the large length of free shim which allowed lateral movement at the panel boundaries. Such a panel was obviously unsuitable for a theoretical analysis of its response.

Following the findings of Appendix 5A1 the experience gained above, and the experimental results of Parrott, a new shim support shown in Figure 5.10 was designed. There then followed a search for a

satisfactory adhesive. "Araldite" proved too brittle, whereas "Evo-stick" created a thick visco-elastic layer which provided too much damping. Other adhesives were tried without success but eventually the problem was solved with "Evo-stick" diluted with petrol. The dilution allowed a thin even layer of the adhesive to be applied without any of the "balling" usually associated with a "rubbery" glue. This type of support was used on a 17cm by 11cm 0.0813cm thick panel which was found to have an experimental frequency of 221 Hz compared with 229 Hz given by the theory (see next section).

It is this panel and support that is used in the experimental investigations in the remainder of this chapter.

5.4.3 Investigation of the panel properties (The Damping Dilemma)

Twenty four hours after the construction on the 4th March 1969 of the simple support described in the previous section, some experiments were performed to determine its fundamental natural frequency w_{11} and critical damping ratio δ. These parameters were measured by two different methods and the results compared.

The first experiment consisted of tapping the panel and photographing the resultant strain (Figure (5.11)). By comparing the "screen wavelengths" of the pahel strain and pistonphone on Figure 5.11, the panel appears to have a fundamental frequency of 221 Hz compared with a theoretical value of 229 Hz. This close agreement with the theory is most encouraging when one bears in mind that such a discrepancy could be accounted for as an error of one thousandth of an inch in the measurement of the panel thickness (0.032 inches). As the panel had an anti-corrosive surface treatment such an error is not unlikely.

In order to measure the strain decay, the time base of the oscilloscope was slowed down and the photograph of Figure 5.7(a) was obtained. On Figure 5.12 the successive peak to peak heights of the oscillations of Figure 5.7(a) are plotted on log-linear graph paper. Apart from a slight regular fluctuation (due to electrical noise from the strain gauge amplifier) the graph is a good example of an exponential decay from which we may calculate the critical damping ratio δ. From elementary damping theory of the simple harmonic oscillator the amplitude at time t is given by:-

$$x(t) = x_o e^{-w \delta t} \qquad (5.2a)$$

where x_o is the amplitude at t = 0. From Equation 5.2a it follows that:-

$$\delta = \frac{\ln (Xo/Xn)}{2\pi N} \qquad (5.3)$$

where Xo and Xn are the heights of the initial and Nth subsequent peaks respectively. Applying Equation (5.3) to Figure 5.12 we find that $\delta = 1.3\%$.

The second experiment involved plotting the panel's resonance curve in response to acoustic excitation. The experimental technique which involved exciting the panel with plane waves from the transmission loss box (1.3) is illustrated in Figures 5.13 and 5.14. The resultant resonance curve is shown in Figure 5.15 from which the panel's resonant frequency is 219.5 Hz. It can be shown that the half power width of the resonance curve (Δ w) is given by:-

$$\Delta w = 2 \delta w_r \qquad (5.4)$$

where w_r is the resonant angular frequency. Applying Equation (5.4) to Figure 5.15 we find δ = 0.82%.

Clearly something appears to be wrong to account for the two widely divergent values of δ. The fundamental principles of elementary damping theory have been disputed by Naylor (5.10) and his assertions were studied but were found to be, in the author's opinion, invalid. Consequently it was decided to repeat the experiments already performed, making modifications wherever possible to improve the accuracy. The accuracy of the resonance curves was increased by using a filter to remove the electrical noise and also by monitoring the sound field. The sound field was adjusted to a constant intensity (105 dB) (measured through the same filter as the strain) at each frequency at which the strain was measured. The equipment used is shown on Figure 5.16 and a resonance curve obtained on the 21st March using this new improved technique is shown in Figure 5.17. This experiment gave the fundamental resonant frequency of 220.6 Hz with δ = 0.585%. Thus the critical damping ratio seems to be reduced with each successive measurement. In order to compare this resonance curve δ with a decay curve δ it was decided to investigate the decay after acoustic excitation so that the amplitudes of vibration be the same in both cases (lest non-linear damping give rise to a discrepancy). Figure 5.18 shows the decay of the acoustic excitation in the sound transmission loss box when the loudspeakers are switched off, which is almost instantaneous in comparison with the subsequent decay of panel strain (Figure 5.19). The panel decay is analysed on Figure 5.20 which is complicated by electrical noise as no filter was employed. From the three straight lines drawn on Figure 5.20 we obtain values of 0.446%, 0.495% and 0.565% for the minimum, most probable, and maximum values of δ.

Although these decay results are not in perfect agreement with the values of the resonance experiment they are of the same order and vastly different from those of the first decay experiment.

It therefore appears that δ has been decreasing during the series of experiments. The final proof of this is seen if we compare the decay of strain after tapping on the 5th and 24th March, shown on Figures 5.7(a) and 5.21 respectively.

Figure 5.22 shows the resonance curve obtained for the first asymetric mode (3,1) from which we obtain $f_{3,1} = 721$ Hz compared with a theoretical value of 770 Hz. This small discrepancy can be explained by an error in the panel dimensions. In order to obtain better agreement with the experimental response of the panel to N-waves it was decided in the light of these preliminary experiments, to assume that the thickness of the steel panel was 0.031 inches as opposed to the micrometer reading of 0.032 which included an anti-corrosive zinc coating. This assumption leads to panel natural frequencies of 221 and 743 Hz for the two modes mentioned above.

5.5 The Analysis of the Panel Response

5.5.1 The general theory

The response of the simply supported panel G (x,y) was analysed into its normal modes such that:

$$G(x,y) = \sum_{n=1}^{\infty} \sum_{m=1}^{\infty} q_{nm} \phi_{nm} \qquad (5.5)$$

where q_{nm} is the generalised displacement of the n,m th mode with mode shape ϕ_{nm} given by:

$$\phi_{nm} = \sin\left(\frac{n \pi x}{a}\right) \sin\left(\frac{m \pi y}{b}\right) \qquad (5.6)$$

where a and b are the panel dimensions in the x and y directions respectively. The set of modes given by Equation (5.6) satisfy the panel boundary conditions (Equations5.2) and are a complete set of orthogonal modes such that by a correct choice of generalised displacements they can be used to represent any arbitrary panel deformation.

For a given excitation such as a pressure p(x,y,t) on the panel surface the generalised displacements may be obtained as solutions of the Lagrange equation of motion:-

$$M_{n,m} \ddot{q}_{n,m}(t) + C_{n,m} \dot{q}_{n,m}(t) + K_{n,m} q_{n;m}(t)$$

$$= L_{n,m}(t) \qquad (5.7)$$

where:-

$M_{n,m}$ is the generalised mass

$$= \rho_p T_p \int_{x=o}^{a} \int_{y=o}^{b} \phi_{n,m}^{2}(x,y)\, dx\, dy \qquad (5.8)$$

$C_{n,m}$ is the generalised damping coefficient

$$= 2M_{n,m}\, w_{n,m}\, \delta_{n,m} \qquad (5.9)$$

$K_{n,m}$ is the generalised stiffness

$$= M_{n,m}\, w_{n,m}^{2} \qquad (5.10)$$

$L_{n,m}(t)$ is the generalised force at time t

$$= \int_{x=o}^{a} \int_{y=o}^{b} \phi_{n,m}(x,y)\; p\,(x,y,t)\, dx\, dy \qquad (5.11)$$

T_p is the panel thickness

ρ_p is the panel density

$\delta_{n,m}$ is the critical damping ratio

$w_{n,m}$ is the undamped angular resonant frequency of the panel

$p\,(x,y,t)$ is the pressure time history on the panel surface.

For a simply supported panel the generalised mass is given by:-

$$M_{n,m} = \rho_p T_p \int_{o}^{a} \int_{o}^{b} \sin^2\left(\frac{n\pi x}{a}\right) \sin^2\left(\frac{m\pi y}{b}\right) dx\, dy$$

$$= \frac{\rho_p T_p\, ab}{4} \qquad (5.12)$$

and for normal incidence the generalised force by:-

$$L_{n,m}(t) = p(t) \int_0^a \int_0^b \sin\left(\frac{n \pi x}{a}\right) \sin\left(\frac{m \pi y}{b}\right) dx\, dy$$

$$L_{n,m}(t) = \begin{cases} 0 & (n \text{ or } m \text{ even}) \\ p(t) \dfrac{4\, a\, b}{n\, m\, \pi^2} & (n \text{ and } m \text{ odd}) \end{cases} \qquad (5.13)$$

Equation (5.7) was solved to find the generalised displacements of the first two volume displacing modes q_{11} and q_{31} using a Duhamel integral technique similar to that employed in the previous chapter. In view of the findings of Section 5.4.3 the panel damping effects were ignored.

The generalised displacements were substituted into Equation (5.5) to find the actual displacement $G(x,y,t)$ which was converted into strain in the x and y directions using Equations (51.4) and (5.15).

$$\sigma_x(x, y, t) = -\frac{T_p}{2} \frac{\partial^2}{\partial x^2} \left[G(x, y, t) \right] \qquad (5.14)$$

$$\sigma_y(x, y, t) = \frac{T_p}{2} \frac{\partial^2}{\partial y^2} \left[G(x, y, t) \right] \qquad (5.15)$$

The calculation of theoretical strain in the x-direction, given the experimental forcing pressure time history in the form of a numerical array, was performed using the Dartmouth Algol computer program RRHSPR which is shown in Appendix A5.3.

5.5.2 Analysis of panel response to steady state acoustic excitation

Before using the above program to calculate the panel strain due to a shock wave the following preliminary calculation was performed to check whether the above Lagrangian-Modal analysis could correctly predict the results of steady state excitation. If the panel is being excited by normal incidence sine waves of amplitude p_o we have:-

$$L_{nm}(t) = p_o e^{j w t} \frac{4 a b}{nm \pi^2} \qquad (5.16)$$

For a steady state solution the Duhamel technique is not applicable but for such a well-defined forcing function we have the analytic solution to Equation (5.7):-

$$q_{nm}(t) = \frac{16 p_o e^{j w t}}{nm \pi^2 \rho_p T_p (w_{nm}^2 - w^2 + 2j w w_{nm} \delta_{nm})} \qquad (5.17)$$

For a lightly damped panel such as the one in question when $w = w_{11}$ the response in modes other than the fundamental is negligible and so at the panel centre the displacement is given by:-

$$G\left(\frac{a}{2}, \frac{b}{2}, t\right) = q_{11}(t) \qquad (5.18)$$

$$= \frac{16 p_o e^{j w t}}{nm \pi^2 \rho_p T_p 2 j w_{11}^2 \delta_{11}} \qquad (5.19)$$

The panel response is controlled by damping which in one of the experiments of Section 5.4.3 was found to be 0.585%. In that same experiment p_o was equivalent to 105 dB and using these two values in Equation (5.19) we arrive

at a theoretical value of the peak displacement of 0.0056 cm. This compares very favourably with the experimental value of 0.0059 cm obtained by integrating the experimental strain according to Equation (5.14). In view of this success we may use the theory with confidence to predict the panel response to transients.

5.5.3 Analysis of panel response to an acoustic transient

Figure (5.32) shows a typical time history for pressure and resultant panel strain along the major panel axis at the panel centre. In order to fix the pressure D.C. line the upper trace was allowed to sweep the screen a second time in the absence of a signal. The location of the strain D.C. line was not so simple however as in the absence of signal the strain gauge amplifier produced electrical noise. The problem was overcome by taking a 1/15 second exposure with the strain trace free running which resulted in the lower bright band of Figure 5.32. The D.C. line must lie within this band and a line was drawn within this band in such a way as to equalise the experimental positive and negative strain.

On Figure 5.33 the experimental time history is compared with the theoretical one calculated from the experimental pressure using the program RRHSPR. The pressure time history of the shock wave is also shown. The indicated strain is that which would be produced in the panel's first two modes by a steady pressure of this magnitude. With reference to the previous chapter the situation approximates to a triangular wave (s = 1), with the fundamental frequency such that $f\tau = 0.3$.

It is seen from Figure 5.33 that the two mode analysis used gives a satisfactory prediction of the experimental strain. The theory correctly predicts the time at which the peak strain occurs and overestimates it by only 20% (1.6 dB). It therefore appears that neglecting the higher panel modes is justified when predicting panel strain. The higher modes would have an even smaller effect upon the panel response than they had upon strain. This is because it follows from Equations (5.14) and (5.15) that the strain in a particular direction is equal to the sum of the responses in the various modes each weighted with the square of the number of anti-nodes in that direction thus favouring the higher modes. Furthermore although the 3,1 ($f\tau$ = 0.9) and higher modes tune better to the N wave than does the fundamental ($f\tau$ = 0.3), this is by virtue of the greater stiffness associated with the higher modes which thus causes a reduction rather than an increase in their response. However, the most important reason why higher modes can be neglected in calculating panel response and strain is their very small generalised force. When calculating this from Equation (5.11) by integrating over the mode shape all but one of the half waves cancel out. Thus the generalised forces of the 3,1; 1,3; 3,3; modes are 1/3; 1/3 and 1/9 of that of the fundamental respectively.

5.6 Summary and Conclusions arising

An inexpensive experimental facility for the generation of high intensity acoustic transients has been established. Although these transients are not perfect N-waves they start with a shock wave which facilitates a prediction of the structural response which they produce.

An ideal simply supported panel has been made and instrumentation developed to measure the panel's strain time history together with that of the pressure wave producing it. It was found that the damping of such a panel can be reduced by a factor of more than two during the course of ageing. This indicates the caution which must be employed when applying the results obtained for the acoustic behaviour of an actual glass window in a specially constructed test house to windows in actual buildings where the putty has aged. Fortunately damping is not of great significance in the response of windows to the sonic bang and so the recent experiments undertaken by Webb of the Royal Aircraft Establishment, Farnborough, are not likely to be in error. However the use of such a test house in investigating steady state phenomena such as transmission loss, where in certain regions of the spectrum the damping is of primary importance, could lead to significant errors.

Finally the experiment of Section (5.5.3) summarised by Figure 5.33 illustrates how a Lagrangian analysis of the panel's first two volume displacing modes by a Duhamel integral technique, can adequately predict the panel's strain time history. This is of particular significance in simplifying the theory of a panel cavity system in the following chapter.

6.0 The Effects of a Closed Cavity behind a Panel upon the Panel's Acoustic Behaviour

6.1 Introduction

In attempting to analyse the damage caused to a large shop window by an actual sonic boom Lowery and Andrews (6.10) were unsuccessful when attempting to use the simple theory of the previous chapter. Bowles and Sugarman (6.11) have shown experimentally that under normal conditions membrane stresses arise under static uniform loading before failure and thus they are, in part, the cause of failure. Freynik (6.12) has made some dynamic measurements of such non-linear membrane stress effects in glass windows using random noise. Acousto-elastic interaction effects are another possible cause for the failure of the simple theory.

The acoustical effects upon a window of the room behind it may considerably affect the window's dynamic behaviour. One possible mode of action is for the room to have a door or corridor and act as a Helmholtz resonator. The pressure in the room will then continue to oscillate and excite the window long after the sonic boom has passed. This situation is similar to that described by Crockett (6.9) in a study of traffic noise. He found that the vibration amplitude of some parts of a building structure continued to increase long after the initial primary exciting force had ceased. This was attributed to the primary noise exciting one lightly damped part of the structure which would then continue to induce a secondary excitation in another part of the structure for many cycles after the primary noise had ceased.

Alternatively if the room is closed and has high transmission loss walls its acoustic field is caused entirely by the window vibration. This acoustic field in turn affects the window and the effect may be regarded

as an acoustic stiffness which may be positive or negative depending upon the frequency and cavity depth (6.1). It is this second type of room effect with which this chapter is concerned. Other authors have studied this problem and in Section 6.2 their work is reviewed and two "rival" theories are found to be equivalent in some respects. Fortunately, the parameters of actual windows, rooms, and sonic bangs allow a considerable simplification of these general theories and the effects of a simple cavity theory upon the panel fundamental frequency, and dynamic response, is compared with experiment in Sections 6.3, and 6.4 respectively. Finally the results are summarised in Section 6.5

6.2 The Panel-Cavity Problem - a Review

6.2.1 Pretlove's Solution

In 1965 Pretlove published a paper (6.1) in which he derived a solution for the free response of a rectangular panel backed by a closed rectangular cavity. The model used is shown in Figure 6.1 and his approach to the problem was as follows:

1. Solve the general wave equation for the acoustic velocity potential ψ in the cavity by assuming separation of variables and a harmonic time depenence:-

$$\text{i.e.} \qquad \psi = f(x)\ g(y)\ h(z)\ e^{j(w\,t + A)} \qquad (6.1)$$

and applying the boundary conditions of zero particle velocity on the five rigid walls to give - using Pretlove's own notation (6.1):-

$$\psi = \sum_{n=o}^{\infty} \sum_{m=o}^{\infty} \cos\left(\frac{n\,\pi\,x}{a}\right) \cos\left(\frac{m\,\pi\,y}{b}\right) L_{nm}$$

$$\cosh\left(\mu_{nm}\,Z\right)\, e^{j(w\,t - A)} \qquad (6.2)$$

2. Assume that the flexible panel has simple supports and hence double sine modes; and that these can be Fourier analysed into double cosine modes such that the fundamental (r = s = 1) panel mode can be expressed:-

$$G = q_{11} \sin\left(\frac{\pi x}{a}\right) \sin\left(\frac{\pi y}{b}\right) e^{j(w t - A_{11})}$$

$$= q_{11} e^{j(w t - A_{11})} \sum_{n=o}^{\infty} \sum_{m=o}^{\infty} \alpha_{nm}^{(11)} \cos\left(\frac{n \pi x}{a}\right) \cos\left(\frac{m \pi y}{b}\right) \qquad (6.3)$$

3. It is observed that this analysis of the panel modes has the same x, y dependence as the acoustic potential (Equation 6.2) and this facilitates the application of the final boundary condition that the particle velocity at the flexible panel is equal to the panel velocity. This leads to the following equation for the acoustic potential in the cavity caused by a panel amplitude q_{11} in its fundamental mode.

$$= j w q_{11} e^{j(w t - A_{11})} \sum_{n=o}^{\infty} \sum_{m=o}^{\infty} \frac{\alpha_{nm}^{(11)} \cosh(\mu_{nm} Z)}{\mu_{nm} \sinh(\mu_{nm} h)} \cos\left(\frac{n \pi x}{a}\right) \cos\left(\frac{m \pi y}{b}\right) \qquad (6.4)$$

where "h" is the depth of the cavity.

4. Pretlove then goes on to calculate the pressure due to this acoustic potential acting upon the panel, and the generalised force that it represents on the Lagrangian equation for each of the panel modes. As this force is proportional to panel displacement it is termed an "acoustic stiffness". The cross acoustic stiffnesses (i.e. the acoustic potential of one panel mode causing a generalised force upon another panel mode) means that the panel modes are no longer independent. Instead of a series of independent Lagrangian equations which were solved to find the in vacuo panel natural frequencies there is now a matrix equation. Pretlove solved the matrix equation by an iterative technique for the case of zero external exciting force to obtain the panel's new natural frequencies and mode shapes.

5. In a later paper (6.2) Pretlove solves the above matrix eigenequations for non zero external forces and was thus able to calculate the transmission of sound into the cavity through the flexible panel.

An identical solution to Pretlove's has also been obtained independently by Dowell and Voss (6.3).

6.2.2 Bhattacharya's Solution

Following an attempt by Kihlman (6.4) at a more complete solution of the problem than Pretlove's which, unfortunately, failed to satisfy all the boundary conditions, Bhattacharya (6.5) has produced a mathematically rigorous solution employing transform theory. He assumes Pretlove's boundary conditions and in addition imposes the condition that the acoustic potential and pressure be zero at $t = 0$.

Apart from being incomplete Pretlove's solution was rejected by Bhattacharya on the grounds of his double cosine analysis of the panel modes (Equation (6.3)) (an objection not shared by the author of this thesis and subsequently admitted, by Bhattacharya, to be invalid (6.6)). However, Pretlove's assumption of a separation of variables solution for the acoustic potential is not justified in the case of inhomogeneous boundary conditions. The solution employs Fourier transforms in the x and y (Pretlove's notation, i.e. the panel plane) directions and a Laplace transform to the time leaving the z variable (cavity depth) untransformed. It yields a solution containing a "steady state" part (i.e. possessing the frequency at which the panel is being forced) and a "transient" part (containing the room eigenfrequencies).

It has been shown (6.7) that the steady state part of the solution is identical to Pretlove's solution and that Bhattacharya's complete

solution represents an unattainable physical situation. The "complete" acoustic potential given in Equation (13) of Reference (6.5) is due entirely to the panel's steady state response. It is physically equivalent to a panel that has been vibrating for a considerable period of time when suddenly a cavity is attached to the back of it. However, it has been shown (6.7) that this objection can easily be overcome by considering a few extra poles in the contour integral for the inverse Laplace transform. This complete solution then represents the acoustic potential of the panel cavity system due to the panel being excited by an acoustic transient.

6.2.3 Conclusions

Despite Pretlove making a non-justifiable assumption regarding the separation of variables (6.6), his solution is identical with the steady state part of Bhattacharya's solution. Although the "general solution" given by Pretlove is not a general solution in the strictly mathematical sense it is correct in representing a particular physical situation. That situation is one of a panel that has been vibrating for a sufficiently long time for cavity transients to be ignored. This theory would obviously not in general be very successful in predicting the response of a panel cavity system to a transient excitation. However, as described in the following section the actual physical parameters of typical windows, rooms, and sonic booms, allow a considerable simplification of Pretlove's cavity panel theory. This simplified theory allows the

cavity-modified panel eigenfrequencies and mode shapes to be used to predict the panel response to a sonic boom.

Bhattacharya's solution on the other hand is more complete. However, unlike Pretlove, Bhattacharya does not consider in detail the effects upon the panel of the back acoustic pressure (although these effects are all stated formally in Appendix B of Reference (6.5)) and so his theory is not so useful in predicting panel response. Consequently, a modification (Section 6.3) and extension (Section 6.4) of Pretlove's solution is used in the remainder of this chapter to predict the effects of a cavity upon panel strain produced by a sonic bang.

6.3 The Effect of the Cavity upon the Panel's Resonant Frequencies

6.3.1 Introduction

In the summer of 1968 Pretlove's Reading group performed a survey of large shop windows in which they measured their aspect ratios and fundamental frequencies. They found that the average aspect ratio was 1.44 and the fundamental frequency of the larger windows was around 5 Hz. This frequency corresponds to an acoustic wavelength of over 200 feet which is almost equal to the spatial extension of a sonic boom. As this is an order of magnitude greater than the depth of cavity likely to be encountered behind a window it is possible to consider the cavity as a static stiffness. Furthermore in view of the findings of the previous chapter it is possible to ignore all the panel modes except the fundamental and first asymmetric mode.

6.3.2 The Theory used

Considering only the first two volume displacing modes we have for the panel deflection

$$G(x,y,t) = q_{11}(t)\,\phi_{11}(x,y) + q_{31}(t)\,\phi_{31}(x,y) \qquad (6.5)$$

where ϕ_{11} and ϕ_{31} are the simply supported mode shapes as defined in the previous chapter.

The nett volume displacement, δV, due to this deflection is:-

$$\delta V = \int_0^a \int_0^b G(x,y,t) \quad dx\ dy$$

$$= q_{11}(t) \int_0^a \int_0^b \sin\left(\frac{\pi x}{a}\right) \sin\left(\frac{\pi y}{b}\right) \quad dx\ dy$$

$$+ q_{31}(t) \int_0^a \int_0^b \sin\left(\frac{3\pi x}{a}\right) \sin\left(\frac{\pi y}{b}\right) dx\ dy$$

$$= \frac{4ab}{\pi^2}\left[q_{11}(t) + \frac{q_{31}(t)}{3} \right] \qquad (6.6)$$

If dynamic pressures are neglected and the compression is assumed to be adiabatic

$$\delta p = p_a \gamma \frac{\delta V}{V}$$

$$= \rho c^2 \frac{4}{\pi^2 h}\left[q_{11}(t) + \frac{q_{31}(t)}{3} \right] \qquad (6.7)$$

This static pressure gives rise to the following generalised forces acting upon the panel modes.

$$L_{11} = \int_0^a \int_0^b \delta p \sin\left(\frac{\pi x}{a}\right) \sin\left(\frac{\pi y}{b}\right) \quad dx\ dy$$

$$= -\delta p \frac{4ab}{\pi^2} \qquad (6.8)$$

$$L_{31} = -\delta p \frac{4ab}{3\pi^2} \qquad (6.9)$$

Thus the equations of motion of the two mode system in the absence of damping and external forces, are:-

$$M_{11}\ddot{q}_{11} + K_{11}q_{11} = -\delta p \frac{4ab}{\pi^2} \qquad (6.10)$$

$$\text{and} \quad M_{31}\ddot{q}_{31} + K_{31}q_{31} = -\delta p \frac{4ab}{3\pi^2} \qquad (6.11)$$

Defining:-

$$\eta = \frac{\text{Acoustic generalised stiffness in the first in-vacuo mode}}{\text{Mechanical generalised stiffness in the first in-vacuo mode}}$$

$$= \frac{K_A}{K_{11}} \qquad (6.12)$$

where K_A is the generalised force on the first in vacuo mode due to unit generalised displacement in that mode. Therefore, combining Equations (6.7) and (6.8) we have:-

$$K_A = \frac{L_{11}}{q_{11}} = \rho c^2 \frac{16ab}{\pi^4 h} \qquad (6.13)$$

Assuming harmonic motion of frequency w, Equations (6.10) and (6.11) can after dividing by K_{11}, be written as

$$-w^2 \frac{M_{11}}{K_{11}} q_{11} + q_{11} + \eta q_{11} + \frac{\eta}{3} q_{31} = 0 \qquad (6.14)$$

$$-w^2 \frac{M_{31}}{K_{11}} q_{31} + \frac{K_{31}}{K_{11}} q_{31} + \frac{\eta}{3} q_{11} + \frac{\eta}{9} q_{31} = 0 \qquad (6.15)$$

or

$$\left[1 + \eta - \Omega^2\right] q_{11} + \frac{\eta}{3} q_{31} = 0 \qquad (6.16)$$

$$\frac{\eta}{3} q_{11} + \left[\left(\frac{9 + \alpha^2}{1 + \alpha^2}\right)^2 + \frac{\eta}{9} - \Omega^2\right] q_{31} = 0 \qquad (6.17)$$

where $$\Omega = \frac{w}{w_o} \qquad (6.18)$$

and α = the aspect ratio of the panel = $\frac{a}{b}$

Defining:-

$$\beta = \left(\frac{9 + \alpha^2}{1 + \alpha^2}\right)^2 \qquad (6.19)$$

in order that Equations (6.16) and (6.17) be satisfied we have that:-

$$\begin{vmatrix} \left[1 + \eta - \Omega^2\right] & \frac{\eta}{3} \\ \frac{\eta}{3} & \left[\beta + \frac{\eta}{9} - \Omega^2\right] \end{vmatrix} = 0 \qquad (6.20)$$

which can be expanded as:-

$$\Omega^4 - \left(1 + \frac{10\eta}{9} + \beta\right)\Omega^2 + \beta + \left(\frac{1}{9} + \beta\right)\eta = 0 \qquad (6.21)$$

This quadratic equation in Ω^2 has the formal analytic solutions:-

$$\Omega_i^2 = \frac{1}{2}\left[1 + \beta + \frac{10\eta}{9} \pm \sqrt{\left(1 = \frac{10\eta}{9} + \beta\right)^2 - 4\left(\beta + \left(\frac{1}{9} + \beta\right)\eta\right)}\right] \qquad (6.22)$$

The solutions of this equation give the new resonant frequencies of the panel which are greater than the in-vacuo eigenfrequencies because of the cavity stiffness. This calculation is performed by the computer program RRHNPR (Appendix A6.1), lines 1 to 300.

6.3.3 The Experiments performed

An adjustable cavity illustrated in Figure 6.2 was built in order to test the theory of the preceding section. Preliminary calculations indicated that the 0.032 inch thick panel used in Chapter Five had too great a mechanical stiffness to be significantly affected by the cavity and so a thinner panel was fitted. Deciding upon the ideal panel thickness had to be something of a compromise due to the various other parameters that had to be considered. In order that the panel be affected by the cavity it should ideally be as thin as possible. However, a thinner panel has a lower fundamental frequency which does not couple so well with the experimental "N-wave". Also as the panel thickness is reduced the thickness of the supporting shims should similarly be reduced in order that the panel remain simply supported. Clearly the shim thickness can not be reduced indefinitely and still remain strong enough to support the panel when subjected to the experimental "N-waves". Finally if the panel is too thin its deflections would be so great as to require a non-linear deflection theory analysis.

Taking all these factors into consideration a panel thickness of 0.022 inches supported by 0.003 inch thick shims was decided upon and fitted.

The resonant frequencies of this panel in the first two volume displacing modes, was measured by plotting its resonance curve when excited by plane sound waves from the transmission loss box, as described

in the previous chapter. The adjustable cavity was then fitted behind the panel and the experiment was repeated for several values of cavity depth. It was noticed from the resonance curves obtained that the presence of a cavity considerably increased the panel damping. The damping remained sufficiently low however to be ignored when calculating the response of the panel to an acoustic transient. The results are shown plotted in Figure 6.3.

In the absence of a cavity ($h = \infty$) there is a discrepancy of about 7 Hz between the theoretical and experimental eigenfrequencies which could be explained by an error of one thousandth of an inch in the panel thickness. The experimental and theoretical curves have a similar shape and so we may assume that the theory of the previous section is correct in predicting panel eigenfrequencies. In particular the difference between the $h = \infty$ and $h = 20$ cm eigenfrequencies (about 8 or 9 Hz), is the same for both the experimental and theoretical curves. Also as the cavity depth is reduced, so is the discrepancy between the two curves. This is because for shallower cavities the panel stiffness is no longer entirely mechanical and so the error in mechanical stiffness (apparent from the discrepancy of the in-vacuo eigenfrequencies) is no longer dominant. It thus appears that we are more accurate in predicting the panel's acousto-mechanical properties than its purely mechanical ones.

6.4 The Effect of the Cavity upon the response of the Panel to Acoustic Transients

6.4.1 Development of the Theory

After calculating the new panel eigenfrequencies w_1 and w_2 ($w_{11}\Omega_1$ and $w_{11}\Omega_2$) from Equation (6.22) the motion is then analysed as the sum of the two new modes with which they are associated.

$$(w_1 \text{ mode}) \quad M_1 \ddot{Q}_1 + K_1 Q_1 = L_1 \tag{6.23}$$

$$(w_2 \text{ mode}) \quad M_2 \ddot{Q}_2 + K_2 Q_2 = L_2 \tag{6.24}$$

where Q_1 and Q_2 are each composed of a mixture of q_{11} and q_{31}. From Equation (6.16) the ratio of q_{31} to q_{11} is given by:-

$$R(w) = \frac{q_{31}}{q_{11}} = \frac{-3}{\eta}\left[1 + \eta - \Omega^2\right] \tag{6.25}$$

Therefore the physical displacement due to the first new mode may be represented as:

$$G_1(x,y,t) = Q_1(t)\ \Phi_1(x,y) \tag{6.26}$$

$$= q_{11}(\phi_{11} + R(w_1)\phi_{31}) \tag{6.27}$$

If we define:-

$$Q_1 = q_{11}(1 - R(w_1)) \tag{6.28}$$

It follows that:-

$$\Phi_1 = \frac{\phi_{11} + R(w_1)\ \phi_{31}}{1 - R(w_1)} \qquad (6.29)$$

Therefore a new generalised displacement (Q_1) of unity represents a physical displacement:-

$$G_1 = Q_1 \Phi_1 \qquad (6.30)$$

$$= \Phi \qquad (6.31)$$

$$= \frac{\phi_{11} + R(w_1)\ \phi_{31}}{1 - R(w_1)} \qquad (6.32)$$

at the centre of the panel $\phi_{11} = +1$, $\phi_{31} = -1$.

$$G = 1 \qquad (6.33)$$

So the definitions of Q_1 and Φ_1 given by Equations (6.28) and (6.29), mean that a generalised displacement of unity represents a unit physical displacement at the panel centre.

We now require to calculate M_1, K_1 and L_1

$$M_1 = \rho T_p \int_0^a \int_0^b \Phi_1^{\,2}(x,y)\ dx\ dy \qquad (6.34)$$

$$= \frac{\rho T_p}{\{1-R(w_1)\}^2} \int_0^a \int_0^b (\phi_{11}^{\,2} + 2R(w_1)\ \phi_{11}\ \phi_{31} + R^2(w_1)\ \phi_{31}^{\,2})\ dx\ dy \qquad (6.35)$$

The middle term of the integral of Equation (6.35) disappears because of the orthogonality of the in-vacuo modes, leaving:-

$$M_1 = \frac{1}{\{1 - R(w_1)\}^2} \{m_{11} + R^2(w_1)m_{31}\} \qquad (6.36)$$

where m_{11} and m_{31} are the generalised masses of the in-vacuo modes.

$$m_{11} = m_{31} = \frac{\rho T_p a b}{4} \qquad (6.37)$$

$$M_1 = \frac{\rho T_p a b}{4} \quad \frac{(1 + R^2(w_1))}{(1 - R(w_1))^2} \qquad (6.38)$$

From this K_1 can be easily found using the relationship:-

$$K_1 = w_1^2 \; M_1 \qquad (6.39)$$

The generalised force in the first new mode (L_1) is given for normal incidence by:-

$$L_1 = p(t) \int_0^a \int_0^b \Phi_1(x,y).\; dx\, dy \qquad (6.40)$$

$$= \frac{p(t)}{1-R(w_1)} \int_0^a \int_0^b (\phi_{11} + R(w_1)\phi_{31}) \; dx\, dy \qquad (6.41)$$

$$= \frac{ab}{2} \; p(t) \left[\frac{1 + \frac{1}{3} R(w_1)}{1 - R(w_1)} \right] \qquad (6.42)$$

With the above values of M_1, K_1, and L_1 it is possible by using a Duhamel technique to calculate the generalised displacement in the first new mode due to an experimental pressure time-history. We can convert this

generalised displacement into physical panel strain as follows.

Given a unit generalised displacement in the first new-mode we have:-

$$G_1 = \Phi_1 = \frac{1}{1 - R(w_1)} \quad (\phi_{11} + R(w_1)\phi_{31}) \tag{6.43}$$

The strain at the panel centre in the x direction is given by:-

$$e_{x1} = \frac{1}{1 - R(w_1)} \quad \frac{\pi^2 T_p}{2 a^2} \quad (1 - 9 R(w_1)) \tag{6.44}$$

and for the y direction:-

$$e_{y1} = \frac{1}{1 - R(w_1)} \quad \frac{\pi^2 T_p}{2 b^2} \quad (1 - R (w_1)) \tag{6.45}$$

The generalised displacement in the second new mode can be calculated in an identical manner except replacing $R(w_1)$ by $R(w_2)$. The actual physical strain for comparison with experiment is calculated by adding the strain due to these two new modes. This calculation is performed by the computer program RRHNPR (Appendix A6.1), lines 300 onwards.

6.4.2 The Experiments performed

A photograph of the pressure and resultant panel strain time histories was taken using the shock tube as described in the previous chapter. The photograph obtained when the panel was backed by a 2.9 cm

deep cavity is shown in Figure 6.4. These experimental results together with the theoretical predictions of the two mode theory described in the previous section are shown in Figure 6.5. It is seen that although this two mode theory predicts the maximum strain reasonably well it bears little relation to the early part of the experimental strain time history. This initial strain time history is due to the higher panel modes which can respond more rapidly to the "N-wave" than the fundamental and 3,1 modes.

The results of the program RRHNPR inform us that although the fundamental frequency is raised from 157.5 to 208.2 Hz there is no appreciable change in the 3,1 eigenfrequency (529.4 to 531.5 Hz). We may therefore assume that higher modes are relatively unaffected by the cavity (by virtue of their higher mechanical stiffness and the smaller volume of air which they displace). Consequently we may add to the previously calculated strain the strain due to these higher in-vacuo modes, completely ignoring cavity effects so far as they are concerned. The results of "adding" the q_{13}, q_{51} and q_{71} mode strain to that already calculated for the Q_1 and Q_2 modes is shown in Figure 6.5. The number of extra modes that could be added was limited by the computer storage available and these three modes were found to have the most significant effect upon the panel strain. The 7,1 mode was chosen as opposed to the 3,3 mode of similar frequency because the former has a larger generalised force and produces 5.45 times as much strain per unit displacement.

It is seen from figure 6.5 that the addition of these extra modes gives an initial theoretical strain in good agreement with the experimental strain. In the later part of the time history the agreement between theory and experiment is not improved by these higher modes because of inaccuracies in their predicted relative phasings after several cycles. This explains why the "shoulder" appears before rather than after the maximum strain.

However, despite the half-millisecond delay (which may be due to dynamic cavity stiffness effects in the higher modes) the maximum strain is correctly predicted to within 13%.

The experimental strain encountered within the experiments of this (and the previous) chapter is 3×10^{-4}. This corresponds to a peak stress of 6×10^{8} which is an order of magnitude lower than the tenacity of steel (6.8). We may therefore safely assume that the panel never goes beyond its elastic limit. If we assume that all this strain is due to the first mode it represents a panel displacement of 0.3 cm and so we are justified in using linear deflection theory.

6.5 Conclusions and the Possibility of Window Damage

A simple theory of acousto-elastic panel stiffening has been justified experimentally. This theory has been extended to predict the response of a panel backed by a closed cavity to an acoustic transient and has been successful in predicting the experimental panel strain to within 13%.

For this type of acousto-elastic effect the cavity stiffness always reduces the panel stress as the cavity stiffness is always positive for actual room, window and sonic boom parameters. Furthermore as the ratio given in Equation (6.25) is always negative for the first new panel mode, the stresses due to its in-vacuo 1,1 and 3,1 components add in the panel centre and are of opposite sign at the panel edges. Therefore, the cavity theory does not in any way explain the tendency for windows to sometimes break first away from their centres which is probably due to glass imperfections.

It is such imperfections which will probably be the cause of any sonic boom window damage. A 2 lb/ft^2 sonic boom acting on a 20 feet by 8 feet by $\frac{1}{4}$ inch thick window with a dynamic magnification factor of 2 (Chapter Four) will produce a maximum tensile stress of 3,000 lb/in^2 which is only half the mean breaking stress of plate glass which is 6,000 lb/in^2 (6.13). However, the breaking stress of glass has a coefficient of variation of 0.25 (6.13) which assuming a normal distribution means that $2\frac{1}{2}$% of those reaching a stress of 3,000 lb/in^2 will suffer damage. A truly normal distribution is however unlikely as the weakest windows are likely to suffer damage from other sources and be replaced. Also only a small proportion of windows will experience the maximum dynamic magnification factor of 2 and so the number of windows actually damaged is likely to be much less than $2\frac{1}{2}$%.

7.0 Conclusions

7.1 The Theory and Measurement of Transmission Loss

In Chapter Two a method of measuring high transmission loss was developed which is now regularly employed in routine laboratory measurements. The experiments of Chapter Two have also provided an upper and lower estimate of the highest transmission loss that can be measured with Liverpool University's new transmission loss suite.

The experimental transmission loss measured for a single brick wall is well within the suite's capabilities and is in good agreement with field measurements obtained by the Building Research Station (2.1). This transmission loss is 10 dB or so below the predictions of mass law due to flexural wave transmission,

The results obtained for the cavity brick wall are similarly in good agreement with field measurements obtained by the Building Research Station (2.1). It has been shown that the main coupling mechanism between the two leaves of the double wall is not through the acoustic coupling of the cavity but is due to mechanical flanking paths. This explains the great discrepancy between the experimental values of transmission loss for a cavity brick wall and the theoretical predictions of multiple reflection theory (2.3) or Beranek and Work (2.4), (2.7) which assume acoustic coupling only.

The results of the accelerometer measurements of Chapter Three have important consequences for both the theory and measurement of transmission loss. It is shown that mass law and Cremer-type theories give, like Rutherford's classical calculation of nuclear scattering, the right answers for the wrong reasons. Although these infinite panel theories provide remarkably accurate predictions of reverberant transmission loss

their prediction of panel response has been shown to be in error by as much as 15 dB. Therefore, these theories and the models on which they are based must be rejected as not representing the true physical facts of the situation. Similarly any multiple panel theories derived from them must be regarded with suspicion. Crocker and Price (3.22) reached similar conclusions by studying the essentially modal theories of Lyon and Maidanik (3.19), (3.20), (3.21) and have since been able to obtain good agreement between these theories and their experimental results for both transmission loss and panel response. The accelerometer measurements have illustrated severe limitations on the use of this method of transmission loss measurement. A letter was written to the Editor of the Journal of Sound and Vibration (3.23) summarising the dangers inherent in the indiscriminate use of this accepted (3.1), (3.8), (3.9) method of measurement.

7.2 Structural Response to Sonic Booms

The calculations of Chapter Four, which were undertaken in conjunction with Mr. M.J. Crocker, provide an upper limit to the theoretical dynamic magnification factor associated with the various N-wave shapes produced by supersonic aircraft. It is seen from Figure 4.20 that the dynamic magnification factor rises to a maximum value of 2.5 at $f\tau = 0.5$ and then at high values of $f\tau$ assumes a value of 2.0. In order that these results be more freely available they have been published in detail (4.14) and provide an aid to the calculation of sonic boom response that has already been requested, used and acknowledged (4.16).

Chapter Five describes the establishment of an experimental shock tube facility and the construction.of a simply supported test panel. The experiments with this facility illustrated the accuracy with which a two mode theory can predict the strain in a simply supported panel caused by normally incident experimental "N-waves". In the absence of the cavity effects described in Chapter Six such a theory can be used with confidence to predict the strain and possibility of damage to a plate glass window subjected to a full scale sonic boom.

When a large window is backed by a shallow room the back acoustic pressures on the window due to the room affect the panel's dynamic behaviour. In Chapter Six this effect is studied both experimentally and theoretically. A theory is given which predicts both the new panel eigenfrequencies and the panel's response to an acoustic transient. This theory may similarly be used with confidence to predict the possibility of damage by a real sonic boom to a room-backed window.

The current interest in sonic bangs is so great that the Royal Aircraft Establishment has produced a 100 page bibliography on the subject (7.1). The results of Chapters 4, 5, and 6 will help add to this store of knowledge which will ultimately be used to determine the acceptability

of various boom levels and regulate supersonic flights accordingly. Even with this knowledge there is still the possibility of accidents. While this thesis was in the course of preparation, RAF jets damaged 20 bungalows near Abingdon (7.2). When such accidents occur this pool of knowledge will be useful in distinguishing between the genuine and frivolous claims for damage.

7.3 Further Work

The most useful extension of the work would be a calculation of the dynamic effects of the cavity upon the panel response. Such effects have already been studied by Pretlove (6.3) but his solution relies upon a computer-time consuming iterative technique. If an analytic solution to the problem could be found it would be useful in the calculation of both panel response and the radiation of sound into an acoustically stiff cavity.

References

1.1 Mulholland, K.A., (1966): Ph.D. Thesis, University of Liverpool.

1.2 Utley, W.A., (1967): Ph.D. Thesis, University of Liverpool.

1.3 Cummings, A., (1968): Ph.D. Thesis, University of Liverpool.

1.4 Mulholland, K.A., Parbrook, H.D., (1965): J. Sound Vib., 2, 502. "The Measurement of Sound Transmission Loss of Panels with Small Transmission Loss".

1.5 Bruel, P.U., (1951): "Sound Insulation and Room Acoustics". Chapman and Hall, London.

1.6 Mulholland, K.A., Parbrook, H.D., Cummings, A, (1967): J. Sound Vib., 6, 324. "The Transmission Loss of Double Panels".

1.7 Mulholland, K.A., Parbrook, H.D., (1967): J. Sound Vib., 5, 499, "Transmission of Sound through Apertures of Negligible Thickness".

1.8 London, A., (1949): Journ. Res. Nat. Bur. Stands. 42, 605. "Transmission of Reverberant Sound through Single Walls".

1.9 Rayleigh Lord (1960): "The Theory of Sound". Constable, London.

1.10 Cremer, L., (1942): Akustiche Zeitshrift 7, 81. "Theory of Sound Attenuation of Thin Walls at Oblique Incidence".

1.11 Ramsey, W.A., (1964): Materials Res. & Standards, 4 (11), 612. "Damage to Ottawa Air Terminal Building produced by a Sonic Boom".

2.1 Parkin, P.H., Purkis, H.J., Scholes, W.E., (1960): "Field Measurements of Sound Insulation between dwellings". Her Majesty's Stationary Office, London.

2.2 Moeller, F.H., (1956): Tek. Ukebl, 93, No.45. "Sound Transmission with Structural Engineering".

2.3 Mulholland, K.A., Parbrook, H.D., Cummings, A., (1967): J. Sound Vib., 6, 324. "The Transmission Loss of Double Panels".

2.4 Beranek, L.L., Work, G.A., (1949): J. Acoust. Soc. Amer., 21, 419. "Sound Transmission through multiple Structures containing Flexible Blankets".

2.5 London, A., (1950): J. Acoust. Soc. Amer., 20, 270. "Transmission of Reverberant Sound through Double Walls".

2.6 White, P.H., Powell, A. (1965): J. Acoust. Soc. Amer. 40, 821. "Transmission of Random Sound and Vibration through a Rectangular Double Wall".

2.7 Mulholland, K.A., Price, A.J., Parbrook, H.D. (1968): J. Acoust. Soc. Amer., 43, 1432. "Transmission Loss of Multiple Panels in a Random Incidence Field."

2.8 Zaborov, V.I., (1968): Soviet Physics-Acoustics, 13, 488. "Indirect Paths of Sound Propagation in Buildings".

2.9 Parkin, P.H., Humphreys, H.R., (1958): "Acoustics Noise and Buildings". Faber.

2.10 Zaborov, V.I., (1969): "Calculation of Sound Insulation of Barrier Constructions in Buildings with regard for Indirect Noise Transmission". (to be published)

3.1 The British Broadcasting Corporation Engineering Division (1967): Research Report No.PH-9. "The Measurement of Sound Insulation in the presence of Flanking Paths".

3.2 Goff, K.W., (1954): J. Acoust. Soc. Amer., 27, 223. "Analog Electronic Correlator for Acoustic Measurements".

3.3 Goff, K.W., (1954): J. Acoust. Soc. Amer., 27, 236. "Application of Correlation Techniques to some Acoustic Measurements".

3.4 Burd, A.N., (1963): Radio & Electron. Engr., 27, 387. "Correlation Techniques in Studio Testing".

3.5 Raes, A.C., (1954): J. Acoust. Soc. Amer., 27, 98. "Tentative method for the measurement of Sound Transmission Losses in Unfinished Buildings".

3.6 Raes, A.C., (1963): Jour. Acoust. Soc. Amer. 35, 1178. "Static and Dynamic Transmission Losses of Partitions".

3.7 London, A., (1941): J. Res. Natn. Bur. Stand., 26, 419. "Measurements of Sound Transmission Loss in the Field".

3.8 The British Broadcasting Corporation Engineering Division (1963): Research Report No.B-078. "The Accelerometer Pick-up as a Diagnostic Tool in Noise Studies in Buildings".

3.9 Utley, W.A., Mulholland, K.A., (1967): J. Sound Vib., 6, 419. "Measurement of Transmission Loss using Vibration Transducers".

3.10 Morse, P.M., (1936): "Vibration and Sound", Second edition 1948, page 338, New York: Mcgraw-Hill Book Company.

3.11 Mulholland, K.A., Parbrook, H.D., (1965): J. Sound Vib., 5, 391. Letter to the Editor. "The Measurement of Transmission Loss".

3.12 Bruel and Kjaer, Naerum, Denmark. "One-inch Condenser Microphones:- Instructions and Applications 4131/32".

3.13 Bruel and Kjaer, Naerum, Denmark. "Vibration Pick-up Preamplifier:- Instructions and Applications, 1606".

3.14 Braddick, H.J.J., (1963): "The Physics of Experimental Method", Chapman & Hall, London.

3.15 Knudsen, V.O., (1932): "Architectural Acoustics". Chap V, John Wiley & Sons Inc., New York.

3.16 Beranek, L.L., (1960): "Noise Reduction". McGraw-Hill Book Co. Inc.

3.17 Cremer, L. (1949): The Physical Society, Acoustics Group Symposium 1949. "Sound Insulation of Panels at Oblique Incidence".

3.18 Cremer, L., (1955): "Insulation of Airborne Sound by Rigid Partitions and Insulation of Impact Sound", secs.11.2 and 11.3 respectively of Bolt Beranek and Newman Inc., WADC Tech Report 52-204, Vol.1, suppl.1, Wright-Patterson Air Force Base, Ohio, 1955.

3.19 Lyon, R.H., Maidanik, G., (1962): J. Acoust. Soc. Amer., 34, 623. "Power Flow between linearly coupled oscillators".

3.20 Maidanik, G., (1962): J. Acoust. Soc. Amer., 34, 809. "Response of Ribbed Panels to Reverberant Acoustic Fields".

3.21 Lyon, R.H., (1963): J. Acoust. Soc. Amer., 35, 1791, "Noise Reduction of Rectangular Enclosures with one Flexible Wall".

3.22 Crocker, M.J., Price, A.J., (1969): J. Sound Vib., 9, "Sound transmission using Statistical Energy Methods.

3.23 Hudson, R.R., Mulholland, K.A., (1969): J. Sound Vib. (1969), 9,(1) 145. Letter to the Editor "Comments on 'Measurement of Transmission Loss using Vibration Transducers' ".

4.1 National Sonic Boom Evaluation Office, 1400 Wilson Boulevard, Arlington, Virginia, U.S.A. 1967: NSBEO-1-67 "Sonic Boom Experiments at Edwards Air Force Base".

4.2 Crocker, M.J., (1967): J. Acoust. Soc. Amer., 42, 1070. "Multimode Response of Panels to Normal and to Travelling Sonic Booms".

4.3 Crocker, M.J., (1967): J. Sound Vib., 6 (1), 38. "Response of Panels to Oscillating and to Moving Shock Waves".

4.4 Crocker, M.J., (1968): AIAA/ASME 9th Structures, Structural Dynamics and Materials Conference, Palm Springs, California, U.S.A. Paper 68-287. "Response of Aerospace Vehicle Skin Panels to Oscillating Shock Waves".

4.5 Crocker, M.J., (1967): University of Liverpool, Department of Building Science, Report BS/A/67-2 "Dynamic Magnification Factor Produced in a Single Degree of Freedom System by an Ideal Sonic Bang".

4.6 Wyle Laboratories Research Staff, (1965): Progress Report on Contract NASA;NAS8-11217. "Dynamic Magnification Factor for Response of Undamped System to an Ideal N-wave".

4.7 Chang, D.H., and Benvriste, J.E., (1966): Int. J. Mech. Sc. 8, 607. "Transient Response of Structural Elements to Travelling Pressure Waves of Arbitrary Shape".

4.8 Arde Associates (1959): WADC U.S. Air Force Techn. Rept.58-169. "Response of Structures to Aircraft Generated Shock Waves".

4.9 Cheng, D.H., (1964): NASA Langley Research Center, U.S.A. "Unpublished work".

4.10 Mayes, W.H., and Newman, J.W., (1966): NASA Langley Research Center, U.S.A. "Unpublished work".

4.11 Crocker, M.J., (1966): Wyle Lab. Res. Staff Rept.WR 66-1. "Multimode Response of Panels to Sonic Boom".

4.12 Crocker, M.J., (1966): Wyle Lab. Res. Staff Rept. WR 66-2. "Theoretical and Experimental Response of Panels to Travelling Sonic Boom and Blast Waves".

4.13 Crocker, M.J., and Sutherland, L.C., (1968): J. Sound Vib. 8 (3). "Instrumentation Requirements for Measurement of Sonic Boom and Blast Waves - A Theoretical Study".

4.14 Crocker, M.J., and Hudson, R.R., (1968): J. Sound Vib. 9 (3), 100. "Structural Response to Sonic Booms".

4.15 Jacobsen, L.S., and Ayre, R.S., (1958): McGraw-Hill Book Co. Inc., New York. "Engineering Vibrations".

4.16 Pretlove, A.J., (1969): J. Sound Vib. (to be published). "The Response of Large Windows to Sonic Bangs".

5.1 Crocker, M.J., (1966): Wyle Laboratories Research Staff, Report WR 66-1, "Multimode Response of Panels to Sonic Boom".

5.2 Crocker, M.J., (1966): Wyle Laboratories Research Staff Report WR 66-2, "Theoretical and Experimental Response of Panels to Travelling Sonic Boom and Blast Waves".

5.3 Crocker, M.J., (1967): J. Acoust. Soc. Amer., 42, 1070. "Multimode Response of Panels to Normal and to Travelling Sonic Booms".

5.4 Warren, C.H.E., (1966): Royal Aircraft Establishment, Technical Report No.66344, "Proposal for a Shock-Tube Facility to Simulate Sonic Bangs".

5.5 Crocker, M.J., (1968): J. Sound Vib., 7 (3), 351. "Instrumentation Requirements for Measurement of Sonic Boom and Blast Waves - A Theoretical Study".

5.6 Crocker, M.J., (1968): Private communication.

5.7 Kinsler, L.E., Frey, A.R., (1962): "Fundamentals of Acoustics", Wiley.

5.8 Parrott, T.L., (1967): The Shock and Vibration Bulletin 1967, p.77. "Strain Response of Simply Supported Beams to Point and Acoustic Loading".

5.9 White, R.W., (1964): Wyle Laboratories Research Staff, Report WR 64-2, "Vibration Characteristics of Beams and Plates mounted on Elastic and Inertial Supports".

5.10 Naylor, V.D., (1969): British Acoustical Society Conference, 'Sonically Induced Vibration of Structures", Liverpool January 1969, Paper D6, "Some fallacies in modern damping theory".

5.11 Stephens, R.W.B., Bate, A.E., (1966): "Acoustics and Vibrational Physics". Edward Arnold, London.

5.12 Hodgman, C.D., (Editor) (1962): "Handbook of Chemistry and Physics". Chemical Rubber Publishing Co., Cleveland, Ohio, U.S.A.

6.1 Pretlove, A.J., (1965): J. Sound Vib., 2 (3), 197. "Free Vibrations of a Rectangular Panel Backed by a Closed Rectangular Cavity".

6.2 Pretlove, A.J., (1966): J. Sound Vib., 3 (3), 252. "Forced Vibrations of a Rectangular Panel backed by a Closed Rectangular Cavity".

6.3 Dowell, E.H., Voss, H.M., (1963): A.I.A.A. Journal I. 476. "The effect of a Cavity on Panel Vibration".

6.4 Kihlman, T., (1967): Acustica 18. "Sound Radiation into a Rectangular Room. Application to airborne sound transmission in buildings".

6.5 Bhattacharya, M.C., Crocker, M.J., (1969): University of Liverpool, Department of Building Science Report BS/A/69/1. "Forced Vibrations of a Panel and Radiation of Sound into a Room". (to be published in Acustica).

6.6 Bhattacharya, M.C., (1969): Private Communication.

6.7 Hudson, R.R., (1969): Private Communication.

6.8 Kaye, G.W.C., Laby, T.H., (1959): "Tables of Physical and Chemical Constants", Longmans London.

6.9 Crockett, J.H.A., (1969): British Acoustical Society Conference 'Sonically Induced Vibration of Structures', Liverpool, January 1969. "Sonically Induced Vibration Damage Pattern by traffic and aircraft in Medieval and Ancient Buildings".

6.10 Lowery, R.L., Andrews, D.K., (1966): NASA CR-66170. "Acoustical and Vibrational Studies relating to an occurence of Sonic Boom Induced Damage to a Window Glass in a Store Front".

6.11 Bowles, R., Sugarman, B., (1962): Glass Technology 3, 156. "The Strength and Deflection Characteristics of large Rectangular Glass Panels under Uniform Pressure.

6.12 Freynik, H.S., (1963): NASA TN D-2025. "The Non-Linear Response of Windows to Random Noise".

6.13 McKinley, R.W., (1964): Materials Research and Standards 4, 594. "Response of Glass in Windows to Sonic Booms".

7.1 Wadsworth, Jill, (1968): "Bibliography on Sonic Bangs". Royal Aircraft Establishment, Library Bibliography No.287.

7.2 The Daily Telegraph, Friday, 2nd May 1969, p.36.

APPENDIX 2.1 - Measurement of Signals Approaching the Noise Level

In measurements of high transmission loss panels the signal in the reception room is often very little above the background noise level. This is especially true at high frequencies where fortunately the noise level is almost constant and so can be used in the calculation of the true signal level.

Referring to Figure I we have from experiment the levels of the noise (AdB) and the signal plus noise (BdB) and wish to calculate the signal level (CdB)

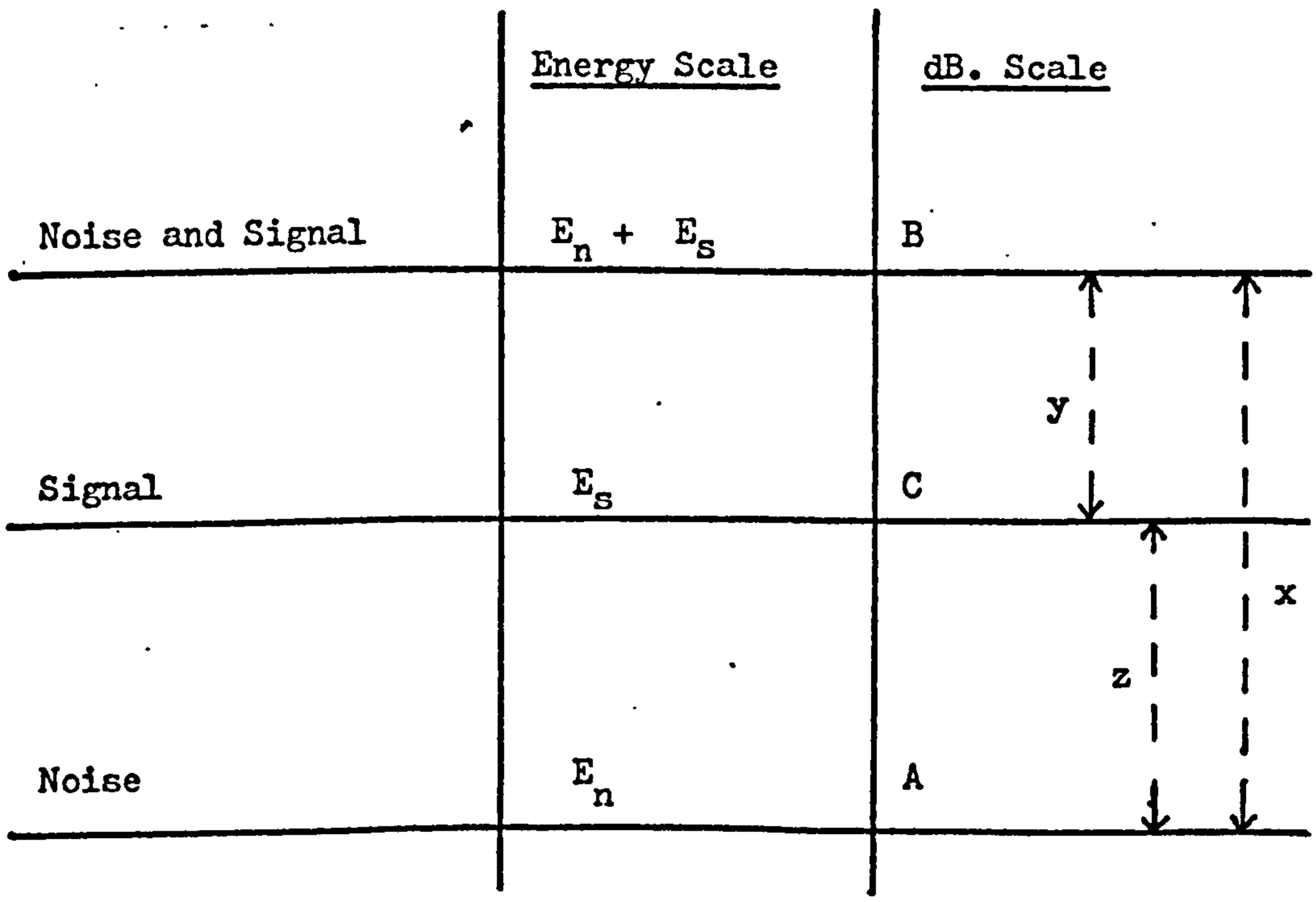

FIGURE 2A.1

$$C = 10 \log \left(\frac{E_s}{E_o}\right) = 10 \log \left[\text{antilog } \left(\frac{B}{10}\right) - \text{antilog } \left(\frac{A}{10}\right)\right] \qquad (2A.1)$$

or:

$$y = B - C = (A + x) - C \qquad (2A.2)$$

$$= A + x - 10 \log \left[10^{\frac{A}{10}} \left(10^{\frac{x}{10}} - 1\right)\right] \qquad (2A.3)$$

$$\approx x - 10 \log \left[\text{antilog } \left(\frac{x}{10}\right) - 1\right] \qquad (2A.4)$$

i.e. If the measured signal is x dB above the noise it exceeds the actual signal by y dB where y is given by:

$$\underline{\underline{y = x - 10 \log \left[\text{antilog } \left(\frac{x}{10}\right) - 1\right]}} \qquad (2A.5)$$

x dB	y dB	z=x-y
0.5	9.6	- 9.1
1.0	6.9	- 5.9
1.5	5.3	- 3.8
2.0	4.3	- 2.3
2.5	3.6	- 1.1
3.0	3.0	+ 0
3.5	2.9	+ 0.8
4.0	2.2	+ 1.8
4.5	1.9	+ 2.6
5.0	1.9	+ 3.3
5.5	1.4	+ 4.1

x dB	y dB	z=x-y
6.0	1.3	+ 4.7
6.5	1.2	+ 5.3
7.0	1.0	+ 6.0
7.5	0.9	+ 6.6
8.0	0.7	+ 7.3
8.5	0.7	+ 7.8
9.0	0.6	+ 8.4
9.5	0.5	+ 9.0
10.0	0.5	+ 9.5
10.5	0.4	+ 10.1

N.B.

The value of y is given to 0.1 dB. An ideal of the error involved in the correction can be gained from the consecutive values of y.

e.g. $x = 5.0 \pm 0.5$ dB $\Rightarrow$ $y = 1.7 \pm 0.3$

APPENDIX A5.1 - The Effect of Shim Stiffness on Simple Supports

A5.1.1 The problem

To ascertain what effect the mounting of a one dimensional panel (i.e. a beam) on shims as shown has upon the mode shapes and frequencies of the panel compared with an ideal simply supported panel.

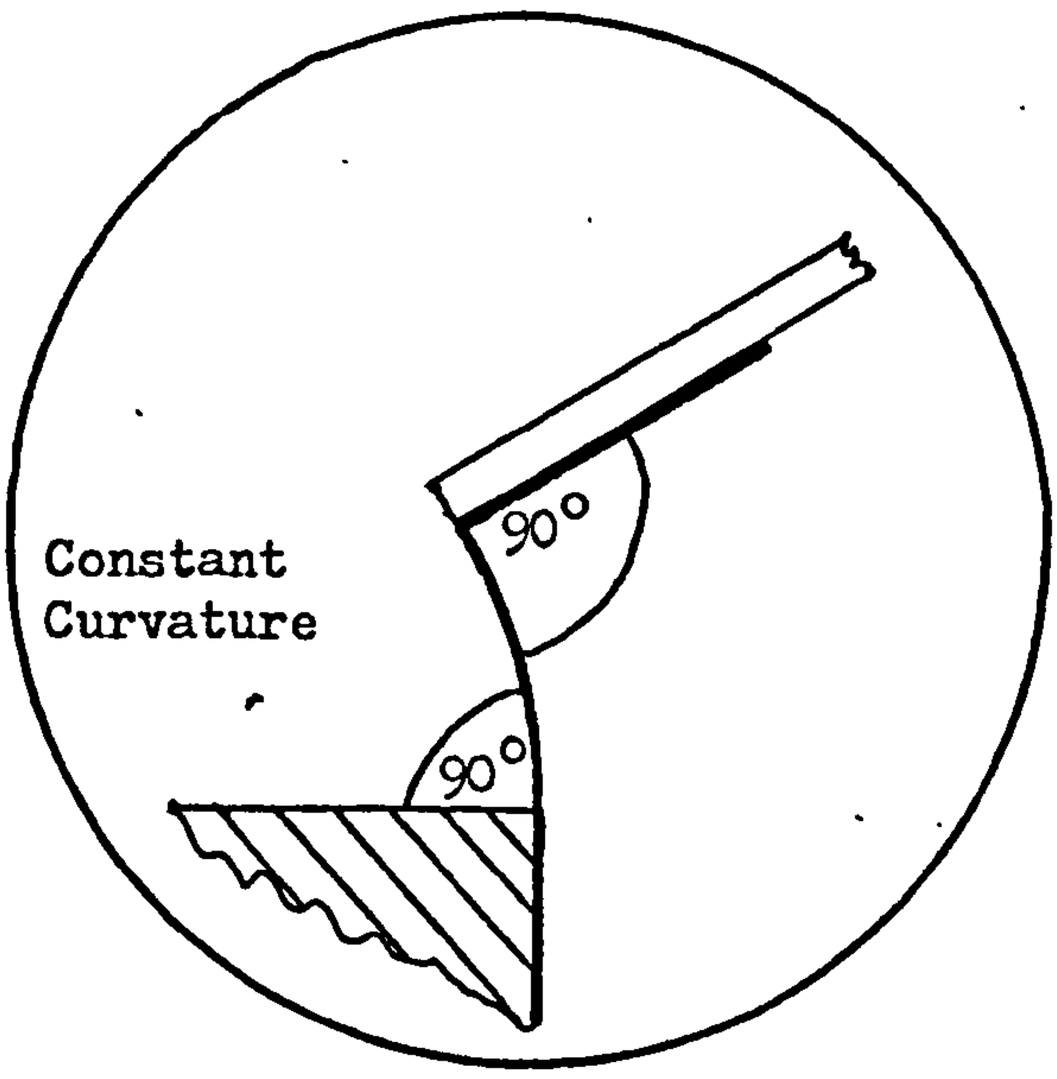

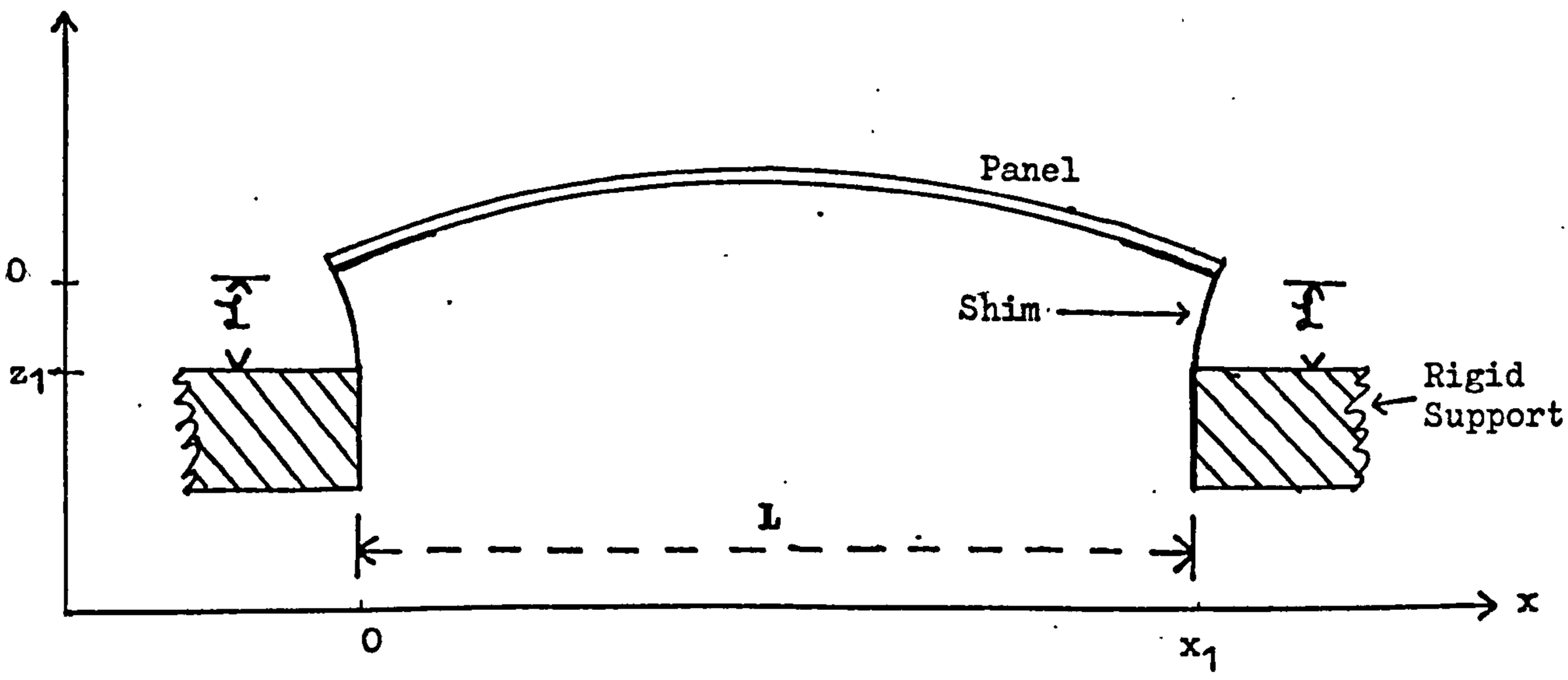

THE SHIM-SUPPORTED PANEL

N.B. The shim parameters have the subscript "s" whereas those of the panel "p" (e.g. z_p z_s).

A5.1.2 Ideal Boundary conditions

$$z_p = \frac{\partial^2 z_p}{\partial x^2} = 0 \text{ , at } x = 0 \text{ and } x_1 \qquad (5A1.1)$$

A5.1.3 Actual Boundary conditions

$$z_s = 0 \text{ ,}$$

$$\text{at } (0, z_1) \text{ and } (x_1 \text{ , } z_1) \qquad (5A1.2)$$

$$\frac{\partial z_s}{\partial x} = \infty$$

i.e. the shims are clamped to the rigid supports.

$$z_s = z_p$$

$$\text{at } (0 \text{ , } 0) \text{ and } (x_1 \text{ , } 0) \qquad (5A1.3)$$

$$\frac{\partial z_s}{\partial x} = -1 \Big/ \left(\frac{\partial z_p}{\partial x}\right)$$

i.e. the shims are clamped to the panel.

We ignore the effects of contraction along the panel and assume that the shim assumes a constant curvature as shown in the inset diagram.

A5.1.4 Perturbation method of calculation employed

We assume that the shim causes only a small perturbation on the mode shape and eigenfrequency of the panel and are thus justified in using

first order perturbation theory as follows:-

1) Assume a pure sine waveform on the panel as one gets in the case of perfect simple supports.

2) Calculate $\partial z_p / \partial x$ at the panel boundaries (0 , 0) and (x_1 , 0), hence $\partial z_s / \partial x$ at these points.

3) Given $\partial z_s / \partial x$ at these points calculate the shim curvature and hence its bending moment.

4) From the continuity of bending moment calculate $\partial^2 z_p / \partial x^2$ at these points.

5) Solve the equation for the panel using the new boundary conditions:-

$$\text{i.e.} \quad \frac{\partial^2 z_p}{\partial x^2} \text{ as calculated in (4)} \left.\begin{array}{l} \\ \\ \\ \text{and } z_p = 0 \end{array}\right\} \text{at } x = 0 \text{ and } x \qquad (5A1.4)$$

This solution yields both the new waveform and also the eigenfrequency.

STEP 1

From Reference 5.7 Equation (3.35) we have for the equation of a plate (beam):-

$$\frac{\partial^2 z_p}{\partial t^2} = K^2 c_L'^2 \frac{\partial^4 z_p}{\partial x^4} \qquad (5A1.5)$$

where $\mathcal{K}^2 = \frac{h^2}{12}$ is the second moment of area and c_L' is the longitudinal plate velocity.

The general solution of Equation 5A1.5 is:-

$$z_p = \cos t\ (w\ t + \phi) \quad A \cosh\left(\frac{w\ x}{v}\right) + B \sinh\left(\frac{w\ x}{v}\right) + C \cos\left(\frac{w\ x}{v}\right) + D \sin\left(\frac{w\ x}{v}\right) \tag{5A1.6}$$

where
$$v^2 = w\ c_L'\ \mathcal{K} \tag{5A1.7}$$

Applying the boundary conditions:-

$$z_p{}^o = \frac{\partial^2 z_p{}^o}{\partial x^2} = 0 \text{ at } x = 0 \text{ and } x_1 \tag{5A1.8}$$

where $z_p{}^o$ refers to the unperturbed value of the plate displacement we have:-

$$z_p{}^o = D \cos\left(w^o t + \phi\right) \sin\left(\frac{w^o x}{v}\right) \tag{5A1.9}$$

and
$$w^o = \frac{n \pi v}{L} \tag{5A1.10}$$

the unperturbed eigenfrequency.

STEP 2

Differentiating Equation (5A1.9) with respect to x we have:-

$$\frac{\partial z_p{}^o(0)}{\partial x} = D \frac{w^o}{v} \cos\left(w^o t + \phi\right) \tag{5A1.11}$$

$$\text{and} \quad \frac{\partial z_p^o(x)}{\partial x} = D \frac{w^o}{v} \cos (w^o t + \phi) (-1)^n \qquad (5A1.12)$$

As the angle between the shim and the panel is always 90^o at (0 , 0) and $(x_1 , 0)$:-

$$\frac{\partial x}{\partial z_s^o}(0,0) = -D \frac{w^o}{v} \cos (w^o t + \phi) \qquad (5A1.13)$$

$$\text{and} \quad \frac{\partial x}{\partial z_s^o}(0,0) = -D \frac{w^o}{v} \cos (w^o t + \phi) (-1)^n \qquad (5A1.14)$$

STEP 3

Expressing the above as Taylor expansions we have:-

$$\frac{\partial x}{\partial z_s^o}(0,0) = \frac{\partial x}{\partial z_s^o}(0,z_1) + \mathcal{L} \frac{\partial^2 x}{\partial z_s^{o2}}(0,0) \qquad (5A1.15)$$

the first term on the right hand side is zero because of the boundary conditions.

$$\frac{\partial^2 x}{\partial z_s^{o2}}(0,0) = \frac{D}{\mathcal{L}} \frac{w^o}{v} \cos (w^o t + \phi) (-1)^n \qquad (5A1.16)$$

Similarly

$$\frac{\partial^2 x\,(x_1,0)}{\partial z_s^{o2}} = \frac{-D}{\mathcal{L}} \frac{w^o}{v} \cos (w^o t + \phi) (-1)^n \qquad (5A1.17)$$

STEP 4

The bending moment must be the same in both the shim and the panel where they join.

$$E_s S_s K_s^2 \frac{\partial^2 x}{\partial z_s{}^o{}^2}(0,0) = - E_p S_p K_p^2 \frac{\partial^2 z_p{}^1}{\partial x^2}(0,0) \qquad (5A1.18)$$

and

$$E_s S_s K_s^2 \frac{\partial^2 x}{\partial z_s{}^o{}^2}(x_1,0) = + E_p S_p K_p^2 \frac{\partial^2 z_p{}^1}{\partial x^2}(x_1,0) \qquad (5A1.19)$$

where E and S represent Young's moduli and total cross sectional areas. Supercript (1) indicates the first order perturbation theory solution.

Defining:-

$$F = \frac{E_s S_s K_s^2}{E_p S_p K_p^2} \qquad (5A1.20)$$

we have for the new first order perturbation theory boundary conditions:-

$$\frac{\partial^2 z_p{}^1}{\partial x^2}(0,0) = \frac{F D}{\ell} \frac{w^o}{v} \cos(w^o t + \phi) \qquad (5A1.21)$$

$$\frac{\partial^2 z_p{}^1}{\partial x^2}(x_1,0) = (-1)^{n+1} \frac{FD}{\ell} \frac{w^o}{v} \cos(w^o t + \phi) \qquad (5A1.22)$$

$$z_p{}^1(x = 0) = z_p{}^1(x_1) = 0 \qquad (5A1.23)$$

STEP 5

The general solution is as before:-

$$z_p^1 = \cos(w^1 t + \phi)\left\{A \cosh\left\{\frac{w^1 x}{v}\right\} + B \sinh\left\{\frac{w^1 x}{v}\right\} + C \cos\left\{\frac{w^1 x}{v}\right\} + D \sin\left\{\frac{w^1 x}{v}\right\}\right\} \quad (5A1.24)$$

Applying Equation (5A1.23) we have:-

$$A + C = 0 \quad (5A1.25)$$

and $$A \cosh\left\{\frac{w^1 L}{v}\right\} + B \sinh\left\{\frac{w^1 L}{v}\right\} + C \cos\left\{\frac{w^1 L}{v}\right\} + D \sin\left\{\frac{w^1 L}{v}\right\} = 0 \quad (5A1.26)$$

differentiating twice with respect to x and applying Equation (5A1.21) we have:-

$$\frac{w^1}{v}(A - C) = \frac{FD}{L} \quad (5A1.27)$$

and applying Equation (5A1.22) we have:-

$$\frac{w^1}{v}\left(A \cosh\left\{\frac{w^1 L}{v}\right\} + B \sinh\left\{\frac{w^1 L}{v}\right\} - C \cos\left\{\frac{w^1 L}{v}\right\} - D \sin\left\{\frac{w^1 L}{v}\right\}\right) = (-1)^{n+1} \frac{FD}{L} \quad (5A1.28)$$

Combining the above four equations and simplifying we have:-

$$\frac{F}{L}\left((-1)^n + \cos \frac{w^1 L}{v} \right) = \frac{-2 w^1}{v} \sin\left\{\frac{I}{w^1 L}\right\} \quad (5A1.29)$$

We now assume that the solutions lie in the region of the unperturbed eigenfrequencies.

$$\text{i.e.} \qquad w^1 = w^o + \Delta w \qquad (5A1.30)$$

Combining Equations (5A1.29), (5A1.30) and (5A1,10) we have for odd values of n :-

$$\frac{F}{L}\left\{ - \cos\left\{\frac{\Delta w\, L}{v}\right\} - 1 \right\} = \frac{- 2\, w^1}{v} \sin\left\{\frac{\Delta w\, L}{v}\right\} \qquad (5A1.31)$$

If we assume:-

$$\frac{\Delta w\, L}{v} \leqslant 0.1 \qquad (5A1.32)$$

$$\text{i.e.} \qquad \frac{\Delta w}{w^o} \leqslant \frac{0.1}{n \pi} \qquad (5A1.33)$$

which is true for small perturbations of the first few modes, we may expand the trigonometric functions of Equation (5A1.31) as far as first powers only:-

$$\frac{F}{L}(- 2) = - \frac{2\, w^1}{v} \frac{\Delta w\, L}{v} \qquad (5A1.34)$$

Substituting for v from Equation (5A1.7) and w^o from Equation (5A1.10) :-

$$\frac{\Delta w}{w^o} = F \frac{L}{L} \frac{1}{n^2 \pi^2} \qquad (5A1.35)$$

When n is even a different equation to (5A1.31) is found. However, like Equation (5A1.31) this second equation leads to Equation (5A1.35).

Therefore, for all modes the non-dimensionalised increase in frequency is given by:-

$$\frac{\Delta w}{w} = \frac{E_s S_s K_s^2}{E_p S_p K_p^2} \frac{L}{d} \frac{1}{n^2 \pi^2} \qquad (5A1.36)$$

If the only difference in geometry between the shim and the panel is their thickness h, and they are made of the same material.

$$\frac{\Delta w}{w^o} = \frac{h_s^3}{h_p^3} \frac{L}{d} \frac{1}{n^2 \pi^2} \qquad (5A1.37)$$

A5.1.5 Conclusions

This formula was compared with some experimental results obtained by Parrott (5.8). The results of Parrott indicate that the imperfections of his simple support were due to some cause other than the shim stiffness perturbation considered in this appendix. His measured frequency was lower than that calculated for ideal simple supports which would seem to indicate that the supports allowed lateral movement. However, the discrepancy between his experimental and theoretical frequencies increased with higher mode numbers. This is most surprising as with the higher mode numbers with many intermediary nodes one would expect the end support

conditions to have very little effect upon the panel eigenfrequencies.

The perturbation theory given above is a very crude approximation to what actually takes place. Apart from the possibility of lateral movement at the supports the effects of the panel foreshortening have been neglected. If the shim were to take the shape shown in the previous diagram it would require the panel to span a greater length when deformed than when it was in its equilibrium position. This is obviously not the case as the deformed panel is foreshortened and the shim would probably take the shape shown below.

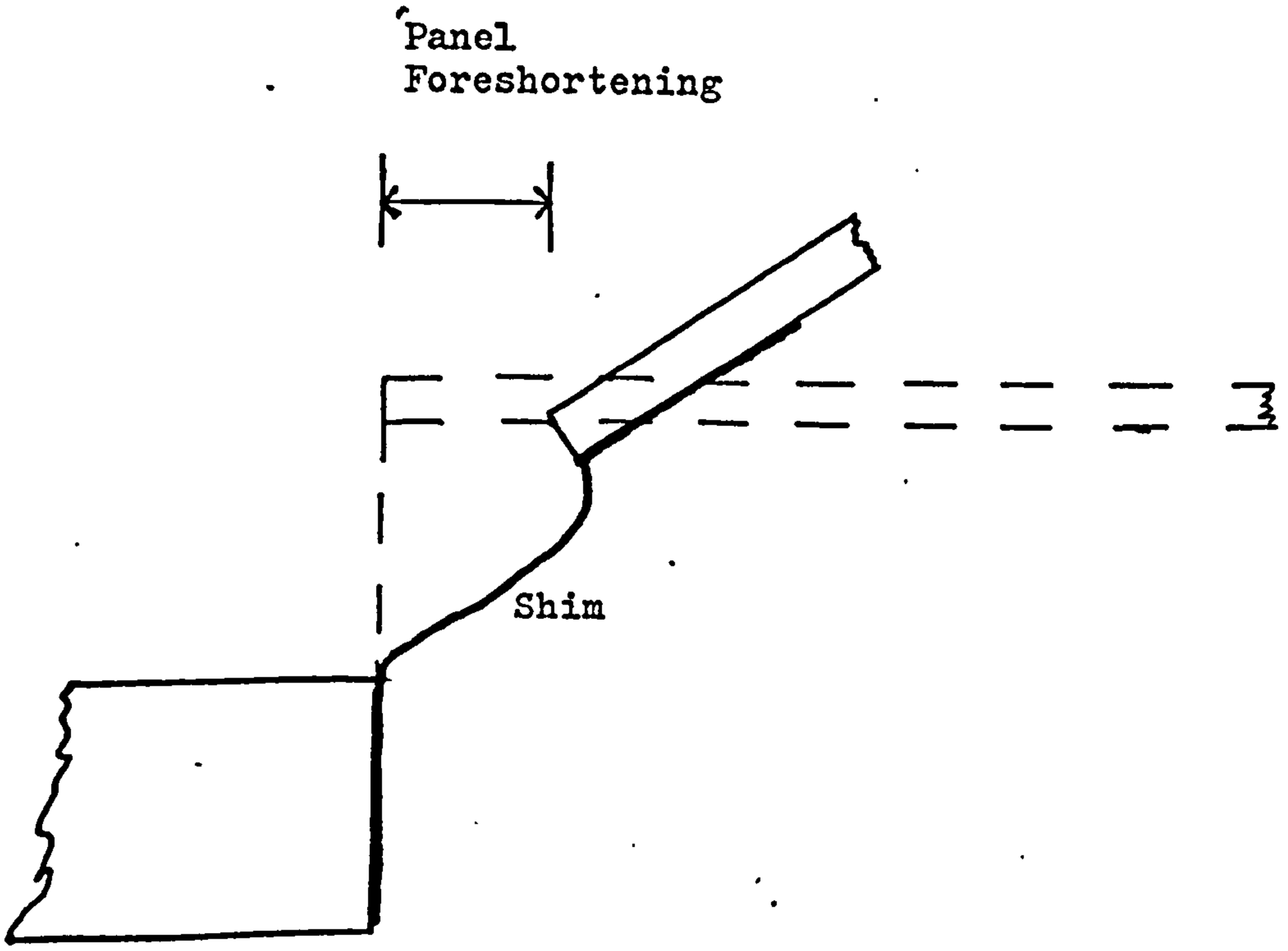

A MORE LIKELY SHIM DEFORMATION

Panel foreshortening would also create a tension in the panel giving rise to membrane forces.

However, in spite of the shortcomings of the theory, equation (5A1.37) can given an order of magnitude estimation of the perturbation and indicate whether a particular support construction is likely to be satisfactory or not.

A thorough investigation of the effects of various edge conditions upon the vibration of plates has been undertaken by White (5.9). However, in order to utilize his results one has to express the panel boundary conditions mathematically in terms of elastic and inertial constraints of translation and rotation. Given a real physical situation, the translation of the support geometry into these idealised mathematical parameters is almost as difficult a problem as determining what effect they will have upon the panel vibration.

APPENDIX A5.2 - Determination of Pressure for Stern Shock-Piling

Equation (5A2.1) below extracted from reference (5.11) Equation 19.39, relates the distance X, required by a sine wave of intensity Δp_m, travelling in a fluid of mean pressure P_o with the ratio of the principal specific heats γ, to change into a sawtooth waveform.

$$\frac{X}{\lambda} = \frac{\gamma}{2(\gamma + 1)} \quad \frac{P_o}{\Delta p_m} \qquad (5A2.1)$$

Taking the total length of shock tube available (29 foot) as X, P_o as 14.7 lb/ft^2, γ as 1.4 and λ as 3 ft we find that the Δp_m = 0.45 lb/ft^2.

APPENDIX A5.3

```
RRHSPR     16:20    MANCHR 26/06/69

100 BEGIN REAL PI,A,B,TP,RP,E,NU,PF,DT,M,W11,W31,F11,F31,LF11,
101 LF31,K11,K31,EX11F,EX31F;
106 ARRAY P,L11,L31[1:100],Q11,Q31,EXT[1:200];
108 INTEGER I,J;
110 PI:=4*ARCTAN(1);
112 READATA(LENGTH,A);READATA(BREADTH,B);
113 READATA(THICK,TP);READATA(PANDEN,RP);
114 READATA(YOUNG,E);READATA(POISSON,NU);
120 READATA(PRESSFAC,PF);READATA(DELTAT,DT);
121 FOR I:=1 STEP 1 UNTIL 100 DO READATA(PRESS,P[I]);
130 M:=RP*TP*A*B/4;
132 W11:=PI↑2*TP*((1/A)↑2+(1/B)↑2)*SQRT(E/(12*RP*(1-NU↑2)));
136 W31:=W11*((3/A)↑2+(1/B)↑2)/((1/A)↑2+(1/B)↑2);
138 K11:=W11↑2*M; K31:=W31↑2*M;
140 F11:=W11/(2*PI); F31:=W31/(2*PI);
142 PRINT("F11","F31"); PRINT(F11,F31);
160 LF11:=PF*A*B/2*DT/(M*W11); LF31:=LF11*W11/(W31*3);
162 FOR I:=1 STEP 1 UNTIL 100 DO
164 BEGIN L11[I]:=P[I]*LF11; L31[I]:=P[I]*LF31;
166 END;
170 EX11F:=PI↑2*TP/(2*A↑2); EX31F:=9*PI↑2*TP/(2*A↑2);
178 PRINT("J","EXT[J]");
180 FOR J:=1 STEP 1 UNTIL 200 DO
182 BEGIN Q11[J]:=0; Q31[J]:=0;
184       FOR I:=1 STEP 1 UNTIL J DO
186       BEGIN IF I>100 THEN GOTO OUT;
187             Q11[J]:=Q11[J]+L11[I]*SIN(W11*(J-I)*DT);
188             Q31[J]:=Q31[J]+L31[I]*SIN(W31*(J-I)*DT);
192       END;
194       OUT:
196       EXT[J]:=EX11F*Q11[J]-EX31F*Q31[J];
198       PRINT(J,EXT[J]);
200 END;
900 DATA LENGTH:=17;
901 DATA BREADTH:=11;
902 DATA THICK:=0.0784;
904 DATA YOUNG:=2$12;
905 DATA POISSON:=0.3;
906 DATA PANDEN:=7.82;
920 DATA PRESSFAC:=1$3;
921 DATA DELTAT:=6.95$-5;
925 DATA PRESS:=43,43.5,42.5,41,40,38,36,32.5,31.5,28,
926 25,22.5,20,15.5,14,10,8.5,6.5,3.5,0.5,
927 -1.5,-3.5,0,1.5,0,-1.5,-2.5,-4,-5,-7,
928 -10,-12,-12.5,-5,-3.5,-5.5,-6,-7,-5.5,-4,
929 -3.5,-3.5,-4,-5.5,-6.5,-5,-4.5,-4,-4,-3.5,
930 -5.5,-9,-7.5,-5.5,-5,-5,-4.5,-5,-6.5,-9,
931 -8.5,-3,-2,-2,-2,-2.5,-3,-3,-3.5,-2,
932 0.5,0,-4,-5,-4.5,2,0,-1.5,-2.5,-1,
933 0.5,1,-4,-6.5,-8,1,0.5,-2,-1,0,
934 0,0.5,-1.5,-4,-5,-7.5,-5,-3,-3,-0.5;
999 END;
```

APPENDIX A6.1

```
RRHNPR     16:36    MANCHR 26/06/69

100 BEGIN REAL PI,A,B,TP,H,E,NU,RP,RA,C,
101 D,M11,M31,K11,K31,KA,ETA,ALP,W0,
102 BET,WC1,WC2,W1,W2,W11,W31,F1,F2,F11,F31,
103 R1,R2,M1,M2,K1,K2,LF1,LF2
104 ,PF,DT,LK1,LK2,EX1,EX2,K13,K71,K51,W13,W71,W51,F13,
105 F71,F51,EX13,EX71,EX51,LF13,LF71,LF51,LK13,LK71,LK51;
106 ARRAY P,LR1,LR2,EXT,Q1,Q2,LR13,LR71,LR51,Q13,Q71,Q51[1:100];
108 INTEGER I,J;
109 PI:=4*ARCTAN(1);
110 READATA (LENGTH,A); READATA (BREADTH,B);
111 READATA(THICK,TP); READATA(DEPTH,H);
112 READATA(YOUNG,E); READATA(POISSON,NU);
113 READATA(PANDEN,RP); READATA(AIRDEN,RA);
114 READATA(AIRVEL,C);
120 D:=TP↑3*E/(12*(1-NU↑2));
121 M11:=RP*TP*A*B/4; M31:=M11;
122 K11:=D*A*B/4*((PI/A)↑2+(PI/B)↑2)↑2;
123 K31:=D*A*B/4*((3*PI/A)↑2+(PI/B)↑2)↑2;
124 KA:=RA*C↑2*16*A*B/(PI↑4*H);
125 ETA:=KA/K11; ALP:=A/B;
126 W0:=SQRT(K11/M11);
130 BET:=((9+ALP↑2)/(1+ALP↑2))↑2;
131 WC1:=SQRT((1+BET+10*ETA/9
132 -SQRT((1+10*ETA/9+BET)↑2
133 -4*(BET+(1/9+BET)*ETA)))/2);
134 WC2:=SQRT((1+BET+10*ETA/9
135 +SQRT((1+10*ETA/9+BET)↑2
136 -4*(BET+(1/9+BET)*ETA)))/2);
137 W1:=W0*WC1; W2:=W0*WC2;
138 W11:=W0; W31:=W11*SQRT(BET);
140 F1:=W1/(2*PI); F2:=W2/(2*PI);
142 F11:=W11/(2*PI); F31:=W31/(2*PI);
150 R1:=-3/ETA*(1+ETA-WC1↑2);
151 R2:=-3/ETA*(1+ETA-WC2↑2);
152 M1:=RP*TP*A*B/4*(1+R1↑2)/(1-R1)↑2;
153 M2:=RP*TP*A*B/4*(1+R2↑2)/(1-R2)↑2;
154 K1:=W1↑2*M1; K2:=W2↑2*M2;
155 LF1:=A*B/2*(1+R1/3)/(1-R1);
156 LF2:=A*B/2*(1+R2/3)/(1-R2);
160 PRINT("A","B","TP","H");
161 PRINT(A,B,TP,H);
162 PRINT("  ");
164 PRINT("E","NU","RP");
165 PRINT(E,NU,RP);
167 PRINT("0");
168 PRINT("F11","F31","F1","F2");
169 PRINT(F11,F31,F1,F2);
170 PRINT("  ");
172 PRINT("R1","R2");
173 PRINT(R1,R2);
175 PRINT("  ");
176 PRINT("K11","K31","KA");
177 PRINT(K11,K31,KA);
180 K13:=K11*(((1/A)↑2+(3/B)↑2)/((1/A)↑2+(1/B)↑2))↑2;
182 K71:=K11*(((7/A)↑2+(1/B)↑2)/((1/A)↑2+(1/B)↑2))↑2;
184 K51:=K11*(((5/A)↑2+(1/B)↑2)/((1/A)↑2+(1/B)↑2))↑2;
1
```

```
190 W13:=SQRT(K13/M11); F13:=W13/(2*PI); PRINT("F13=",F13);
192 W71:=SQRT(K71/M11); F71:=W71/(2*PI); PRINT("F71=",F71);
194 W51:=SQRT(K51/M11); F51:=W51/(2*PI); PRINT("F51=",F51);
200 EX13:=PI↑2*TP/(2*A↑2); LF13:=A*B/6;
202 EX71:=49*PI↑2*TP/(2*A↑2); LF71:=A*B/14;
204 EX51:=25*PI↑2*TP/(2*A↑2); LF51:=A*B/10;
300 PRINT("  ");PRINT("  ");PRINT("  ");PRINT("  ");
301 READATA(PRESSFAC,PF); READATA(DELTAT,DT);
302 PRINT("PF","DT"); PRINT(PF,DT); PRINT("  ");
303 LK1:=PF*DT*LF1/(M1*W1);  LK2:=PF*DT*LF2/(M2*W2);
304 LK13:=PF*DT*LF13/(M11*W13); LK71:=PF*DT*LF71/(M11*W71);
305 LK51:=PF*DT*LF51/(M11*W51); FOR I:=1 STEP 1 UNTIL 100 DO
306 BEGIN READATA(PRESS,P[I]);
307       LR1[I]:=LK1*P[I];  LR2[I]:=LK2*P[I];
308      LR13[I]:=LK13*P[I]; LR71[I]:=LK71*P[I]; LR51[I]:=LK51*P[I];
310 END;
320 EX1:=1/(1-R1)*PI↑2*TP/(2*A↑2)*(1-9*R1);
322 EX2:=1/(1-R2)*PI↑2*TP/(2*A↑2)*(1-9*R2);
326 PRINT("Q1+Q2-Q13-Q71+Q51 MODES");
328  PRINT("J","EXT[J]");
330 FOR J:=9 STEP 1 UNTIL 100 DO
331 BEGIN Q1[J]:=0;Q2[J]:=0;Q13[J]:=0;Q71[J]:=0;Q51[J]:=0;
332 FOR I:=1 STEP 1 UNTIL J DO
334 BEGIN Q1[J]:=Q1[J]+SIN(W1*(J-I)*DT)*LR1[I];
335       Q2[J]:=Q2[J]+SIN(W2*(J-I)*DT)*LR2[I];
336       Q13[J]:=Q13[J]+SIN(W13*(J-I)*DT)*LR13[I];
337       Q71[J]:=Q71[J]+SIN(W71*(J-I)*DT)*LR71[I];
338       Q51[J]:=Q51[J]+SIN(W51*(J-I)*DT)*LR51[I];
340 END;
350 EXT[J]:=Q1[J]*EX1+Q2[J]*EX2-Q13[J]*EX13-Q71[J]*EX71+Q51[J]*EX51;
360 PRINT(J,EXT[J]);
370 END;
900 DATA LENGTH:=17;
901 DATA BREADTH:=11;
902 DATA THICK:=0.05588;
903 DATA DEPTH:=2.9;
904 DATA YOUNG:=2$12;
905 DATA POISSON:=0.3;
906 DATA PANDEN:=7.82;
907 DATA AIRDEN:=1.21$-3;
908 DATA AIRVEL:=34300;
920 DATA PRESSFAC:=-2.91$3;
921 DATA DELTAT:=2.9$-5;
925 DATA PRESS:=32.5,31,30,29,28,27,26.5,25.5,25,24,
926 23,24,23,22,21,20,19,17.5,16.5,15,
927 13.5,11.5,11,10,9.5,8.5,8,7,6,4,
928 2.5,2,1.5,0.5,-0.5,-1,-1.5,-2.5,-3,-4,
929 -4.5,-4,-3.5,-3,-3,-3,-2,-2.5,-3,-3.5,
930 -4.5,-5,-5,-5,-5.5,-5.5,-6,-8,-8.5,-9.5,
931 -11,-11,-11,-6.5,-4.5,-4,-4.5,-3,-1.5,-2,
932 -2.5,-3.5,-4,-3,-1,-0.5,0,-0.5,-1.5,-3,
933 -2.5,-3,-4,-4,-3,-2,-1,0,1,2,
934 2,1.5,0.5,0,0,0,-1,-2.5,-2,-2;
999 END;
```

FIGURE 2.1 - THE SOUND MEASURING EQUIPMENT NORMALLY EMPLOYED IN THE MEASUREMENT OF TRANSMISSION

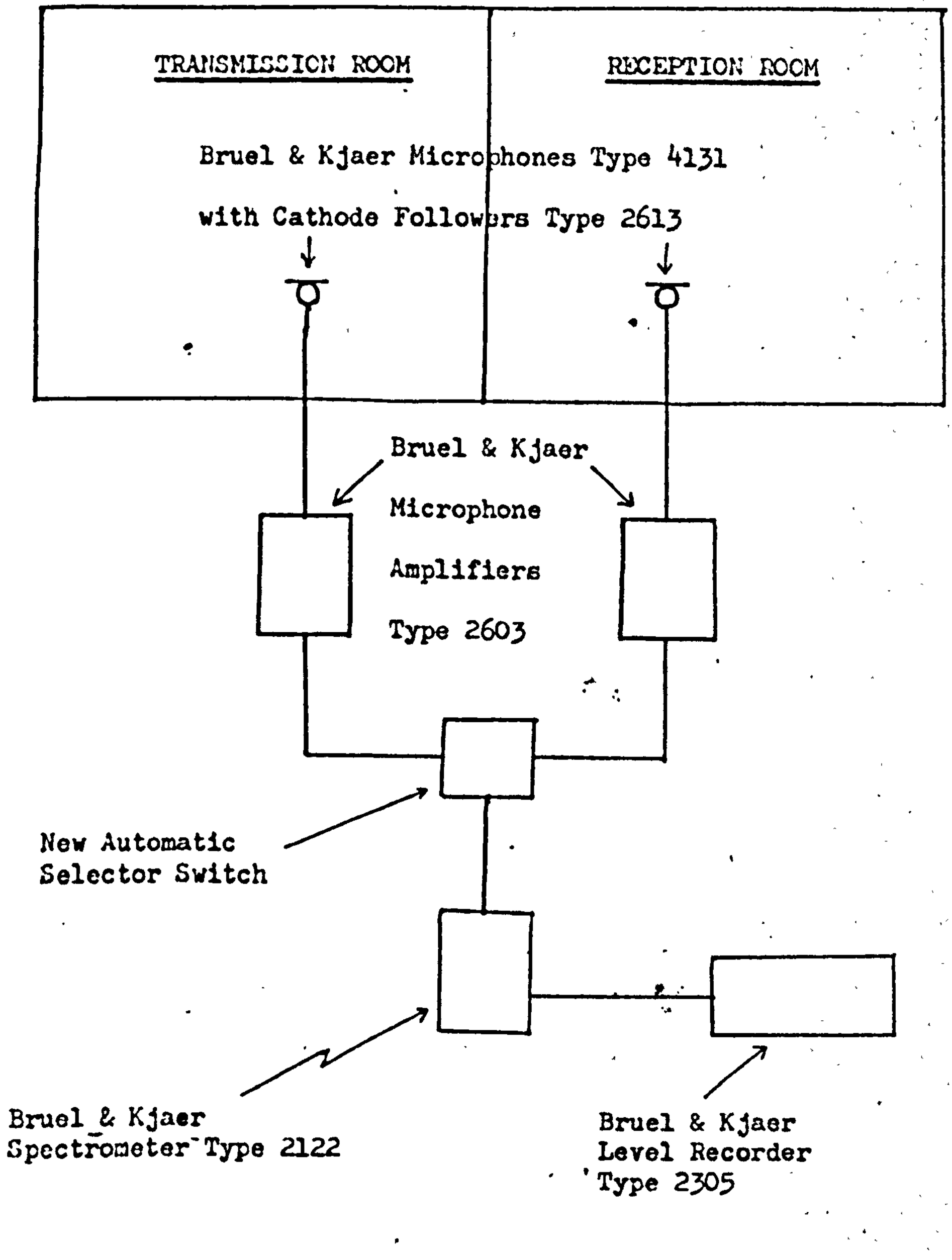

FIGURE 2.2 - THE MODIFIED SOUND MEASURING EQUIPMENT USED TO MEASURE THE HIGH VALUE OF TRANSMISSION LOSS

FIGURE 2.3 - THE EFFECT OF THE ELECTRICAL NOISE CORRECTION

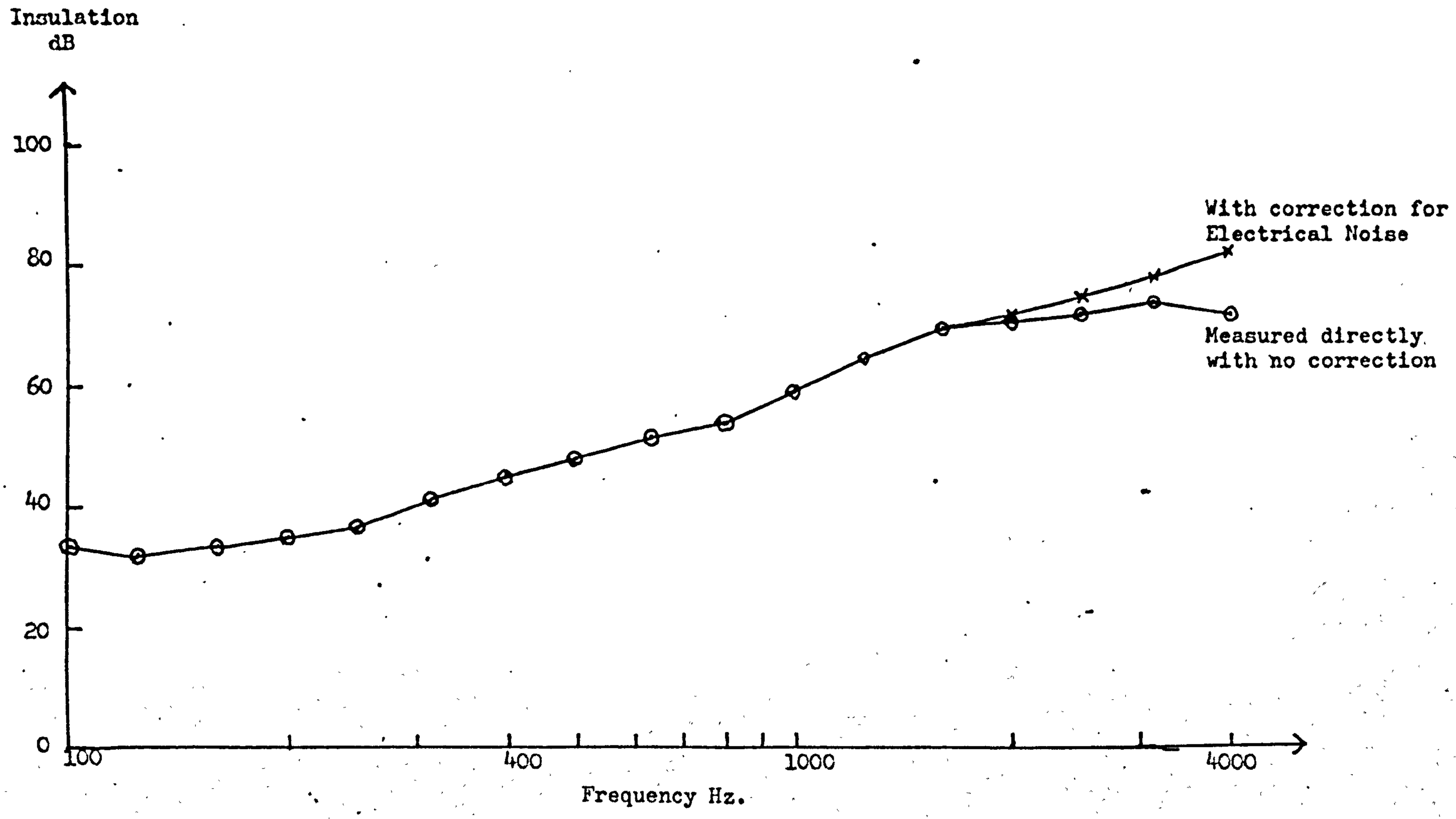

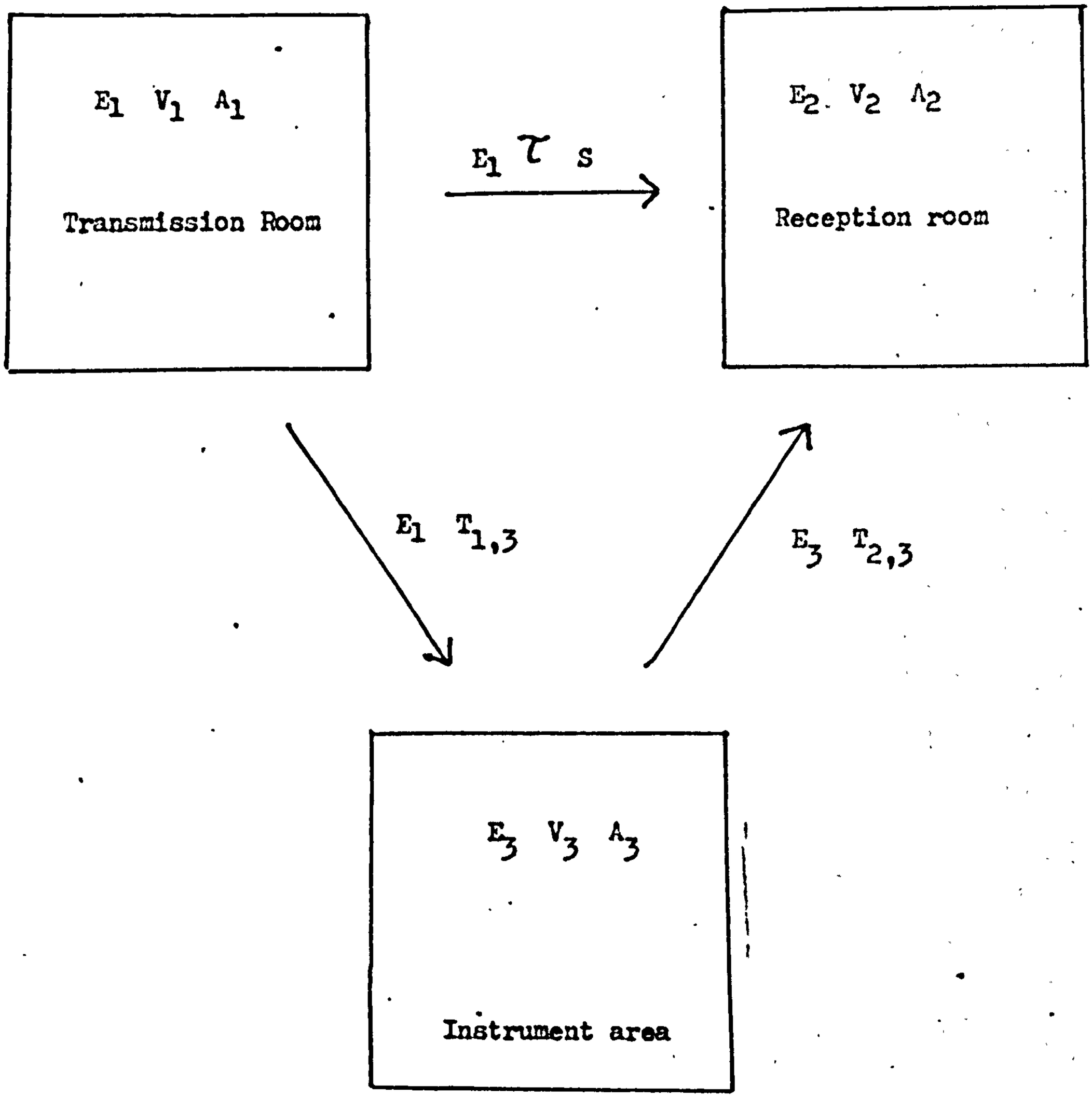

FIGURE 2.4 - SCHEMATIC REPRESENTATION OF LABORATORY FLANKING PATHS

FIGURE 2.5 - THE EFFECTS OF AIRBORNE FLANKING PATHS

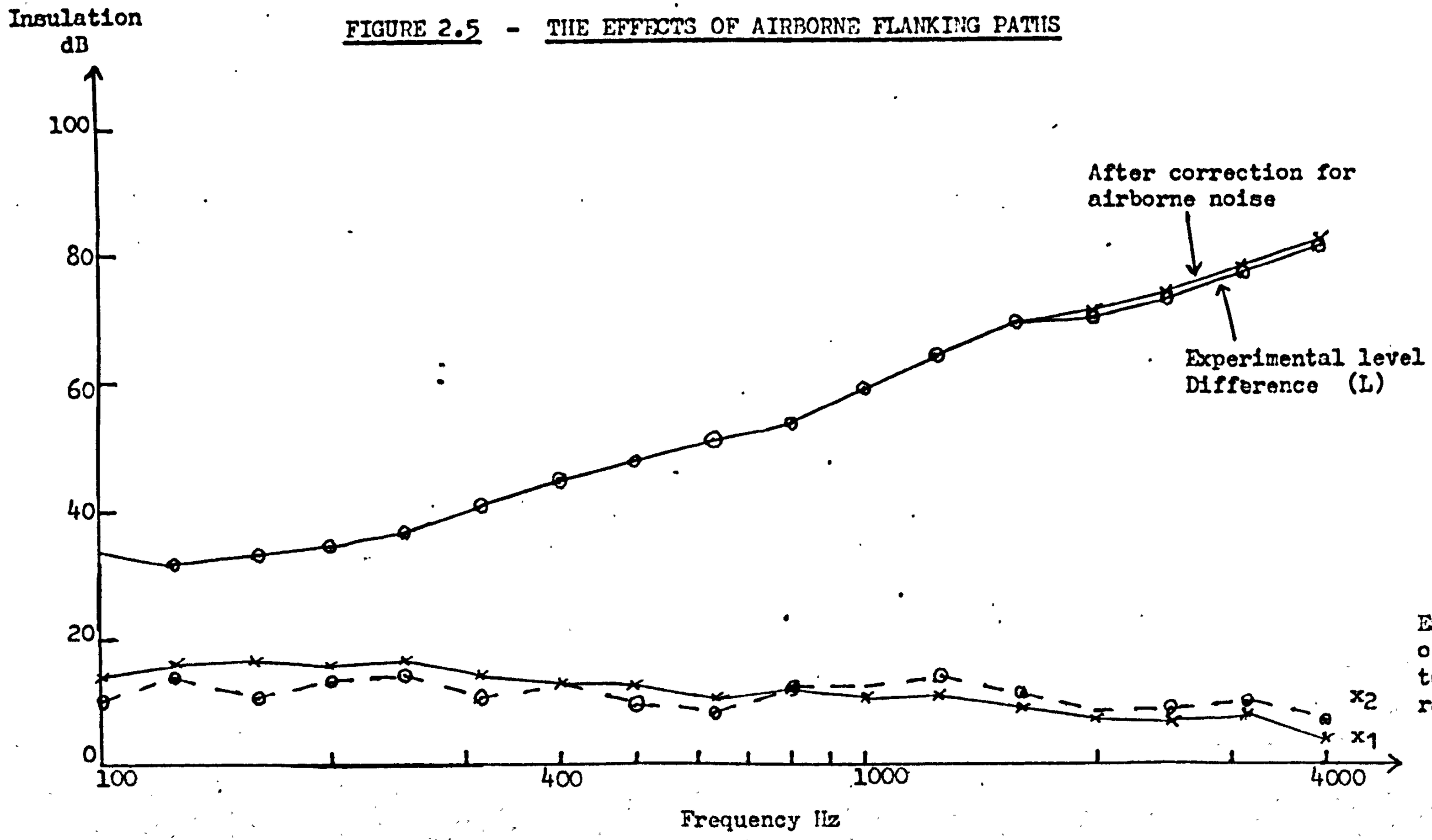

FIGURE 2.6 - THE LIMITING TRANSMISSION LOSS OF THE SUITE

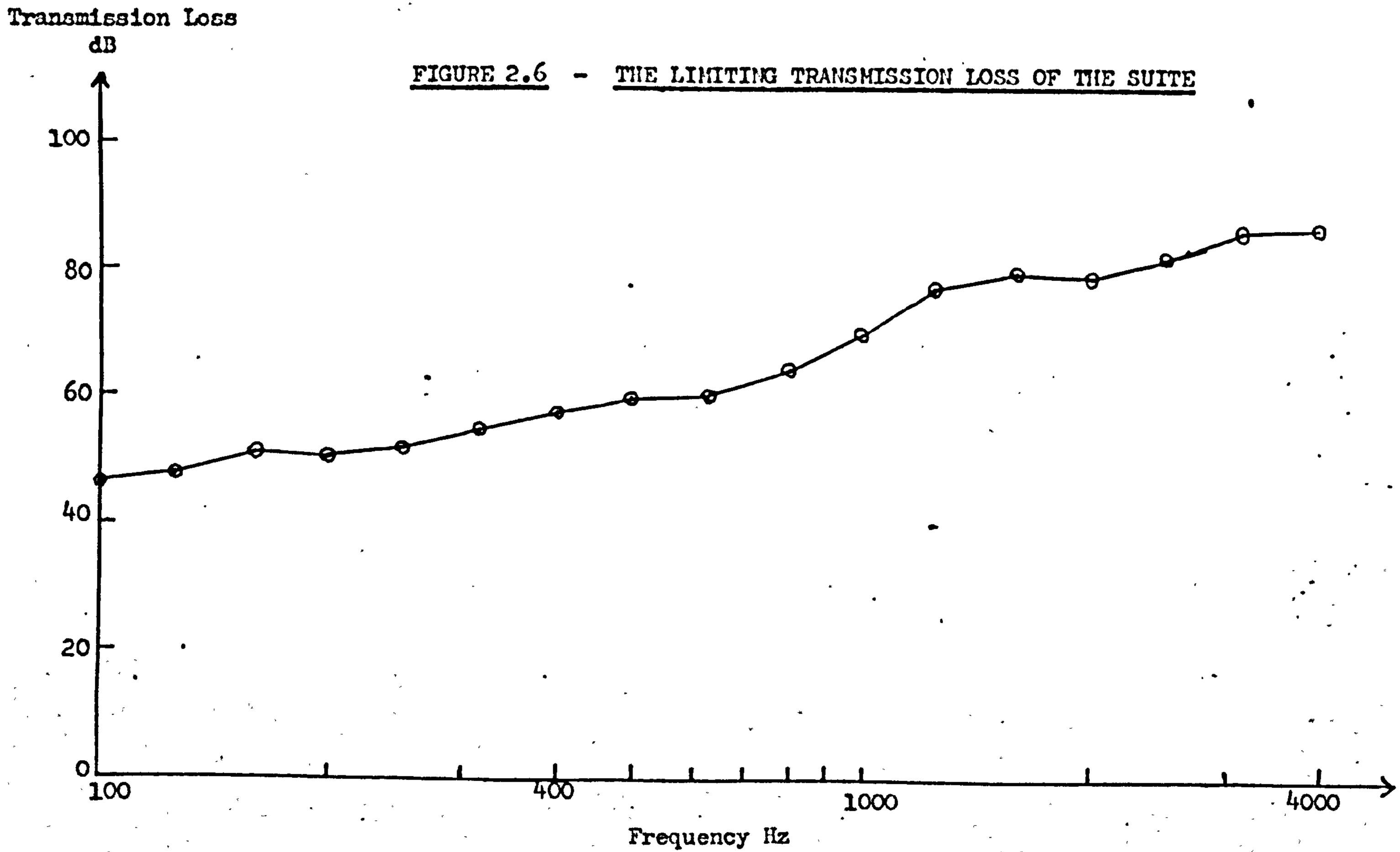

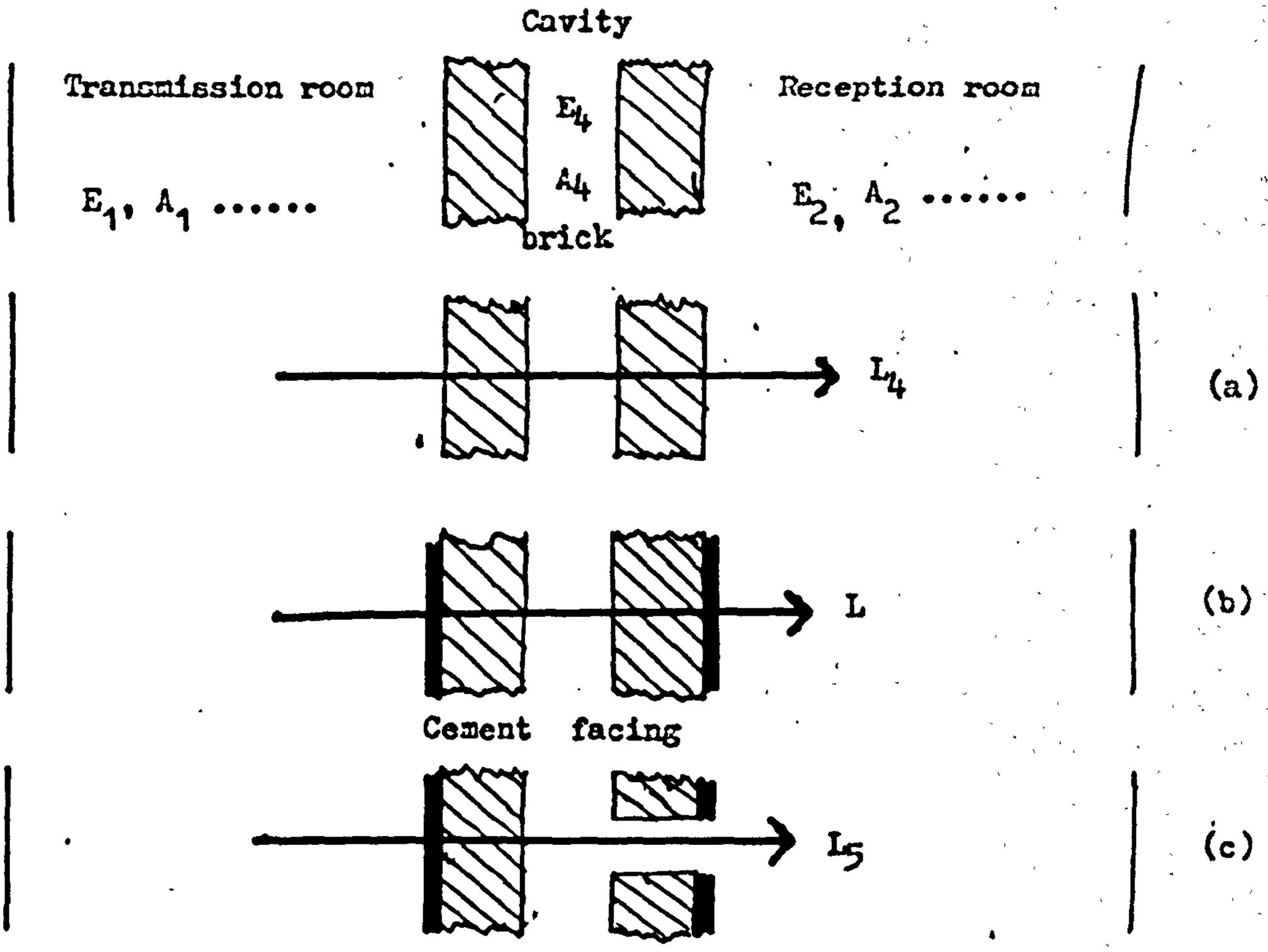

FIGURE 2.7 - THE BRICK WALL CONSTRUCTIONS INVESTIGATED

FIGURE 2.8 - SEMI EMPIRICAL PREDICTIONS OF THE LEVEL DIFFERENCE PRODUCED BY A DOUBLE BRICK WALL IN THE ABSENCE OF FLANKING

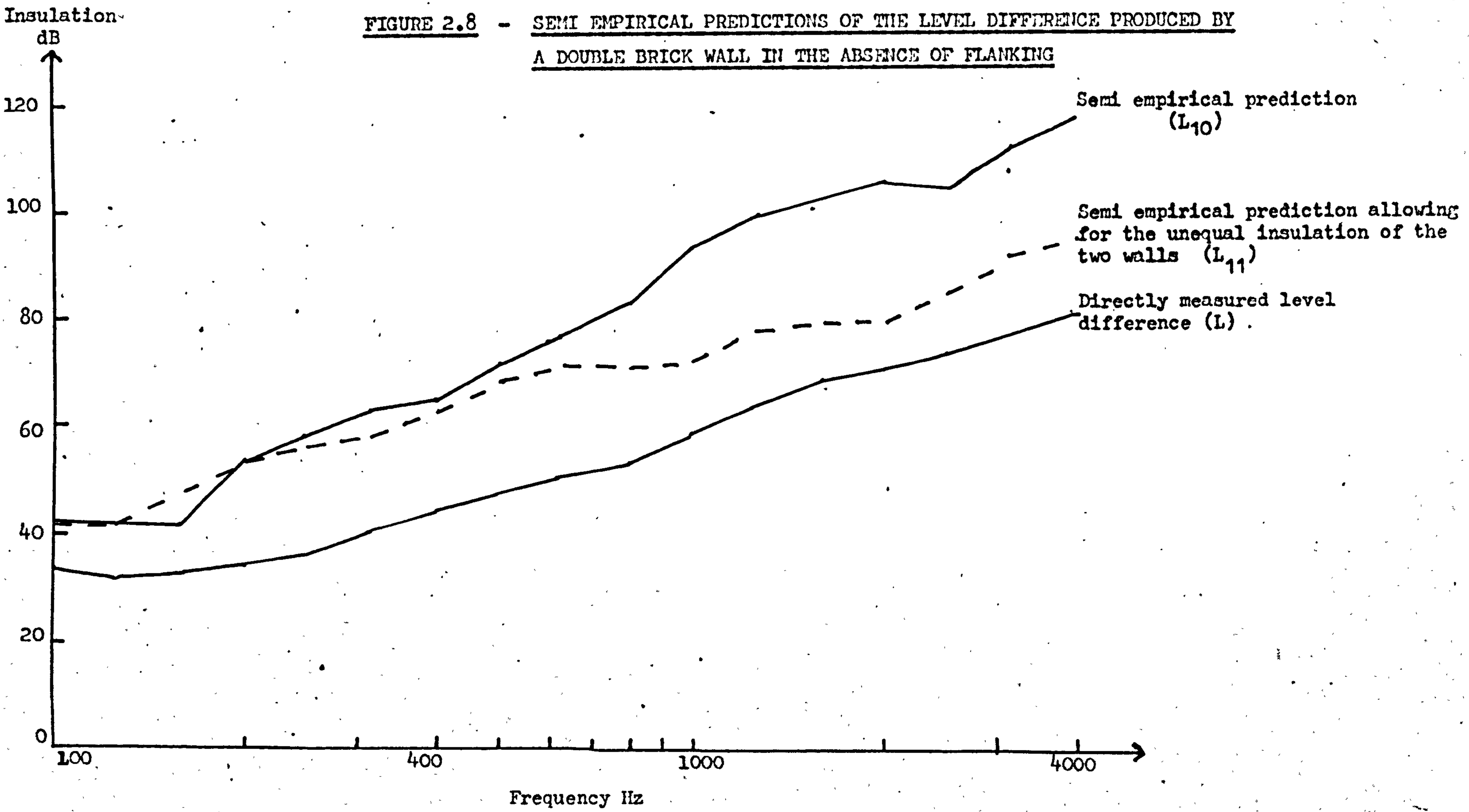

FIGURE 2.9 - THE UNEQUAL INSULATION OF THE TWO WALLS

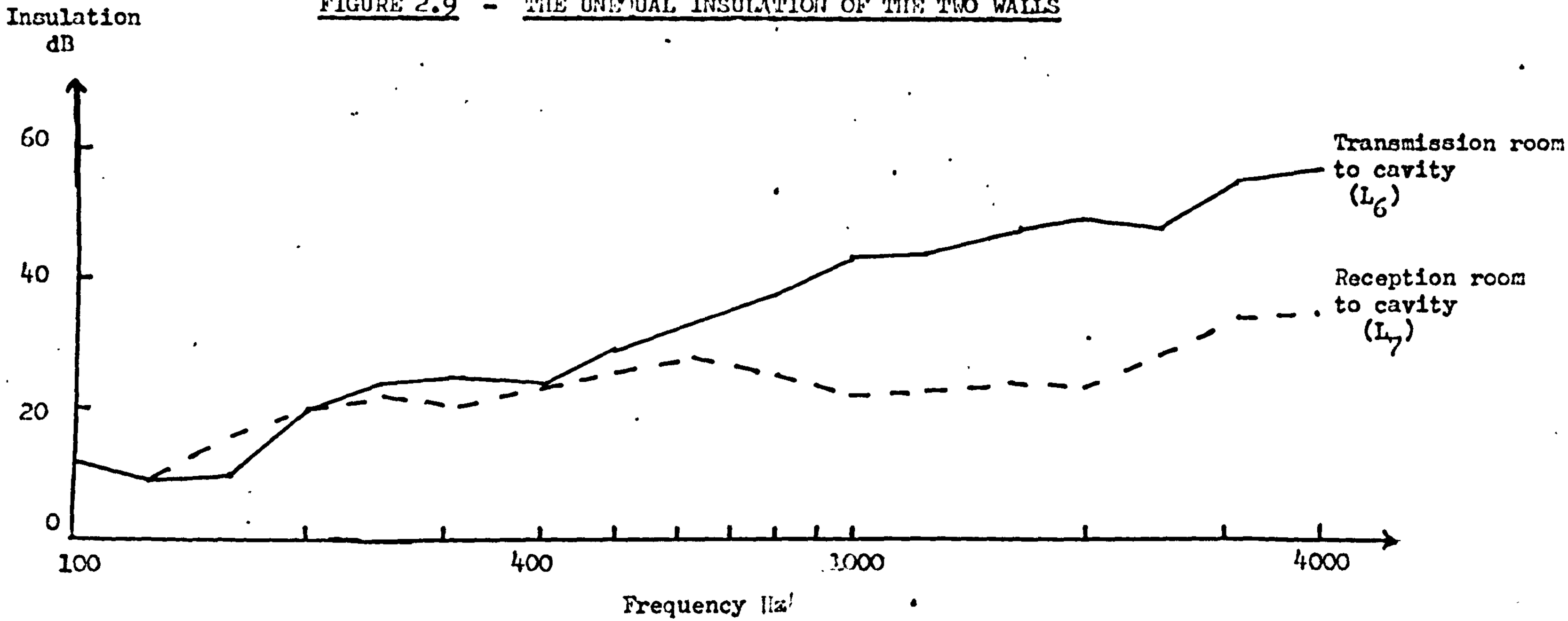

FIGURE 2.10 - THE TRANSMISSION LOSS OF A SINGLE BRICK WALL

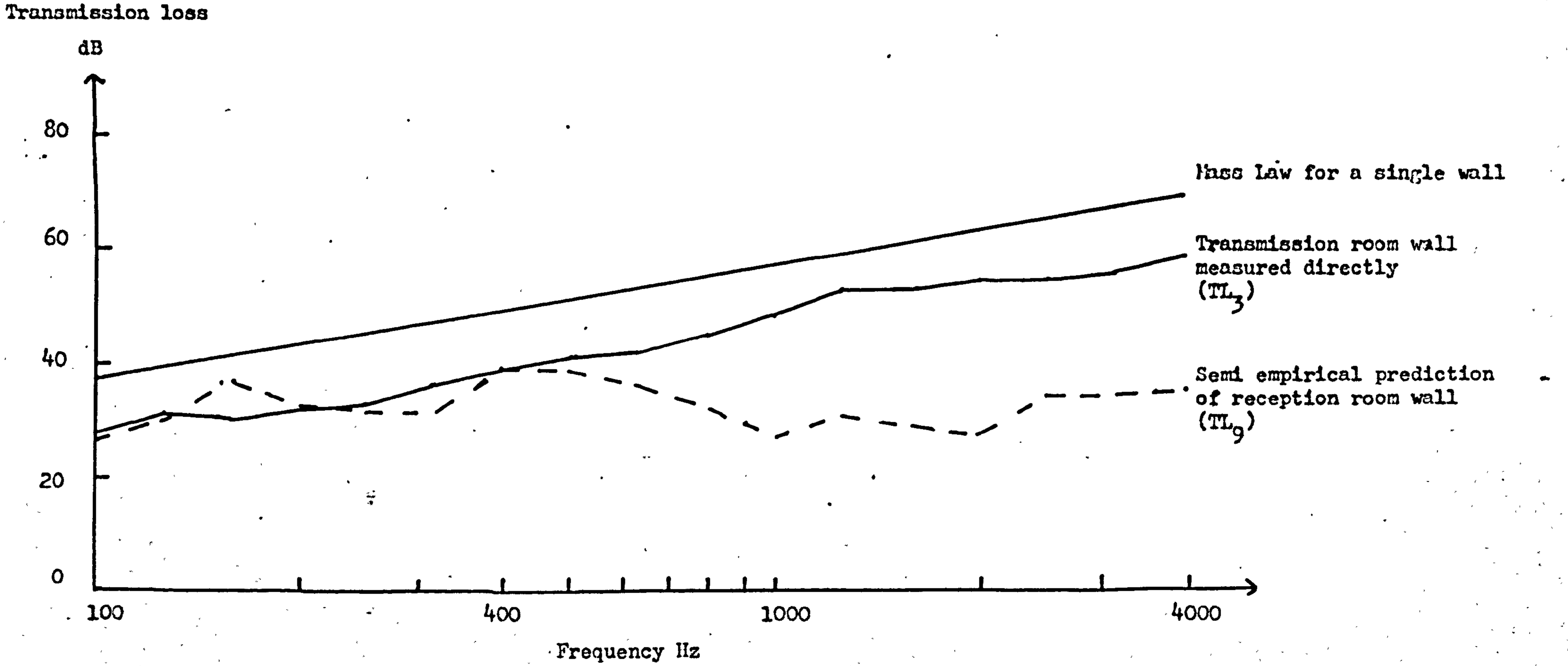

FIGURE 2.11 - THE TRANSMISSION LOSS OF A DOUBLE BRICK-WALL

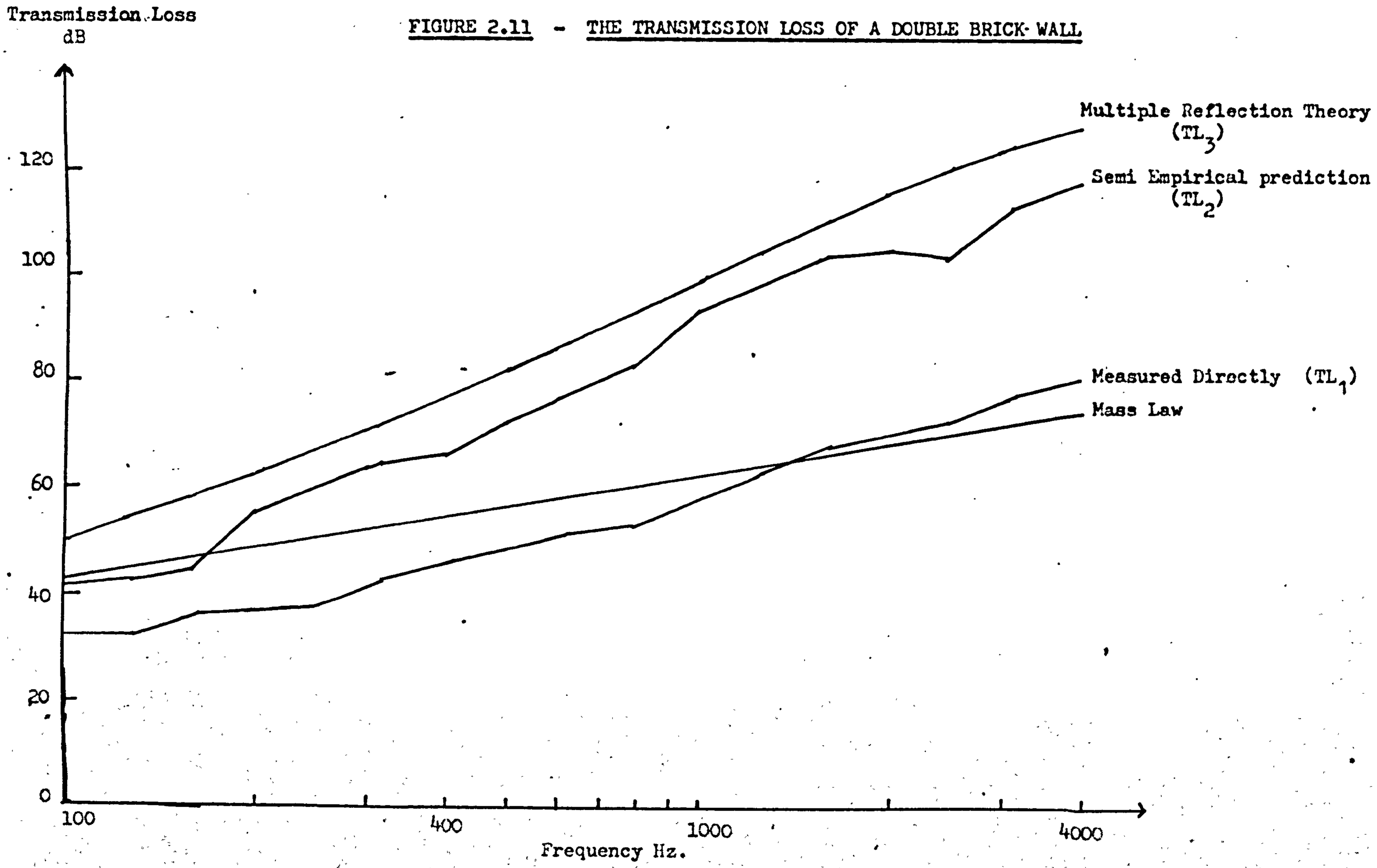

FIGURE 2.12 - THE EFFECT OF FACING THE DOUBLE BRICK WALL WITH CEMENT

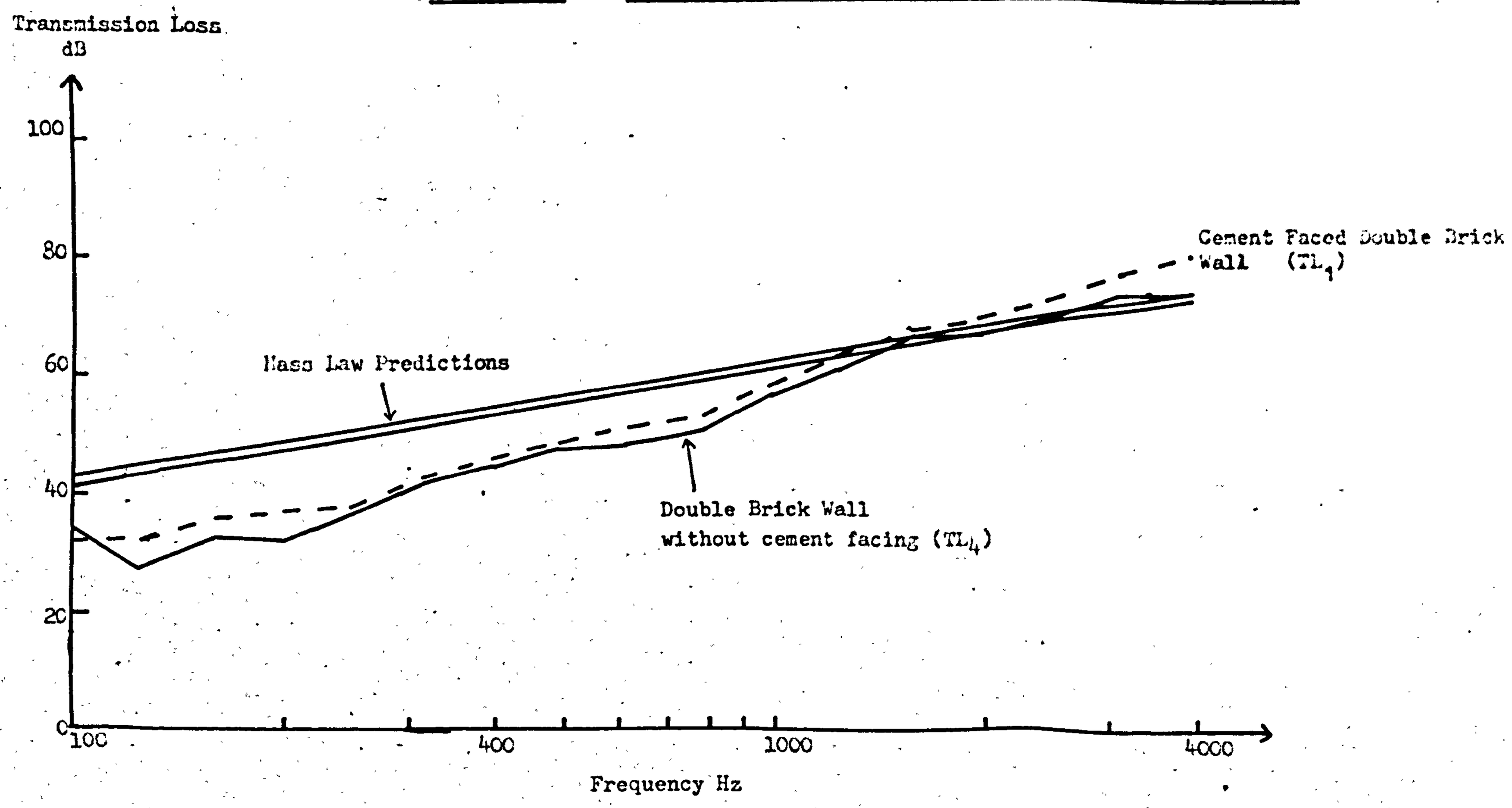

FIGURE 2.13 - THE TRANSMISSION LOSS OF A SINGLE BRICK WALL

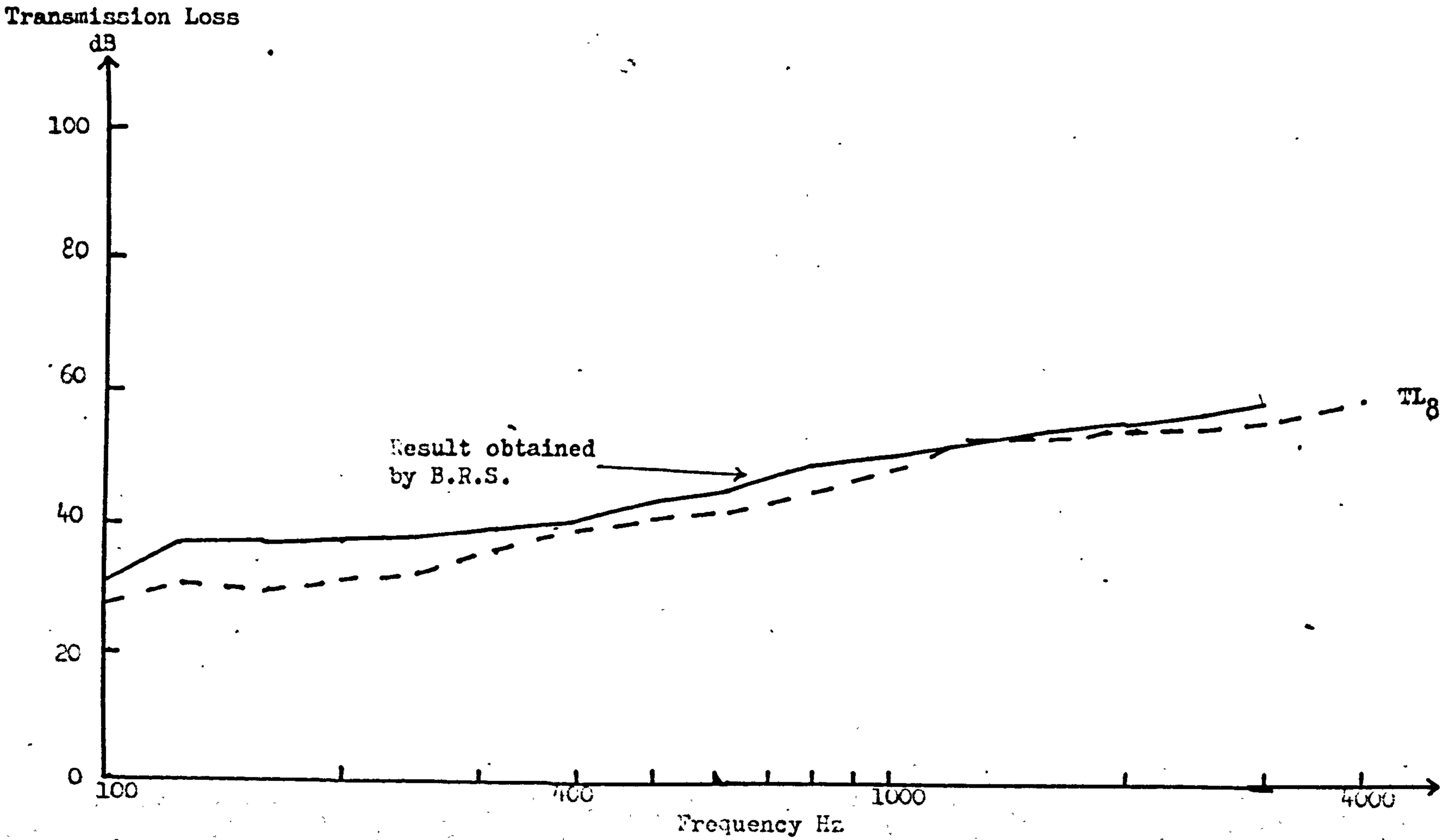

FIGURE 2.14 - THE TRANSMISSION LOSS OF A DOUBLE BRICK WALL

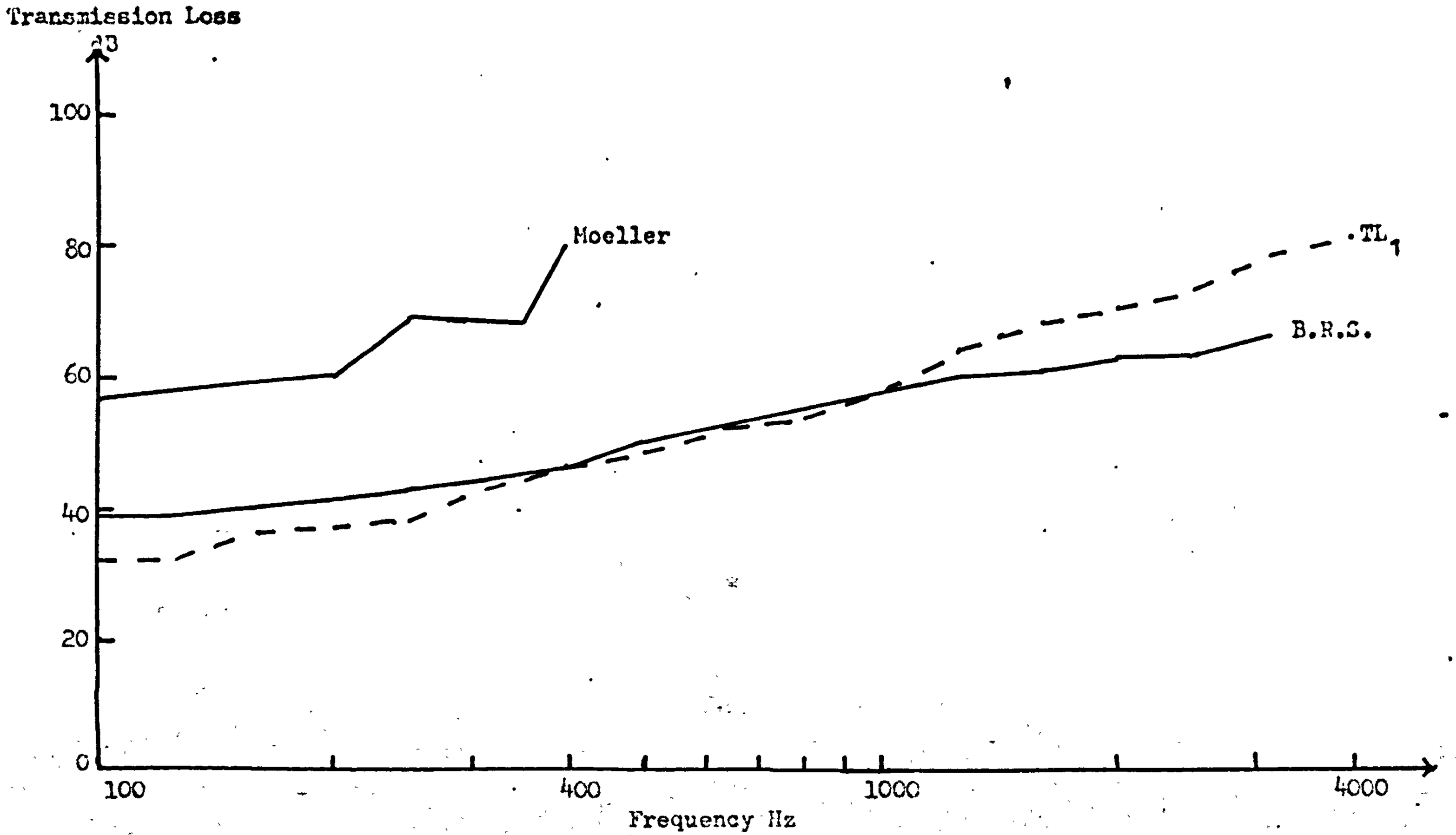

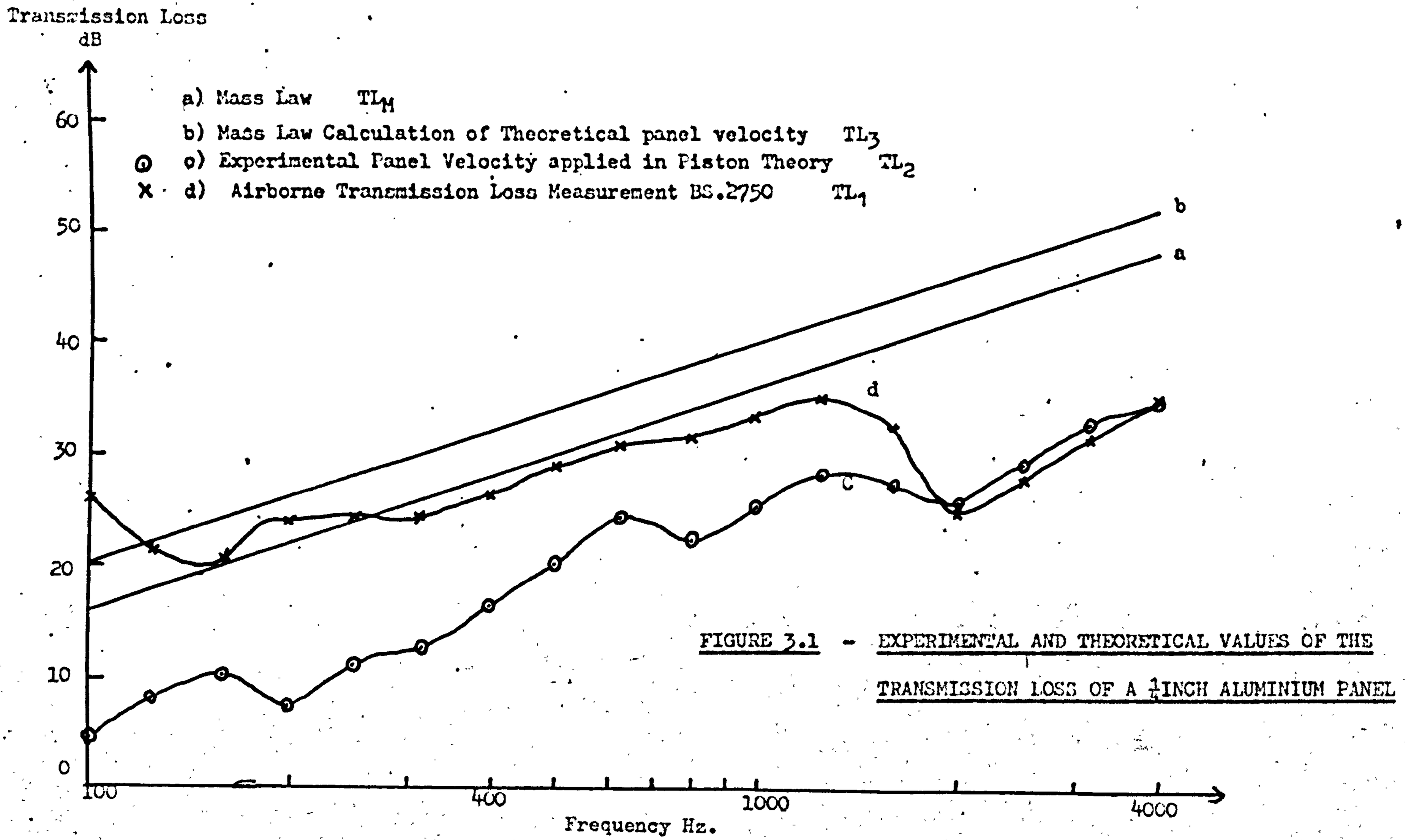

FIGURE 3.1 - EXPERIMENTAL AND THEORETICAL VALUES OF THE TRANSMISSION LOSS OF A $\frac{1}{4}$INCH ALUMINIUM PANEL

FIGURE 3.2 - THE RADIATION EFFICIENCY OF A $\frac{1}{4}$INCH ALUMINIUM PANEL

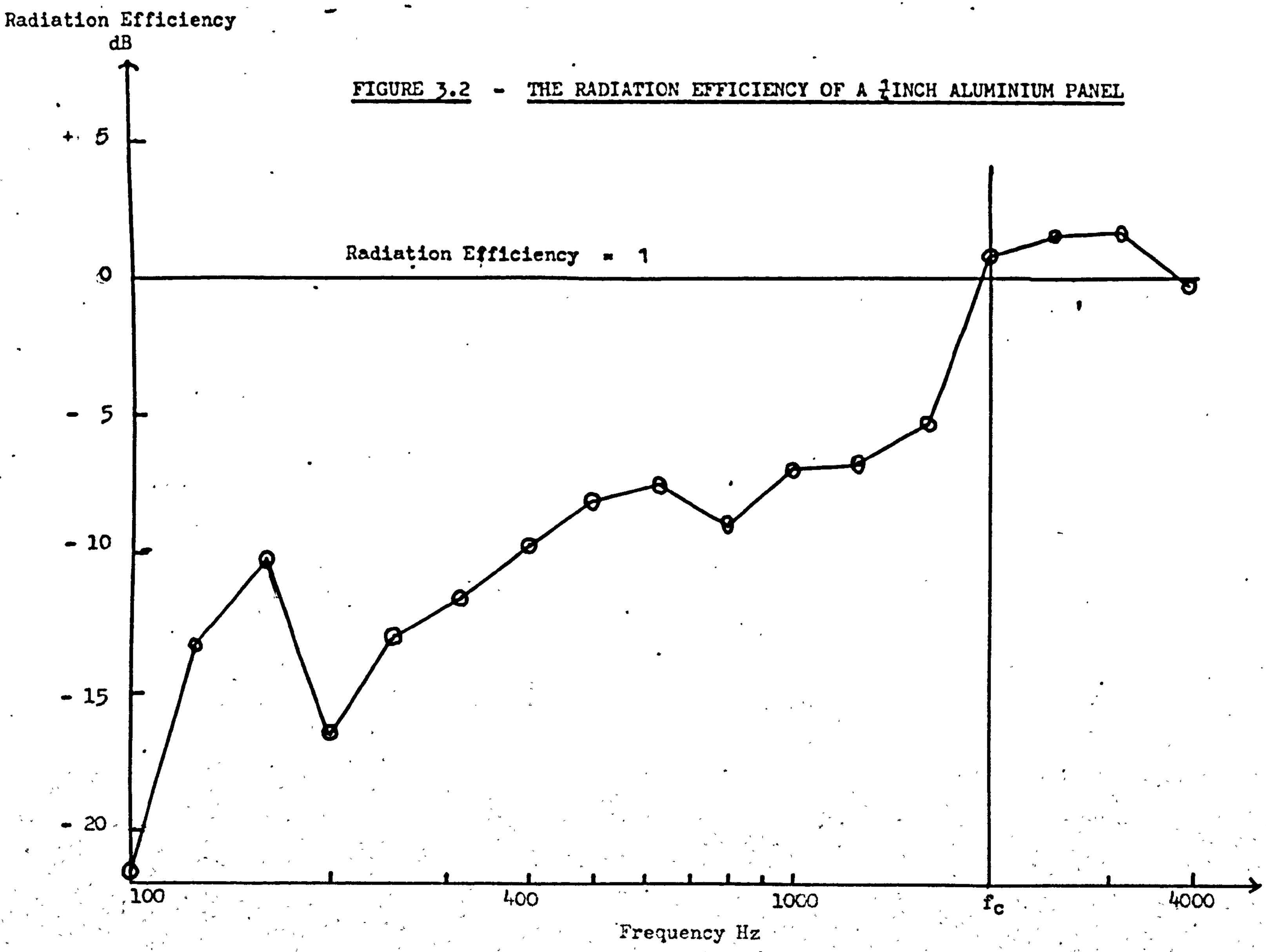

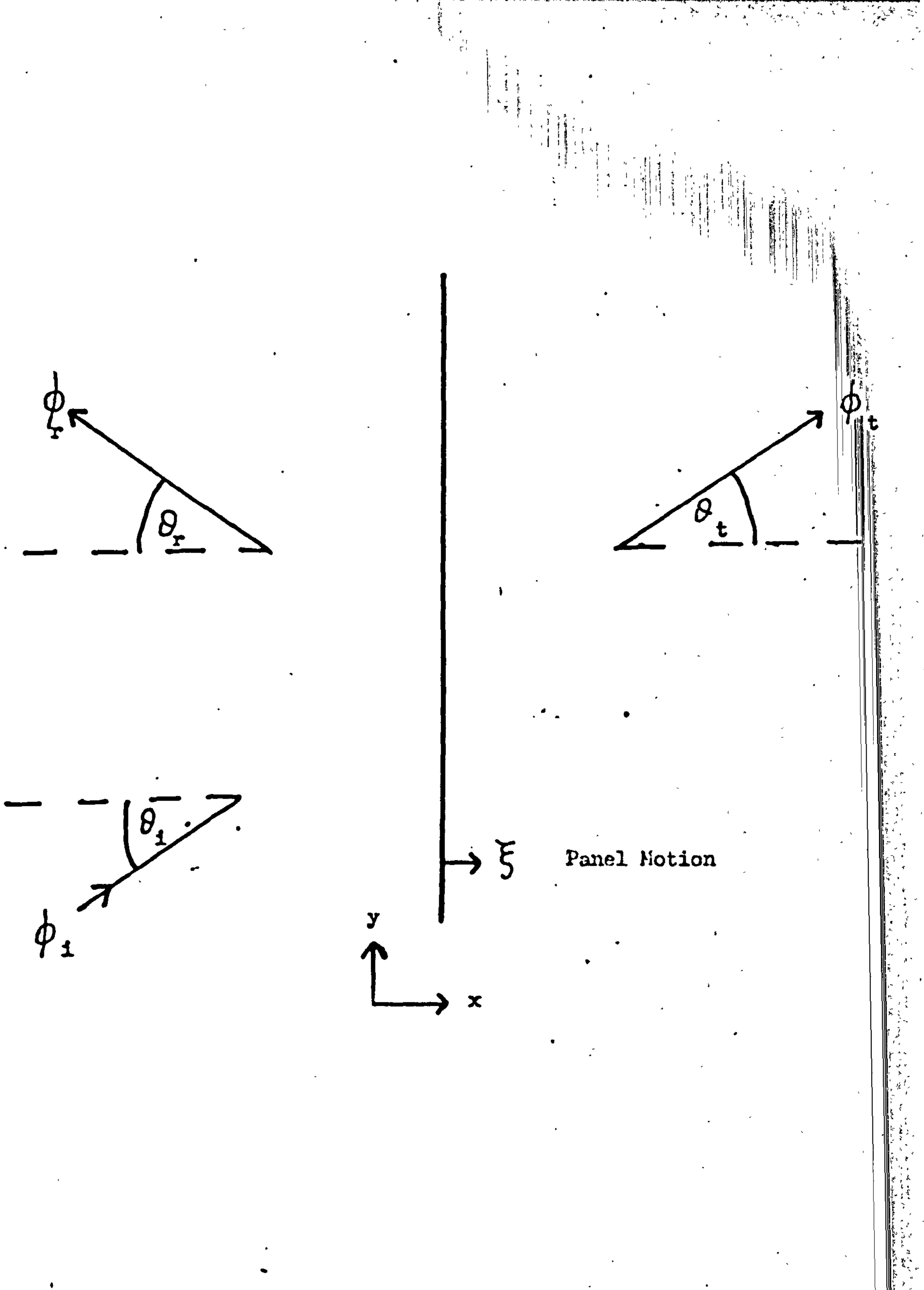

FIGURE 3.3 - TRANSMISSION LOSS MECHANISM

FIGURE 3.4 - PREDICTION OF THE TRANSMISSION LOSS COINCIDENCE EFFECT

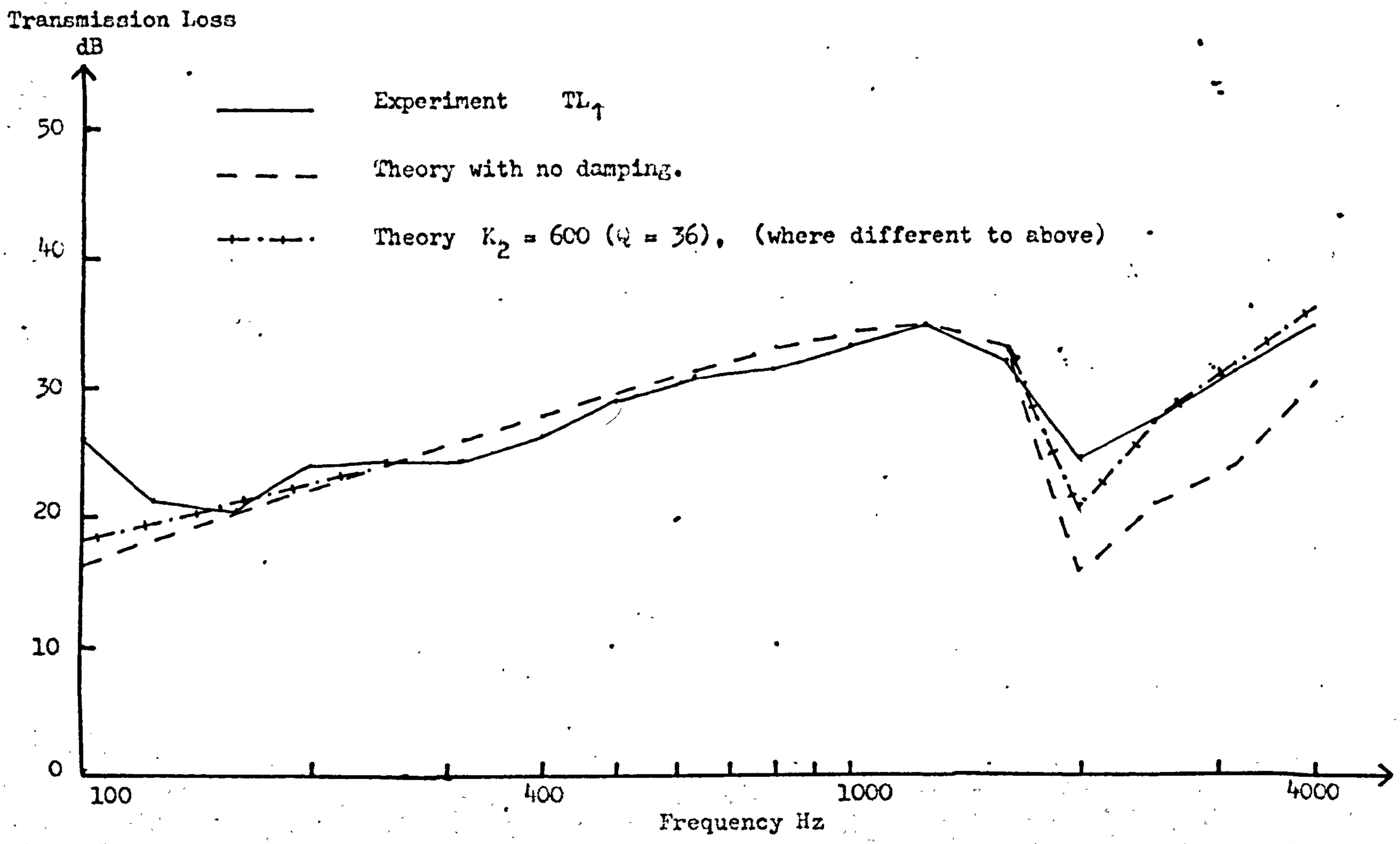

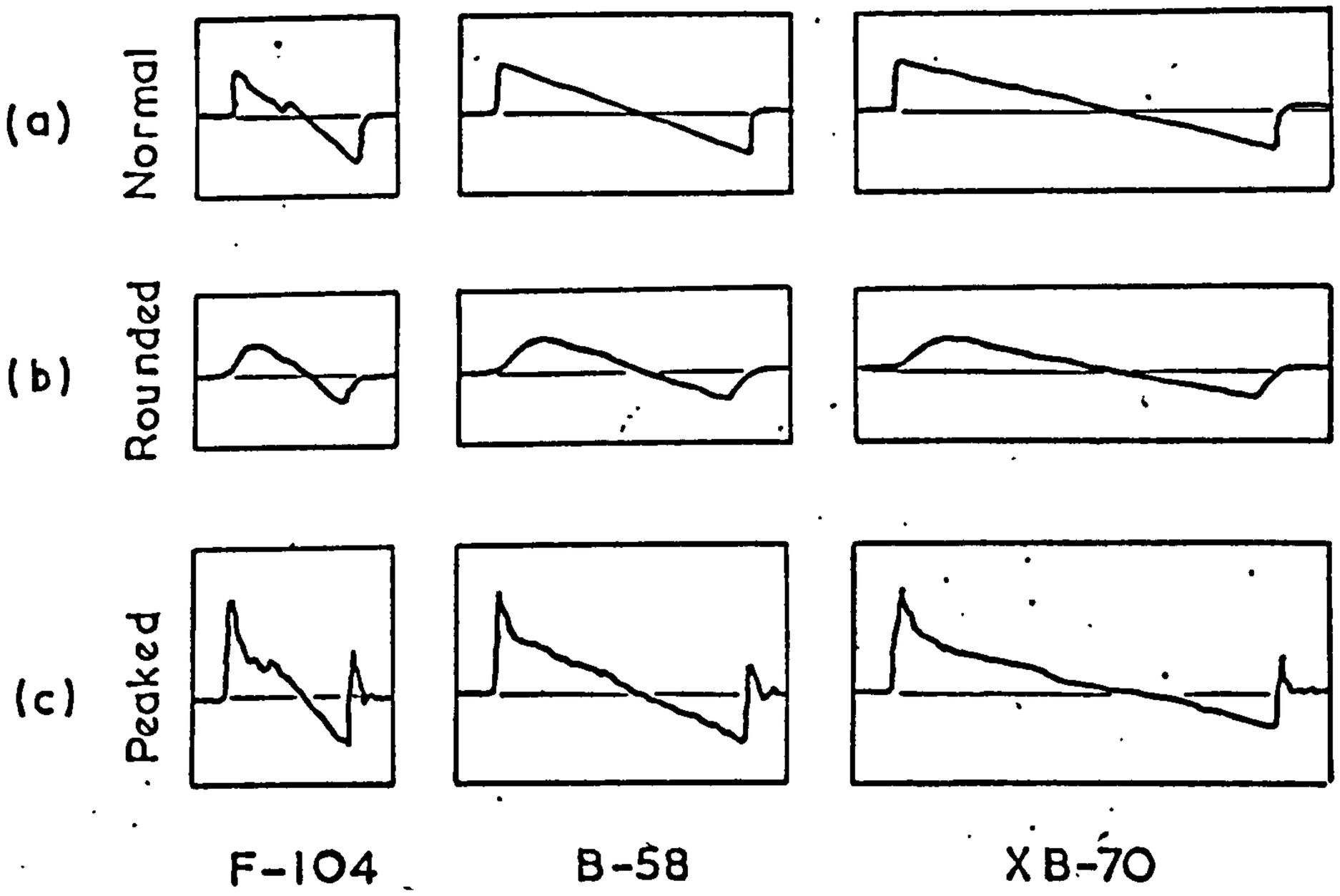

FIGURE 4.1 - Typical Pressure-time Histories of Sonic Booms, measured at ground level produced by small, medium and large aircraft flying in Steady Flight at their cruising altitudes.

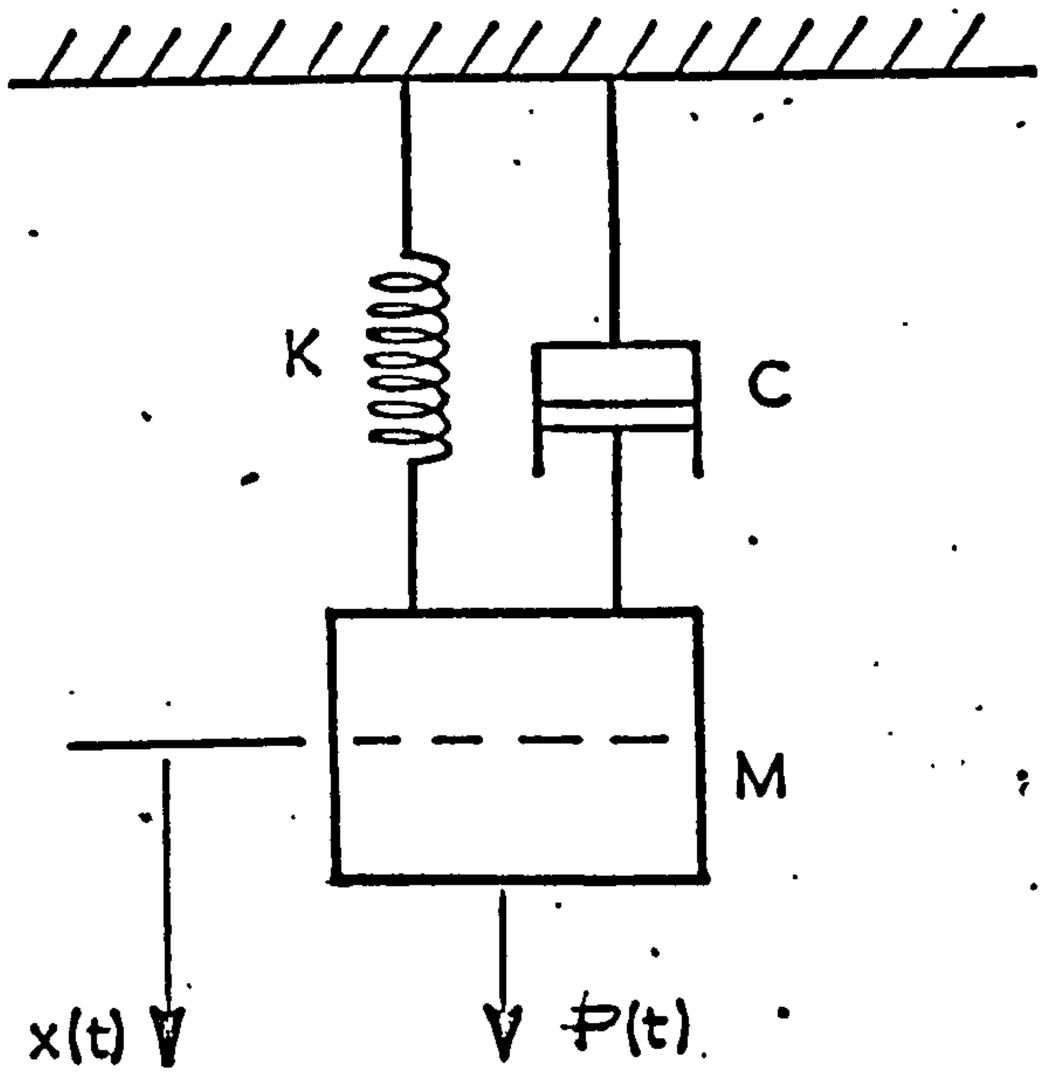

FIGURE 4.2 - Damped Mass-Spring System.

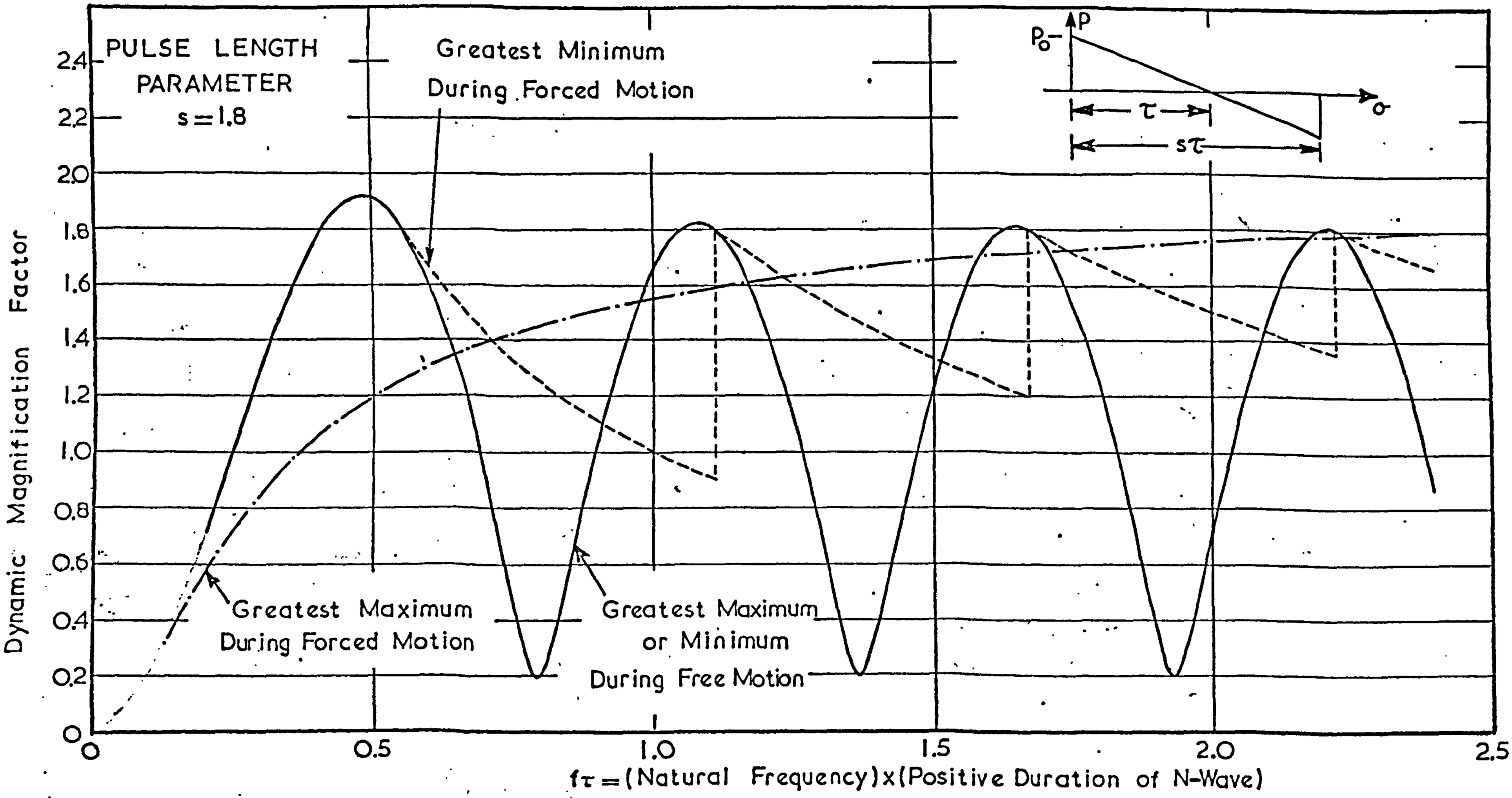

FIGURE 4.3 - Dynamic Magnification Factor for Response of an Undaped Simple System to an Asymmetrical sonic boom (s = 1.8)

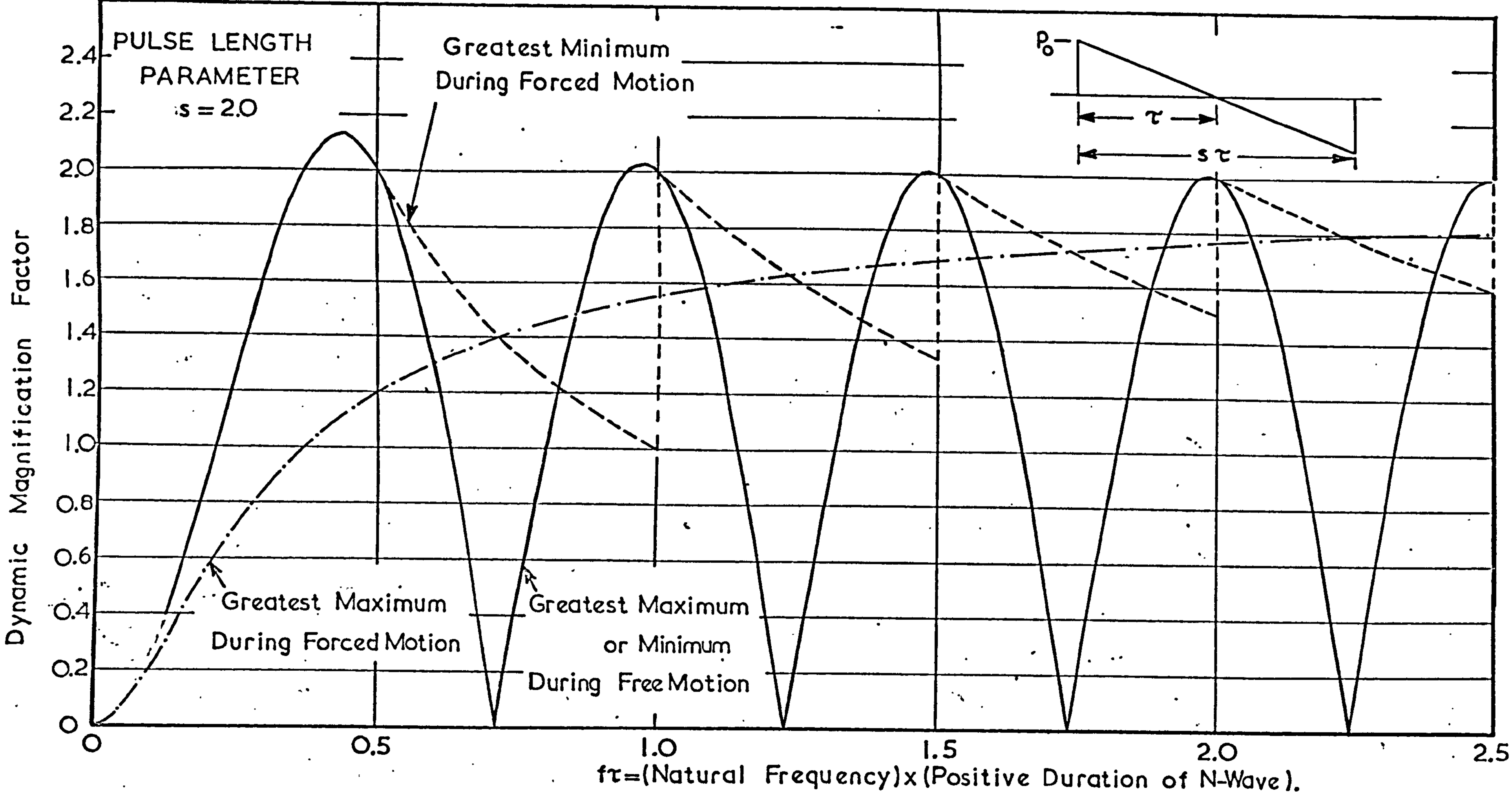

FIGURE 4.4 - Dynamic Magnification Factor for Response of an Undaped Simple System to an Asymmetrical sonic boom (s = 2.0)

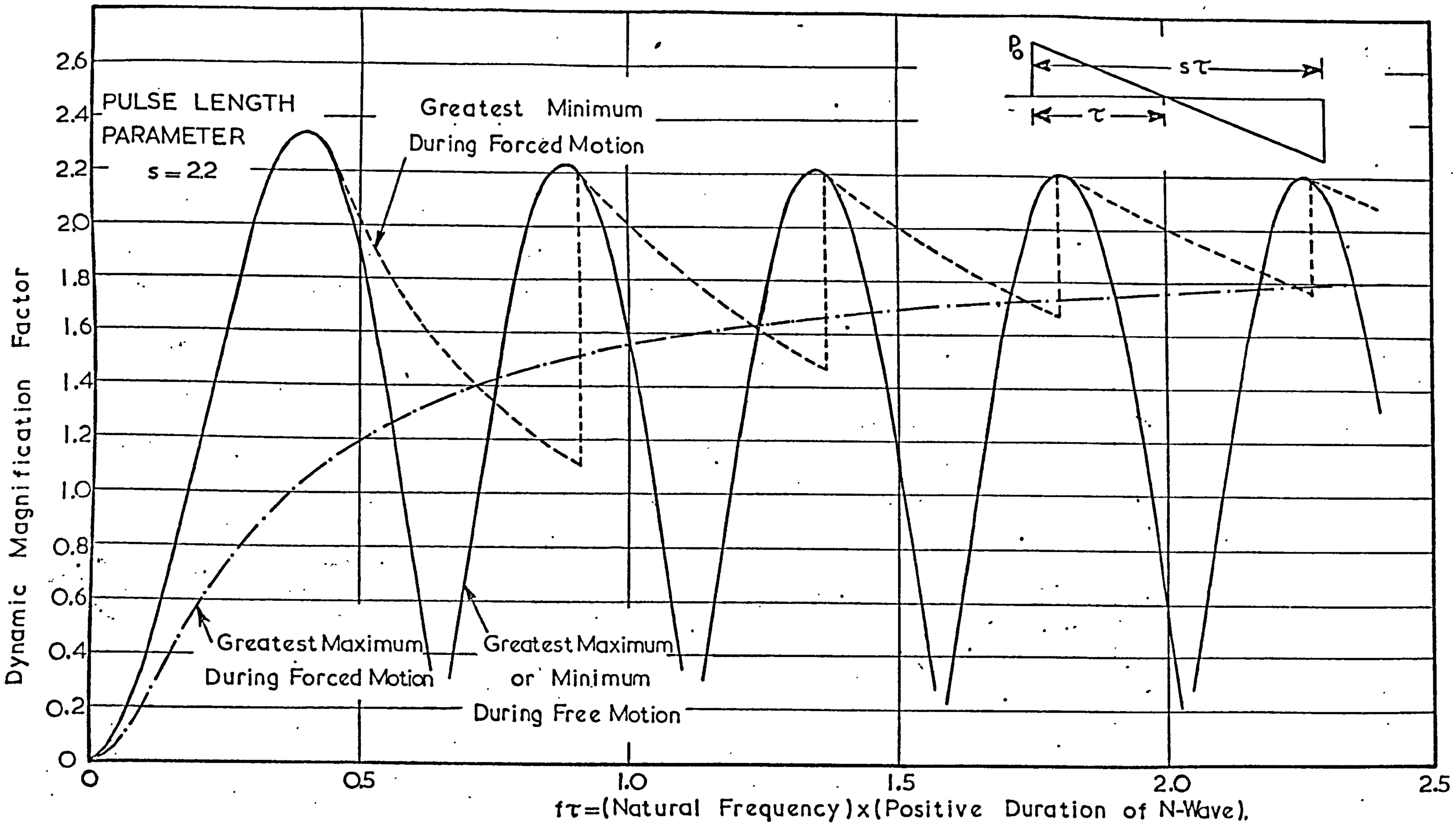

FIGURE 4.5 - Dynamic Magnification Factor for response of an undamped simple system to an asymmetrical sonic boom (s = 2.2)

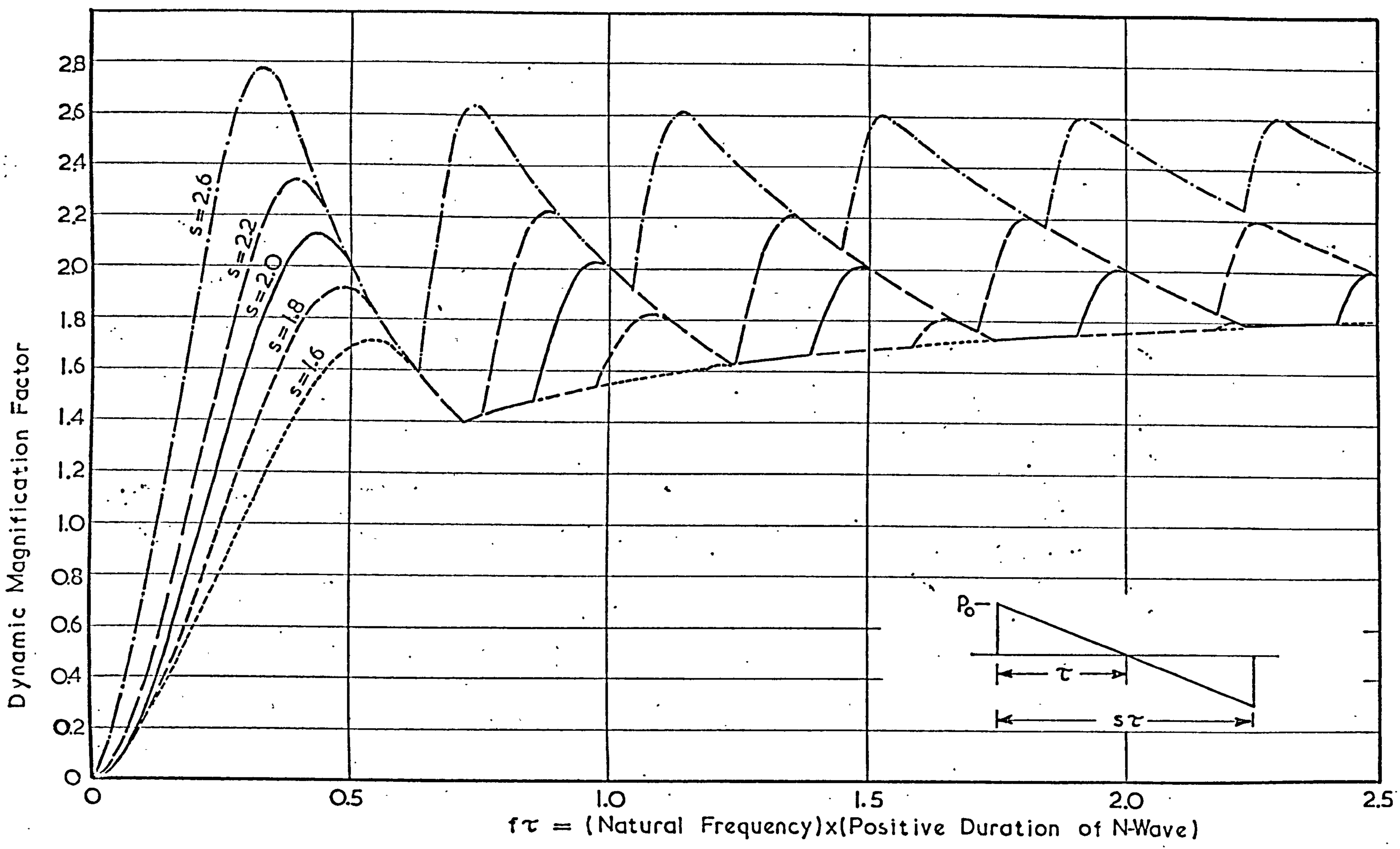

FIGURE 4.6 - Variation of Dynamic Magnification factors for response of an undamped simple system to an asymmetrical sonic boom as a function of the pulse length ratio s.

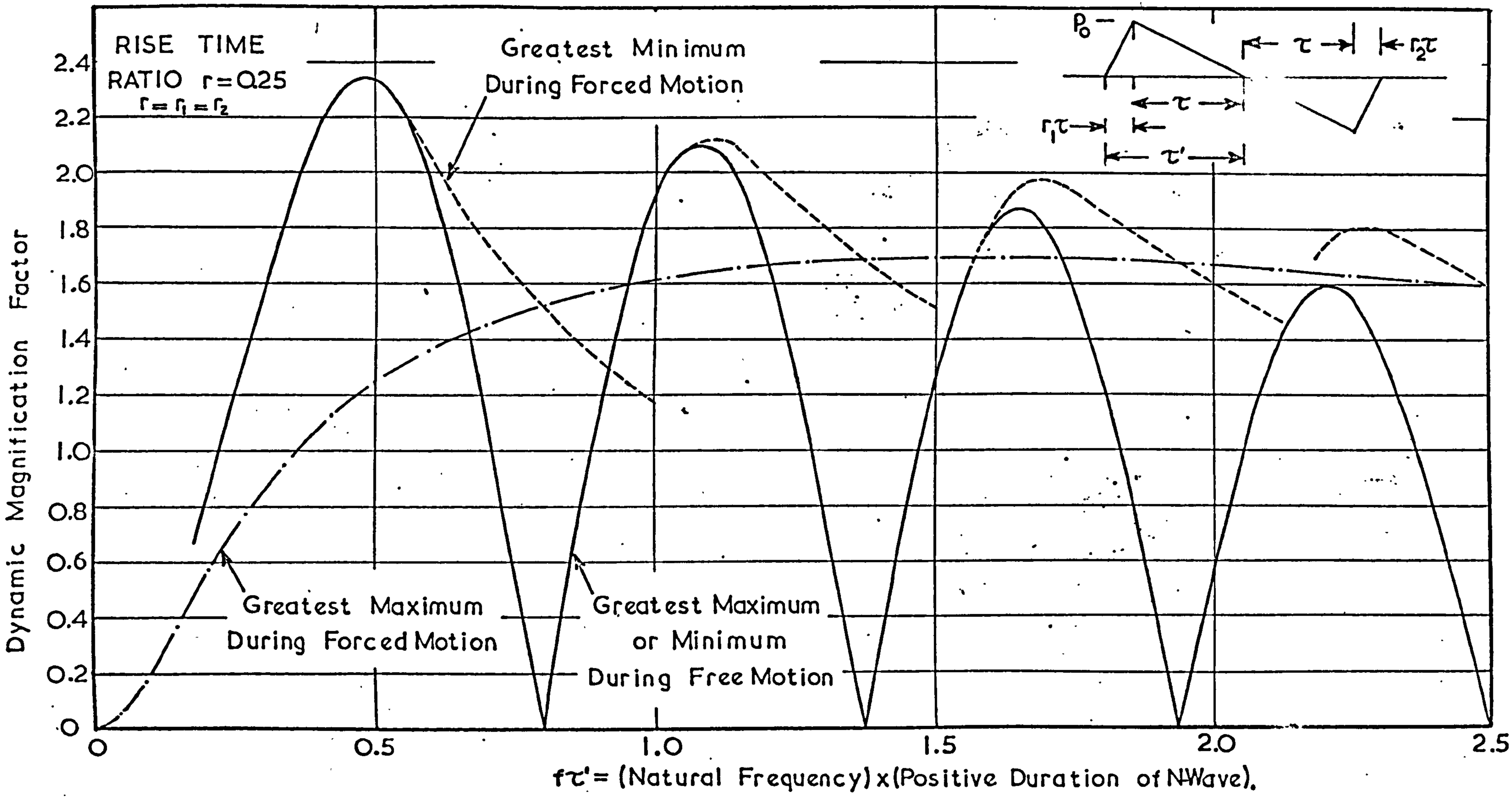

FIGURE 4.7 - Dynamic Magnification Factor for response of an undamped simple system to a sonic boom with a finite rise time (r = 0.25)

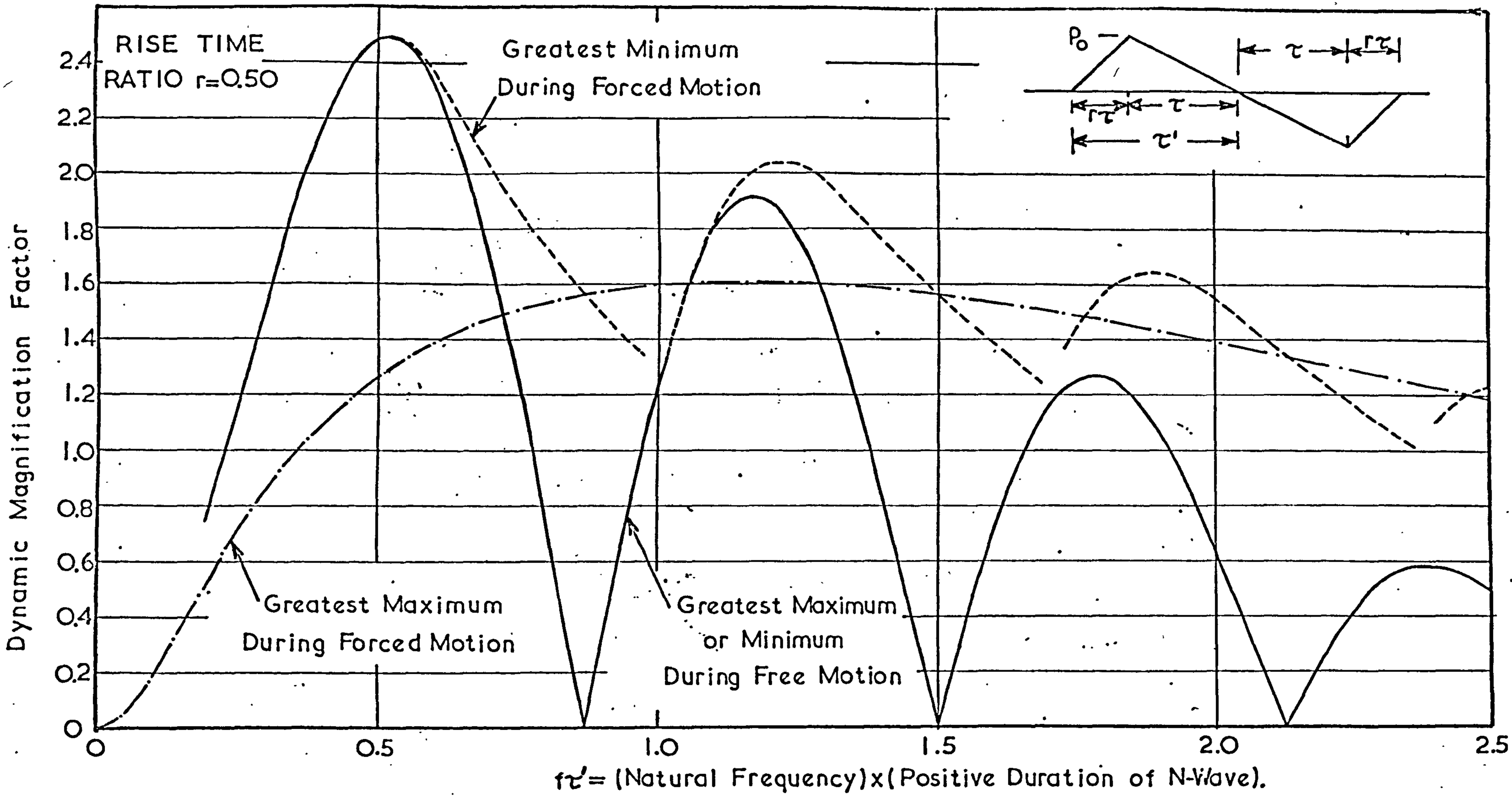

FIGURE 4.8 - Dynamic Magnification Factor for response of an undamped simple system to a sonic boom with a finite rise time (r = 0.5)

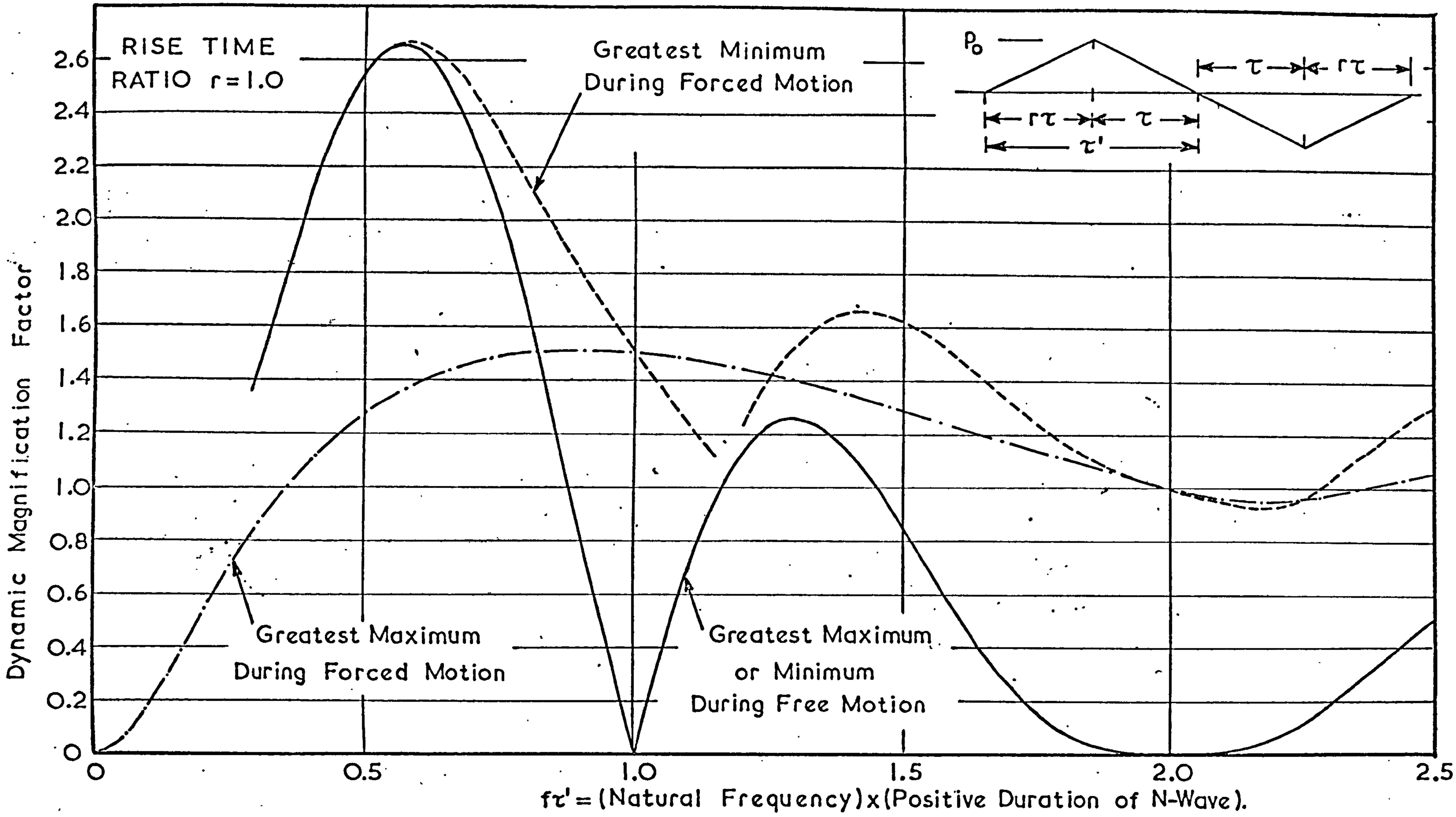

FIGURE 4.9 - Dynamic Magnification Factor for response of an undamped simple system to a sonic boom with a finite rise time (r = 1.0)

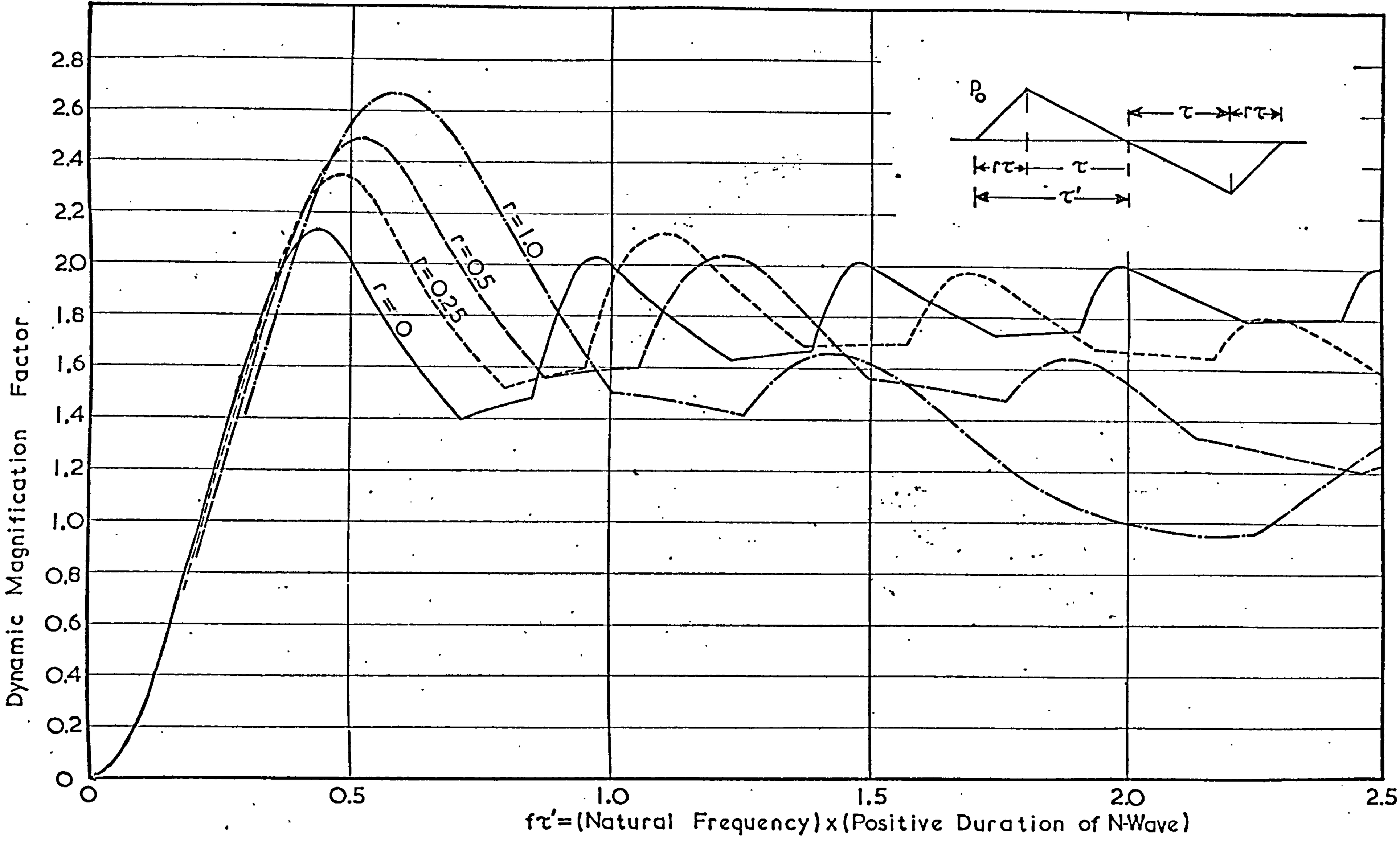

FIGURE 4.10 - Variation of Dynamic Magnification factors for response of undamped simple system to sonic booms as a function of rise time r.

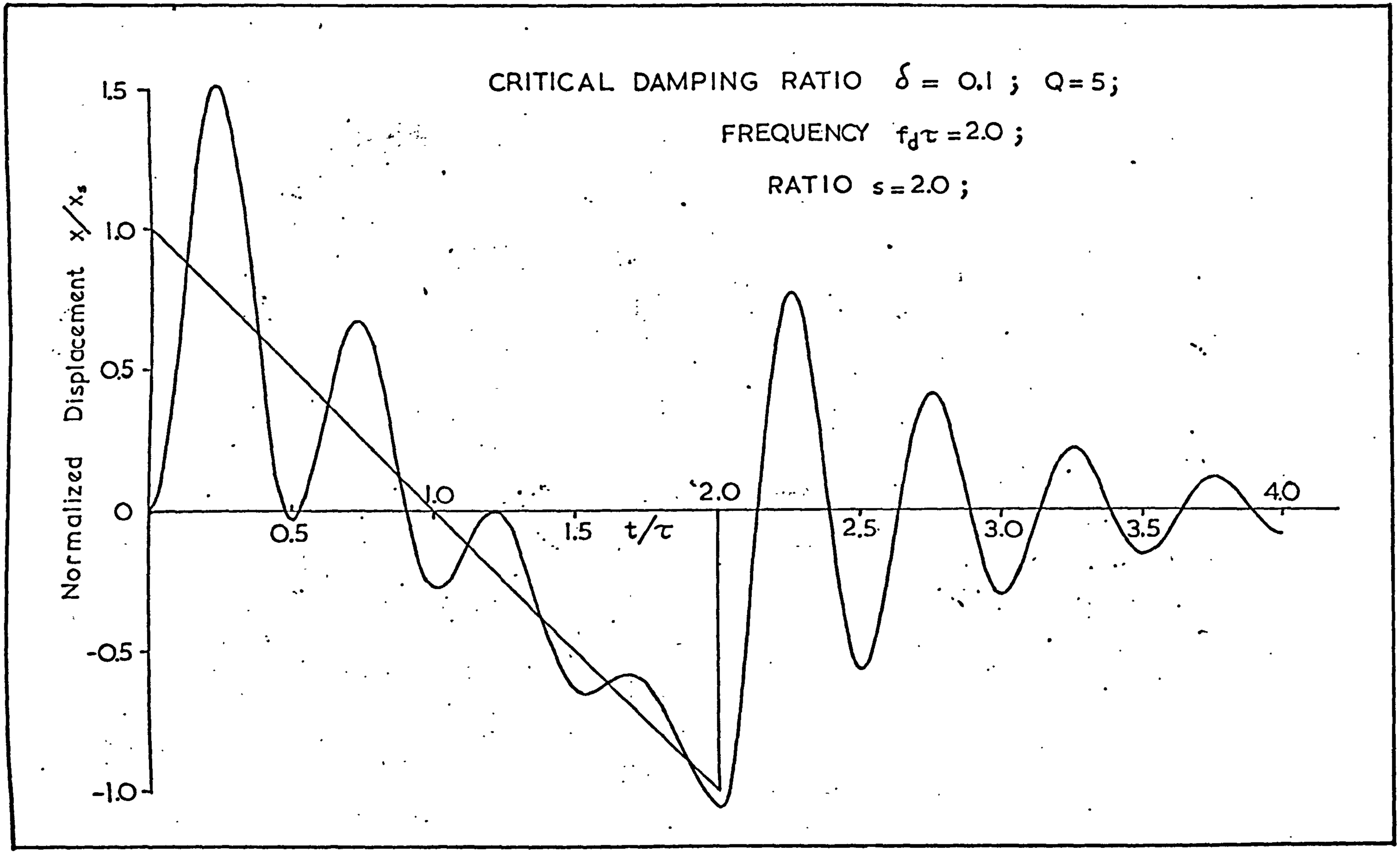

FIGURE 4.11 - Typical time history of the response of a Damped Mass-Spring system to a symmetrical sonic boom ($\delta = 0.1$)

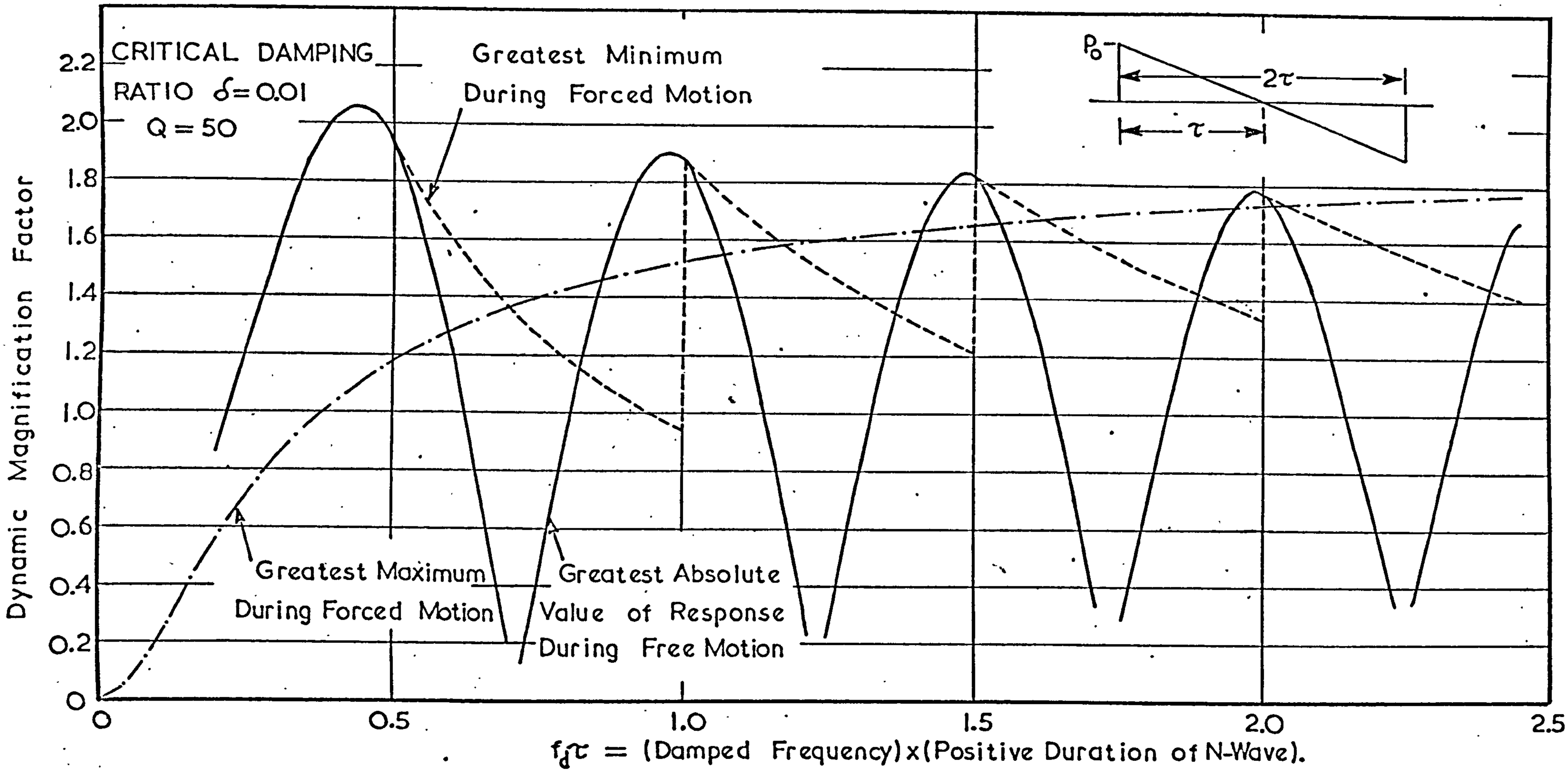

FIGURE 4.12 - Dynamic Magnification factor for response of a damped mass-spring system to a symmetrical sonic boom (δ = 0.01)

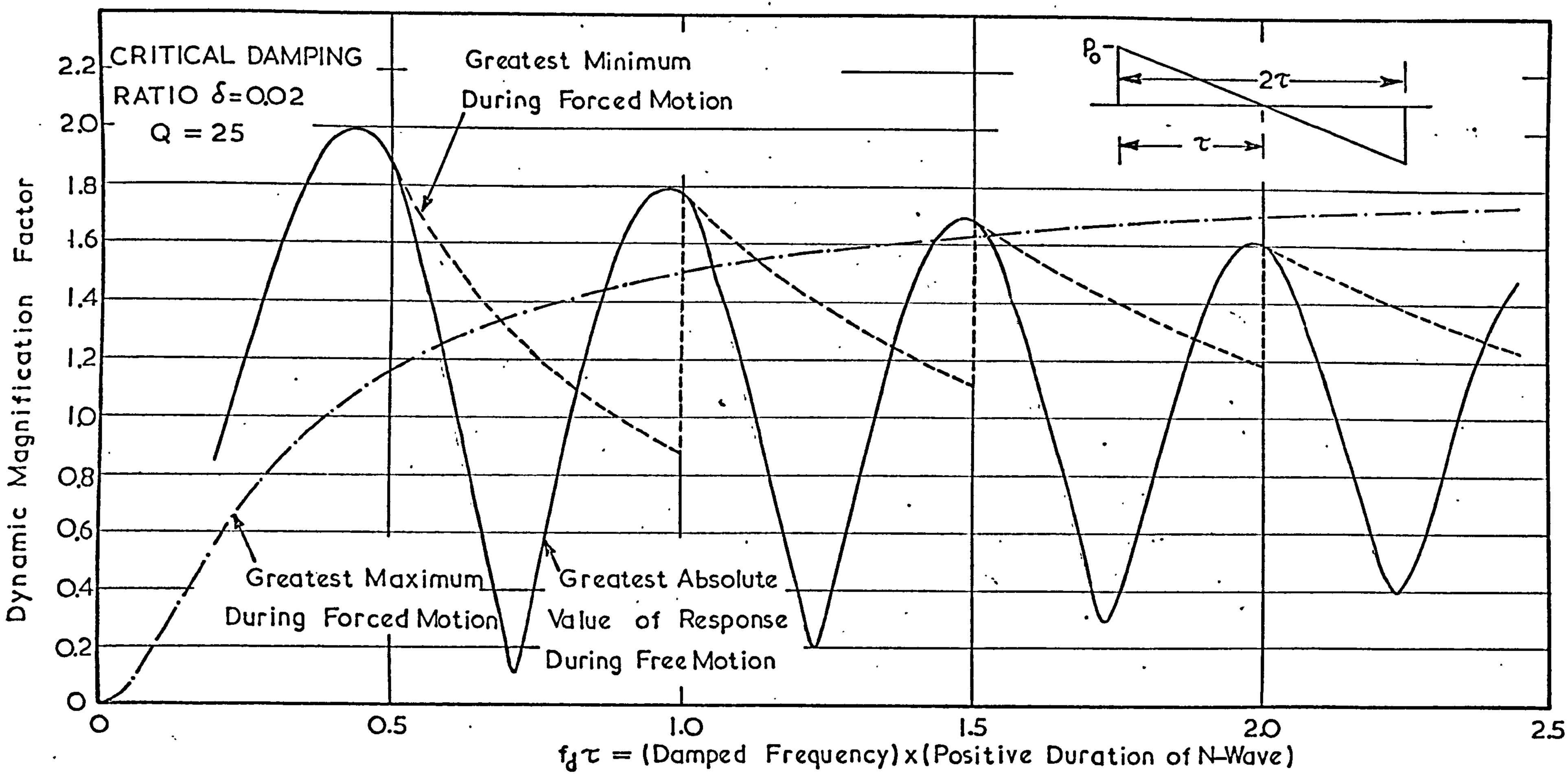

FIGURE 4.13 - Dynamic magnification factor for response of a damped mass-spring system to a symmetrical sonic boom (δ = 0.02)

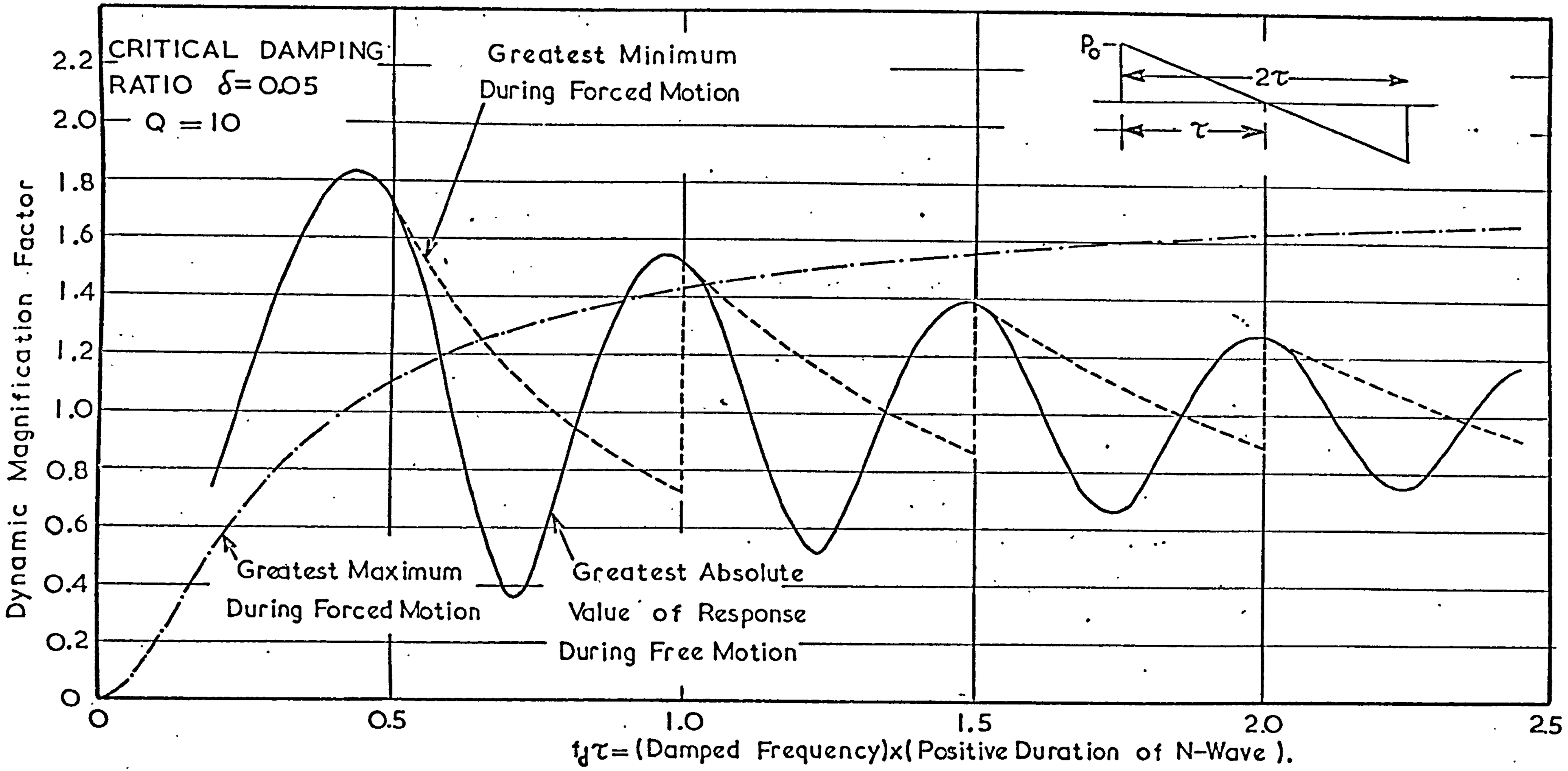

FIGURE 4.14 - Dynamic magnification factor for response of a damped mass-spring system to a symmetrical sonic boom (δ = 0.05)

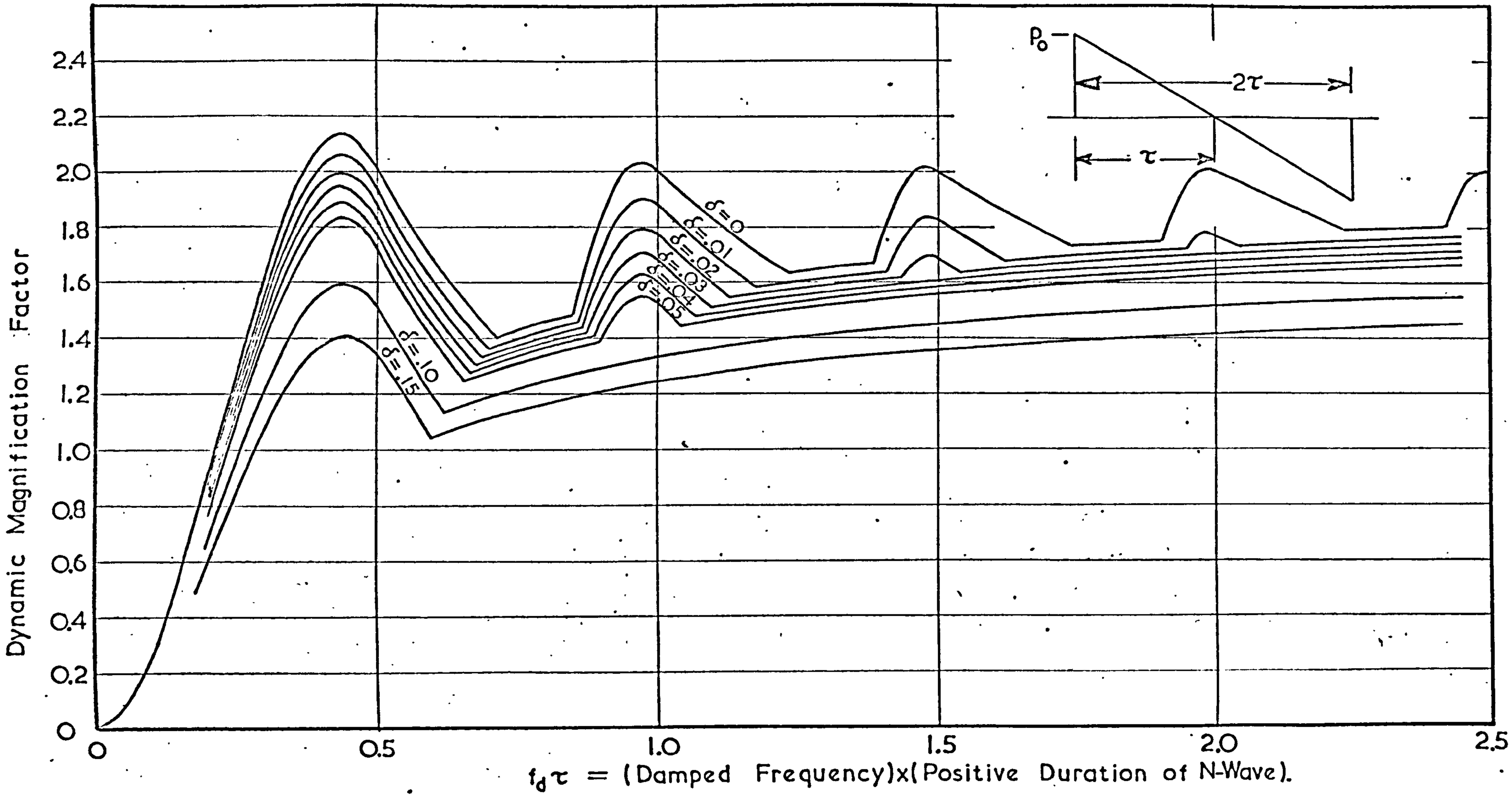

FIGURE 4.15 - Variation of dynamic magnification factors for response of a damped mass-spring system to a symmetrical sonic boom as a function of damping δ.

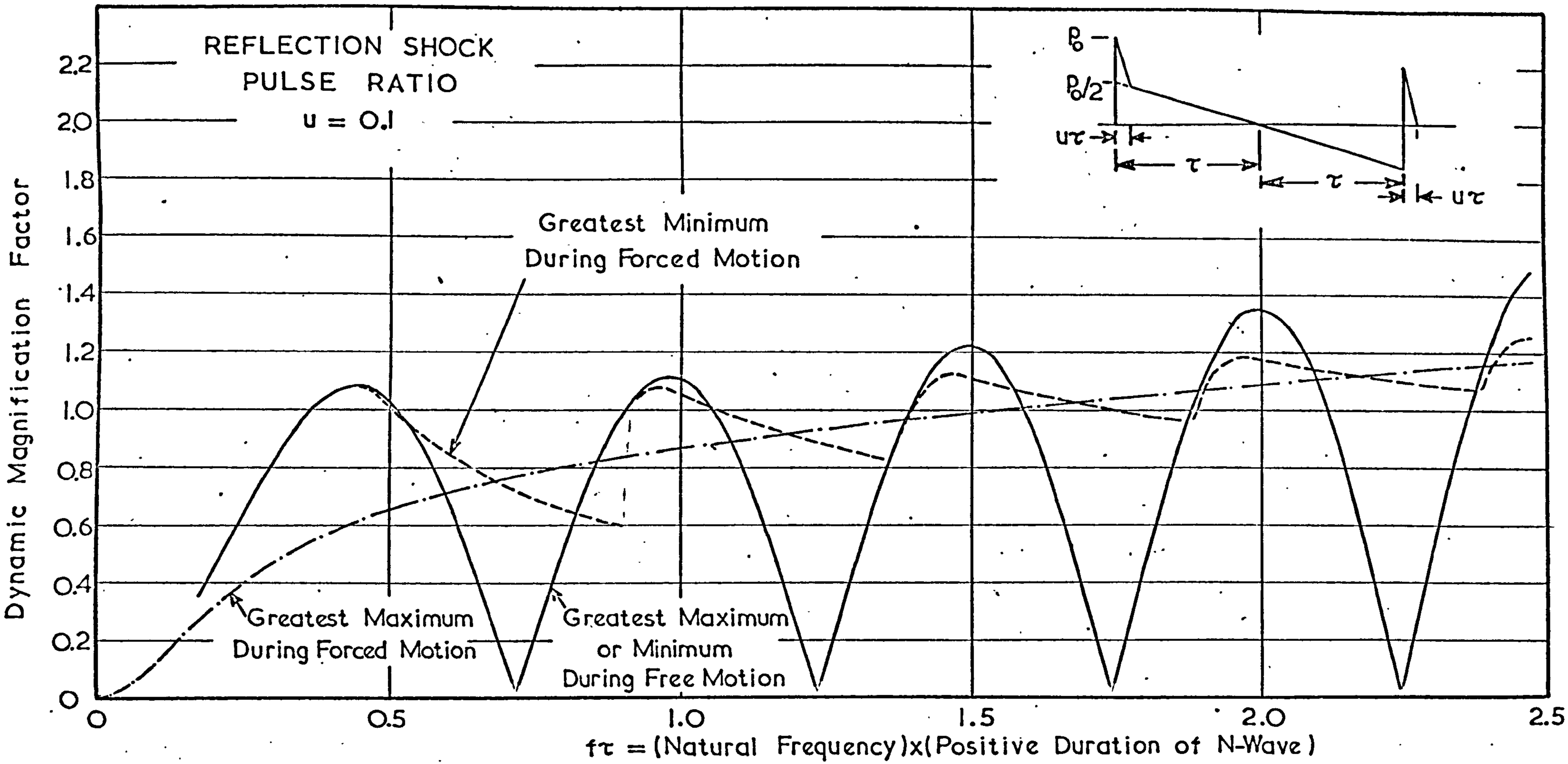

FIGURE 4.16 - Dynamic Magnification factor for response of an undamped simple system to a sonic boom with reflection shocks (u = 0.1)

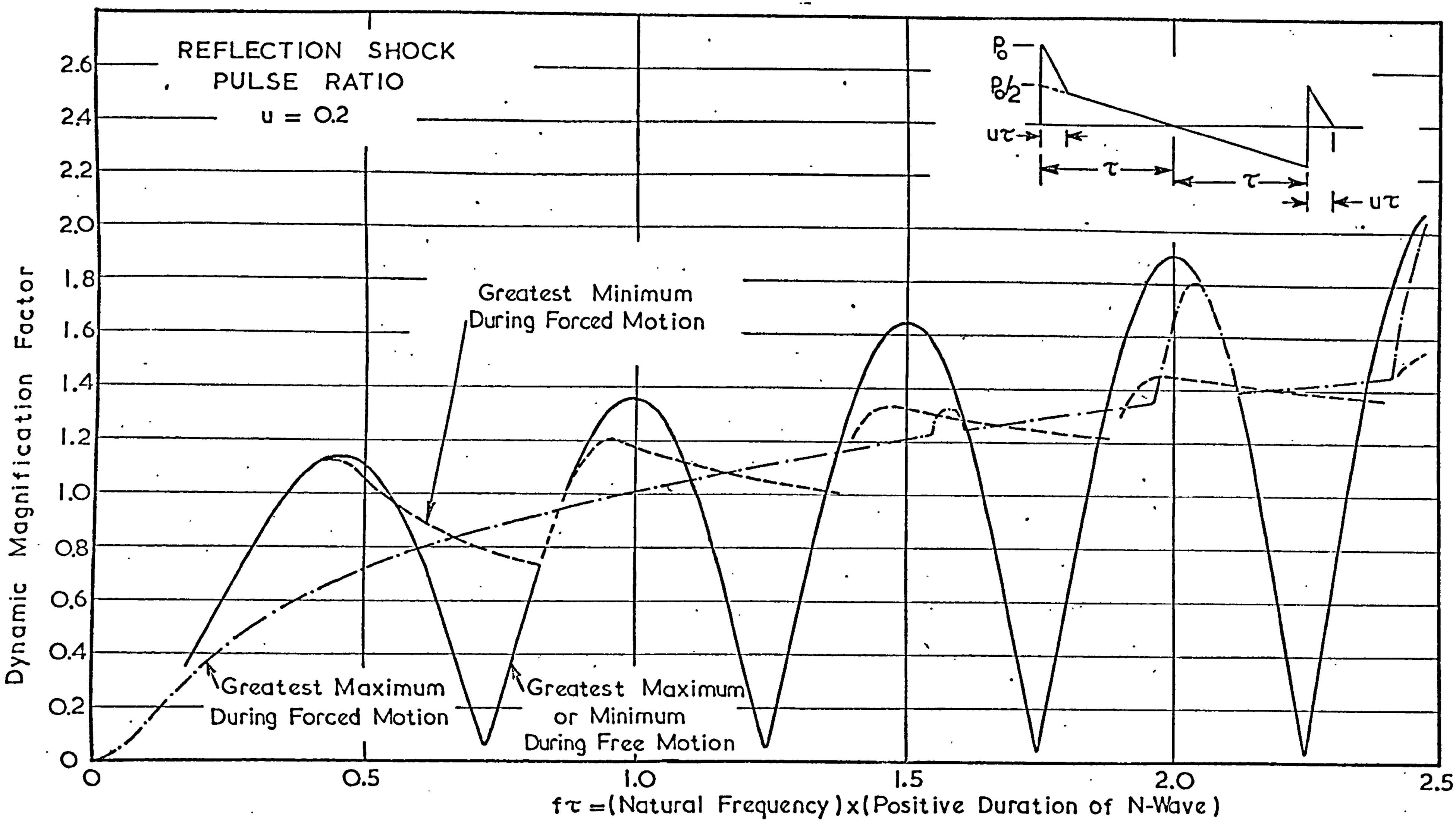

FIGURE 4.17 - Dynamic magnification factor for response of an undamped simple system to a sonic boom with reflection shocks (u = 0.2)

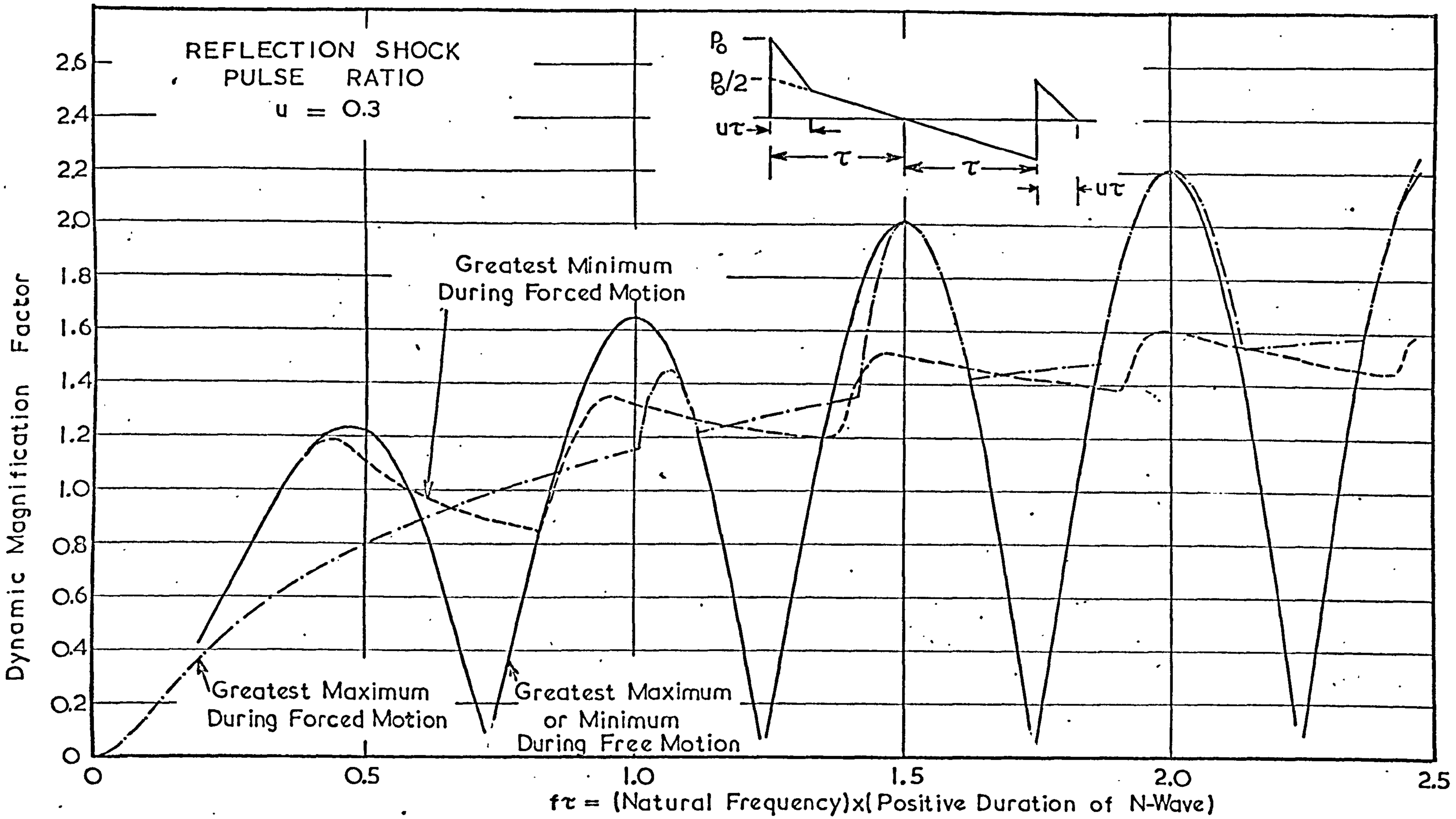

FIGURE 4.18 - Dynamic magnification factor for response of an undamped simple system to a sonic boom with reflection shocks (u = 0.3)

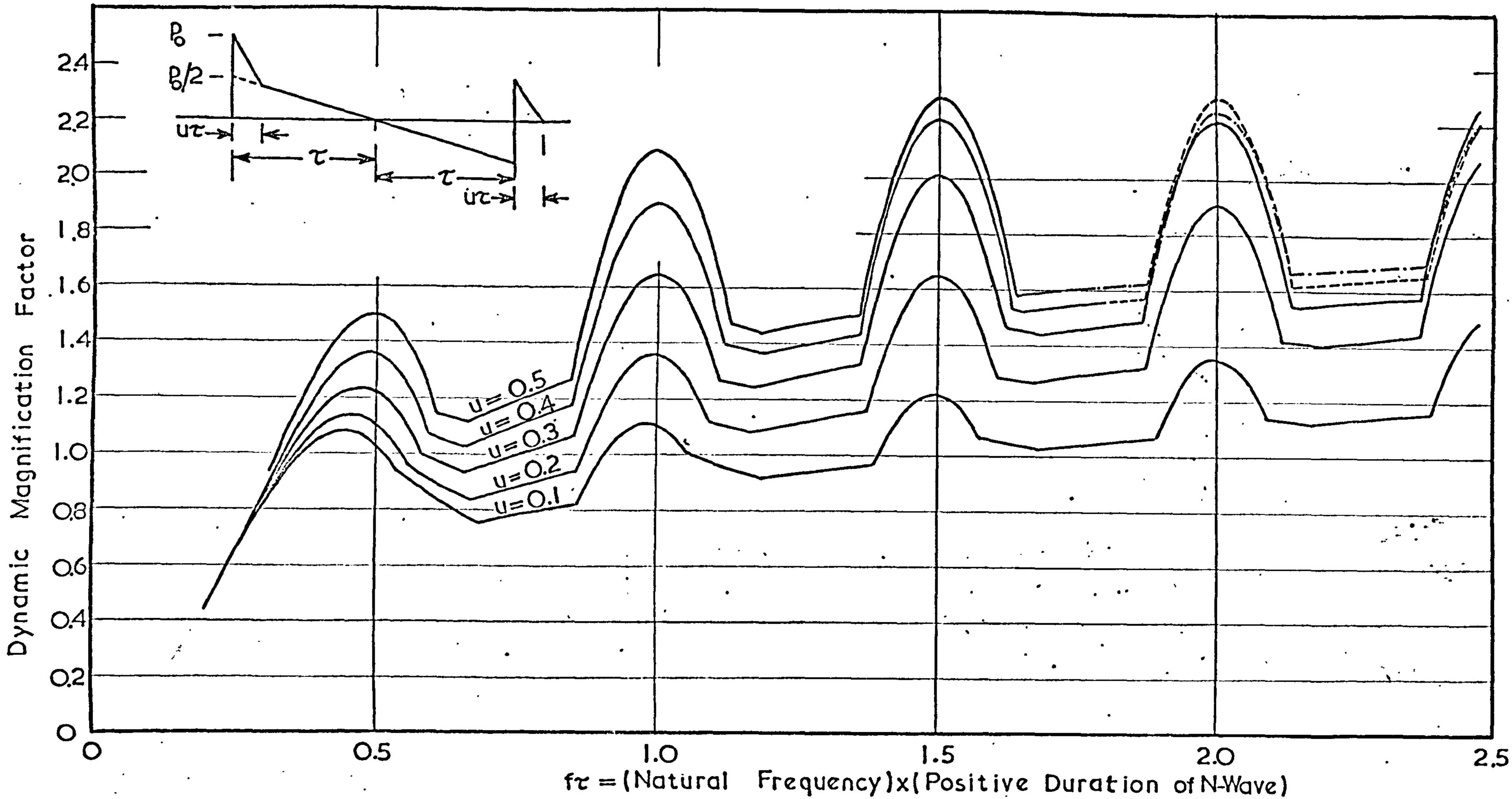

FIGURE 4.19 - Variation of dynamic magnification factors for response of an undamped simple system to a sonic boom with reflection shocks as a function of the reflection shock pulse ratio u.

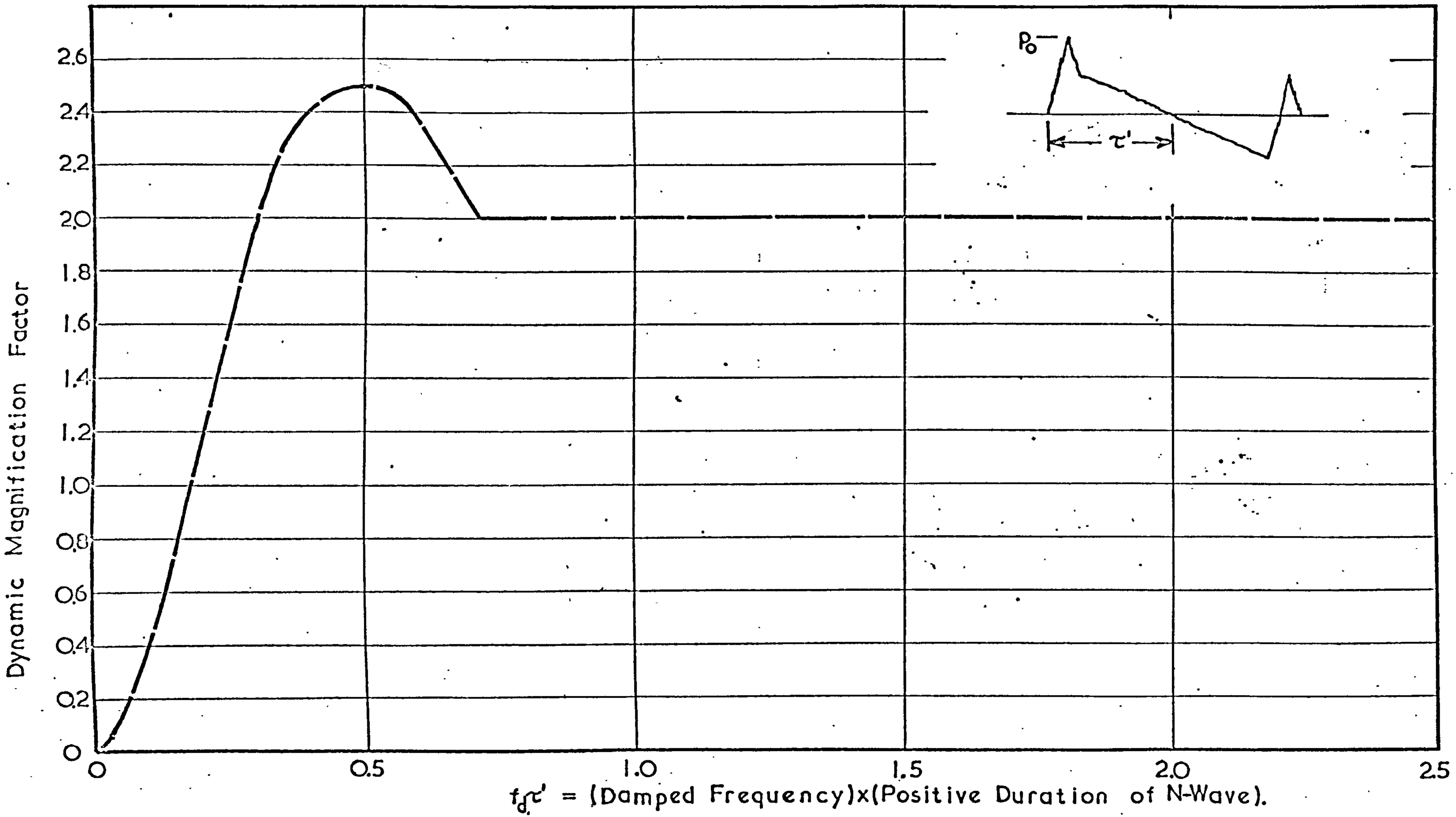

FIGURE 4.20 - Envelope of dynamic magnification factor curves for use in assessing possibility of damage

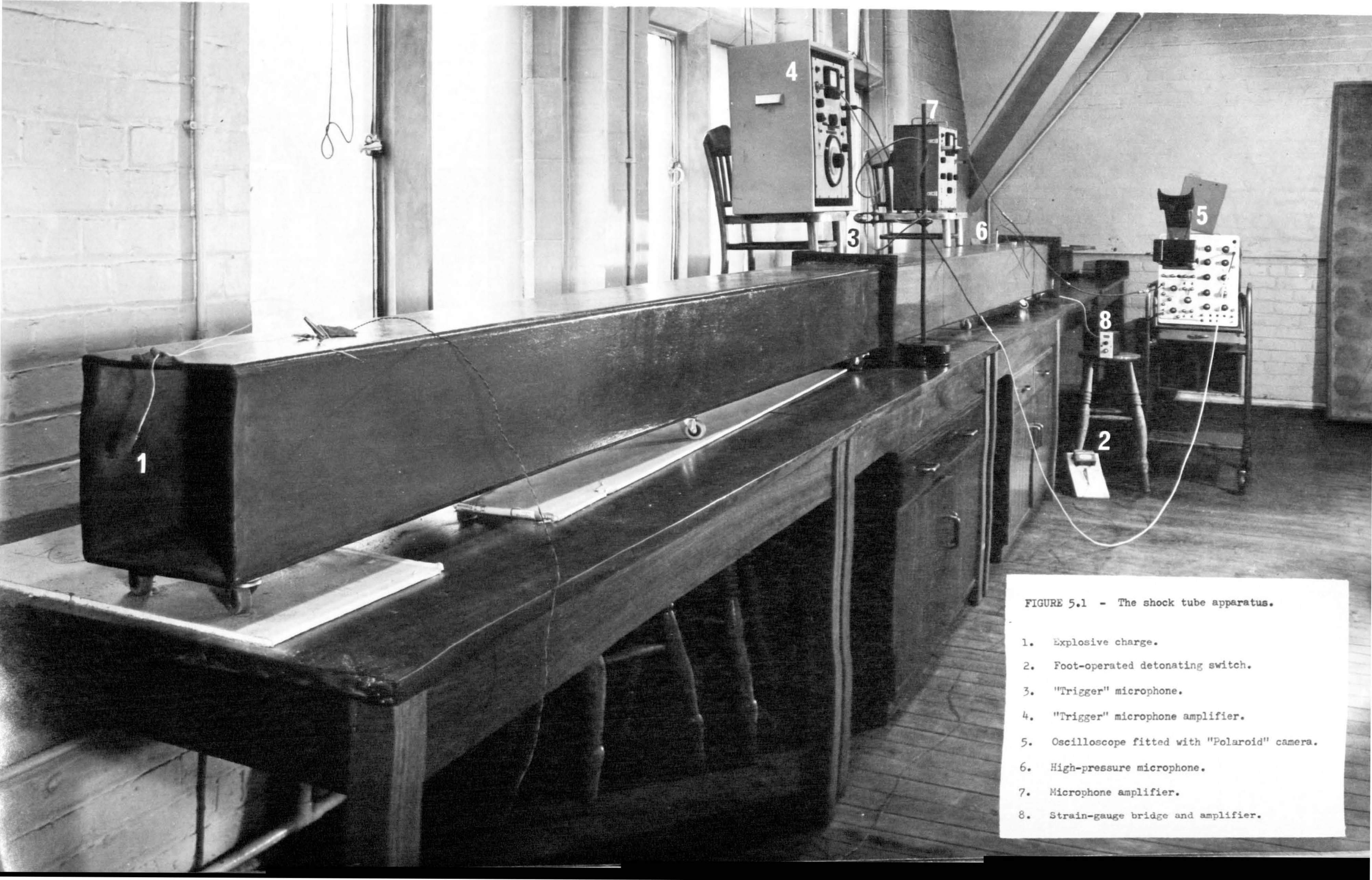

FIGURE 5.1 - The shock tube apparatus.

1. Explosive charge.
2. Foot-operated detonating switch.
3. "Trigger" microphone.
4. "Trigger" microphone amplifier.
5. Oscilloscope fitted with "Polaroid" camera.
6. High-pressure microphone.
7. Microphone amplifier.
8. Strain-gauge bridge and amplifier.

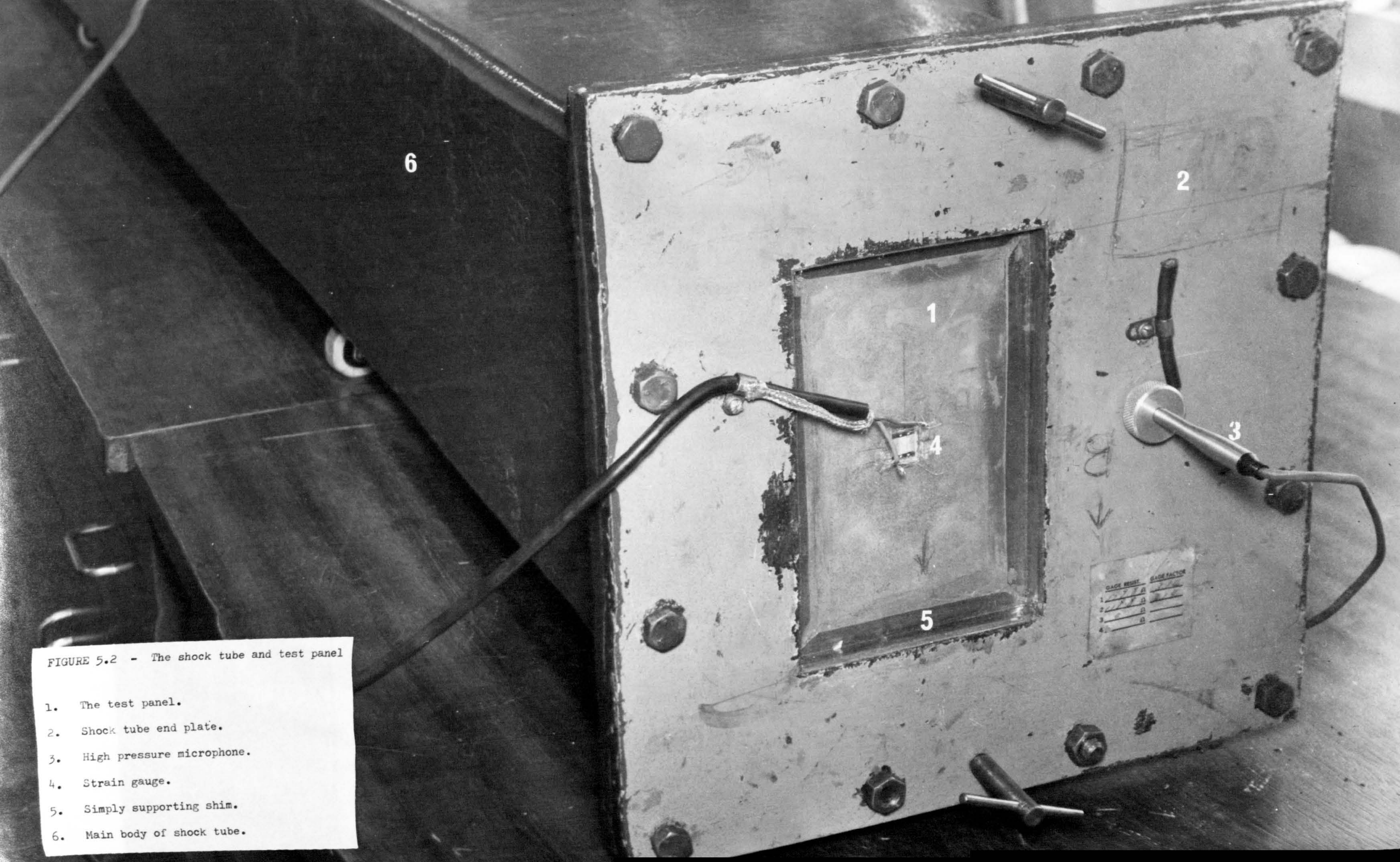

FIGURE 5.2 - The shock tube and test panel

1. The test panel.
2. Shock tube end plate.
3. High pressure microphone.
4. Strain gauge.
5. Simply supporting shim.
6. Main body of shock tube.

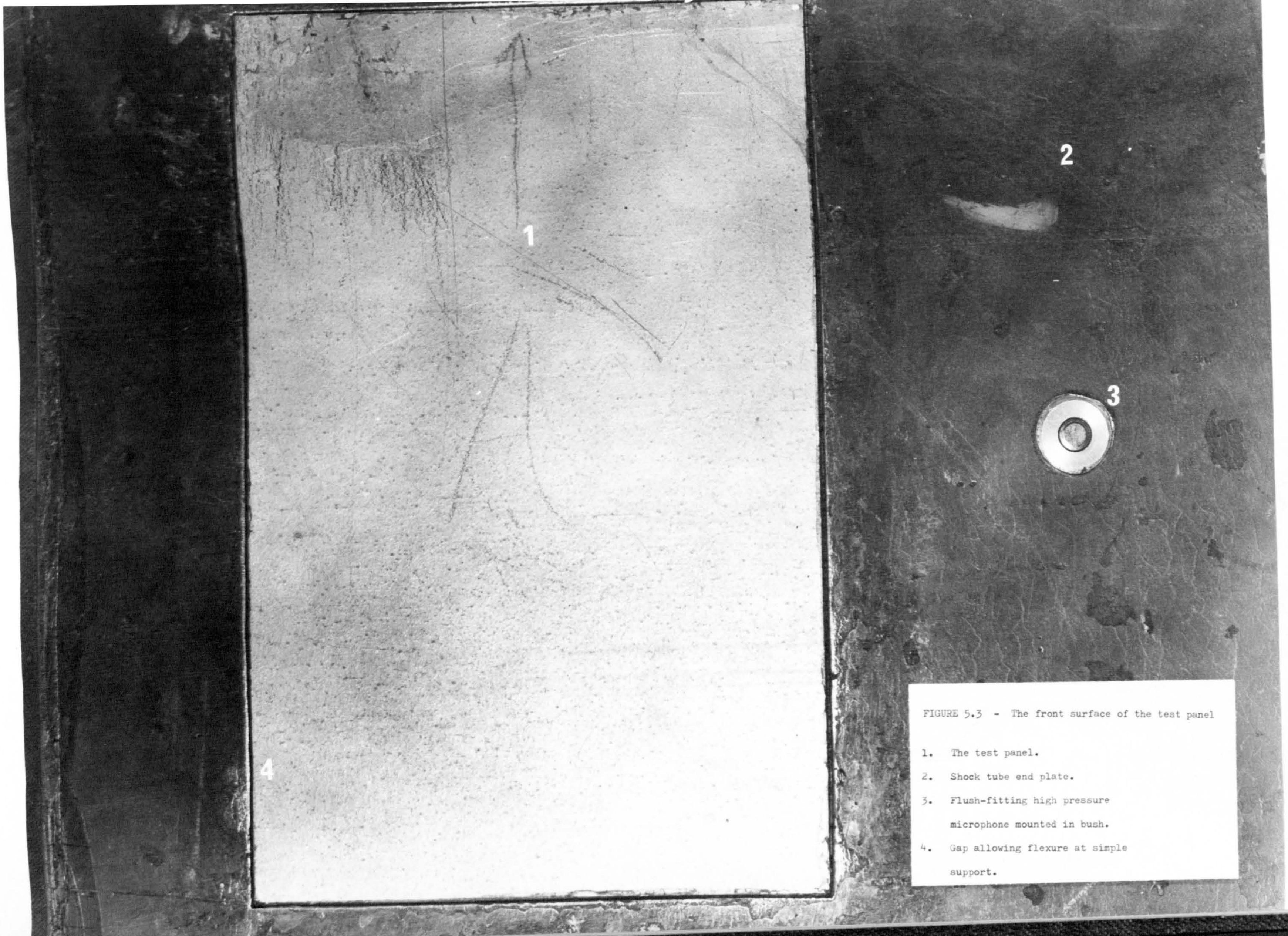

FIGURE 5.3 - The front surface of the test panel

1. The test panel.
2. Shock tube end plate.
3. Flush-fitting high pressure microphone mounted in bush.
4. Gap allowing flexure at simple support.

FIGURE 5.4 - THE SHOCK TUBE

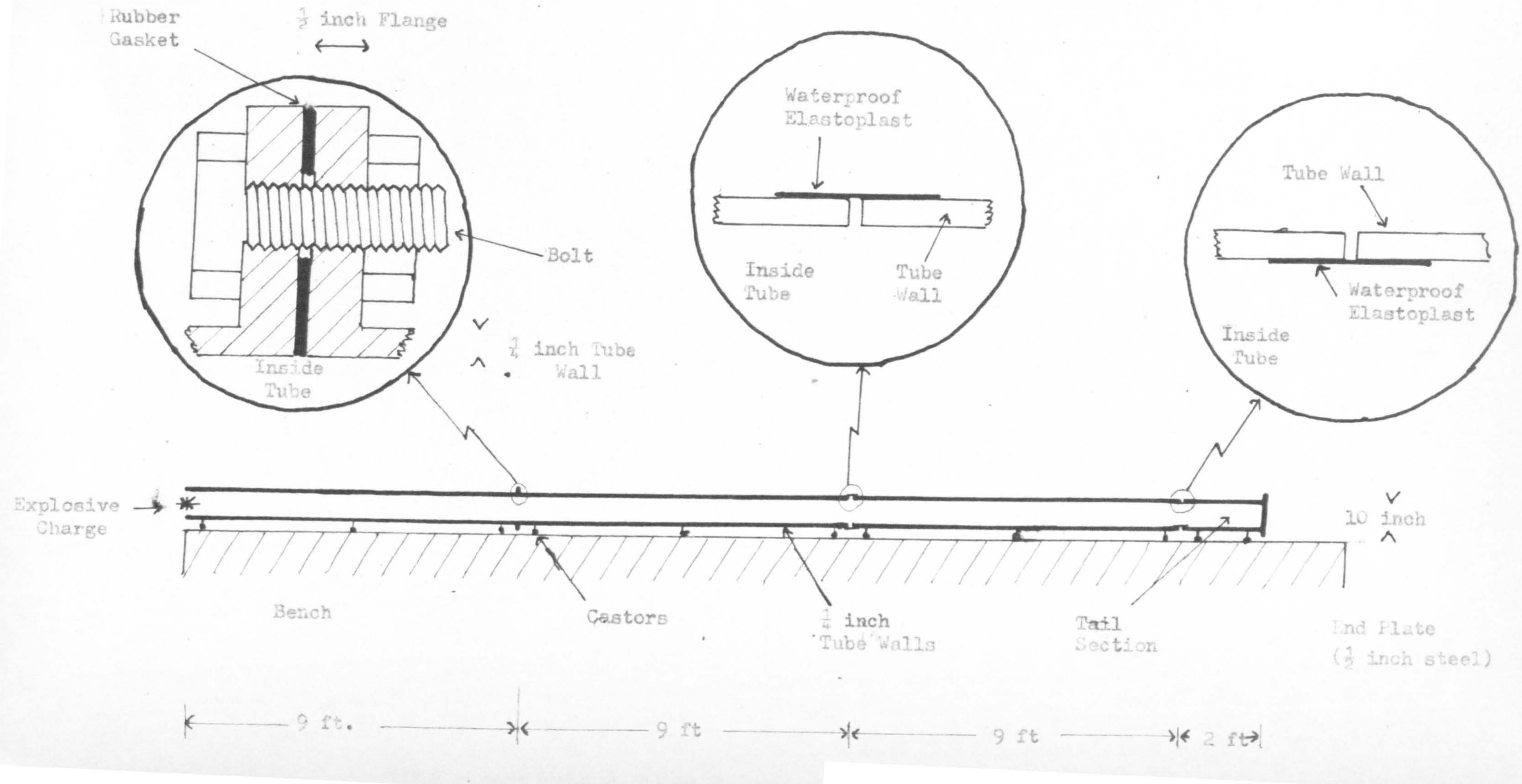

FIGURE 5.5 - THE SHOCK TUBE INSTRUMENTATION

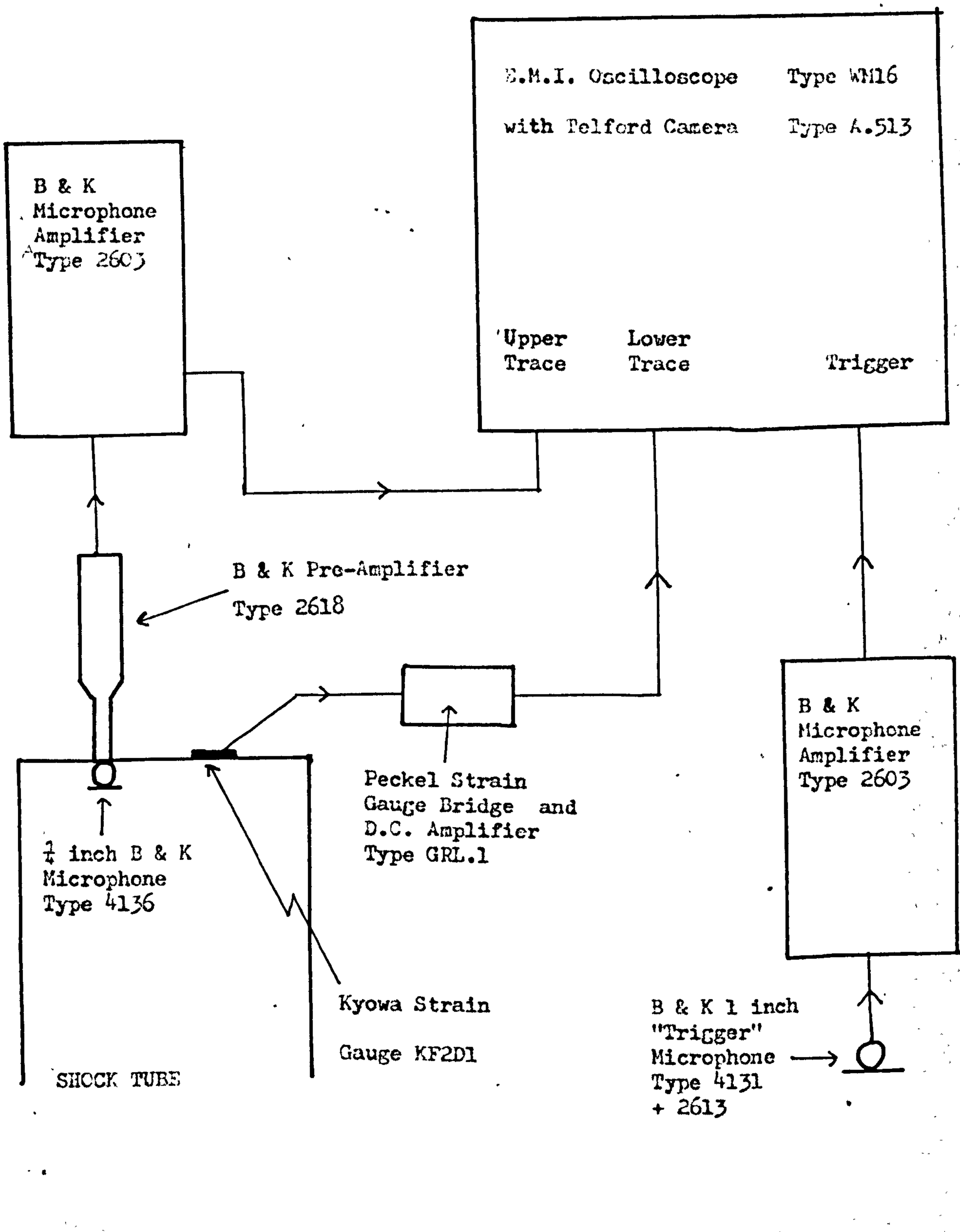

FIGURE 5.6 - THE MICROPHONE BUSH

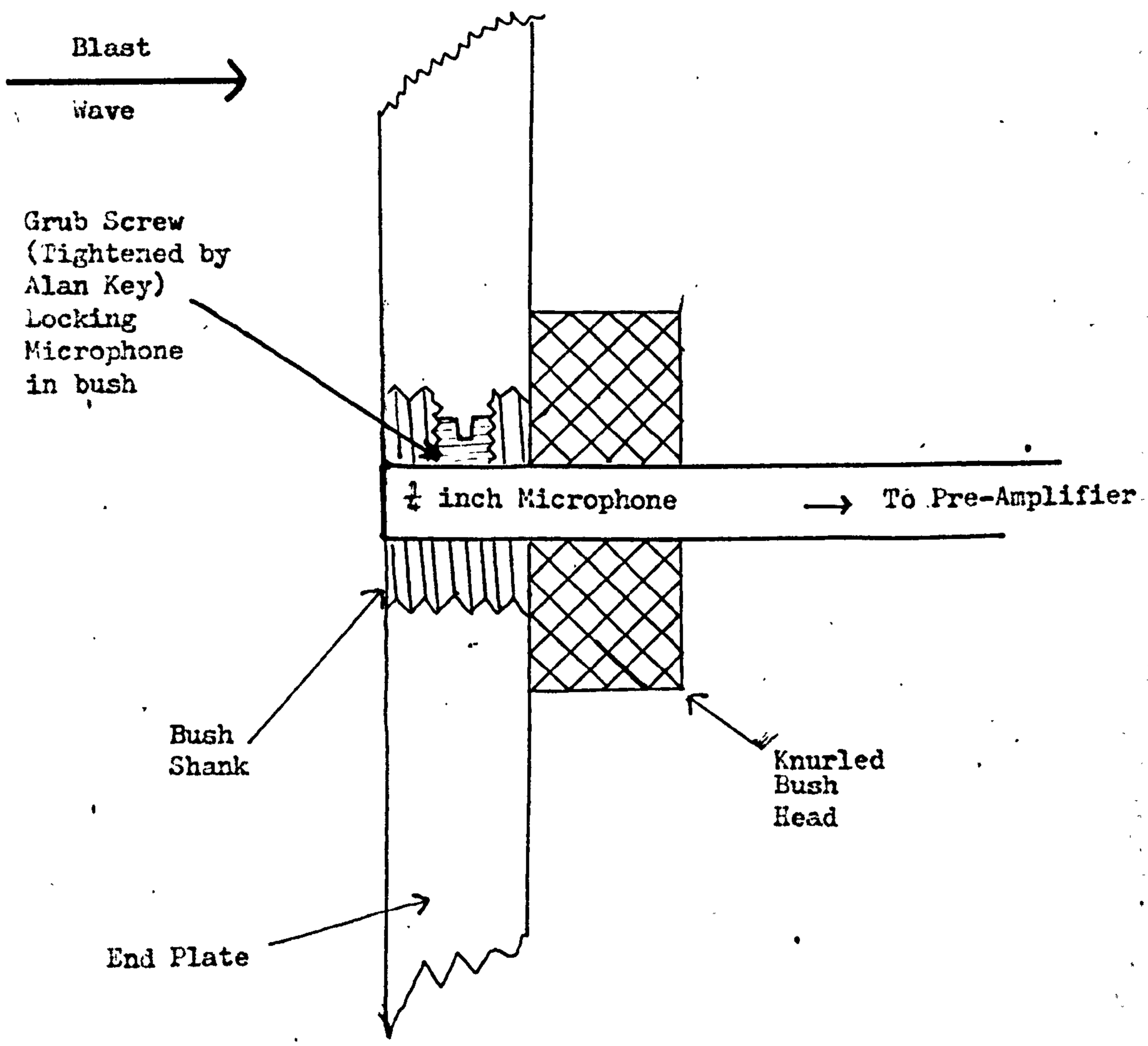

FIGURE 5.7 - THE DANGERS OF USING AN INTERNAL TRIGGER AS DEMONSTRATED BY THE DECAY OF STRAIN AFTER TAPPING THE PANEL

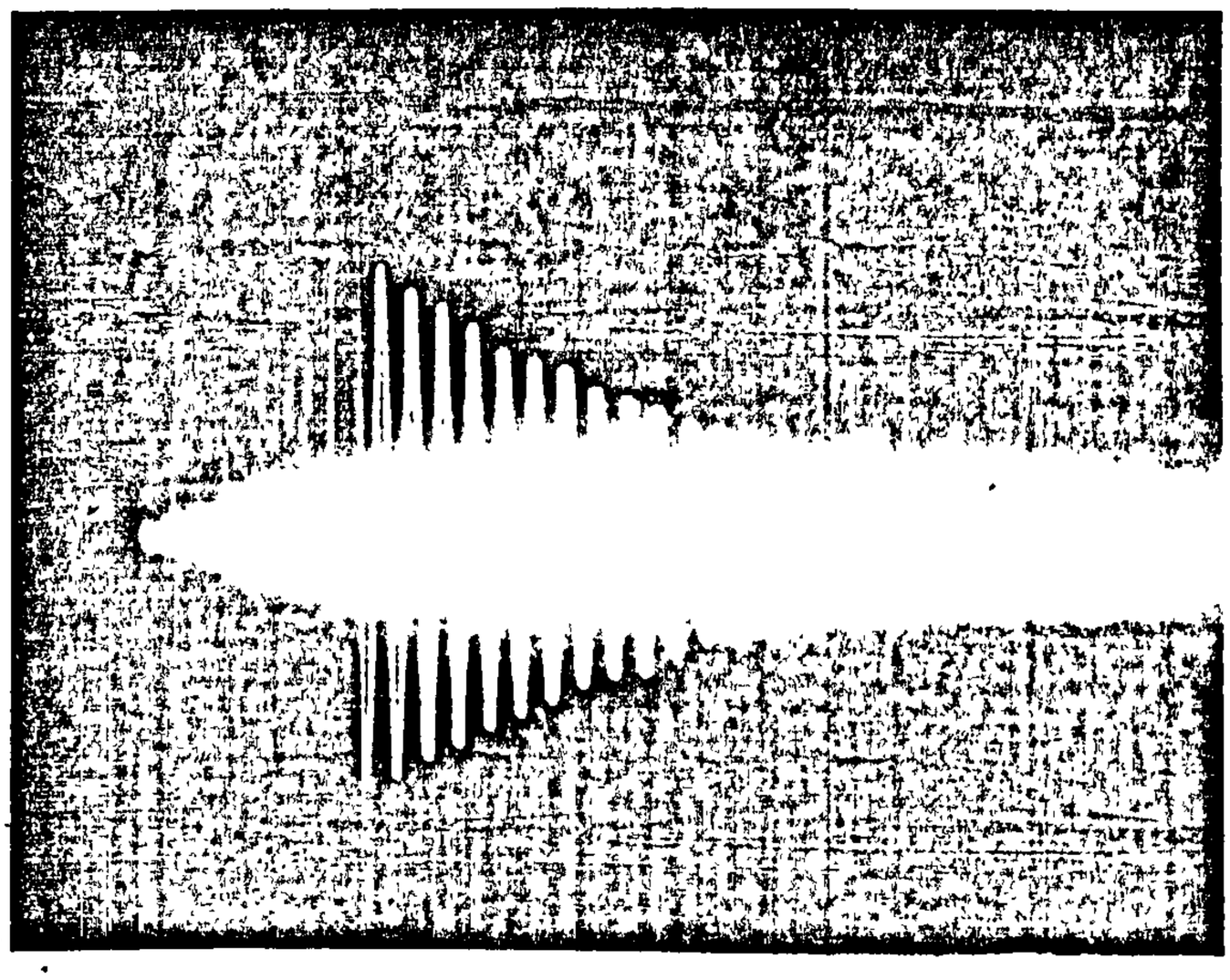

5.7(a) - Free Running Time Base.

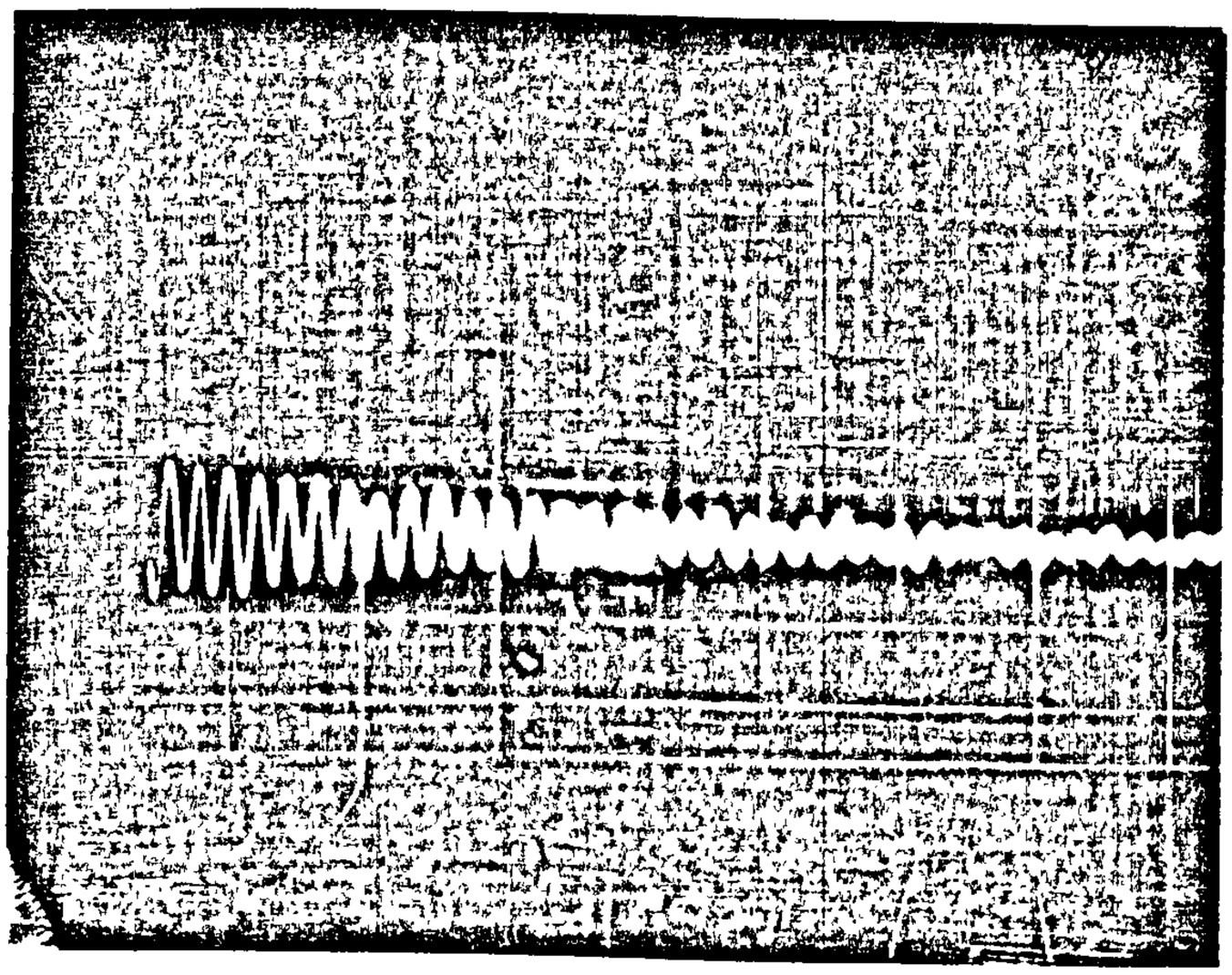

5.7(b) - Time Base on Internal Trigger

FIGURE 5.8 - The Original Design for a Simple Support

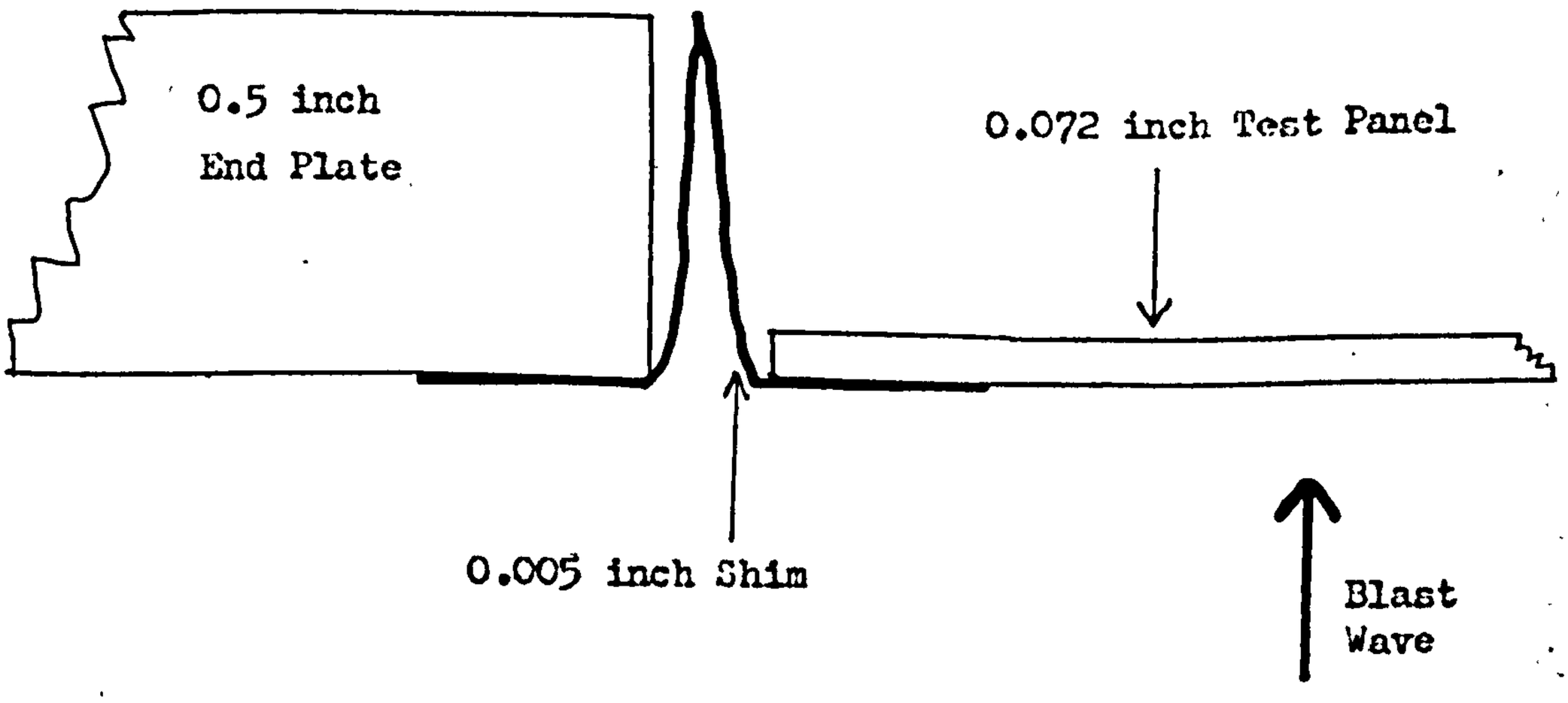

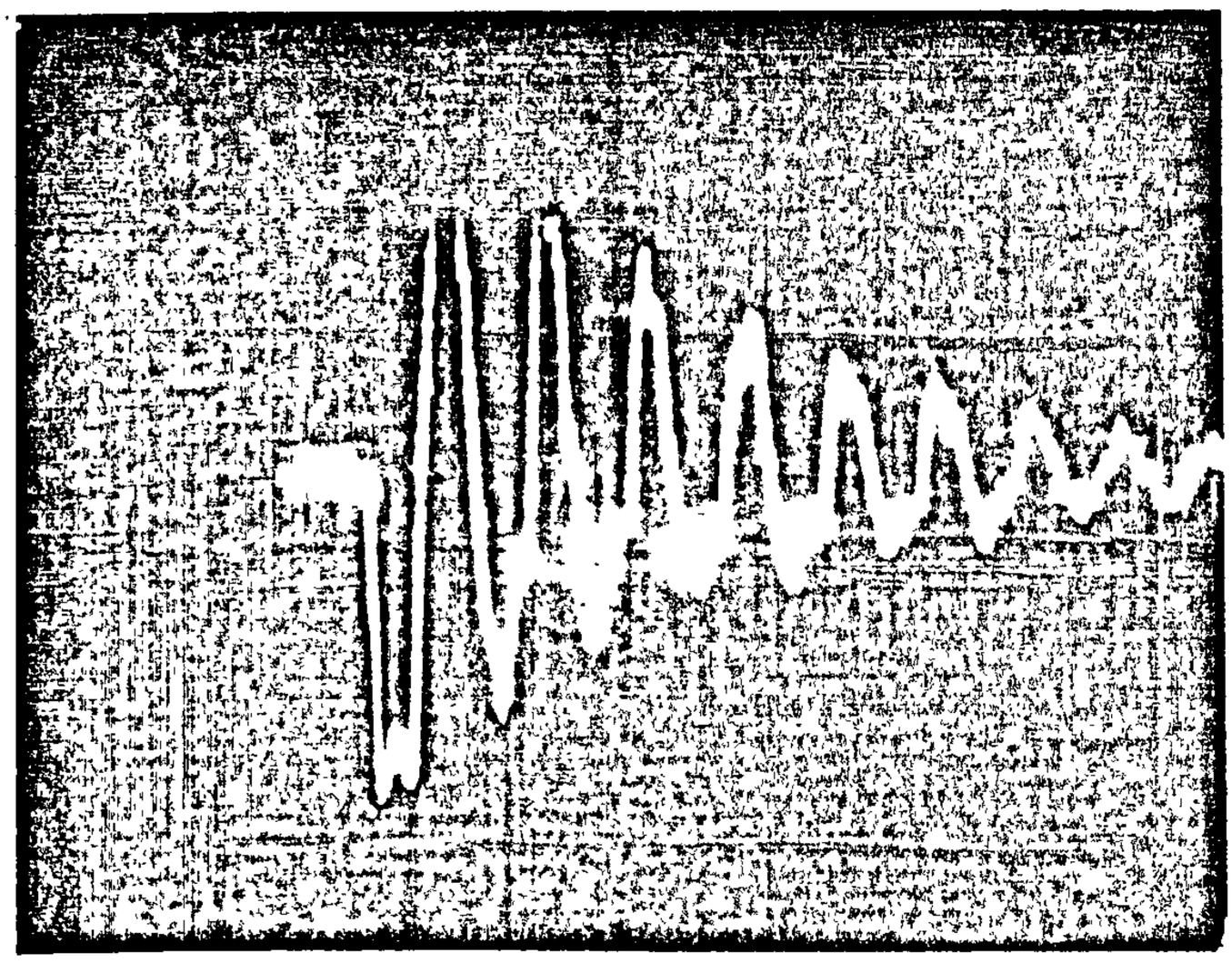

FIGURE 5.9 - THE DECAY OF STRAIN IN THE FIRST SIMPLY SUPPORTED PANEL

FIGURE 5.10 - THE FINAL DESIGN FOR A SIMPLE SUPPORT

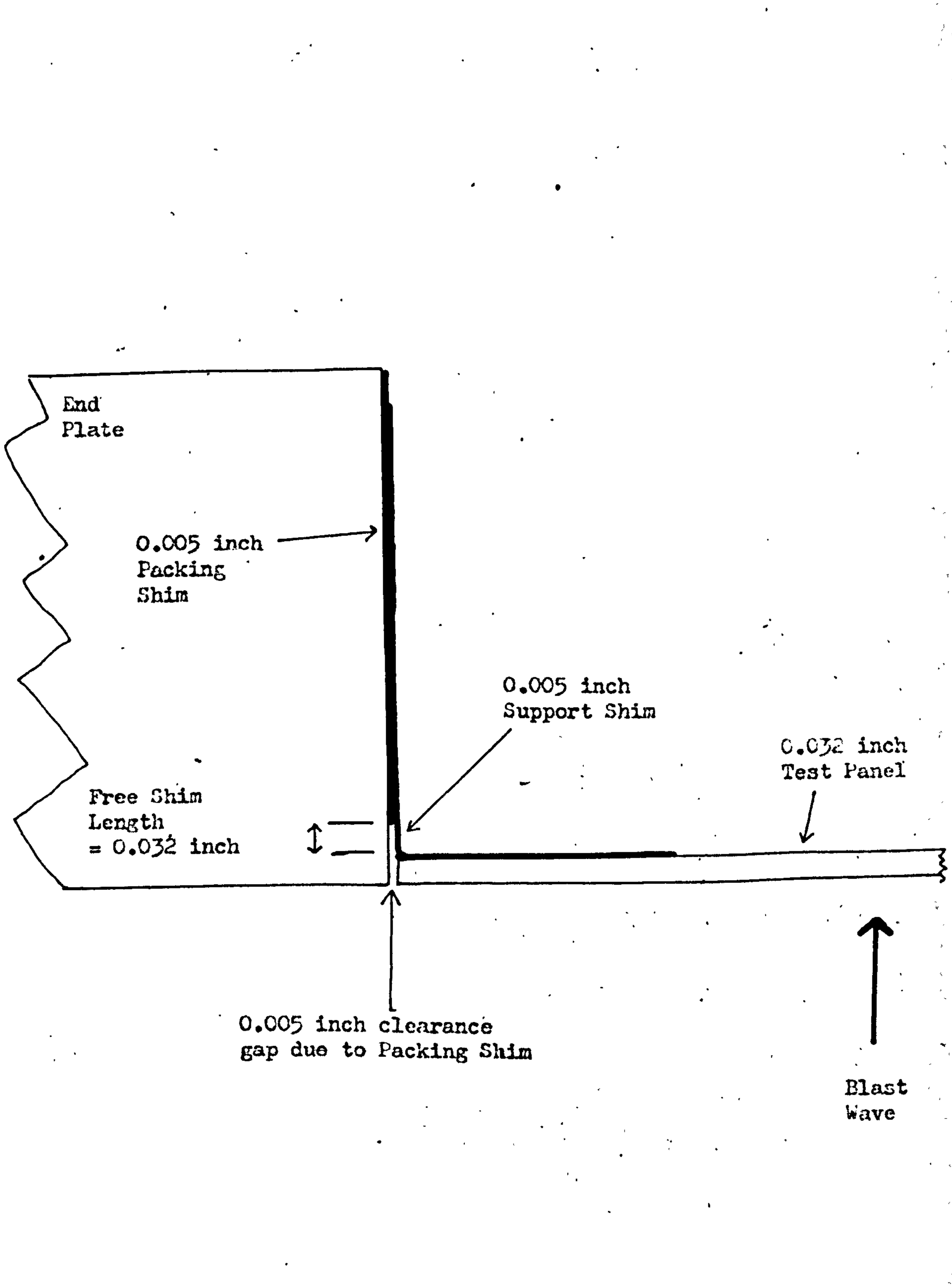

FIGURE 5.11 - PANEL STRAIN AFTER TAPPING FOR THE FINAL SIMPLY SUPPORTED PANEL

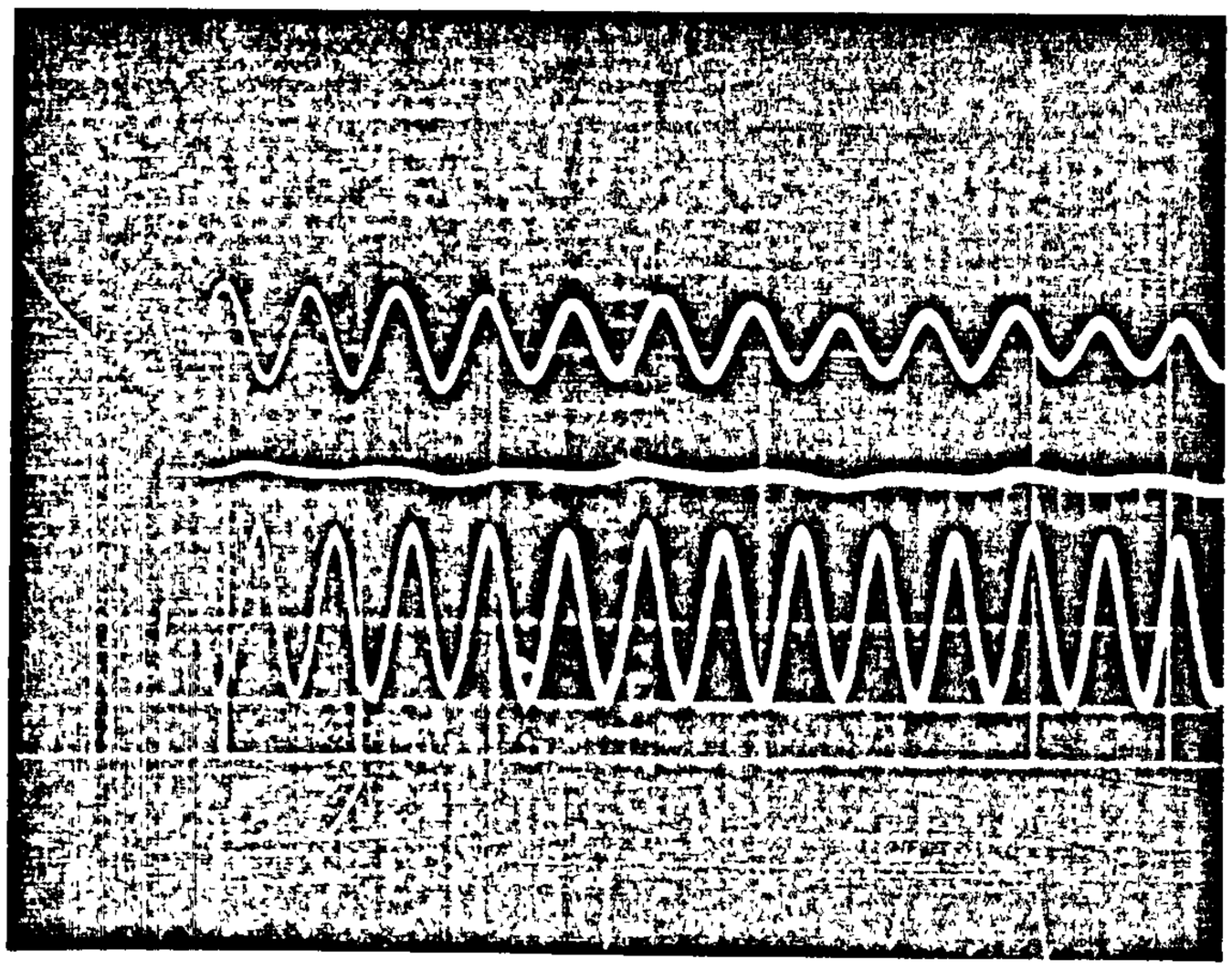

Upper Trace:- Strain of panel excited by tapping with finger.

Middle Trace:- Electrical noise from strain gauge amplifier.

Lower Trace:- New pistonphone with frequency of 250 ± 10 Hz.

Crest Height (Measured as Crest to Crest distance in 1/16 inch. Between crest in question and previous negative crest)

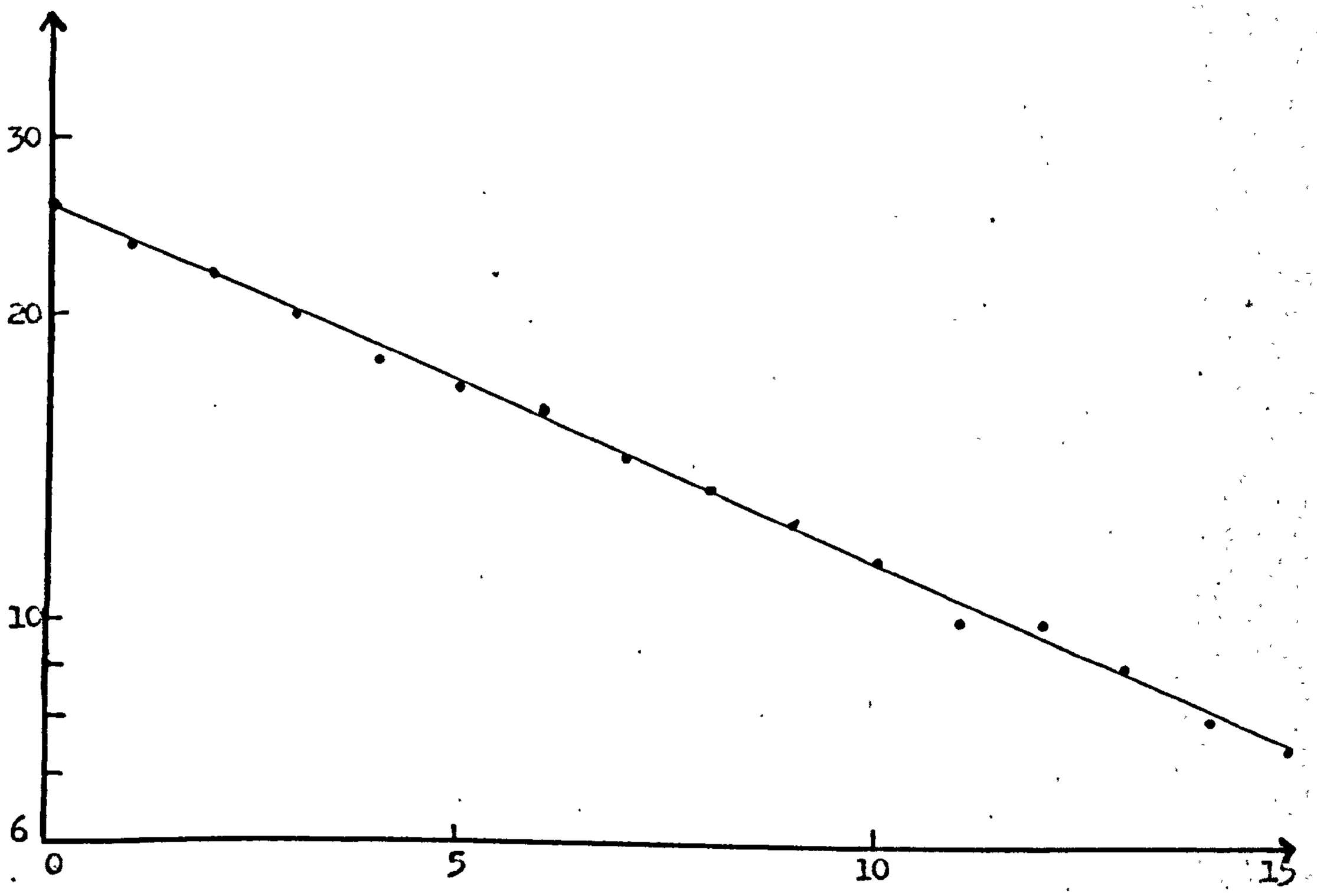

FIGURE 5.12 - DECAY OF PANEL STRAIN AFTER TAPPING (TAKEN FROM FIGURE 5.7(a))

FIGURE 5.13 - THE TRANSMISSION LOSS BOX

(for further design and construction details see Reference 1.3)

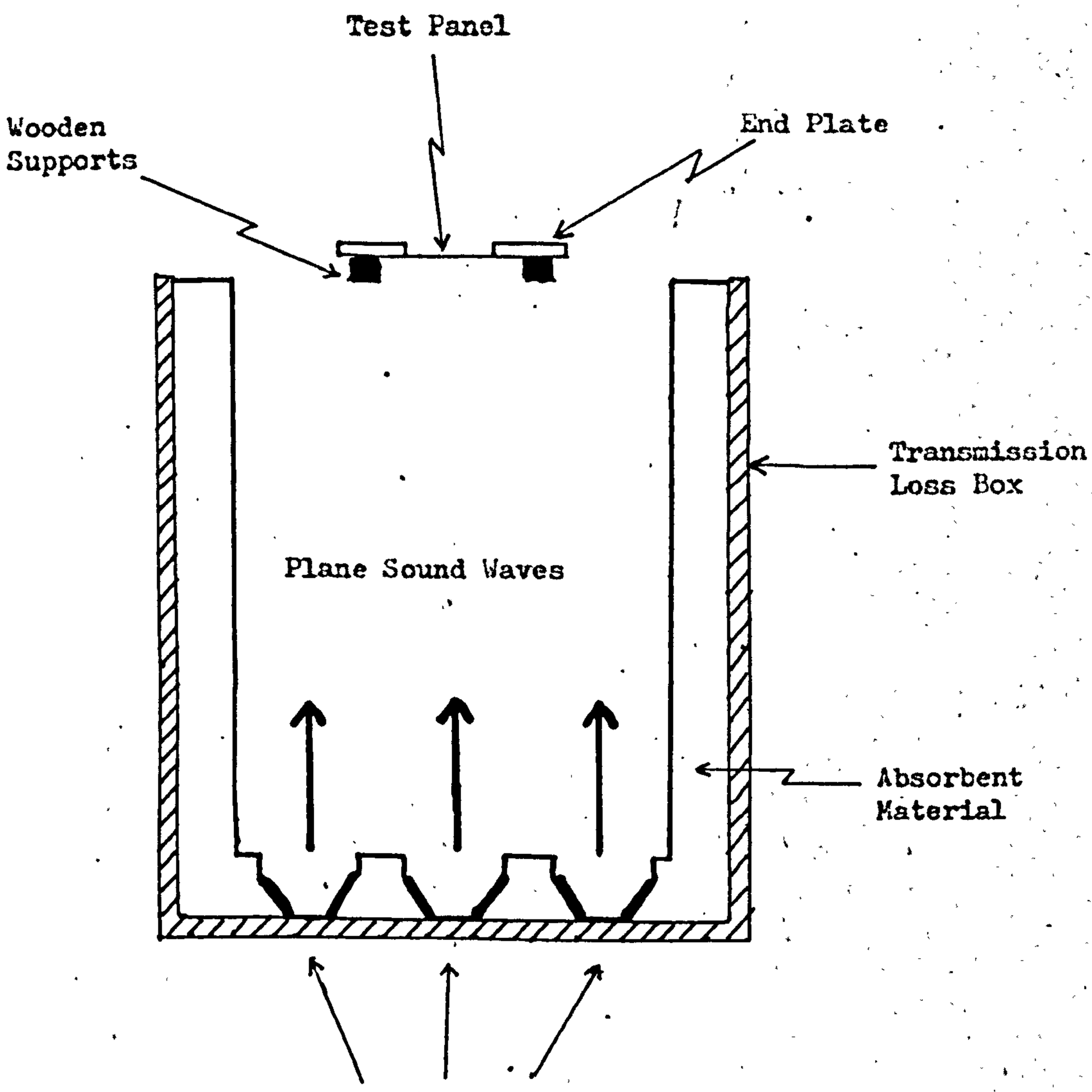

FIGURE 5.14 - THE ORIGINAL TRANSMISSION LOSS BOX INSTRUMENTATION

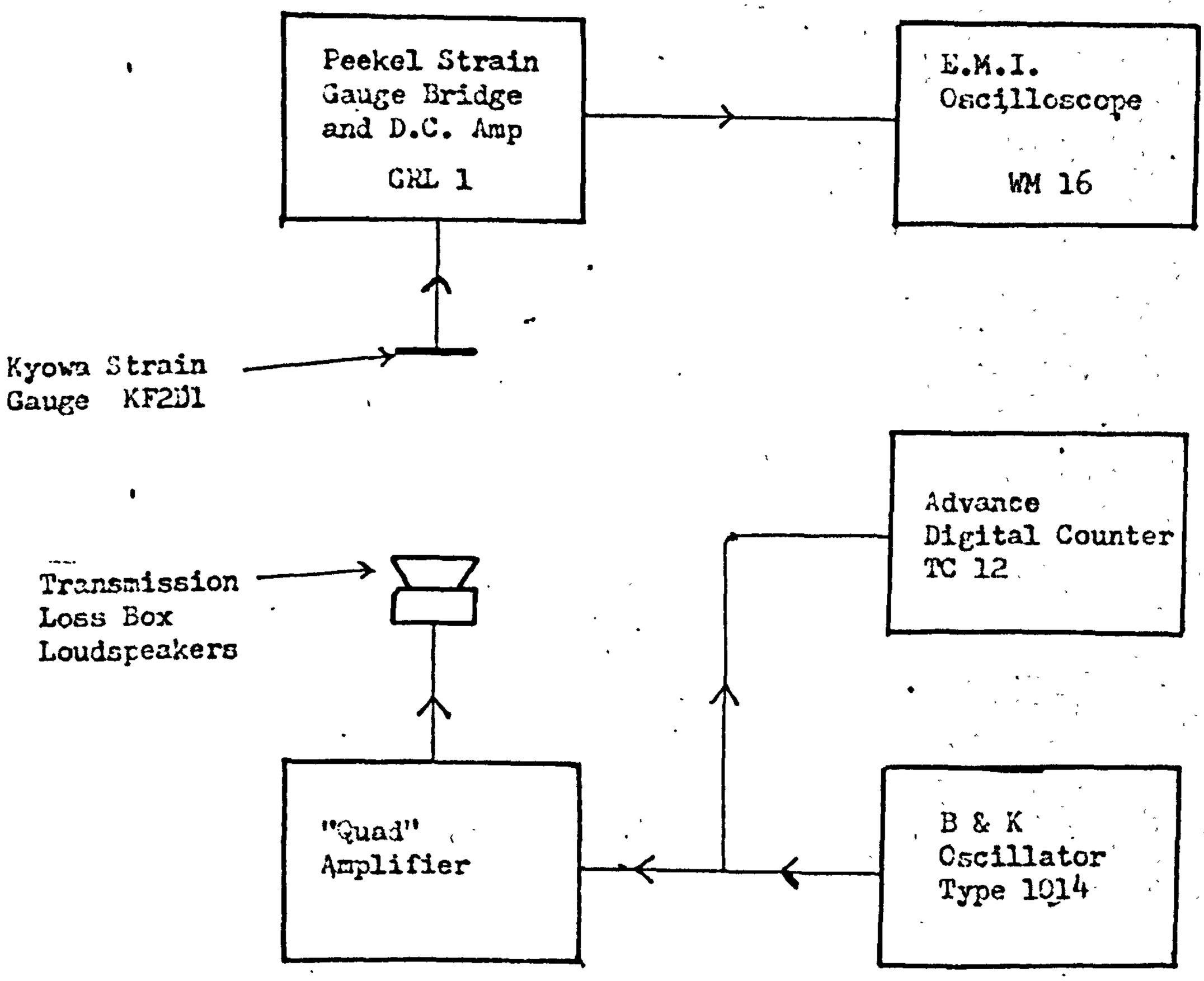

FIGURE 5.15 - RESONANCE OF THE PANEL FUNDAMENTAL

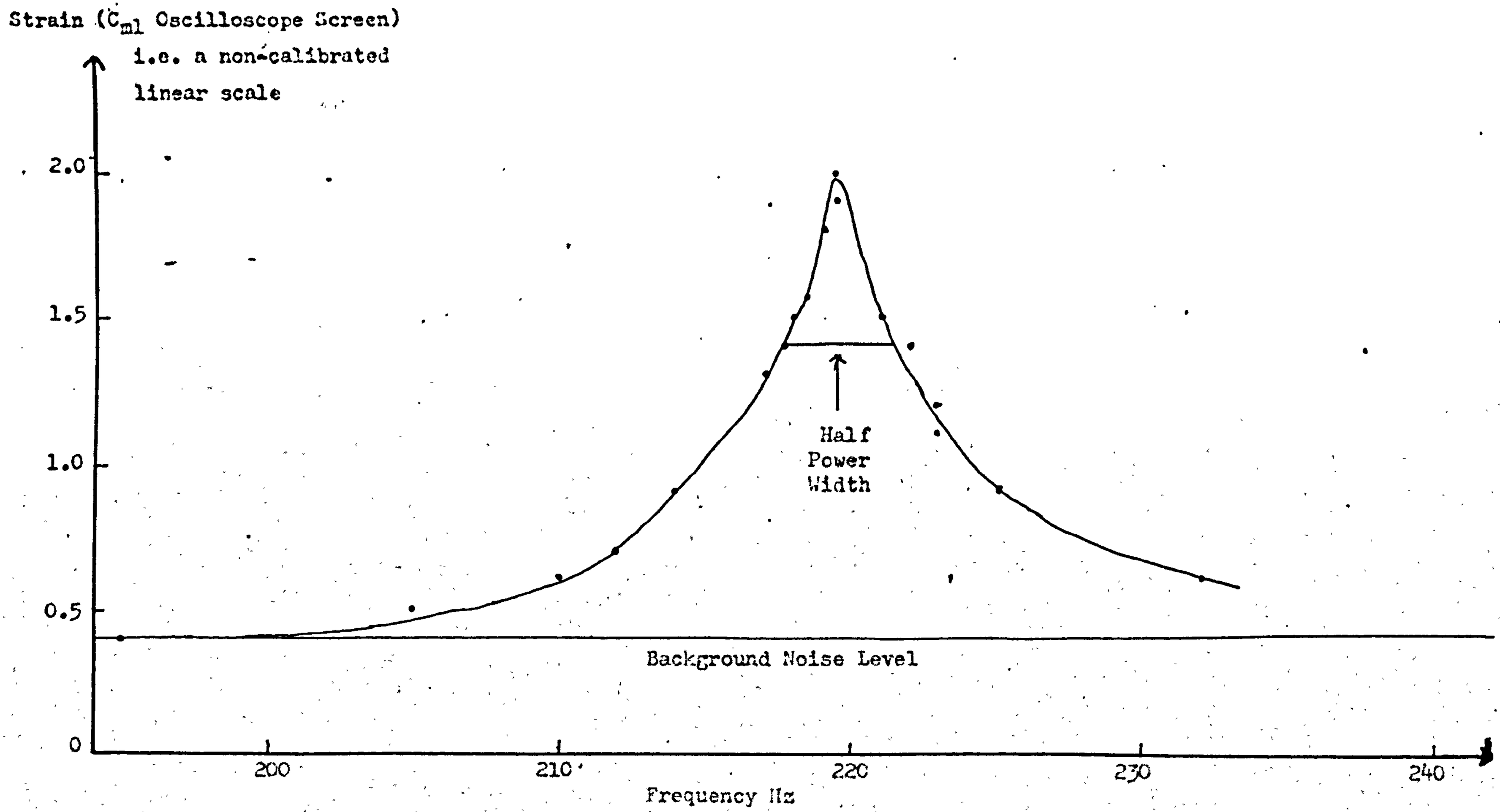

FIGURE 5.16 - MODIFIED TRANSMISSION LOSS BOX INSTRUMENTATION

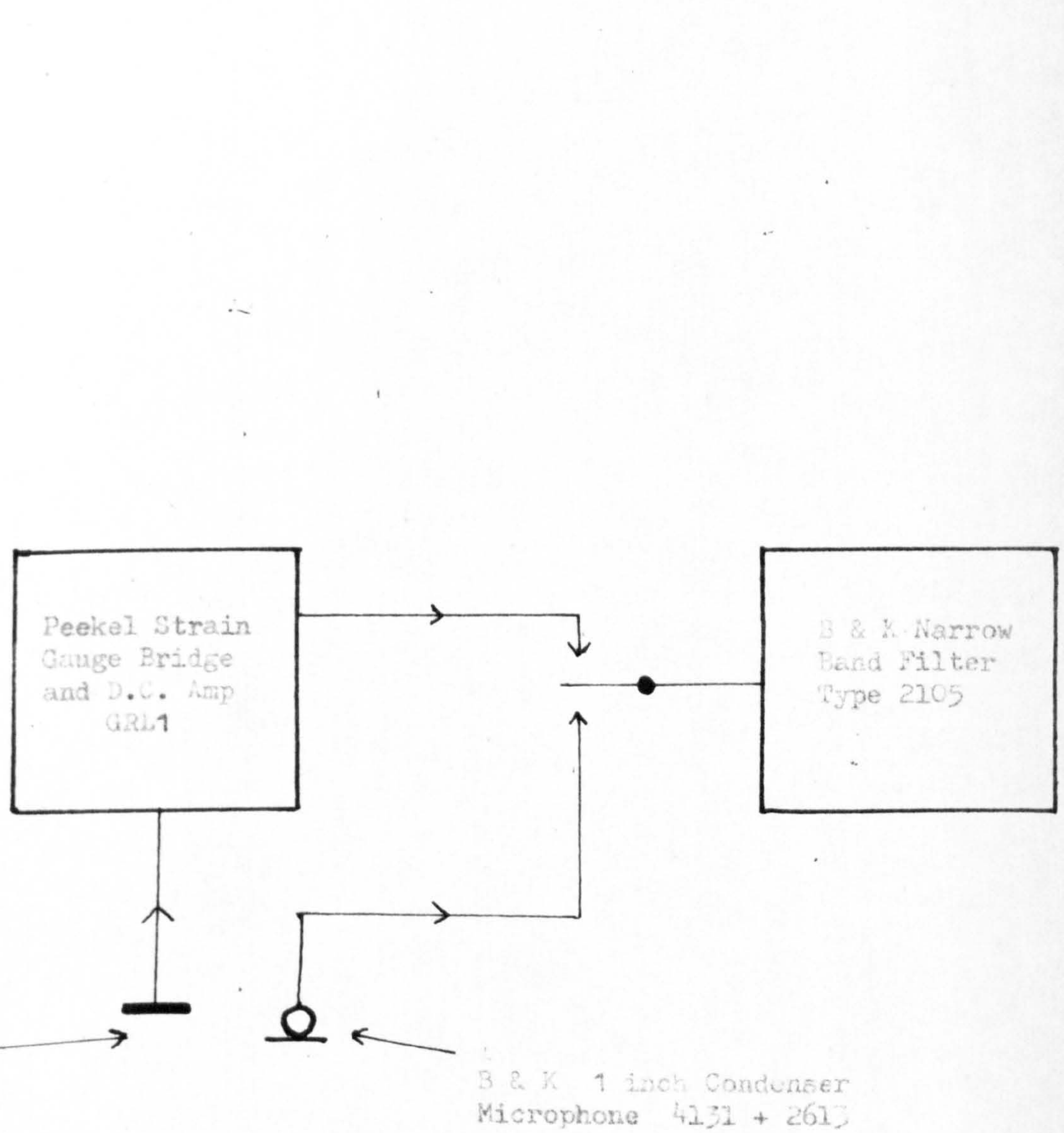

(Sound Generation as per Figure (5.14))

FIGURE 5.17 - RESONANCE OF THE PANEL FUNDAMENTAL (Excited by 105 dB S.P.L. at all frequencies)

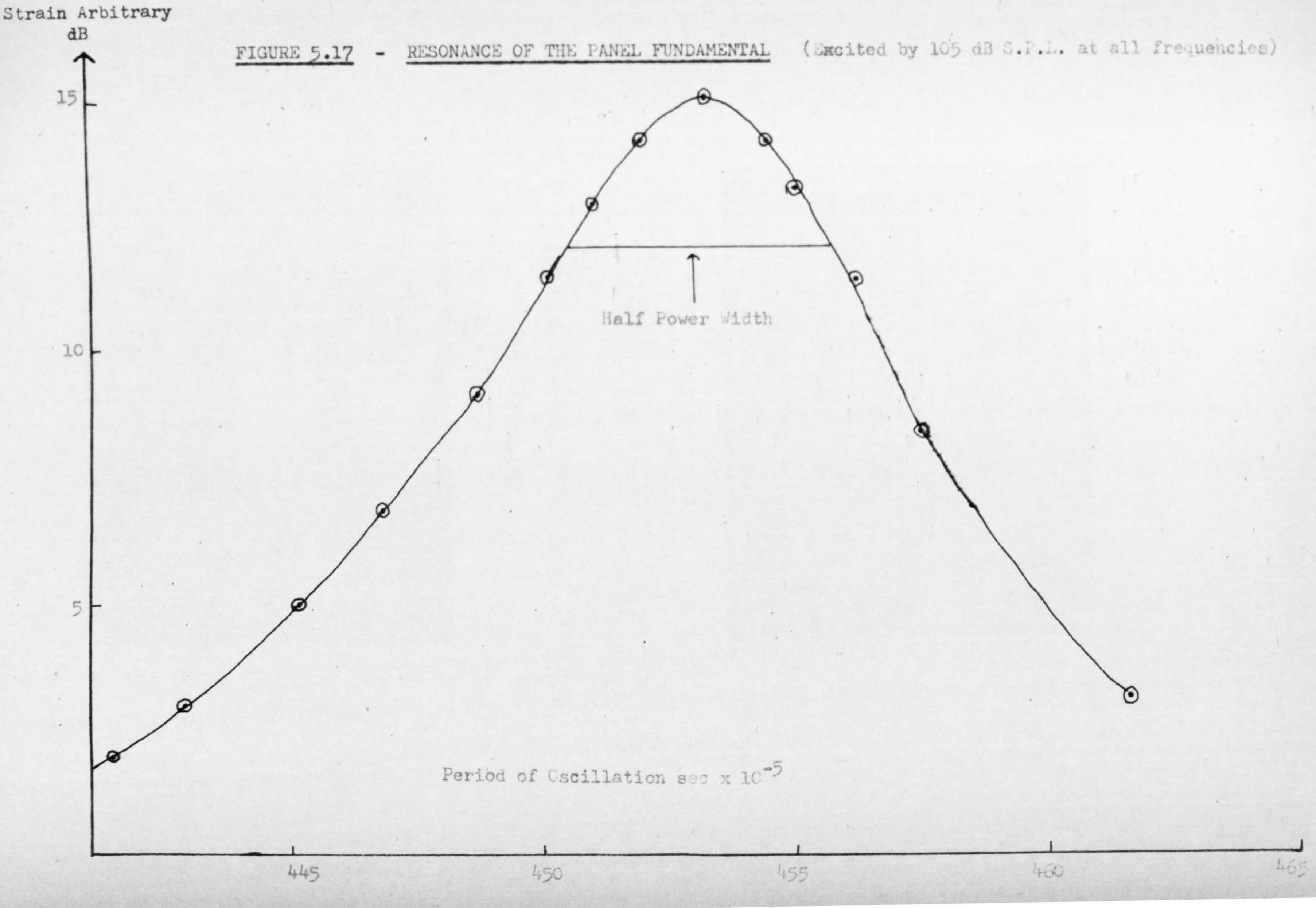

FIGURE 5.18 - THE DECAY OF SOUND IN THE TRANSMISSION LOSS BOX

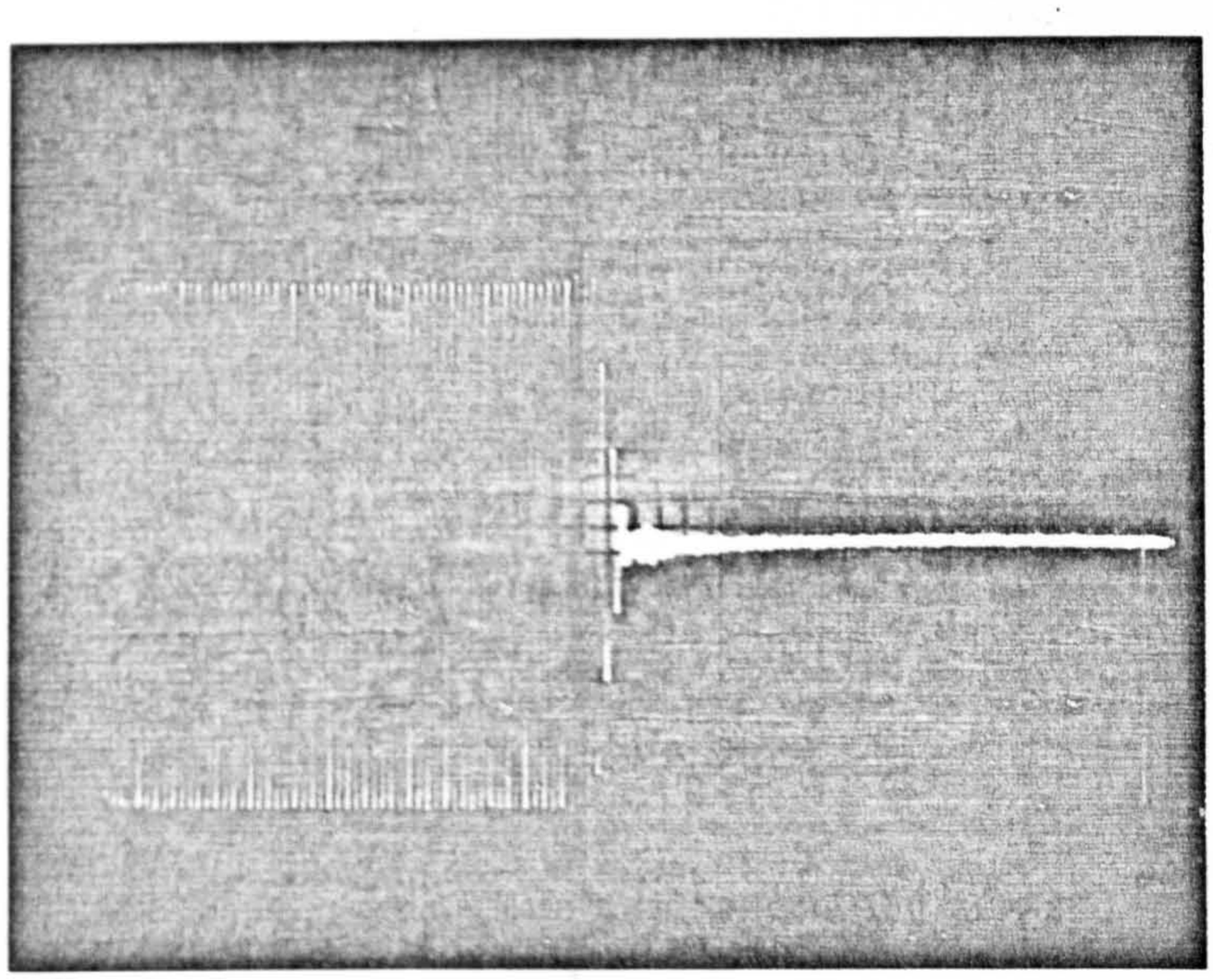

FIGURE 5.19 - THE DECAY OF STRAIN AFTER ACOUSTIC EXCITATION IN THE TRANSMISSION LOSS BOX

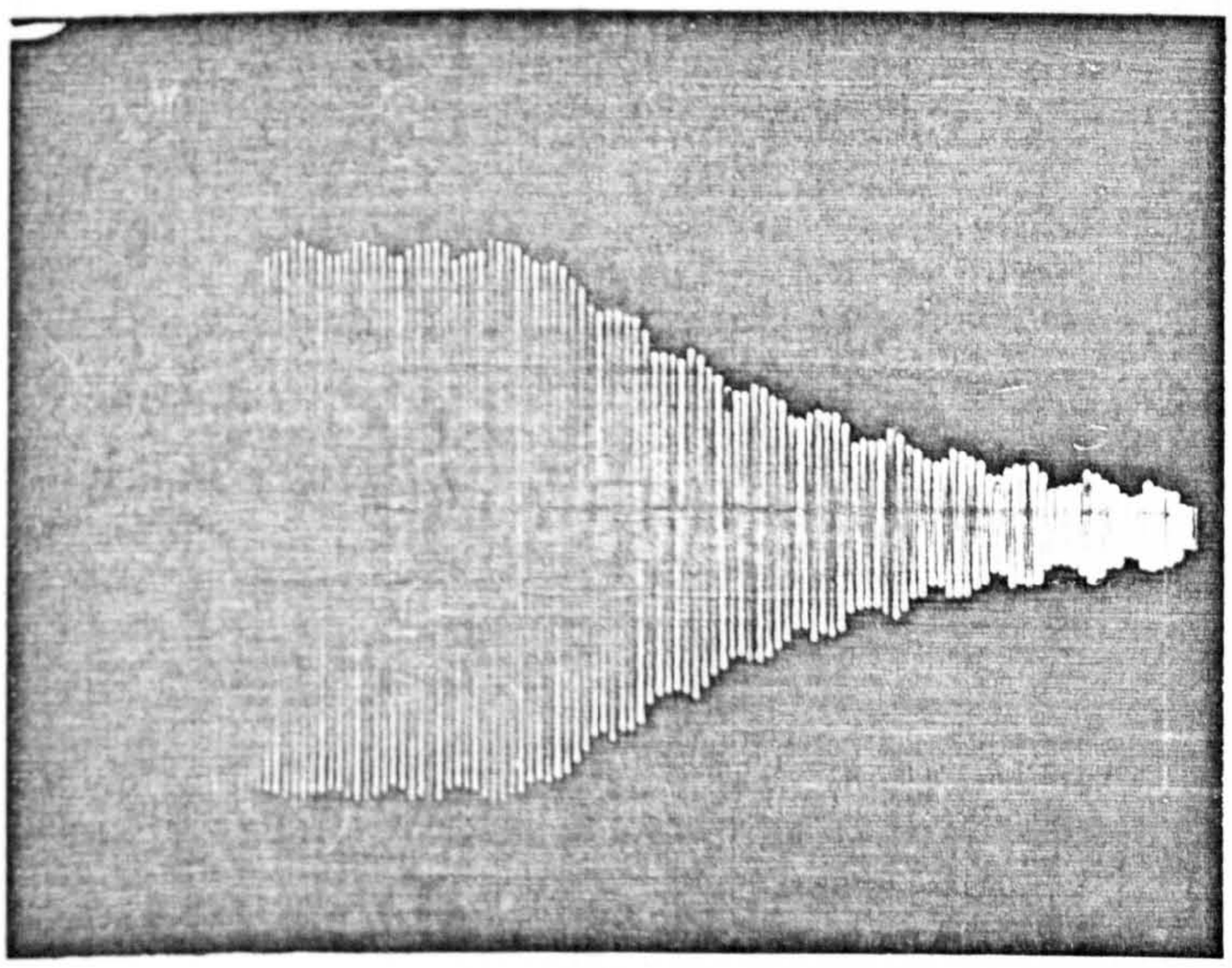

FIGURE 5.20 - THE DECAY OF ACOUSTICALLY EXCITED STRAIN

(from Figure (5.19))

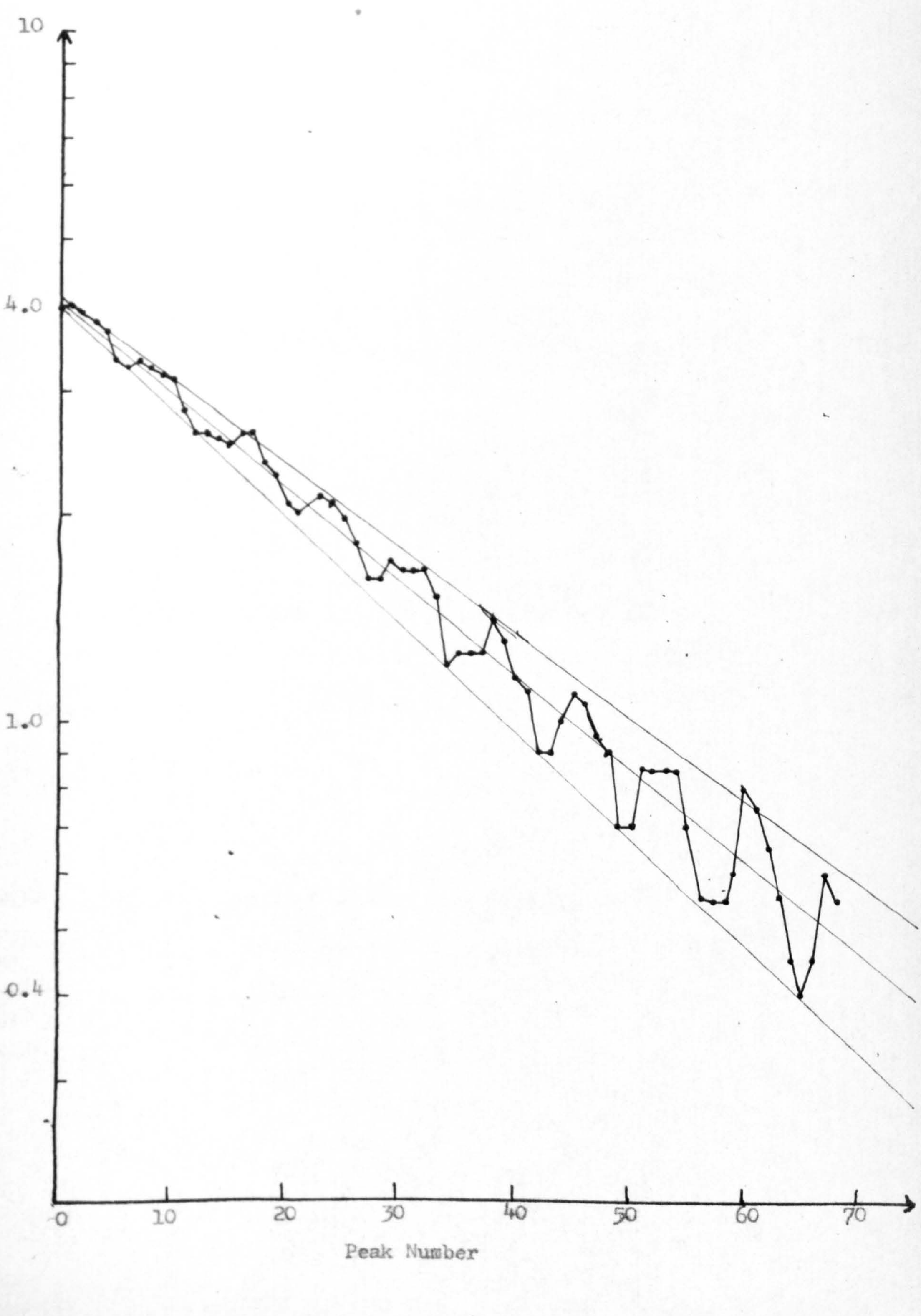

FIGURE 5.21 - DECAY OF PANEL STRAIN AFTER TAPPING (24.3.69)

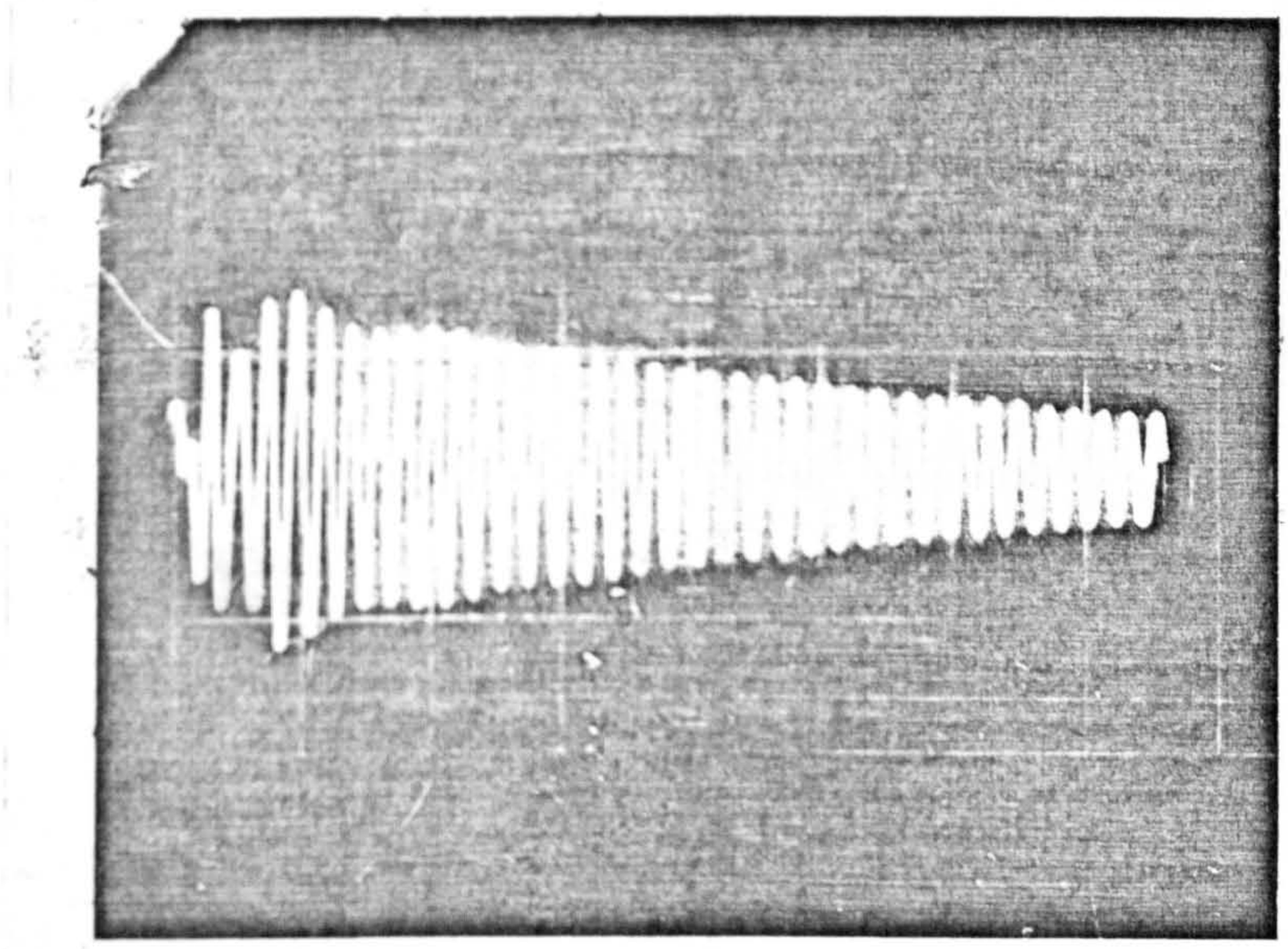

(Compare with results of similar experiment performed on 5.3.69 (Figure 5.7(a)) to see how damping has decreased.)

FIGURE 5.22 - RESONANCE OF THE 3,1 PANEL MODE

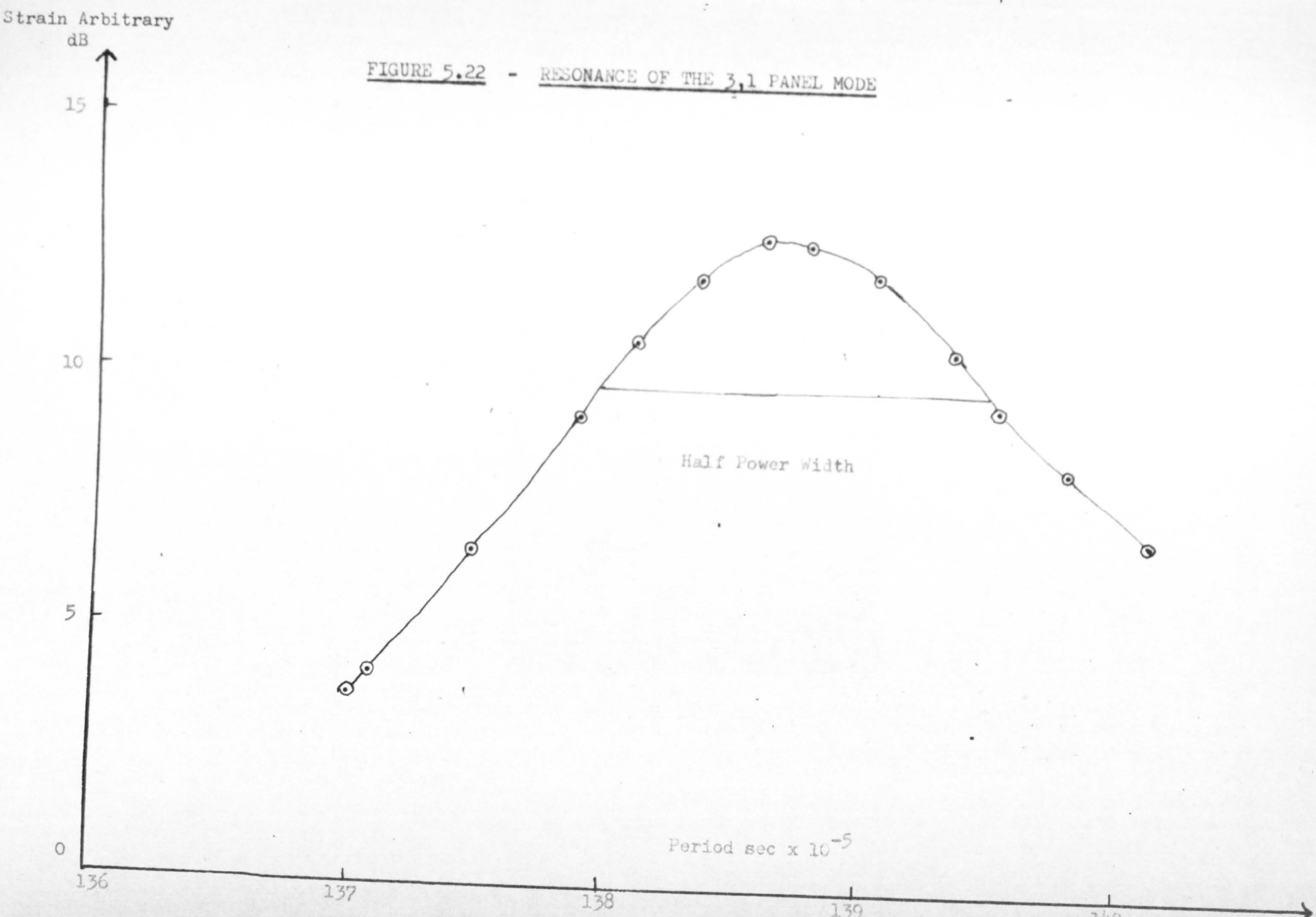

FIGURE 5.23 - FIREWORK PRESSURE WAVE MEASURED AT NORMAL INCIDENCE

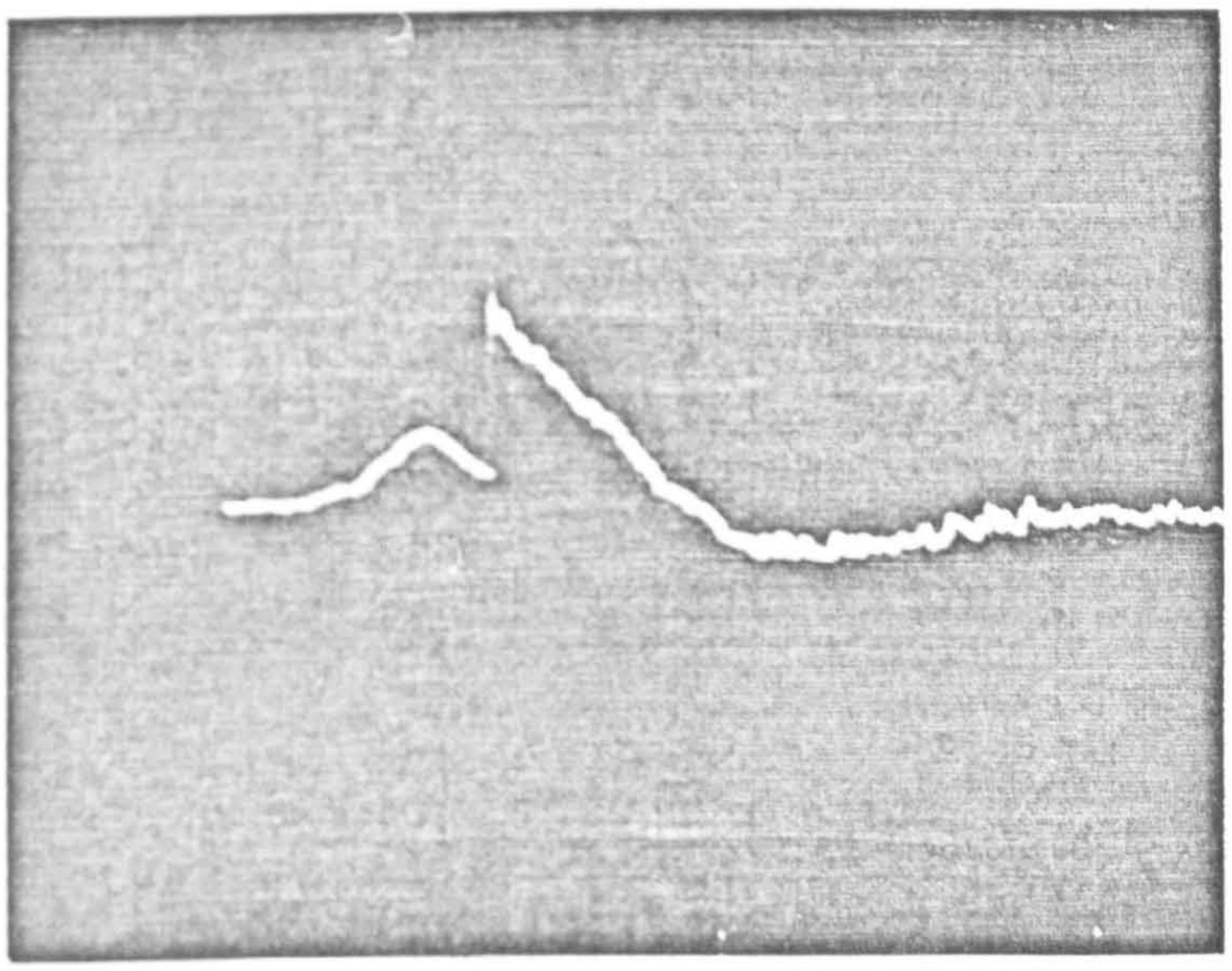

FIGURE 5.24 - FIREWORK PRESSURE WAVES MEASURED AT GRAZING INCIDENCE

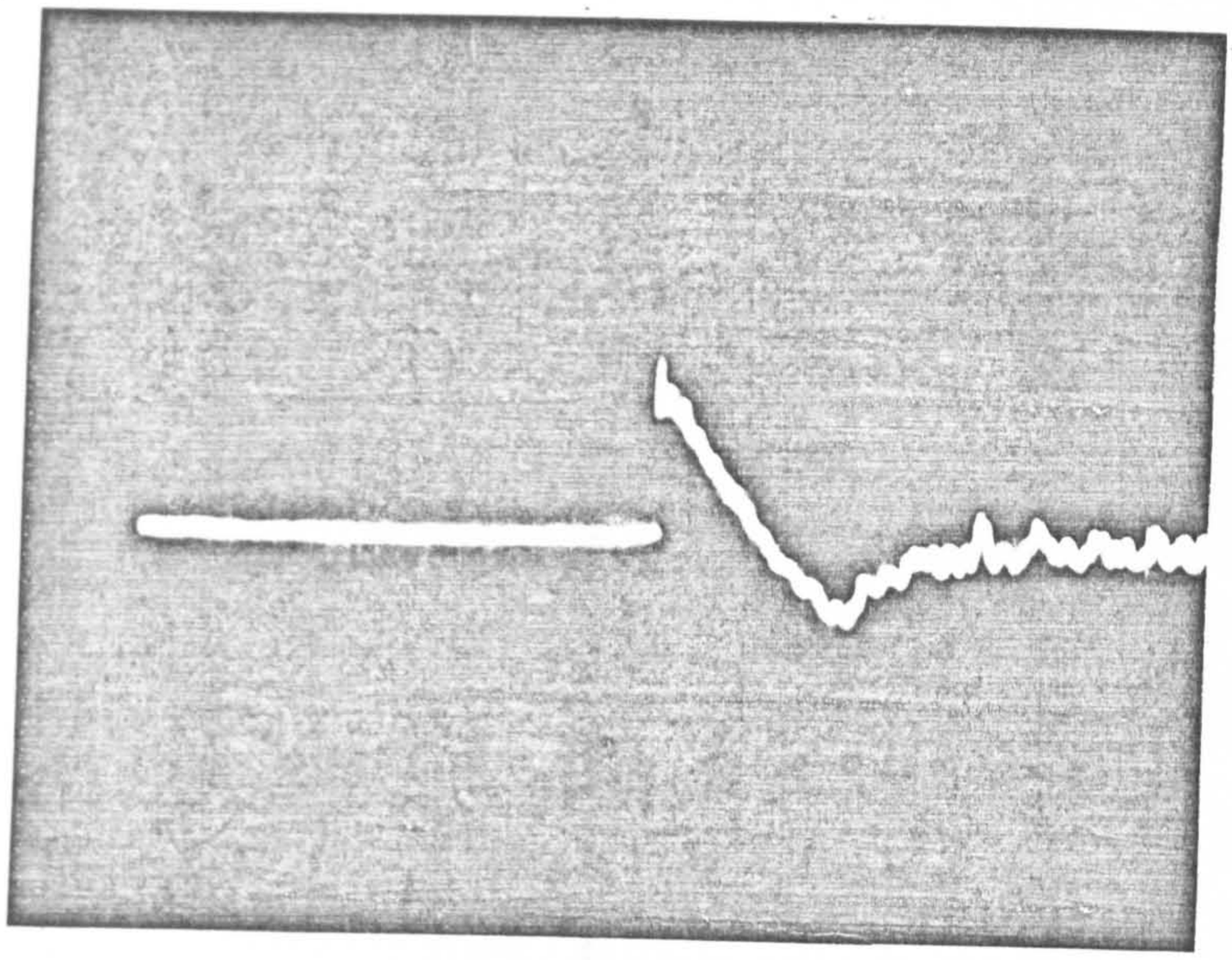

5.24(a) "Clean Waveform"

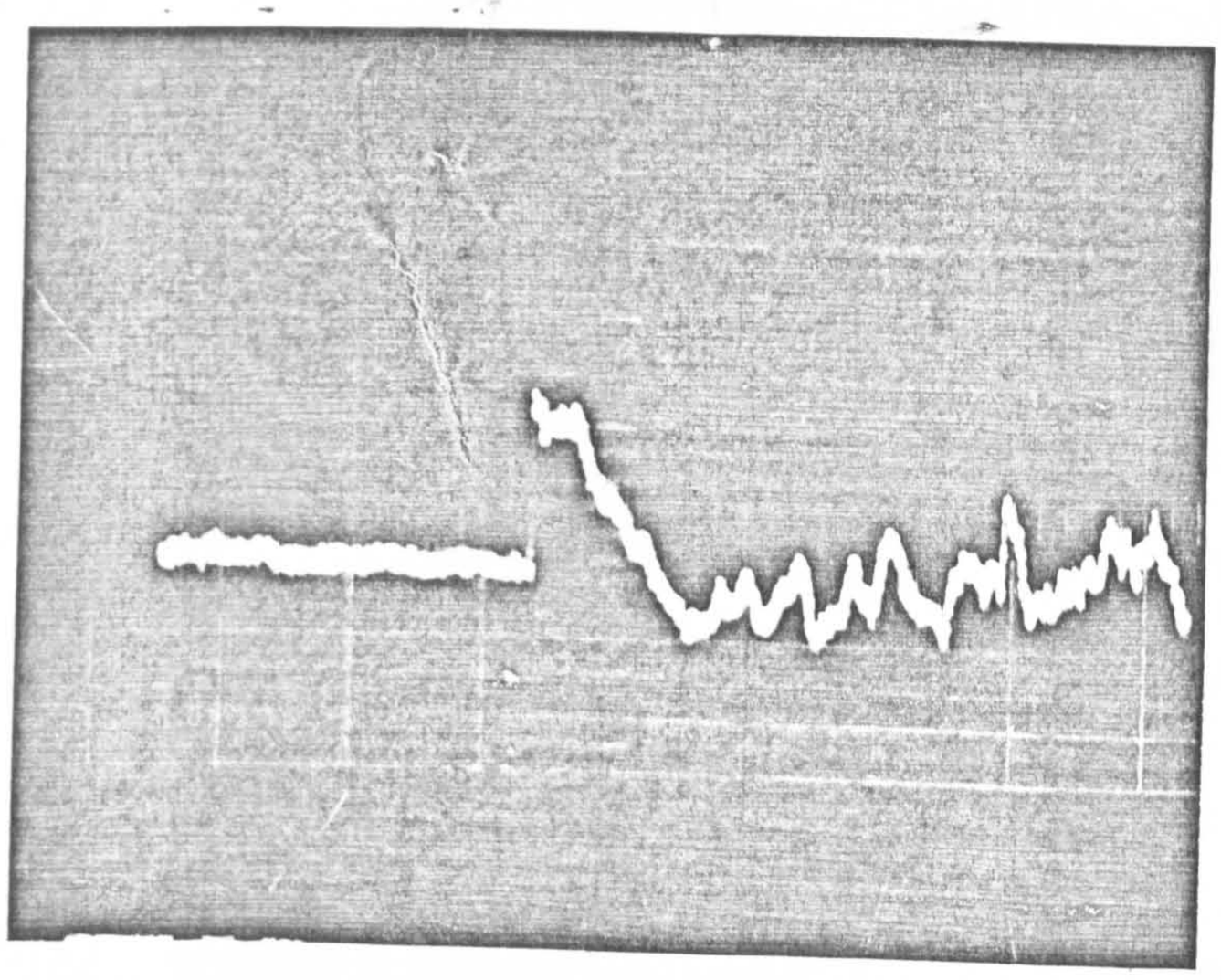

5.24(b) Variation that may occur

FIGURE 5.25 - PRESSURE WAVE DUE TO 1st ELECTRICALLY DETONATED CHARGE MEASURED AT NORMAL INCIDENCE

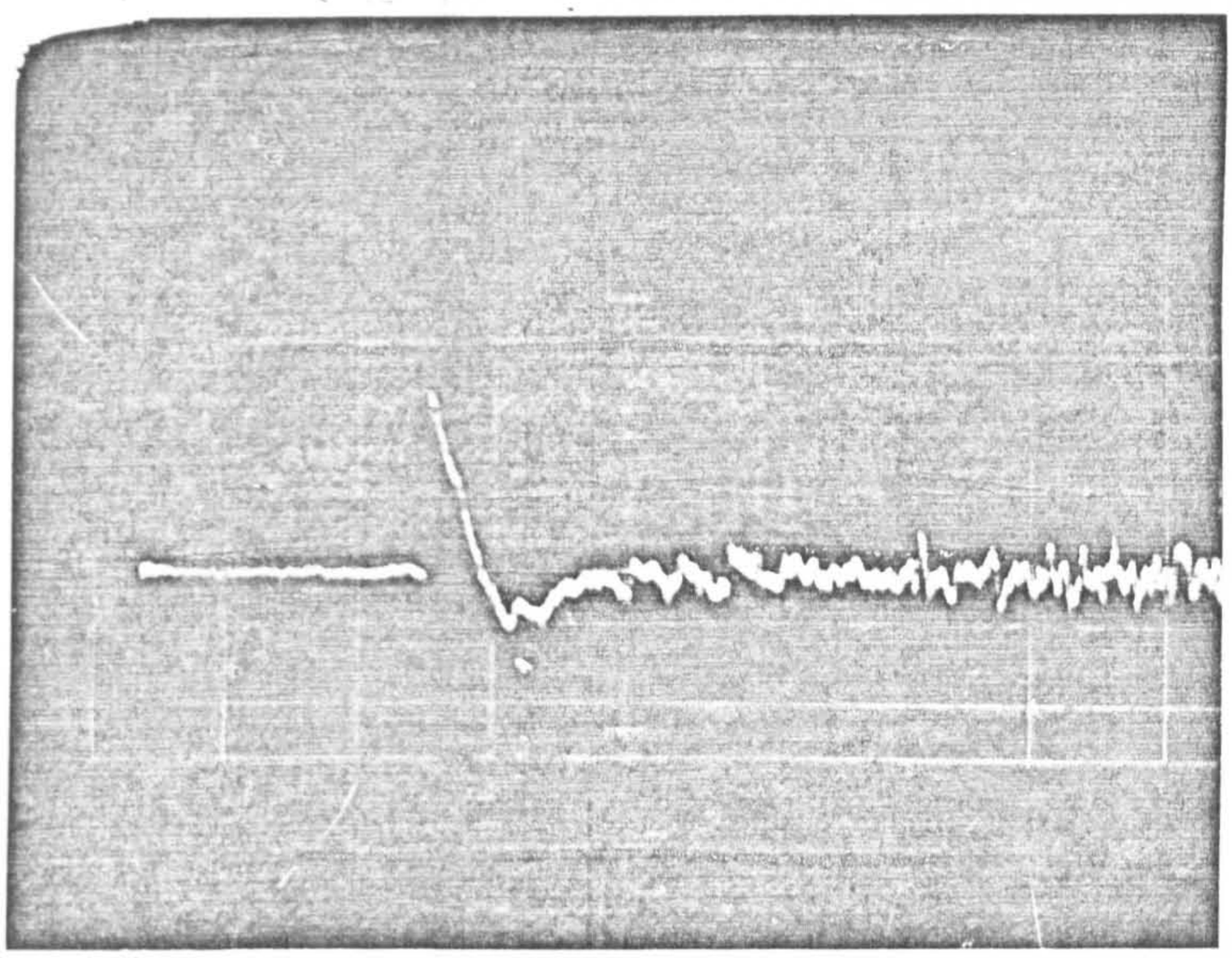

FIGURE 5.26 - PRESSURE WAVE DUE TO 2nd ELECTRICALLY DETONATED CHARGE MEASURED AT NORMAL INCIDENCE

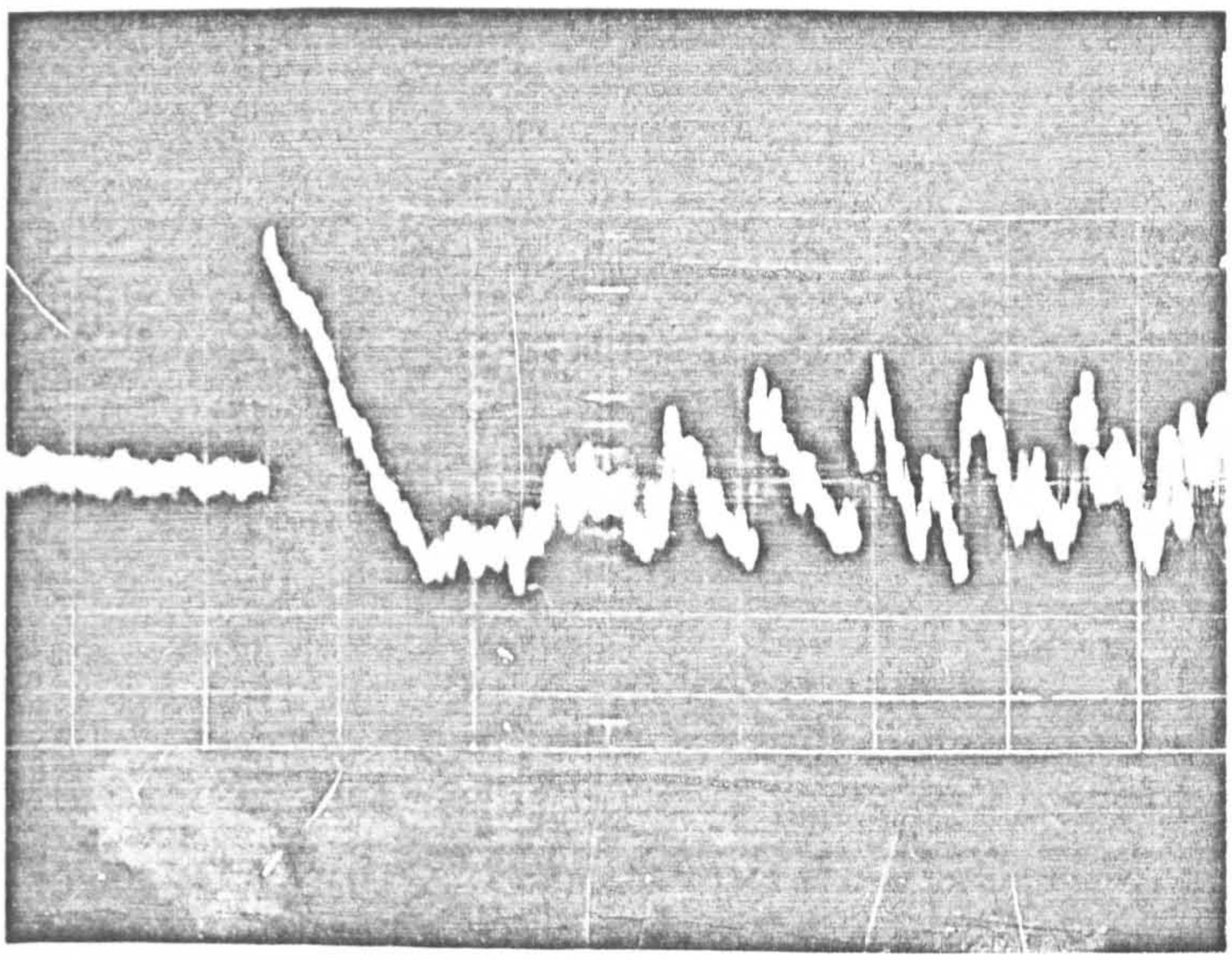

FIGURE 5.27 - PRESSURE WAVES DUE TO THIRD ELECTRICALLY DETONATED CHARGES MEASURED AT NORMAL INCIDENCE

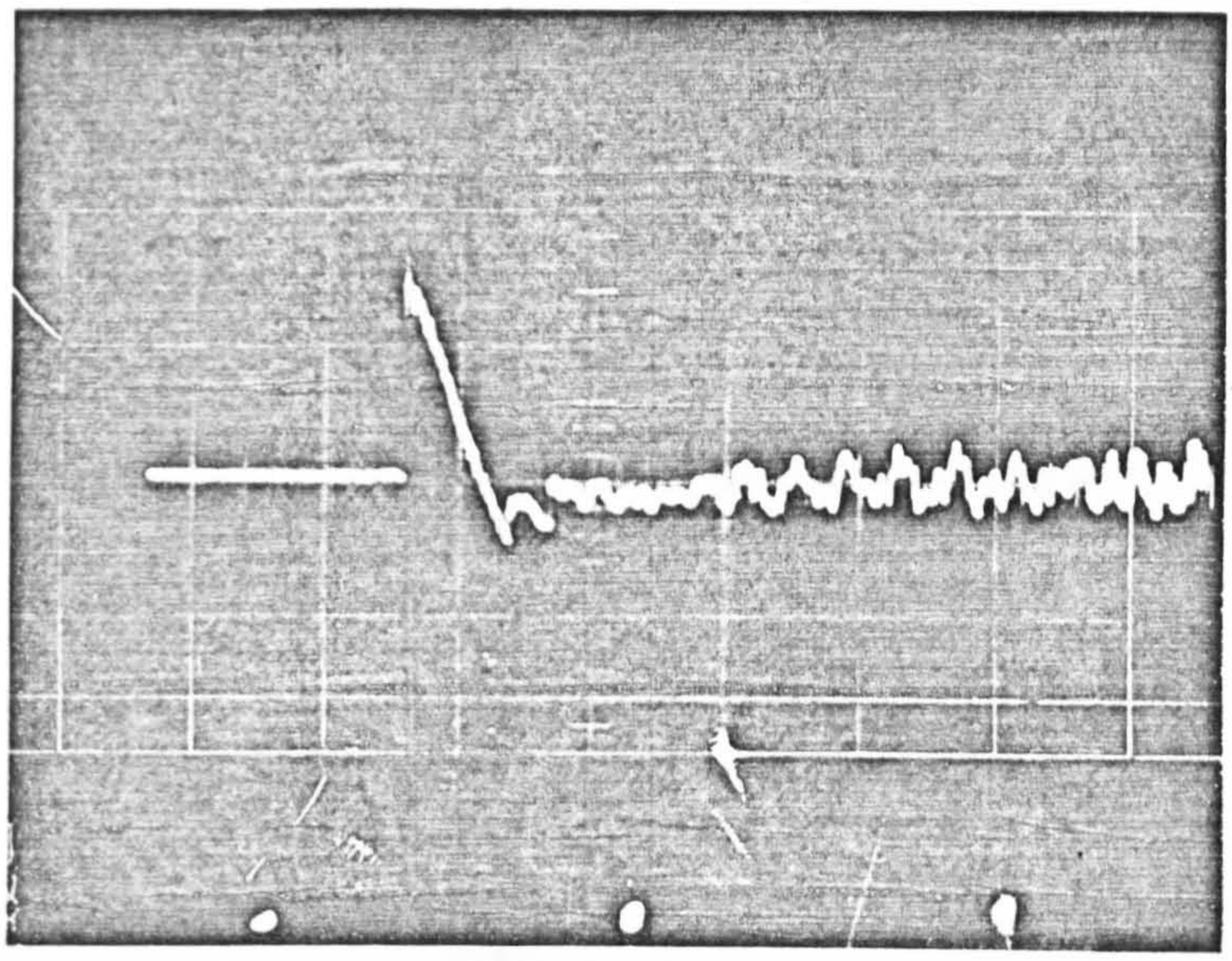

5.27(a)

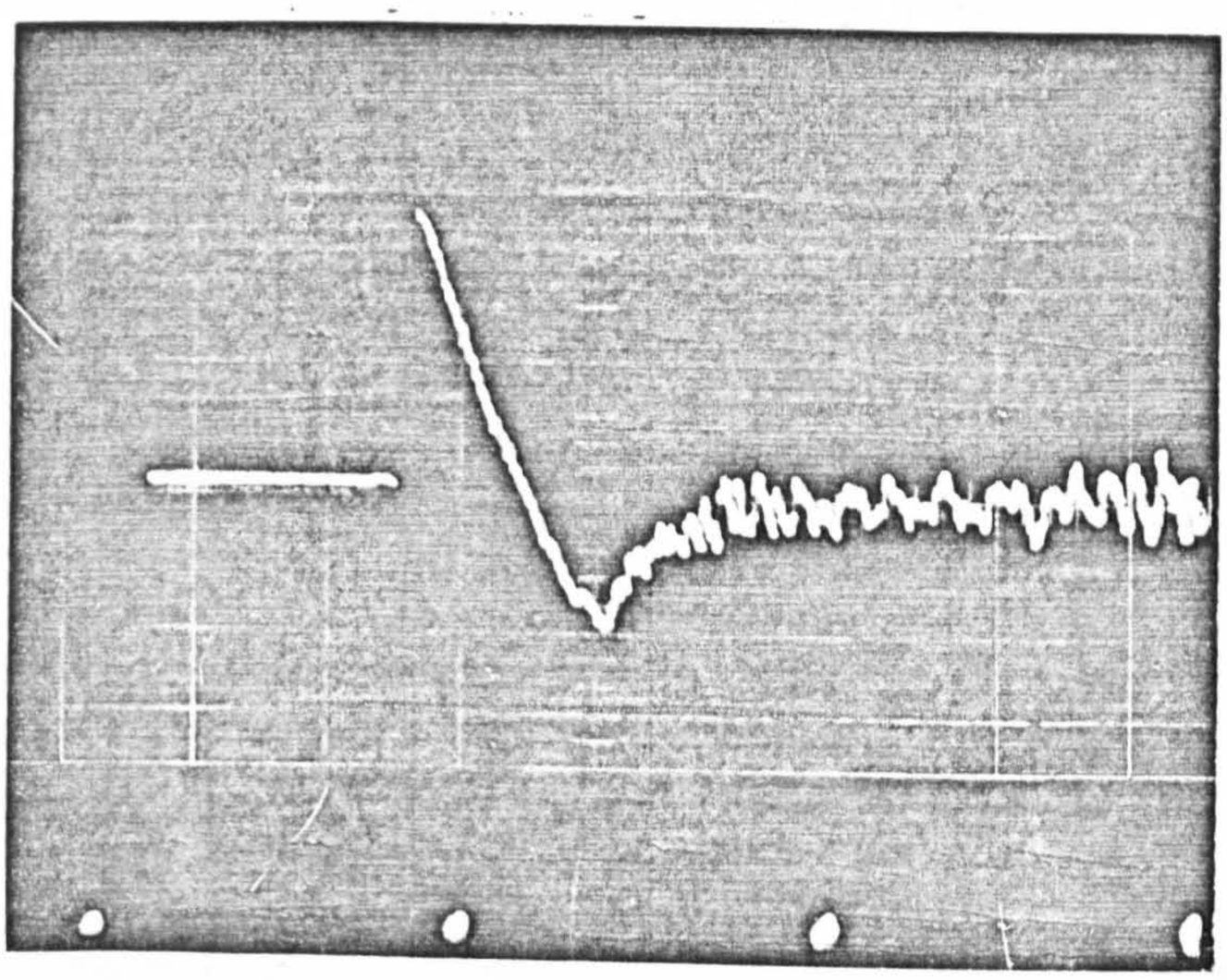

5.27(b)

FIGURE 5.28 - FIREWORK VARIABILITY

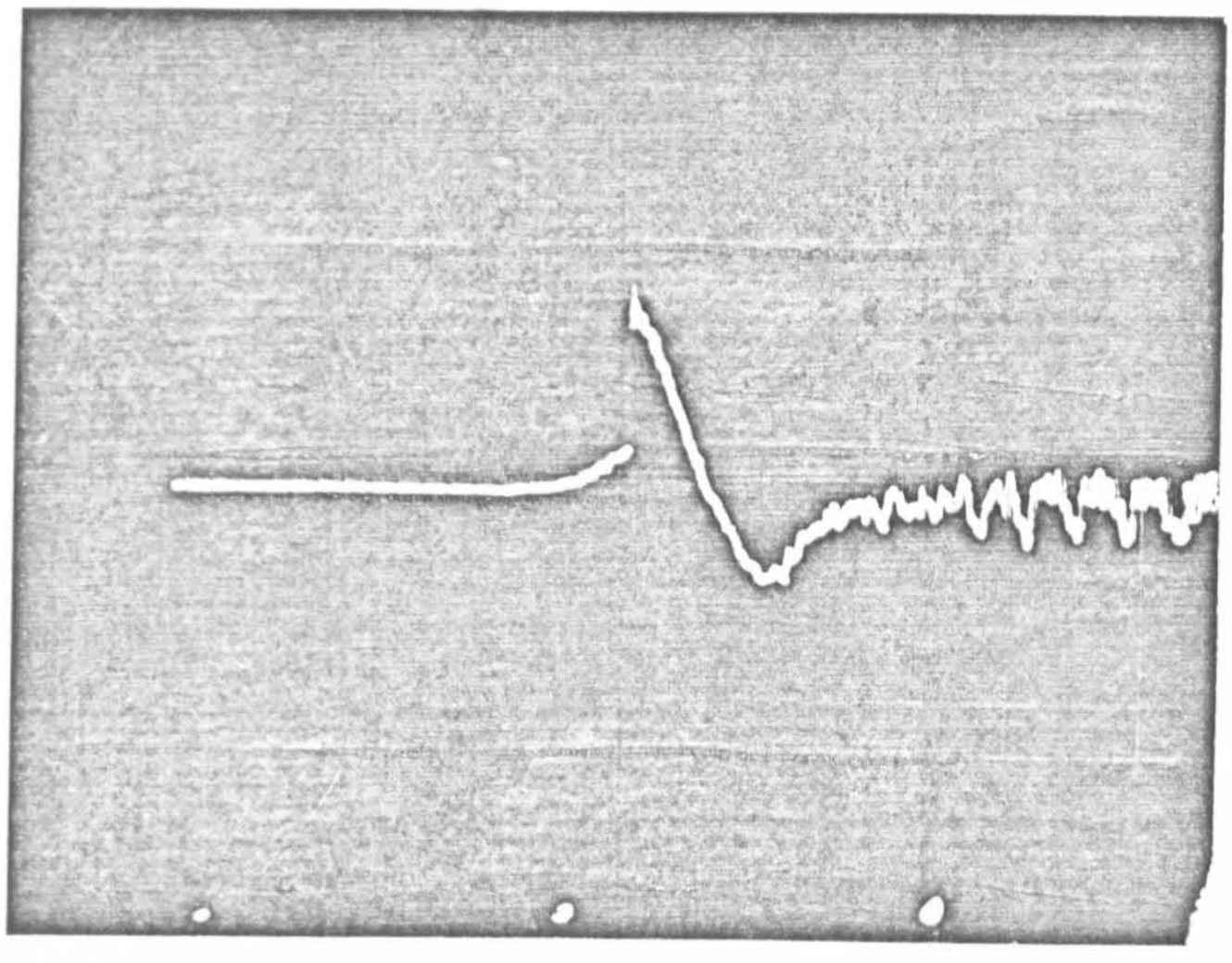

5.28(a)

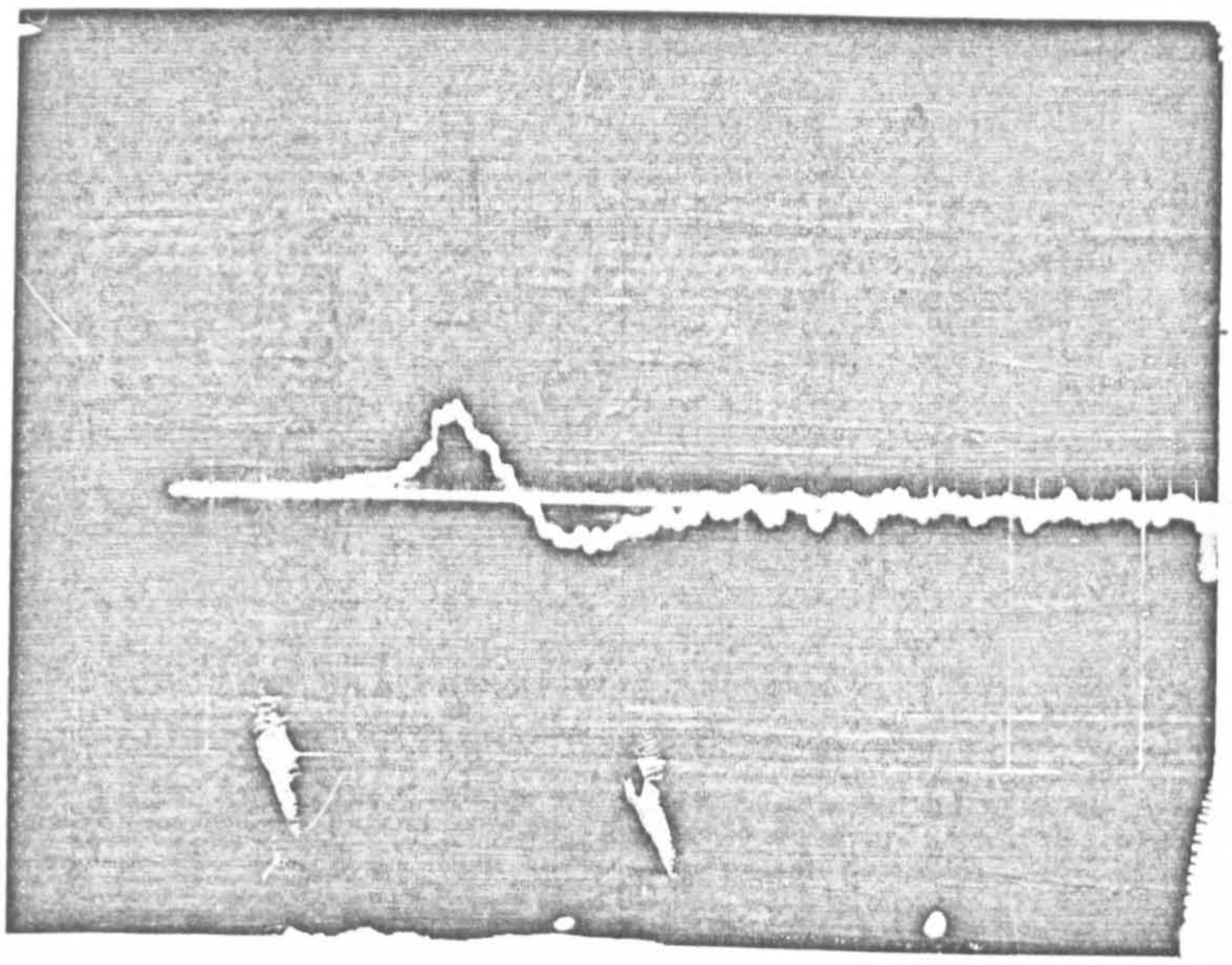

5.28(b)

FIGURE 5.28 - FIREWORK VARIABILITY

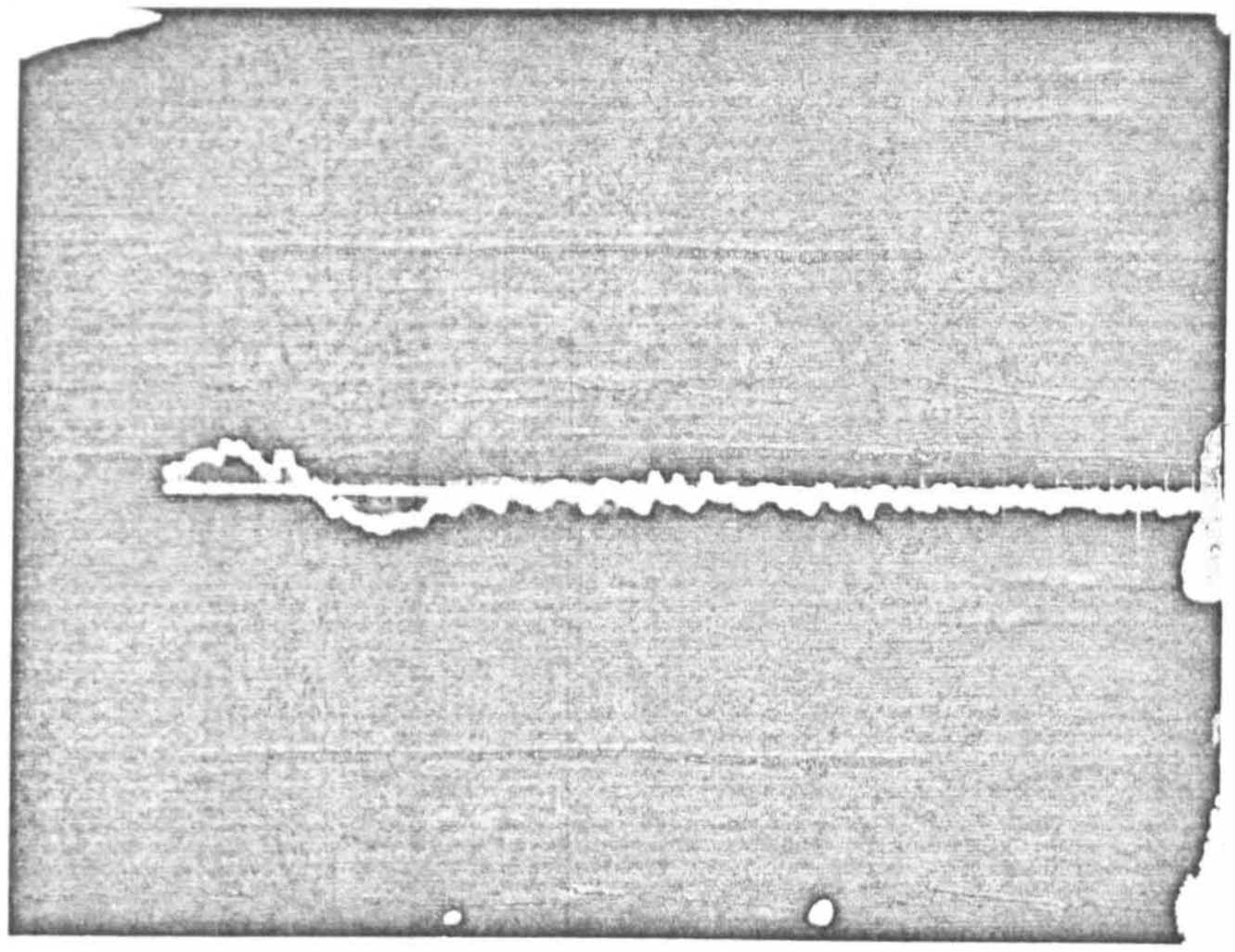

5.28(c)

FIGURE 5.29 - SHOCK REFLECTION

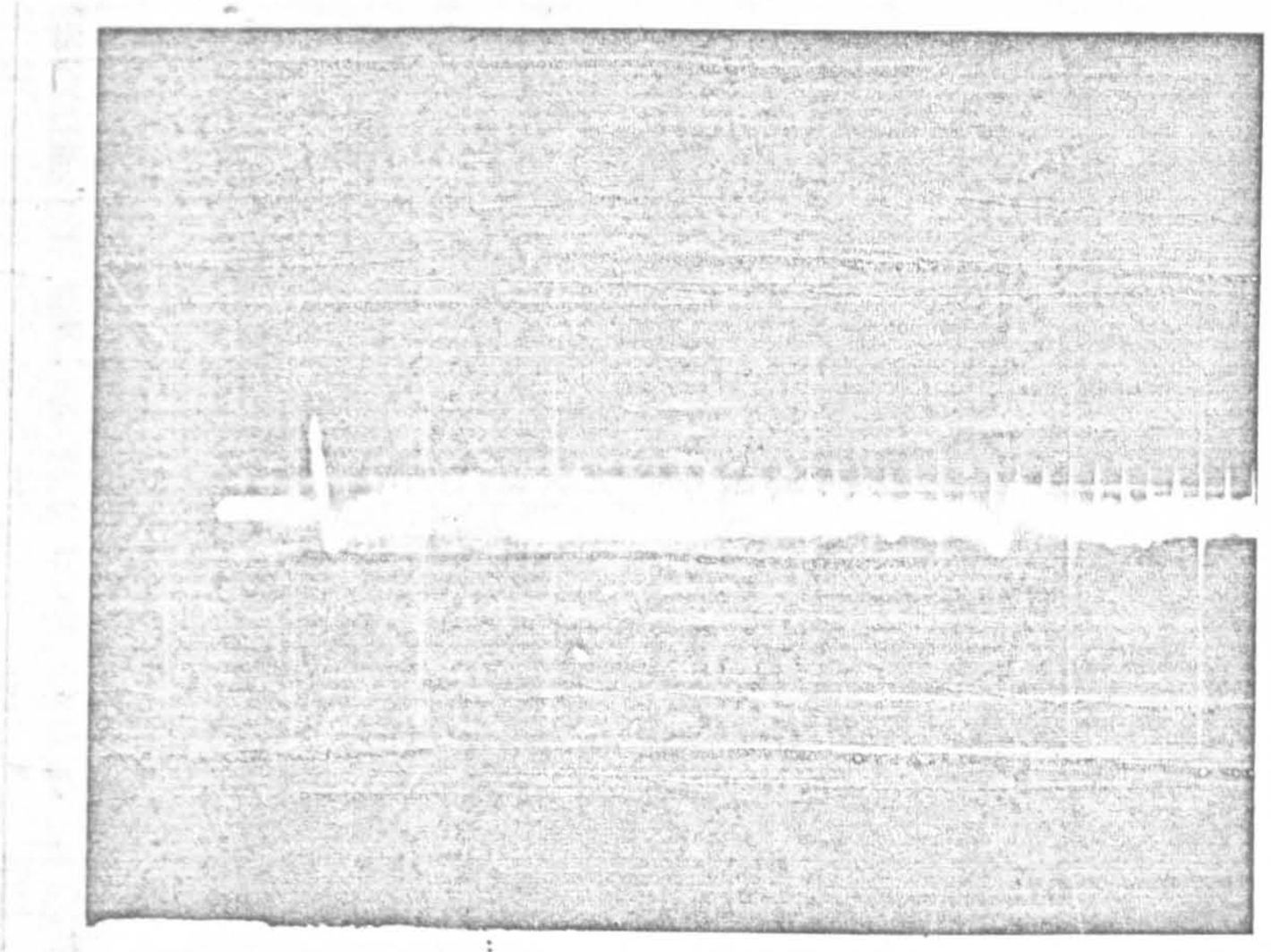

FIGURE 5.30 - ACCELEROMETER ON MAIN SHOCK TUBE

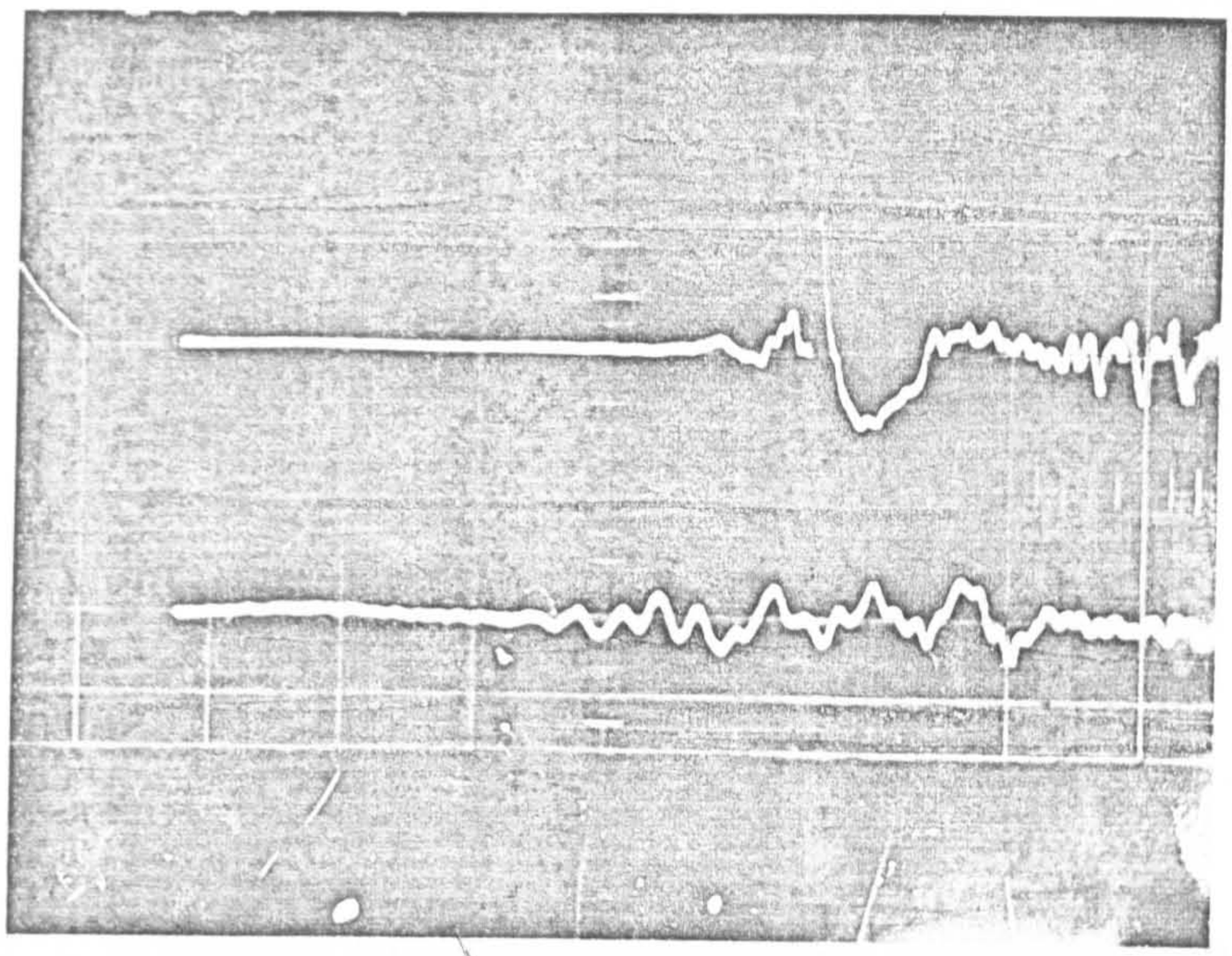

Upper Trace:- Pressure Wave

Lower Trace:- Accelerometer on Main Shock Tube.

FIGURE 5.31 - ACCELEROMETER ON END SECTION OF SHOCK TUBE

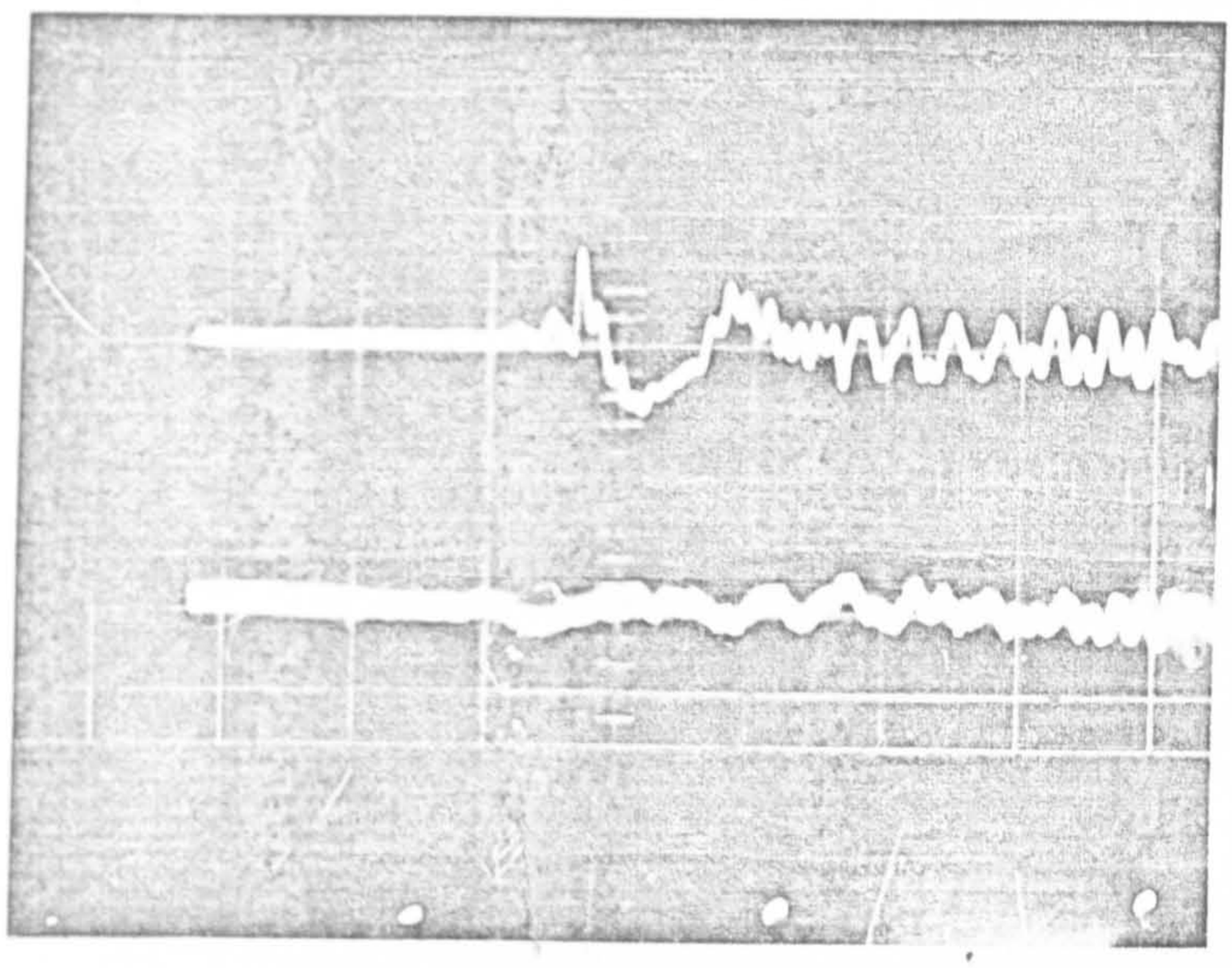

Upper Trace:- Pressure Wave

Lower Trace:- Accelerometer on end section of shock tube.

FIGURE 5.32 - EXPERIMENTAL PRESSURE AND STRAIN TIME HISTORY

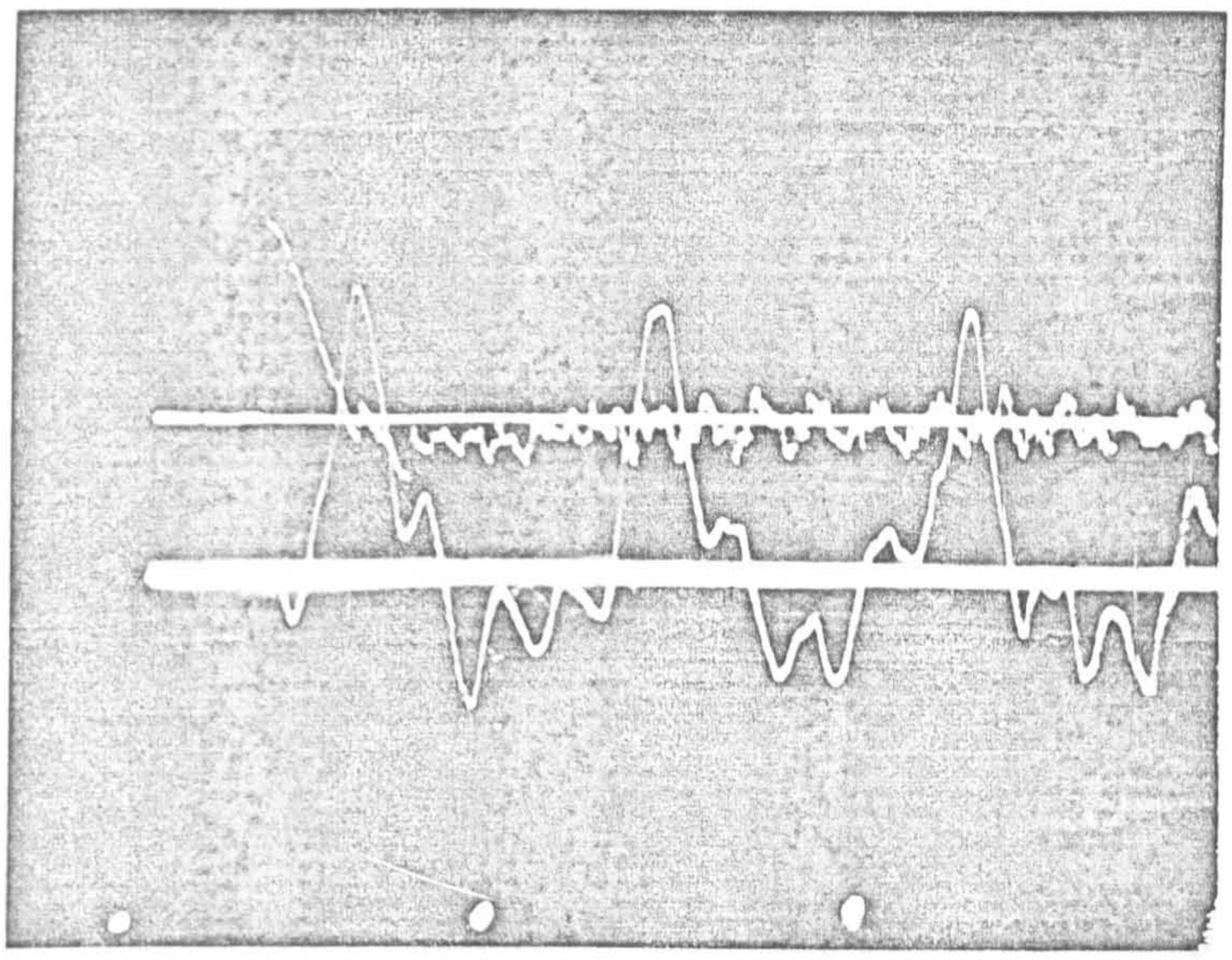

Upper Trace:- Pressure Wave

Lower Trace:- Resultant strain at panel centre along major axis.

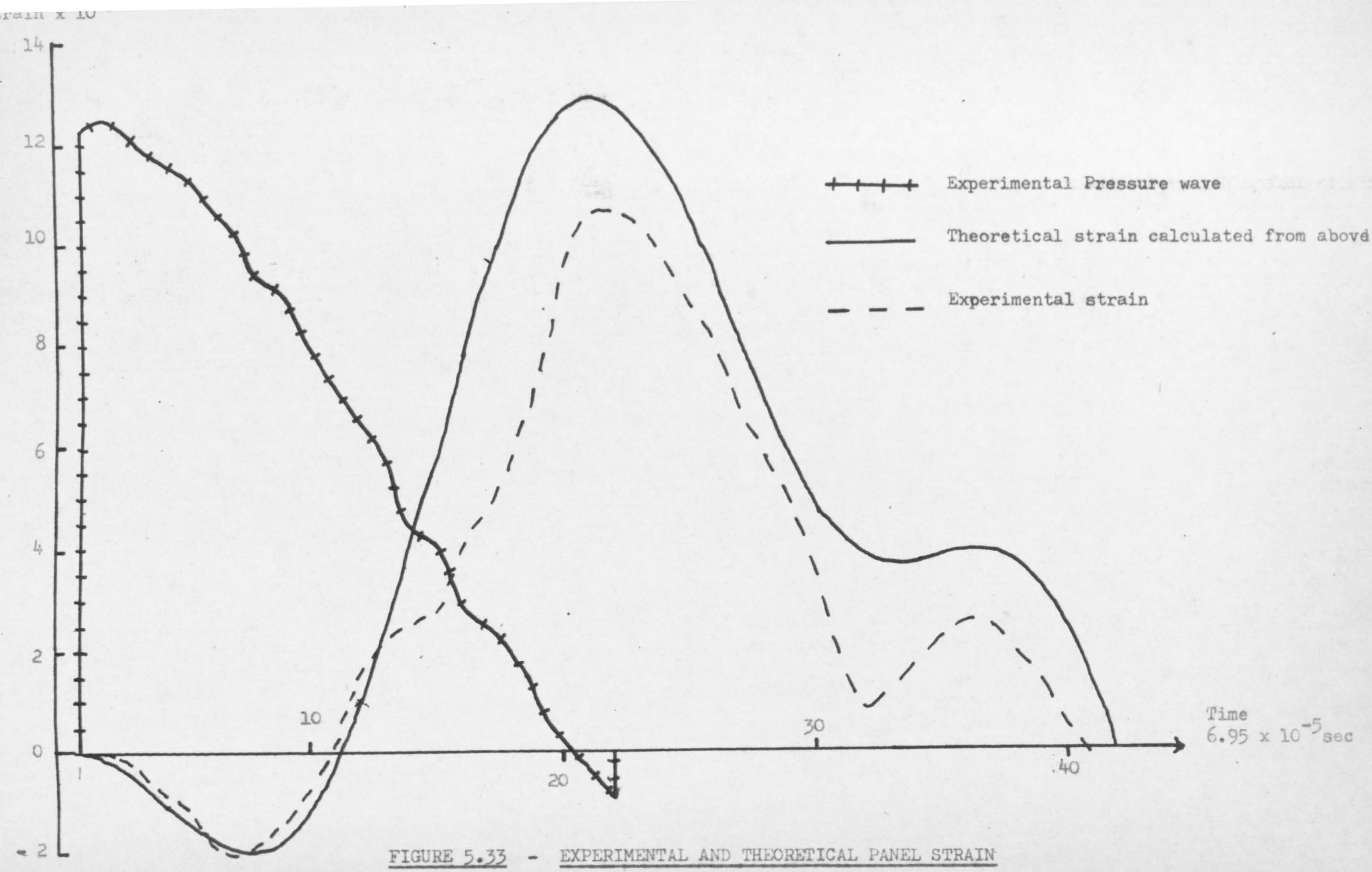

FIGURE 5.33 - EXPERIMENTAL AND THEORETICAL PANEL STRAIN

FIGURE 6.1 - THE PANEL CAVITY THEORETICAL MODEL

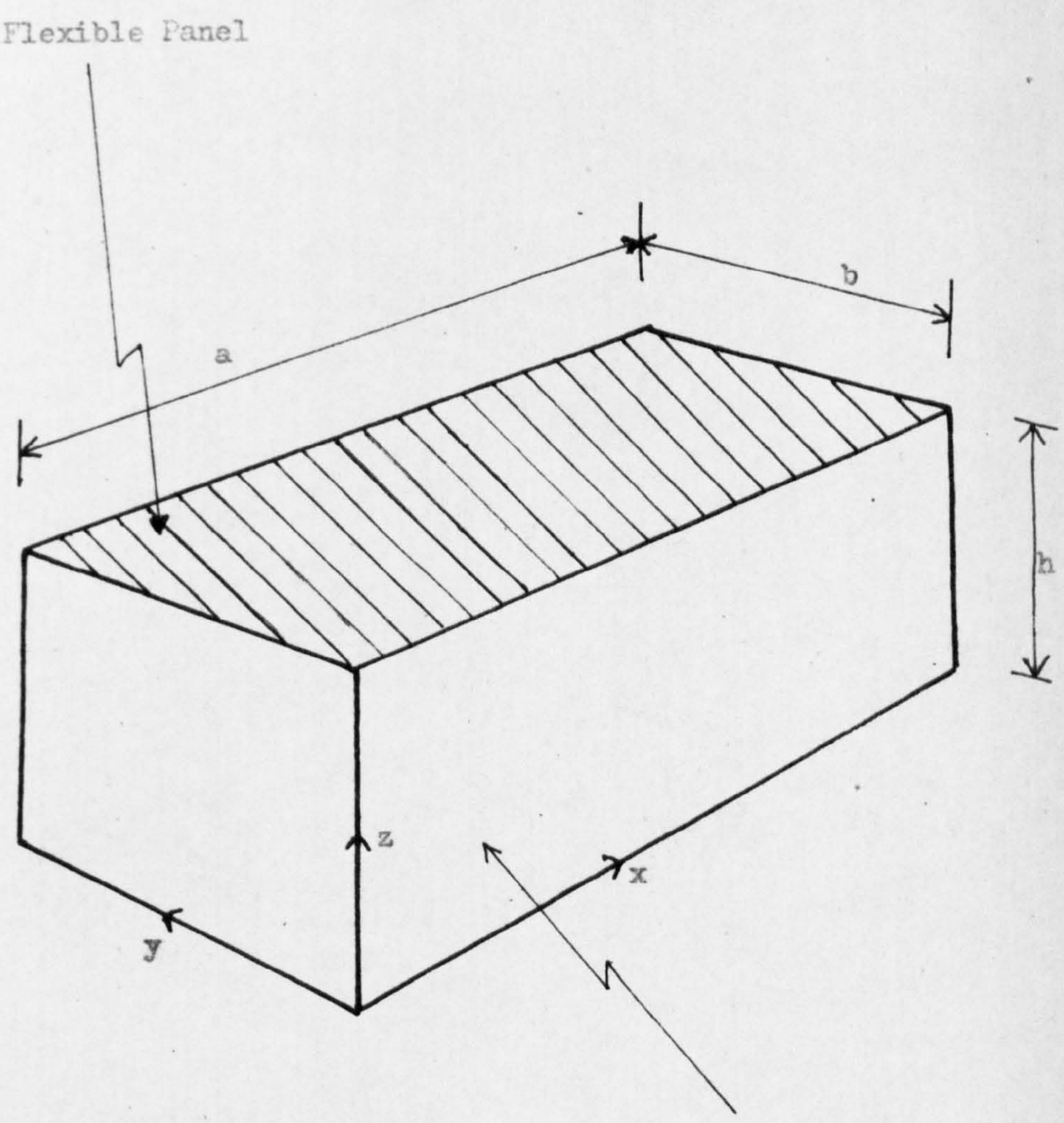

FIGURE 6.2 - THE EXPERIMENTAL ADJUSTABLE CAVITY

FIGURE 6.3 - THE EFFECTS OF A CAVITY UPON THE PANELS FUNDAMENTAL FREQUENCY

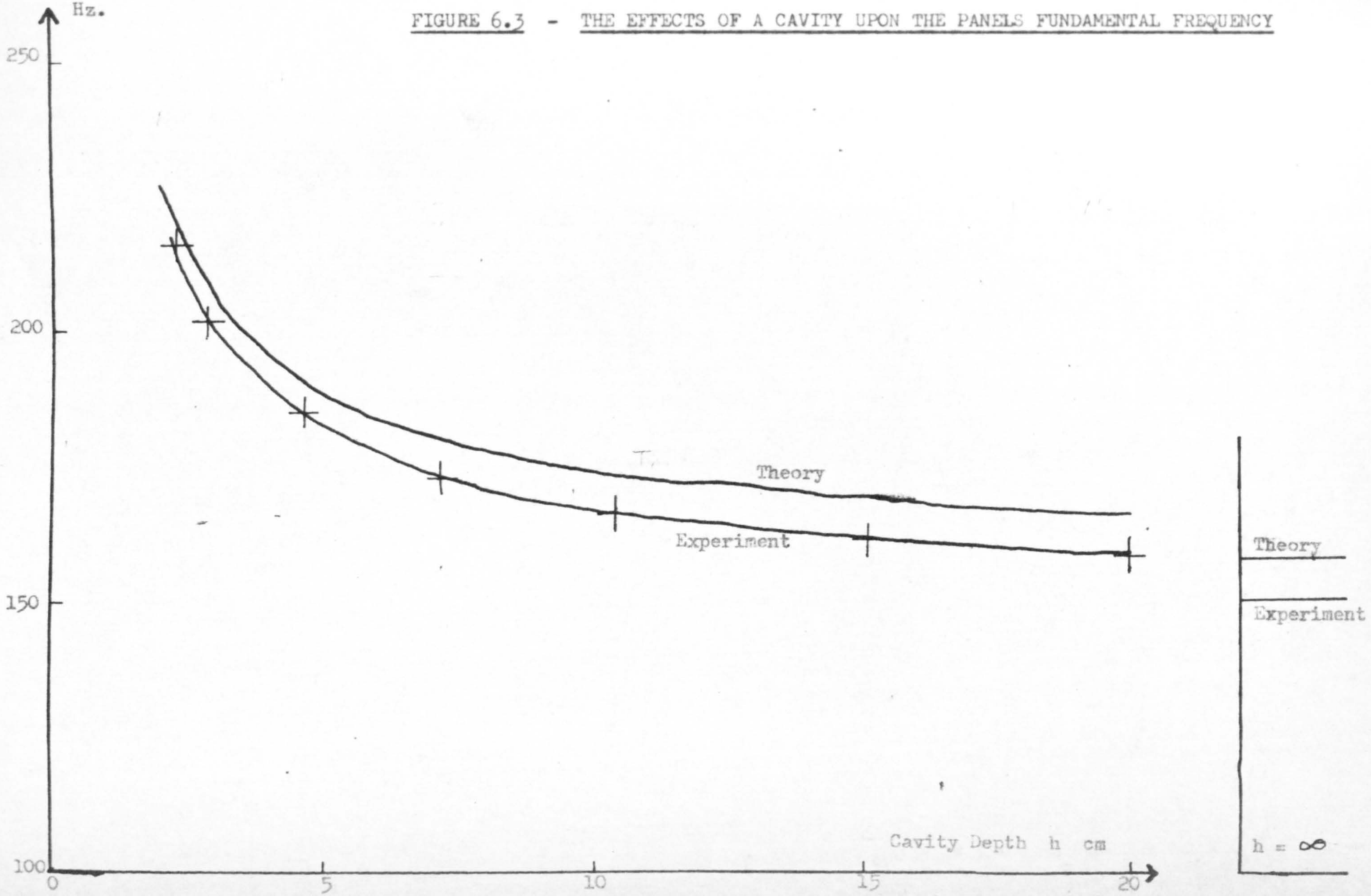

FIGURE 6.4 - EXPERIMENTAL PRESSURE AND STRAIN TIME HISTORIES WITH A 2.9cm CAVITY

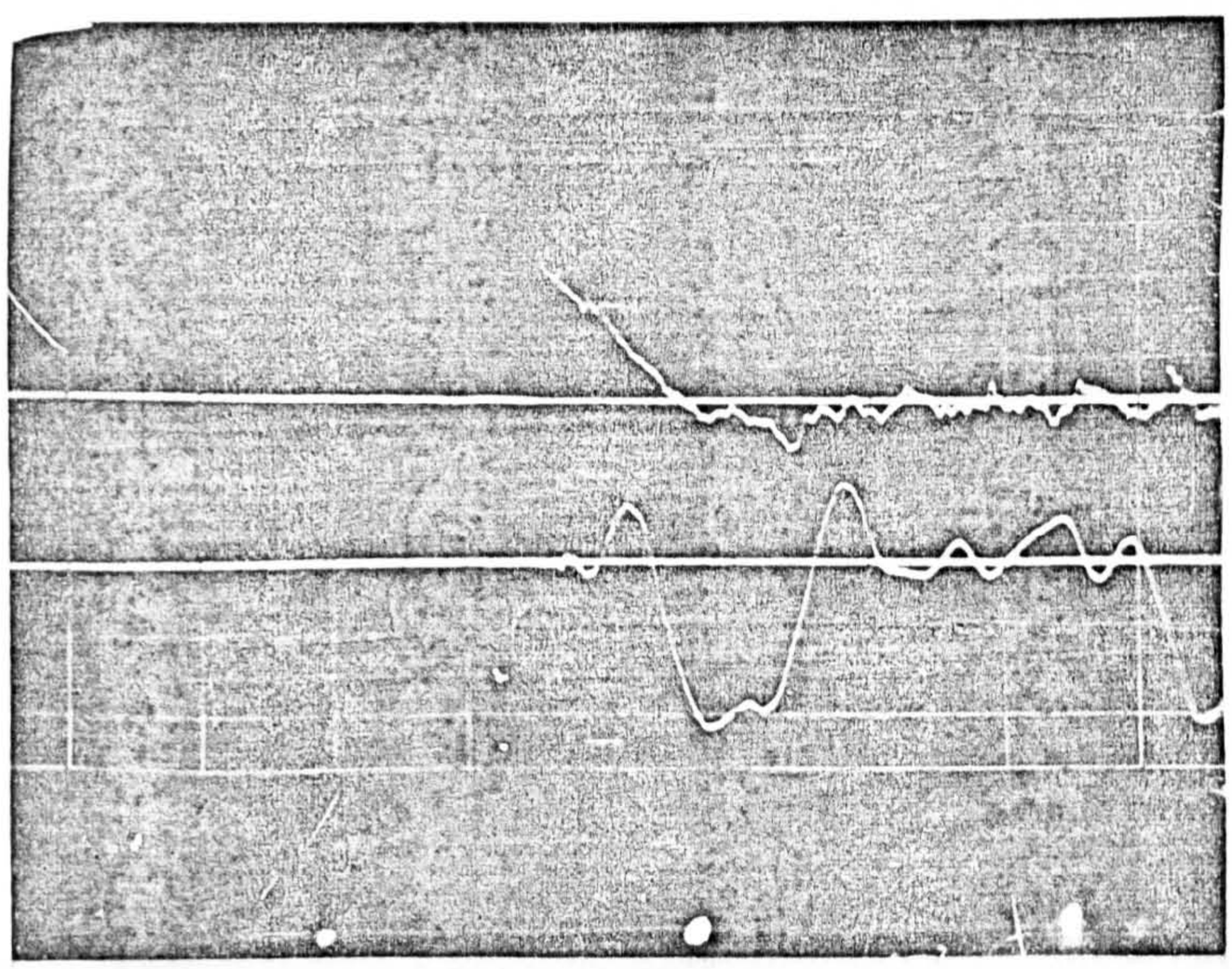

FIGURE 6.5 - PANEL STRAIN WITH A 2.9 cm CAVITY

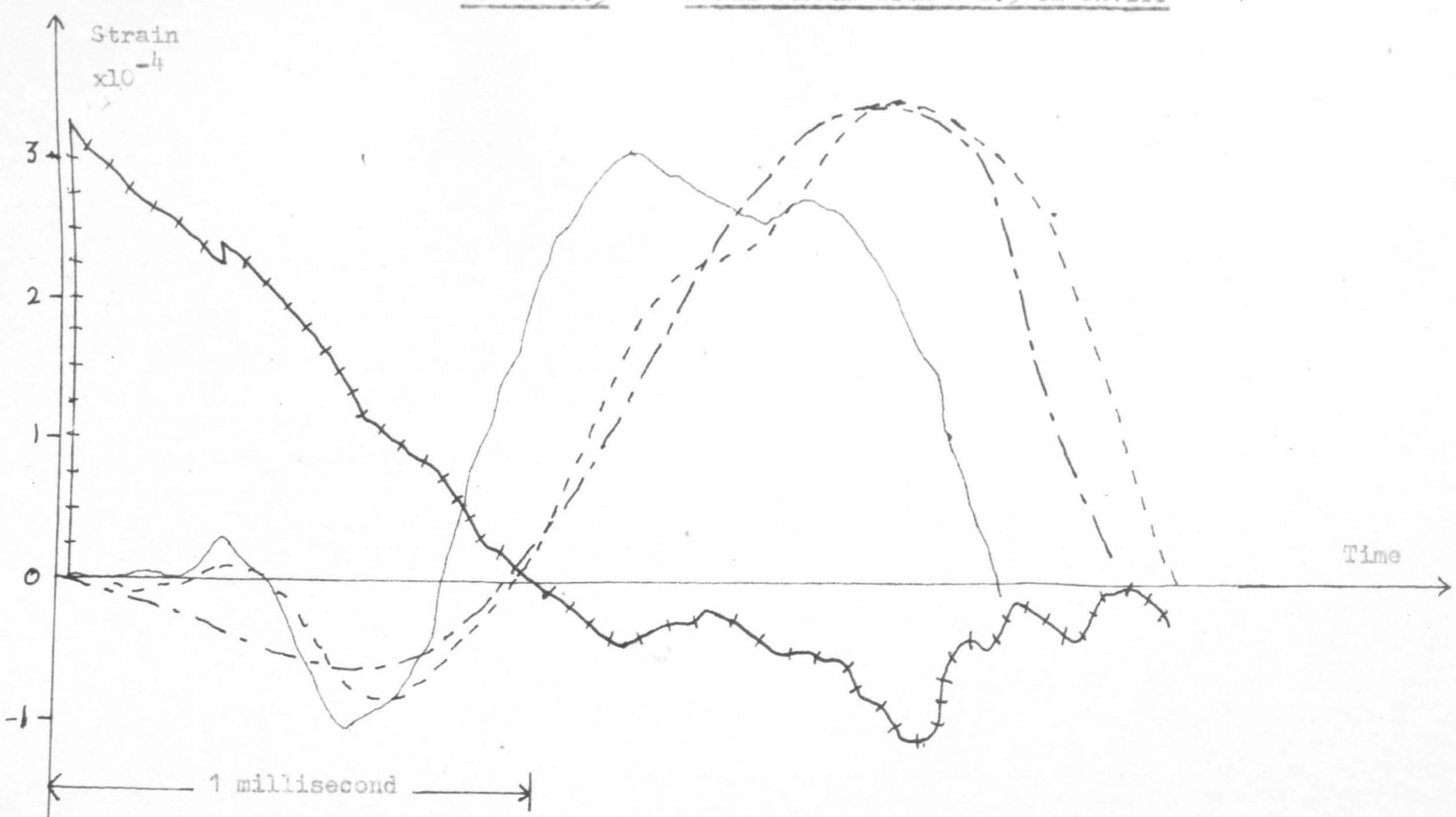

J. Sound Vib. (1969) 9 (1), 145–146

LETTERS TO THE EDITOR

COMMENTS ON "MEASUREMENT OF TRANSMISSION LOSS USING VIBRATION TRANSDUCERS"

In a recent paper Utley and Mulholland [1] described a method of transmission loss measurement using vibration transducers. We should like to make some further comments on this subject.

First, on page 419, the previous workers make the assumption that the sound energy falling on a unit area of wall per second should be

$$E_f = E_0 \text{ antilog } (L_1/10)$$

where L_1 is the measured sound level in the transmission room and E_0 is "the reference energy level", which we assume to mean the standard reference energy flux of 10^{-16} W/cm^2. They state that this is the simplest assumption available to apply to a fairly empirical theory. However, we consider that a better assumption would be to apply the normal diffuse field correction factor of $\frac{1}{4}$ and thus allow the incident flux to be

$$E_f = \frac{E_0}{4} \text{ antilog } (L_1/10).$$

This would alter Utley and Mulholland's first equation for τ to

$$\tau = 4(\tfrac{1}{2}\rho c U_0^2)/[E_0 \text{ antilog } (L_1/10)],$$

a reduction in estimated transmission loss of 6 dB.

The effect of such a reduction is to reduce the estimated transmission loss to between 10 and 15 dB below the measured value. Thus, there is no longer any agreement between the measured value of transmission loss and the value predicted by applying measured vibration amplitudes to the above formula. Further tests have shown that in general the transmission loss estimated by our formula is up to 15 dB below the measured value below the coincidence frequency but that at and above the coincidence frequency the two values are in agreement [Figure 1, curves c and d]. This has led to the idea of a "radiation efficiency" that is small below coincidence where the panel wavelength is shorter than that of the corresponding acoustic waves, rising to unity at and above the coincidence frequency.

The above theory may be loosely termed the piston theory. By carrying out a computation similar to that described in the latter part of reference 1 it is possible to calculate the amplitude of panel vibration predicted by the "mass law" theory. This value used in the piston theory gave a value of transmission loss 3 dB higher than the value predicted directly from mass law [Figure 1, curves a and b].

Our results show that such a calculated value of transmission loss should be 3 dB above the directly calculated mass law value. However, in the same paper the authors observe that the measured vibration amplitude is up to 15 dB greater than it should be according to the mass law, and so the measured values of transmission loss using the above method should be 12 dB below mass law.

It is seen that this is in fact the case below coincidence and so "low frequency discrepancy" reported by the previous workers is worse than originally suspected, but this can now be

explained. The fact that observed vibration amplitudes are higher than expected has been explained by Crocker and Price [2] using modal energy method theories developed by Lyon and Maidanik [3, 4]. The inevitable conclusion to be drawn here is that except in cases where

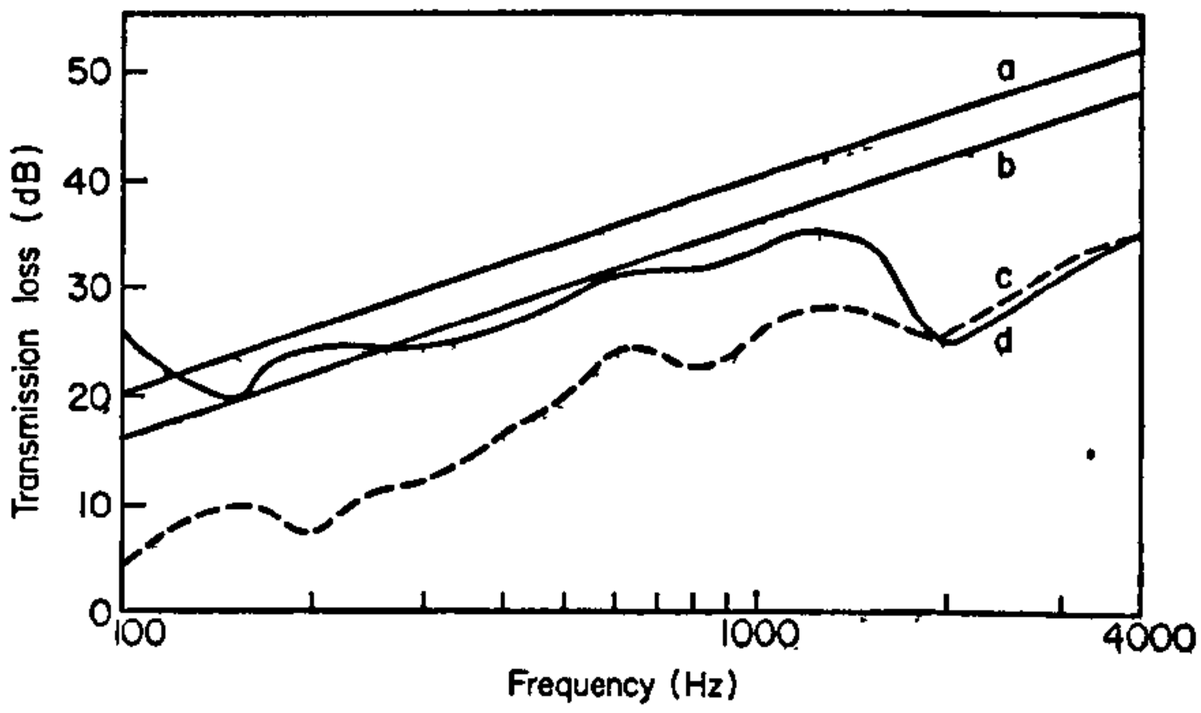

Figure 1. The transmission loss of a ¼ in. aluminium panel. (a) Mass law calculation of theoretical panel velocity applied in piston theory; (b) direct mass law calculation; (c) experimental panel velocity applied in piston theory; (d) airborne measurement (B.S. 2750).

one can be certain to be working above the coincidence frequency [the work reported by Ward (BBC Report No. B.078) on brick walls is an example of this], "membrane" theories of transmission loss that ignore panel size effects are erroneous and should be discarded in favour of the new theories.

Department of Building Science,
The University of Liverpool,
P.O. Box 147,
Liverpool, England

R. R. HUDSON
K. A. MULHOLLAND

Received 4 *October* 1968

REFERENCES

1. W. A. UTLEY and K. A. MULHOLLAND 1967 *J. Sound. Vib.* **6**, 419. Measurement of transmission loss using vibration transducers.
2. M. J. CROCKER and A. J. PRICE 1969 *J. Sound Vib.* **9**. Sound transmission using statistical energy methods.
3. H. L. LYON and G. MAIDANIK 1962 *J. acoust. Soc. Am.* **34**, 623. Power flow between linearly coupled oscillators.
4. G. MAIDANIK 1962 *J. acoust. Soc. Am.* **34**, 809. Response of ribbed panels to reverberant acoustic fields.

ABSTRACT

The purpose of the work reported in this thesis is to give a satisfactory theoretical analysis of the problem of sound transmission through finite single and double panel structures. The effects of panel size, damping and stiffness are accounted for in the theory and in the double panel system the effect of absorbing material in the air cavity is also allowed for.

In the first part of this thesis existing theories for sound transmission through infinite panel systems are reviewed and in some cases extended. Later, sound radiation from finite panels is studied and the results are then applied to the problem of sound transmission through finite single and double panels using a statistical energy method of analysis. Throughout this work direct comparison is made between theoretical predictions and experiment wherever possible. Existing problems are defined and suggestions are made of the direction in which future work might proceed.

J. Sound Vib. (1967) **6** (1) 163

LETTERS TO THE EDITOR

EVALUATION OF INVERSE COTHANGENT OF COMPLEX ARGUMENT FOR USE IN TRANSMISSION LOSS THEORY

When calculating the transmission loss of multiple wall structures in random incidence fields, it is necessary to use numerical analysis to perform the complicated integrals involved.

When employing the theory of Beranek and Work [1], the inverse cothangent of a complex argument must be found in order to solve the equations for the transmission loss. This complex argument is given by the ratio

$$Z = \frac{\text{Complex terminating impedance}}{z_o}$$

zo = characteristic impedance of the medium carrying the incident sound. It can be seen that $|Z|$ will be either greater than or less than unity in roughly equal proportions.

In short it is necessary to solve the equation

$$Z' = \text{arcoth}\,(Z),$$

i.e.

$$x+jy = \text{arcoth}\,(A+jB) \qquad (1)$$

for $|Z|$ lying anywhere on the complex plane.

Nonograms of complex hyperbolic functions [2] for use in this context do exist, but for random incidence fields it is necessary to compute many values of arcoth(Z) for each value of the mean transmission loss evaluated. It is, therefore, essential to have available numerical methods for solving equations (1).

For $|Z| > 1$ the following rapidly converging series may be used:

$$Z' = \frac{1}{Z}+\frac{1}{3Z^3}+\frac{1}{5Z^5}+\ldots, \text{etc.}$$

But it appears that no equivalent series exists when $|Z| < 1$. In this case, which often occurs in practice, it is necessary to resort to numerical methods. It can be shown that equation (1) reduces to the following non-linear equations:

$$\cosh(x)\cos(y)+B\cosh(x)\sin(y)-A\sinh(x)\cos(y) = 0; \qquad (2)$$

$$\sinh(x)\sin(y)-B\sinh(x)\cos(y)-A\cosh(x)\sin(y) = 0. \qquad (3)$$

Equations (2) and (3) can be solved using linear interpolation methods, thus giving values of arcoth(Z) for $|Z| < 1$.

A procedure has been written in ALGOL 60 to evaluate arcoth (Z) for all $|Z| \neq 1$. Copies of this procedure are available either in print-out form or on eight channel paper tape in KDF 6/9 code. Copies will be sent on request.

A. J. PRICE
K. A. MULHOLLAND

Department of Building Science,
The University,
Liverpool,
England.

Received 27 February 1967

REFERENCES

1. L. L. BERANEK and G. A. WORK 1949 *J. acoust. Soc. Am.* **21**, 419. Sound transmission through multiple structures containing flexible blankets.
2. J. RYBNER 1955 *Nomogrammer Over Komplekse Hyperbolske Fonktioner*. Copenhagen: Jul. Gjellerups Forlag.

Reprinted from THE JOURNAL OF THE ACOUSTICAL SOCIETY OF AMERICA, Vol. 43, No. 6, 1432–1435, June 1968

Transmission Loss of Multiple Panels in a Random Incidence Field

K. A. MULHOLLAND, A. J. PRICE, AND H. D. PARBROOK

Department of Building Science, The University of Liverpool, Liverpool 3, England

In this paper, the method of predicting the transmission loss of multilayer panels first proposed by Beranek and Work is used and developed to the point where the method can be applied under conditions where sound is incident on the panel from any angle or from many angles simultaneously as in the random incidence field. Doubts expressed recently about the accuracy of the theory are removed, and the method is shown to be a powerful tool for the prediction of transmission loss.

INTRODUCTION

THERE are three theoretical methods of deriving an expression for the sound insulation provided by a multiple layer construction:

(1) The ray or multiple-reflection method (Mulholland and Parbrook[1]).

(2) The progressive-wave method (London[2]).

(3) The impedance-transfer method (Beranek and Work[3]).

The first method was used by two of the authors to investigate double panels with an air gap between them. The method was shown to give results identical with the other two more rigorous methods. The ray method is however not easily applicable to the case of insulation by finite thickness panels because the total internal reflection phenomenon results in imaginary directions for the rays. London's wave method, in which progressive solutions of the wave equation within the various layers of a multiple panel lead to a solution of the problem, must then be used. This involves the solution of $2N$ simultaneous equations (where N is the number of medium interfaces), and the method becomes unwieldy with multiple layered systems. The impedance-transfer method developed by Beranek and Work is easier to apply; in fact, with a little practice it is possible to write down expressions for the transmission loss of a wide range of panels of any degree of complexity without having to resort to algebra or analysis. Beranek and Work developed their method rigorously for the case of normal incidence waves only, and it is the purpose of this paper to show how this useful method can be extended to cover the case of oblique incidence waves and the more practical random incidence field.

I. APPLICATION OF BERANEK AND WORK METHOD TO SIMPLE PANELS

White and Powell[4] recently stated that the Beranek-Work method is not of practical use since it only gives an expression for the ratio of the pressure on the face of a panel to the pressure transmitted, which may yield an error of up to 6 dB for the transmission loss. To take a simple example, consider a wave at normal incidence to a septa of impedance $j\omega m$, such that the incident sound pressure is P_i, while the pressure on the face is P_f, and the pressure due to the transmitted wave is P_t. Using the Beranek–Work method, we find

$$P_f/P_t=(\rho c+j\omega m)/\rho c. \tag{1}$$

Beranek and Work state that the insulation is thus

$$TL_B=10\log[1+(\omega m/\rho c)^2], \tag{2}$$

whereas the mass law is

$$TL=10\log[1+(\omega m/2\rho c)^2]. \tag{3}$$

However, it is a simple matter to correct this apparent discrepancy by considering the ratio P_i/P_f.

For a surface of impedance Z, P_i/P_f is given by

$$P_i/P_f=(Z+\rho c)/2Z. \tag{4}$$

[1] K. A. Mulholland and H. D. Parbrook, J. Sound Vibration (to be published).
[2] A. London, J. Acoust. Soc. Am. 22, 270–279 (1950).
[3] L. L. Beranek and G. A. Work, J. Acoust. Soc. Am. 21, 419–428 (1949).
[4] P. White and A. Powell, J. Acoust. Soc. Am. 40, 821–832 (1965).

With the Beranek–Work method, Z is easily found for any set of panels; in the present case, $Z=\rho c+j\omega m$. Thus

$$P_i/P_f=(2\rho c+j\omega m)/2(\rho c+j\omega m); \tag{5}$$

whence, using Eqs. 1 and 4,

$$\frac{P_i}{P_f}=\left[\frac{\rho c+j\omega m}{\rho c}\right]\times\left[\frac{2\rho c+j\omega m}{2(\rho c+j\omega m)}\right]. \tag{6}$$

This gives a modified Beranek–Work transmission loss

$$TL_B{}^1=10\log[1+(\omega m/2\rho c)^2]. \tag{7}$$

This agrees with the mass-law expression. The objections raised by White and Powell are therefore invalid, and the Beranek–Work method can be accurately applied to all panel constructions.

II. EXTENSIONS OF BERANEK–WORK METHOD TO INTERFACE BETWEEN TWO MEDIA AT OBLIQUE INCIDENCE

If a ray of potential ϕ_i is incident on an interface of an angle θ in a medium ρ_1, there will be a ray of potential ϕ_t transmitted at an angle θ_2 in the second medium of density ρ_2. The angle θ_2 is given by

$$\theta_2=\arcsin[(c_2/c_1)\sin\theta_1]. \tag{8}$$

If $c_2>c_1\sin\theta_1$, then θ_2 will be complex[5]; the complex notation immediately gives this as an evanescent wave in the second medium. Using the continuity of pressure and surface velocity, the relation between ϕ_t and ϕ_i is found to be

$$\frac{\phi_i}{\phi_t}=\frac{\rho_2c_2\cos\theta_2+\rho_1c_1\cos\theta_2}{2\rho_1c_2\cos\theta_1}. \tag{9}$$

Now the entrance impedance normal to a surface at oblique incidence is found from

$$Z=\frac{P}{V_n}=\frac{j\omega\rho_2\phi}{jk_2\cos\theta_2\phi}=\frac{\rho_2c_2}{\cos\theta_2}. \tag{10}$$

Similarly, the exit impedance is $\rho_1c_1/\cos\theta_1$. If we apply the Beranek–Work method using these impedances, this gives $P_f/P_t=1$ (no boundary impedance) and

$$\frac{P_i}{P_f}=\frac{\rho_2c_2/\cos\theta_2+\rho_1c_1/\cos\theta_1}{2\rho_2c_2/\cos\theta_2}. \tag{11}$$

The resulting formula

$$\frac{P_i}{P_f}=\frac{\rho_2c_2\cos\theta_1+\rho_1c_1\cos\theta_2}{2\rho_2c_2\cos\theta_1} \tag{12}$$

is not identical with Eq. 9 since ϕ_i/ϕ_t is not P_i/P_t. Now $P_t=j\omega\rho_2\phi_t$ and $P_i=j\omega\rho_1\phi_i$; and therefore, from Eq. 12,

$$\frac{P_i}{P_t}=\frac{j\omega\rho_1\phi_i}{j\omega\rho_2\phi_t}=\frac{\rho_2c_2\cos\theta_1+\rho_1c_1\cos\theta_2}{2\rho_2c_2\cos\theta_1}, \tag{13}$$

which gives

$$\frac{\phi_i}{\phi_t}=\frac{\rho_2c_2\cos\theta_1+\rho_1c_1\cos\theta_2}{2\rho_1c_2\cos\theta_1}. \tag{14}$$

This equation is identical with Eq. 9, which implies that the Beranek–Work method can be usefully and accurately applied to this case. Of course, the transmission loss across the face is given by neither of these two expressions (Eqs. 9 and 12) but by the ratio of the incident and transmitted intensities given by

$$10\log\left[\frac{\rho_2}{\rho_1}\left|\frac{P_t}{P_i}\right|^2\right]=10\log\left[\frac{\rho_1}{\rho_2}\left|\frac{c_2\phi_t{}^2}{c_1\phi_i{}^2}\right|\right].$$

III. TRANSMISSION LOSS OF A THIN SEPTUM AT OBLIQUE INCIDENCE

Consider a wave incident on an interface at angle θ. Let the pressure of the incident wave be P_i and the pressures on either side of the interface be P_f and P_t, respectively.

A thin septum is commonly considered to have an impedance $j\omega m$; at oblique incidence this becomes $j\omega m\cos\theta$.

Repeating the arguments of Sec. II, we at once arrive at the following expressions:

$$\frac{P_t}{P_f}=\frac{\rho c}{\rho c+j\omega m\cos\theta}, \tag{15}$$

$$\frac{P_i}{P_f}=\frac{2\rho c+j\omega m\cos\theta}{2(\rho c+j\omega m\cos\theta)}, \tag{16}$$

$$\frac{P_i}{P_t}=1+\frac{j\omega m\cos\theta}{2\rho c}. \tag{17}$$

This is the usual mass-law expression.

IV. TRANSMISSION LOSS OF A MEDIUM OF FINITE THICKNESS

For both the Beranek–Work and for the London wave-matching methods, we can assume the following solutions of the wave equation within the three regions:

Region 1:

$$\phi_ie^{j(\omega t-k_1x\cos\theta_1-k_1y\sin\theta_1)}+\phi_ie^{j(\omega t+k_1x\cos\theta_1-k_1y\sin\theta_1)}, \tag{18}$$

Region 2:

$$A\cosh(-jk_2x\cos\theta_2+\Phi)e^{j(\omega t-k_2y\sin\theta_2)}, \tag{19}$$

[5] Because of this and other factors, it is assumed that *all* quantities in this paper except ω and ρ and the usual constants are complex. ω and ρ are chosen as real quantities because of degeneracy. It can be seen that computer programs based on this theory will need a wide range of complex-number subroutines, including sophisticated ones for inverse circular and hyperbolic functions. These have been developed in ALGOL 60 and are available on request.

Region 3:

$$\phi_t e^{j(\omega t - k_1 x \cos\theta_1 - k_1 y \sin\theta_1)}, \tag{20}$$

where $\theta_2 = \arcsin[(c_2/c_1)\sin\theta_1]$ or, more usefully:

$$\cos\theta_2 = [1 - (c_2/c_1)^2(1-\cos^2\theta_1)]^{\frac{1}{2}}.$$

Using the London method, the usual pressure- and velocity-matching conditions permit the following quantities to be set out after some labor:

$$P_i/P_t = 1, \tag{21}$$

$$\Phi = \operatorname{arcoth}(\rho_1 c_1 \cos\theta_2/\rho_2 c_2 \cos\theta_1), \tag{22}$$

$$P_2/P_1 = \cosh(jk_2 d\cos\theta_2 + \Phi), \tag{23}$$

$$P_f/P_2 = 1. \tag{24}$$

Now

$$Z_{face} = (\rho_2 c_2/\cos\theta_2)\coth(jk_2 d\cos\theta_2 + \Phi), \tag{25}$$

and hence

$$\frac{P_i}{P_f} = \frac{\rho_2 c_2 \coth(jk_2 d\cos\theta_2+\Phi)\cos\theta_1 + \rho_1 c_1 \cos\theta_2}{2\rho_2 c_2 \coth(jk_2 d\cos\theta_2+\Phi)\cos\theta_1}. \tag{26}$$

The Beranek–Work method allows us to write down all the above expressions directly without solving any simultaneous equations, provided that the entry and exit impedances $\rho c/\cos\theta$ are used.

Combining the equations or using Beranek–Work's method allows the following expression to be obtained for the pressure ratio across the whole septum:

$$\frac{P_i}{P_t} = \left[\frac{\rho_2 c_2 \coth(jk_2 d\cos\theta_2+\Phi)\cos\theta_1 + \rho_1 c_1 \cos\theta_2}{2\rho_2 c_2 \coth(jk_2 d\cos\theta_2+\Phi)\cos\theta_1}\right] \times \left[\frac{\cosh(jk_2 d\cos\theta_2+\Phi)}{\cosh(\Phi)}\right]. \tag{27}$$

V. ADDITION OF IMPERVIOUS THIN SEPTA TO LAYERS OF FINITE THICKNESS

Having demonstrated the application of the Beranek–Work method to the oblique incidence insulation of finite thickness panels, we now finally proceed to a combination of finite thickness layers and thin impervious septa, as depicted in Fig. 1. In Sec. III, it is demonstrated that by using an impedance $j\omega m\cos\theta$ it is possible to obtain an oblique incidence mass law by using the Beranek–Work method, but when an impervious septum is flanked by two different media, there are two different angles (θ_1 and θ_2) involved.

Hence the question arises: Do we use θ_1 or θ_2 or some combination of the two when including the impedance of a septum? This question can be answered by solving for the pressure ratio across such septa using the London pressure- velocity-matching method and observing the result.

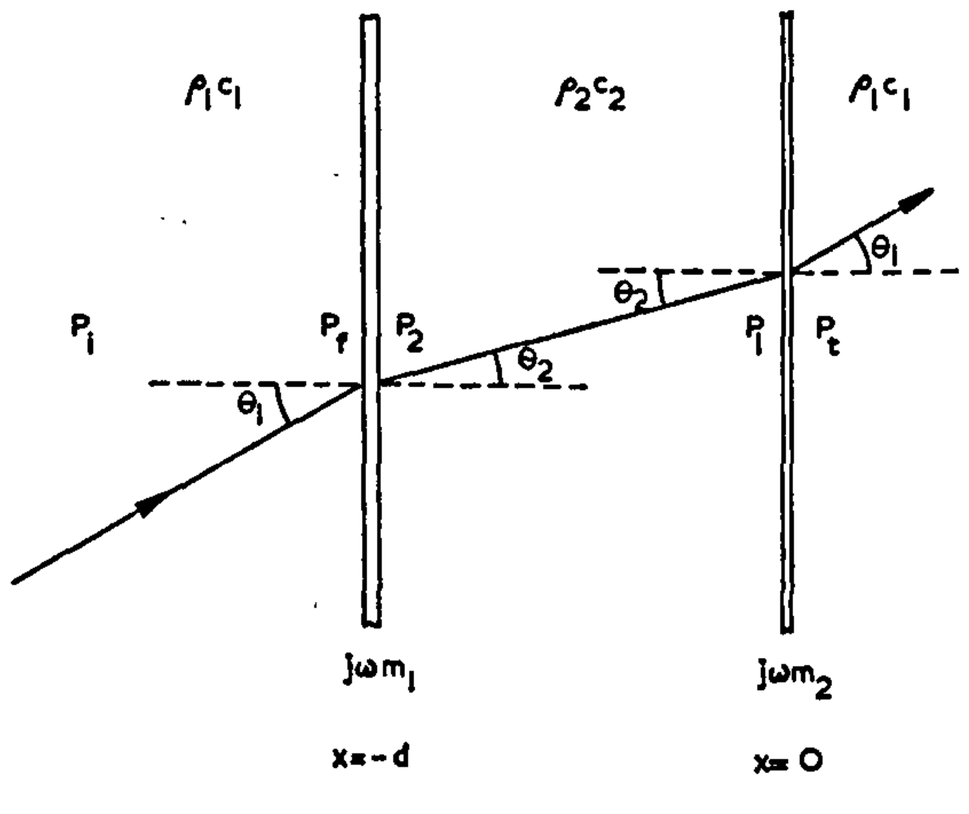

FIG. 1. Schematic diagram of the transmission process through a finite thickness panel with thin impervious septa on both faces.

Using the wavefunctions of Sec. IV, at $x=0$, we find (normal velocities equal, put $y=t=0$)

$$jk_2\cos\theta_2 A\sinh(\Phi) = jk_1\cos\theta_1\phi_t \tag{28}$$

and

$$j\omega\rho_2 A\cosh(\Phi) - j\omega\rho_1\phi_t = j\omega m_1 jk_1\cos\theta_1\phi_t. \tag{29}$$

By dividing, we find

$$\rho_2 c_2\coth(\Phi) = \frac{(j\omega m_1\cos\theta_1+\rho_1 c_1)\cos\theta_2}{\cos\theta_1}, \tag{30}$$

giving

$$\Phi = \operatorname{arcoth}\left[\frac{(j\omega m_1\cos\theta_1+\rho_1 c_1)}{\rho_2 c_2}\cdot\frac{\cos\theta_2}{\cos\theta_1}\right]. \tag{31}$$

We also note that

$$\frac{A}{\phi_t} = \frac{k_1\cos\theta_1}{k_2\cos\theta_2}\cdot\frac{1}{\sinh(\Phi)}; \tag{32}$$

and the pressure ratio

$$\frac{P_1}{P_t} = \frac{j\omega\rho_2 A\cosh(\Phi)}{j\omega\rho_1\phi_t} = \frac{\rho_2 k_1\cos\theta_1\coth\Phi}{\rho_1 k_2\cos\theta_2}, \tag{33}$$

which yields

$$P_1/P_t = (j\omega m_1\cos\theta_1+\rho_1 c_1)/\rho_1 c_1. \tag{34}$$

It can now be seen that Eqs. 31 and 34 could both be written down directly using the Beranek–Work method, provided that the impedance of the wall septum at $x=0$ was taken as $j\omega m\cos\theta_1$. The wall impedance is a function, not of the angle of incidence as might be expected, but of the angle of refraction. Equation 31 is found by direct comparison of impedance at $x=0$ before the interface, thus:

EXIT IMPEDANCE $= \rho_2 c_2\coth\Phi/\cos\theta_2$
$=$ INPUT IMPEDANCE $= j\omega m_1\cos\theta_1+\rho_1 c_1/\cos\theta_1$,

giving, as before,

$$\Phi=\operatorname{arcoth}\left[\frac{(j\omega m_1\cos\theta+\rho_1c_1)}{\rho_2c_2}\cdot\frac{\cos\theta_2}{\cos\theta_1}\right]. \quad (35)$$

The pressure ratio is found from

$$P_1/P_i=(\rho_1c_1+j\omega m_1\cos\theta_1)/\rho_1c_1, \quad (36)$$

which is identical to Eq. 34.

Similarly, if the equations of continuity at $x=-d$ are worked through, the following expressions for face impedance and P_f/P_2 are obtained.

$$Z_{face}=\frac{\rho_2c_2\coth(jk_2d\cos\theta_2+\Phi)+j\omega m_2\cos\theta_2}{\cos\theta_2} \quad (37)$$

and

$$\frac{P_f}{P_2}=\frac{\coth(jk_2d\cos\theta_2+\Phi)+j\omega m_2\cos\theta_2}{\coth(jk_2d\cos\theta_2+\Phi)}. \quad (38)$$

Both these equations can be written down using the Beranek–Work idea provided that the wall impedance is taken as $j\omega m_2\cos\theta_2$.

Note that again the *refracted* angle is used to modify the mass impedance of the wall.

Familiarity with the concepts explained by Beranek and Work, together with the few simple rules concerning the use of θ developed in this paper, makes it possible to write down directly expressions for the oblique-incidence sound insulation of any combination of impervious septa, air gaps, and uniform layers of finite thickness. As an example, the complete expression for a double sandwich panel such as is discussed in the Introduction is

$$\frac{P_i}{P_t}=\left[\frac{\rho_1c_1\cos\theta_2+(\rho_2c_2\coth(jk_2d\cos\theta_2+\Phi)+j\omega m_2\cos\theta_2)\cos\theta_1}{2\cos\theta_1\coth(jk_2d\cos\theta_2+\Phi)}\right]\times\left[\frac{\cosh(jk_2d\cos\theta_2+\Phi)}{\cosh(\Phi)}\right]\left[\frac{\rho_1c_1+j\omega m_1\cos\theta_1}{\rho_1c_1}\right], \quad (39)$$

$$\Phi=\operatorname{arcoth}\left[\frac{(j\omega m_1\cos\theta_1+\rho_1c_1)}{\rho_2c_2}\cdot\frac{\cos\theta_2}{\cos\theta_1}\right]. \quad (40)$$

VI. RANDOM INCIDENCE FIELDS

Now that we have a method for finding the transmission coefficient $\tau(\theta)$, it is, in theory, possible to obtain an expression for the random incidence transmission coefficient $\bar{\tau}$ using the usual integral

$$\bar{\tau}=\int_0^{\theta_2}\tau(\theta)\cos\theta\sin\theta d\theta\Big/\int_0^{\theta_2}\cos\theta\sin\theta d\theta. \quad (41)$$

Such an integration is not possible analytically; but it is a straightforward task to perform it numerically with a computer. The results thus obtained bear direct comparison with laboratory measurement.

J. Sound Vib. (1969) 9 (3), 454–468

STRUCTURAL RESPONSE TO SONIC BOOMS

M. J. CROCKER AND R. R. HUDSON

Department of Building Science, University of Liverpool, Liverpool 3, *England*

(*Received* 27 *May* 1968)

The response of a damped mass spring system to an N wave is examined. In particular, the dependence of the response upon structural damping, upon the ratio of total to positive phase duration, and upon the rise time of the N wave is determined. The cases of response to N waves with shock reflection and to repeated N waves are also studied. The results in this paper are given in terms of dynamic magnification factors which are expressed as functions of the non-dimensionalized frequency $f\tau$. A final curve of dynamic magnification factor against $f\tau$ is produced which envelopes the effects of varying positive to negative phase duration, rise time, shock reflections and structural damping. This curve may be used to determine the possibility of damage due to overflights of a supersonic transport.

1. INTRODUCTION

A supersonic aircraft in flight produces a pressure disturbance on the ground which is commonly known as a sonic boom or bang. In the case of a supersonic transport flying at 70,000 ft, the sonic boom may be experienced in a corridor up to about 100 miles wide on the ground under the flight path of the aircraft. Two of the undesirable effects produced by the sonic boom are the annoyance it causes to people and the effect it has upon buildings. In this paper only the response of structures to sonic booms is considered.

Typical pressure-time histories [1] of sonic booms measured at ground level are shown in Figure 1 for small, medium and large aircraft flying at their cruising altitudes. The total durations (2τ) of the sonic booms shown are of the order of 0·1, 0·2 and 0·3 sec, respectively, while the overpressure is about 2 to 3 lb/ft^2. The time histories in Figure 1 are seen to have the shape of a capital letter N. For this reason sonic booms are sometimes termed N waves. Unless an aircraft flies supersonically at low altitude, it is unlikely that the pressure wave produced will be strong enough to cause fracture in any of the structural members of a building. However, if a building component such as a window has a built-in stress then on occasions when the sonic boom is magnified the extra stress induced by the boom can cause failure. Magnification of the sonic boom may be caused by reflection from the ground or walls, by acceleration or manoeuvring of the aircraft or by atmospheric focusing. Even if structural failure does not occur, sonic booms will cause building members to vibrate and rattle which is annoying and psychologically undesirable.

For these reasons it is necessary to understand how structures respond to N waves and to know how the response of a structural member depends upon the structural and sonic boom parameters. With this knowledge it may be possible to estimate the likelihood of damage to windows due to supersonic overflights and to make recommendations to minimize the response of building structural members to sonic booms.

In this paper, a structural member is considered to be represented by a mass-spring-damper system and the sonic boom is represented by an idealized mathematical expression. The sonic

boom and structural parameters are varied one at a time in order to find the dependence of the structural response upon the variations of each parameter.†

Sonic booms are by no means repeatable and the pressure-time history depends upon several factors including location, atmospheric absorption and the speed, size and weight of the aircraft. The three main types of sonic booms normally observed are shown in Figure 1. The "normal" *N* wave is most often observed. However, as is shown in Figure 1(a) the positive phase duration often is not equal to the negative phase duration. The effect upon the

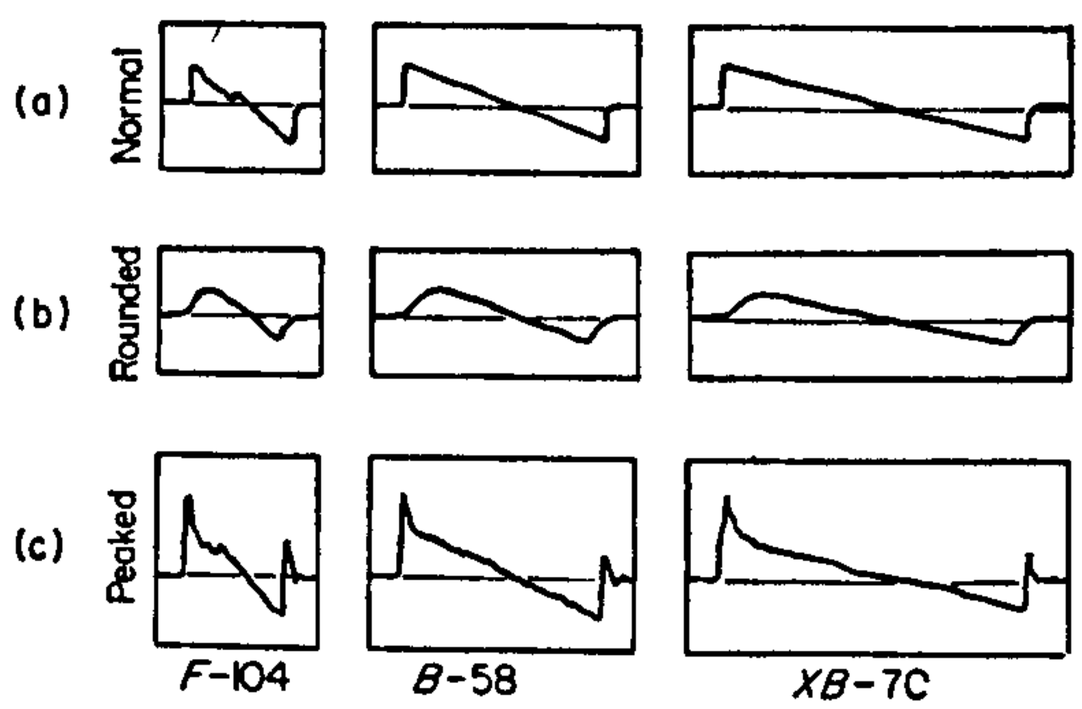

Figure 1. Typical pressure-time histories of sonic booms, measured at ground level produced by small, medium and large aircraft flying in steady flight at their cruising altitudes [1].

structure of varying the ratio of the total duration to the positive phase duration is examined in section 3. Sometimes, the sonic boom is "rounded" due to atmospheric absorption of the high frequency content of the *N* wave [Figure 1(b)]. This effect which produces a finite rise time is examined in section 4. Sonic booms are also observed with "peaks" [Figure 1(c)]. The peaks are often produced by reflection from the ground or buildings. This effect is examined in section 6. The effect of structural damping upon response is examined in section 5. Finally all these effects of variations in sonic booms are considered and a dynamic magnification factor curve (Figure 20) is produced which may be used to predict possible damage to building components such as windows due to overflights of a supersonic transport.

2. RESPONSE OF A SIMPLE SYSTEM TO AN IMPULSE

Suppose that the damping in a structure is small or else that the system can be idealized by an equivalent single degree-of-freedom system. Then in the first case, each mode, or in the second case, the equivalent system, may be represented by the simple mass-spring-damper system shown in Figure 2. The equation of motion for this system is

$$M\ddot{x}(t) + C\dot{x}(t) + Kx(t) = p(t). \tag{1}$$

If the system is subjected to a force $p(\sigma)$ which varies with time σ, then provided that the initial displacement and velocity are zero, the displacement at time t during the excitation is [2–5]

$$x(t) = \frac{1}{M\omega_d} \int_{\sigma=0}^{t} p(\sigma)\, e^{-\frac{C}{2M}(t-\sigma)} \sin\left[\omega_d(t-\sigma)\right] d\sigma \tag{2}$$

† Since completion of this paper, an independent investigation into some of the phenomena discussed in this paper has been published (D. H. CHENG and J. E. BENEVISTE 1968 *Trans. N.Y. Acad. Sci., Series II*, 30, 457). Cheng and Beneviste use different methods but arrive at somewhat similar results to the present authors, although there are some detailed differences.

where ω_d is the damped angular resonance frequency which is given by

$$\omega_d^2 = \omega^2 - \left(\frac{C}{2M}\right)^2 = \omega^2(1 - \delta^2) \tag{3}$$

where ω is the undamped angular resonance frequency given by $\omega^2 = K/M$ and δ is the critical damping ratio. Equation (2) is only valid if the damping is subcritical: $(C/2M)^2 < K/M$. If the excitation ends at time $s\tau$, then the displacement after excitation at time t is given by equation (2) with the upper limit of integration changed to $s\tau$.

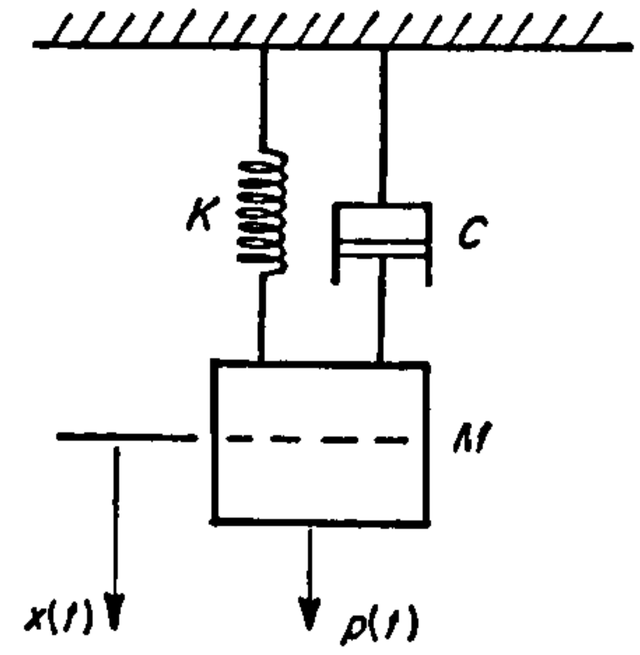

Figure 2. Damped mass-spring system.

3. RESPONSE OF A MASS-SPRING SYSTEM TO AN ASYMMETRICAL *N* WAVE

The effect of a symmetric *N* wave upon a single degree-of-freedom system has recently been evaluated by several authors [5, 6, 7]. Previous results given in the literature appear to have been incorrect [8, 9] or incomplete [10]. However, in practice, sonic booms are usually somewhat asymmetric [Figure 1(a)]. To account for this asymmetry the pulse length parameter s has been introduced [2, 11, 12, 13, 14].

Suppose a mass-spring system is subjected to an *N* wave, the force-time history experienced by the system being (see inset to Figure 3)

$$\left.\begin{aligned} p(\sigma) &= p_0(1 - \sigma/\tau), \quad (0 < \sigma < s\tau), \\ p(\sigma) &= 0, \quad (-\infty < \sigma < 0 \quad \text{and} \quad s\tau < \sigma < \infty). \end{aligned}\right\} \tag{4}$$

For an undamped system $C \to 0$. The response of the system may be obtained by substituting equations (4) into equation (2). The response must be divided into two time regimes: first, during forced motion and second, during free motion.

3.1. RESPONSE DURING FORCED MOTION

For time $0 < \sigma < s\tau$ from equations (2) and (4), if the damping C is zero, the displacement is

$$x(t) = \frac{1}{M\omega} \int_{\sigma=0}^{t} p_0(1 - \sigma/\tau) \sin[\omega(t - \sigma)]\, d\sigma, \tag{5}$$

$$x(t) = \frac{p_0}{M\omega^2}\left[1 - \frac{t}{\tau} - \cos\omega t + \frac{1}{\omega\tau}\sin\omega t\right]. \tag{6}$$

3.2. RESPONSE DURING FREE MOTION

For time $s\tau < \sigma < \infty$ from equations (2) and (4), if the damping C is zero, the displacement is

$$x(t) = \frac{1}{M\omega} \int_{\sigma=0}^{s\tau} p_0(1 - \sigma/\tau) \sin[\omega(t - \sigma)]\, d\sigma, \tag{7}$$

$$x(t) = \frac{p_0}{M\omega^2}\left[(1 - s)\cos[\omega(s\tau - t)] + \frac{\sin[\omega(s\tau - t)]}{\omega\tau} - \cos\omega t + \frac{\sin\omega t}{\omega\tau}\right]. \tag{8}$$

3.3. DYNAMIC MAGNIFICATION FACTOR DURING EXCITATION

The displacement, x_s, due to a static force p_0 is given by equation (1) with $\ddot{x}(t) = \dot{x}(t) = 0$, thus $x_s = p_0/K$. However, $K = M\omega^2$, (see reference 5, Appendix A), and thus $x_s = p_0/(M\omega^2)$. Thus from equation (6) the normalized displacement during excitation is

$$\frac{x(t)}{x_s} = 1 - \frac{t}{\tau} - \cos\omega t + \frac{1}{\omega\tau}\sin\omega t. \tag{9}$$

The times at which maxima or minima of the displacement occur are obtained by differentiating equation (9) with respect to time and equating the result to zero. The maximum value of the displacement will occur at the time

$$t = \frac{2}{\omega}\tan^{-1}(\omega\tau). \tag{10}$$

The minima of the normalized displacement will occur at times

$$t = 2n\pi/\omega, \quad (n = 1, 2, 3, \ldots). \tag{11}$$

Since equations (10) and (11) must also satisfy the relation $t \leqslant s\tau$ it is seen from equation (11) that there can be no minimum for $\omega\tau < 2\pi/s$.

The maximum value of the normalized displacement is given by substituting equation (10) into equation (9) by using half angle formulae [5]:

$$\frac{x_{\max}}{x_s} = 2\left[1 - \frac{\tan^{-1}(\omega\tau)}{\omega\tau}\right]. \tag{12}$$

It may be shown [14] that there is a maximum during forced motion provided $\tan^{-1}(\omega\tau)$, $< (s/2)\omega\tau$. Thus for $s > 2$, there must always be a maximum during forced motion. For $s < 2$, there will be no maximum during forced motion for $\omega\tau$ less than some limiting value.

The minimum value of the normalized displacement is found by substituting equation (11) into equation (9) and choosing the largest value of n which satisfies the relation $s\tau \geqslant 2n\pi/\omega$:

$$\frac{x_{\min}}{x_s} = -2n\pi/(\omega\tau). \tag{13}$$

For any particular value of the non-dimensionalized frequency $f\tau$, the dynamic magnification factor may be defined as the greatest maximum or minimum value of the normalized displacement which can occur. The dynamic magnification factor is so named because it represents the ratio of the dynamic to static displacement of the system.

3.4. DYNAMIC MAGNIFICATION FACTOR AFTER EXCITATION

From equation (8) the normalized displacement is

$$\frac{x(t)}{x_s} = (1-s)\cos[\omega(s\tau - t)] + \frac{\sin[\omega(s\tau - t)]}{\omega\tau} - \cos\omega t + \frac{\sin\omega t}{\omega\tau}. \tag{14}$$

Maxima or minima of the displacement occur when $\dot{x}(t)/x_s = 0$, that is for times

$$t_{\max,\min} = \frac{1}{\omega}\tan^{-1}\left[\frac{(1-s)\sin(\omega s\tau) - \dfrac{\cos(\omega s\tau)}{\omega\tau} + \dfrac{1}{\omega\tau}}{(1-s)\cos(\omega s\tau) + \dfrac{\sin(\omega s\tau)}{\omega\tau} - 1}\right]. \tag{15}$$

Substitution of equation (15) into equation (14) gives the maximum or minimum value of the normalized displacement after excitation; this calculation was conducted using a digital computer. Equations (12) and (13) were evaluated by hand.

3.5. DISCUSSION

Plots of the dynamic magnification factor against non-dimensionalized frequency $f\tau$ are given in Figures 3, 4, 5 and 6 for several representative values of s.

It is observed that as s is increased the frequencies at which the large free response peaks occur are decreased. Increasing s also has the effect that these peaks grow in magnitude and emerge further above the curve for the greatest maximum of displacement during forced motion which is independent of s. Fortunately, in practice, there is not a great variation in s and it is usually found that $1{\cdot}6 < s < 2{\cdot}2$, and for most sonic booms $s \leqslant 2{\cdot}0$.

For a symmetric N wave $s = 2$ and equation (15) gives the solution

$$t_{\max,\min} = \tau + n\pi/\omega,$$

provided

$$\tan\omega\tau \neq \omega\tau.$$

It can be shown [5, 14] that the second equation gives the values of $\omega\tau$ at which there is zero free motion, that is at which nulls occur. This equation is satisfied by

$$\omega\tau \approx (n + \tfrac{1}{2})\pi, \quad n = 1, 2, 3\ldots,$$

and this solution becomes progressively better as n increased. For values of s other than 2·0 the nulls disappear although there is still a minimum of free response at certain values of $\omega\tau$.

4. RESPONSE OF A MASS-SPRING SYSTEM TO AN N WAVE WITH A FINITE RISE TIME

Suppose an undamped mass-spring system is subjected to an N wave with a finite rise time and decay. Such an idealized N wave (see the inset to Figure 7) is a good approximation to measured sonic booms [see Figure 1(b)]. Using the notation of the inset to Figure 7, the force-time history of such an N wave (for $r_1 = r_2 = r$) is

$$\left.\begin{aligned} &p = 0, \quad (-\infty < \sigma < 0, \quad t_3 < \sigma < \infty),\\ &p = p_0[\sigma/(r\tau)], \quad (0 < \sigma < t_1),\\ &p = p_0[r + 1 - \sigma/\tau], \quad (t_1 < \sigma < t_2),\\ &p = p_0(1-s)\left[\frac{(2r+s)\tau - \sigma}{r\tau}\right], \quad (t_2 < \sigma < t_3), \end{aligned}\right\} \tag{16}$$

where

$$t_1 = r_1\tau, \quad t_2 = (r_1 + s)\tau \quad \text{and} \quad t_3 = (r_1 + r_2 + s)\tau.$$

The case where $r_1 \neq r_2$ is studied in reference 14.

Figure 3

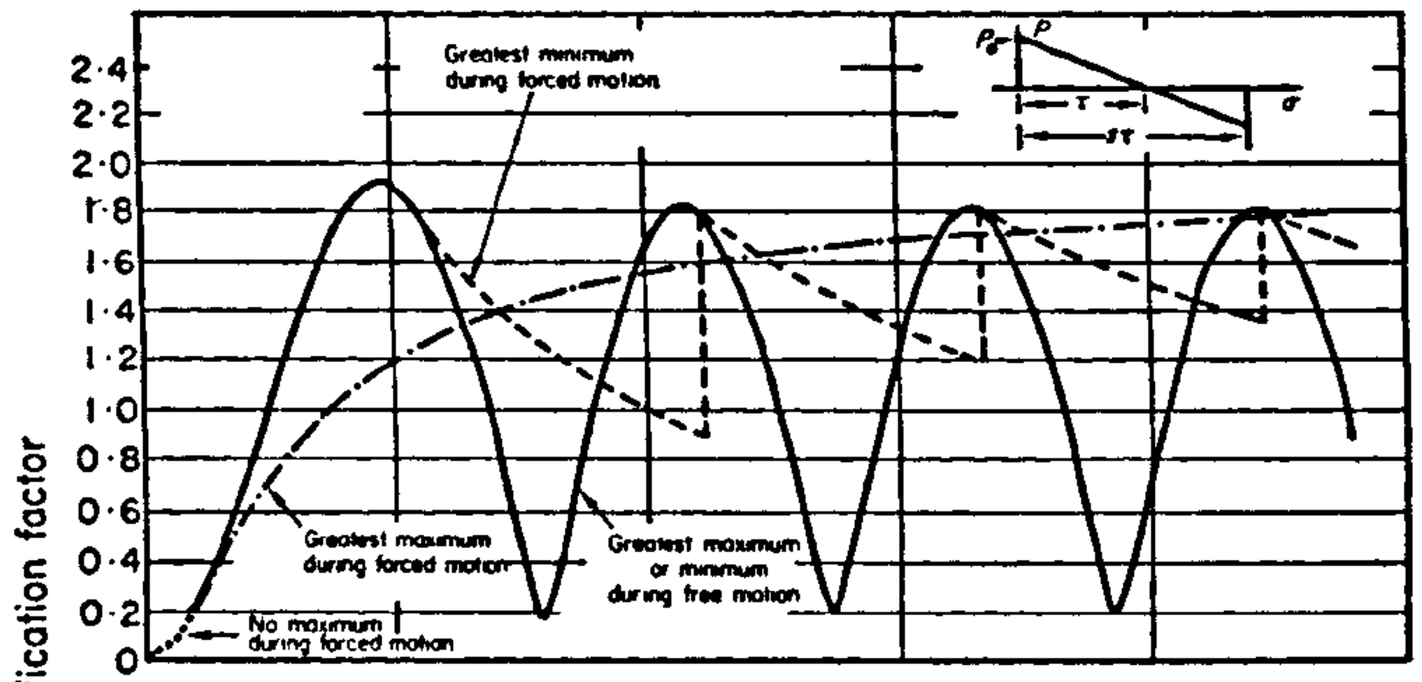

Figure 4

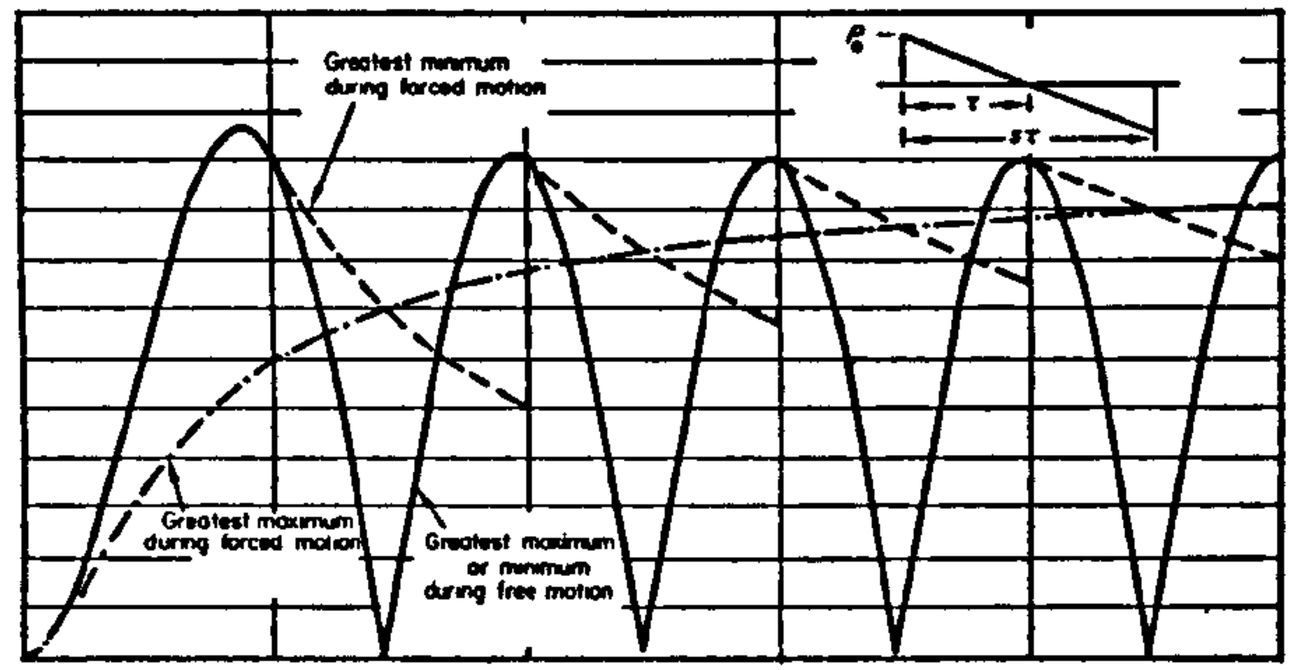

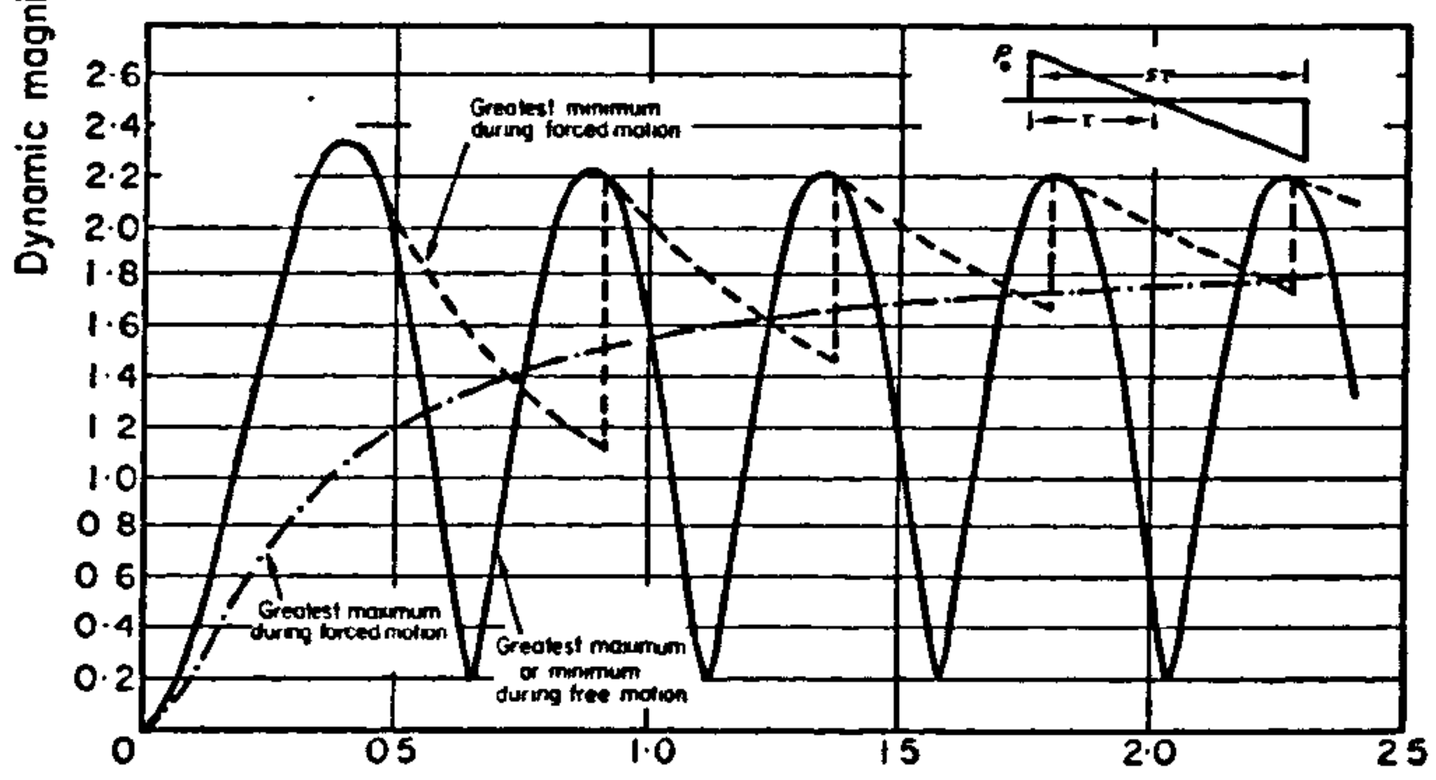

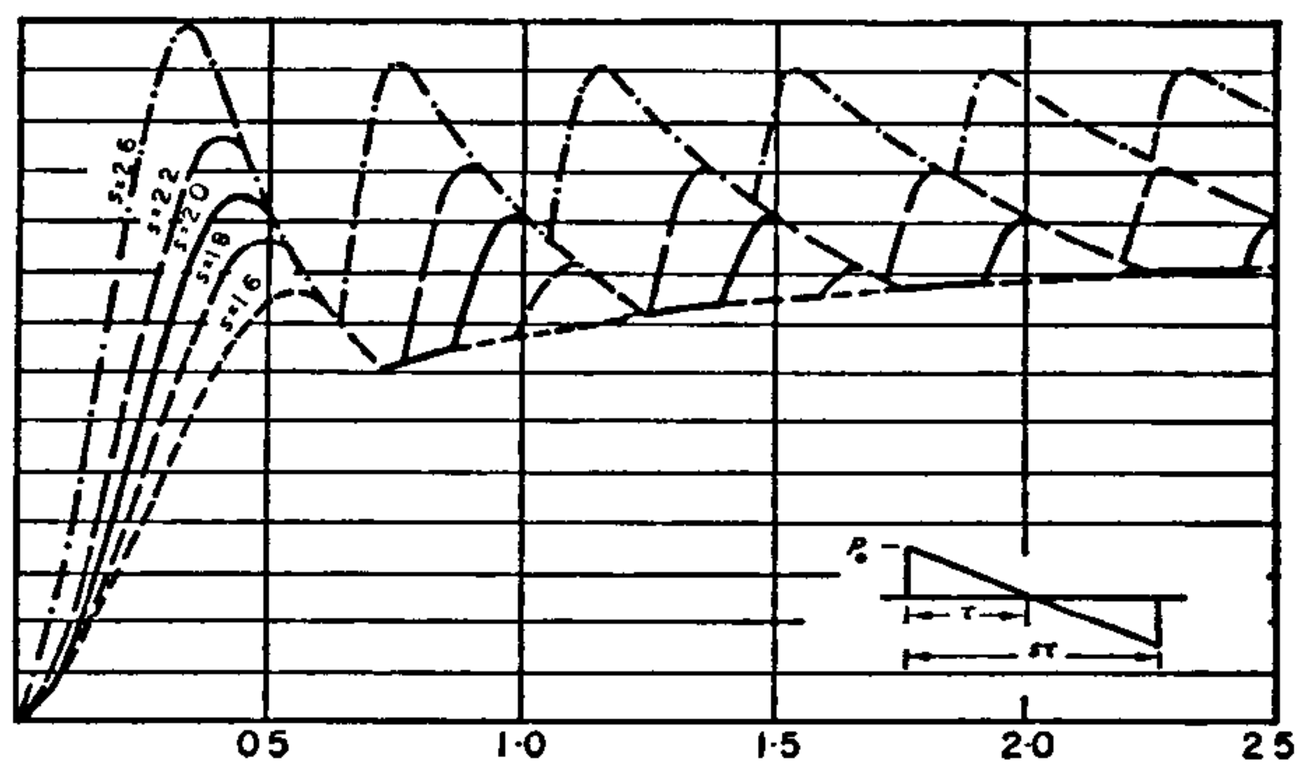

$f\tau$ = (Natural frequency) x (positive duration of N-wave)

Figure 5

Figure 6

Figure 3. Dynamic magnification factor for response of an undamped simple system to an asymmetrical sonic boom ($s = 1{\cdot}8$).

Figure 4. Dynamic magnification factor for response of an undamped simple system to a symmetrical sonic boom ($s = 2{\cdot}0$).

Figure 5. Dynamic magnification factor for response of an undamped simple system to an asymmetrical sonic boom ($s = 2{\cdot}2$).

Figure 6. Variation of dynamic magnification factors for response of an undamped simple system to an asymmetrical sonic boom as a function of the pulse length ratio s.

The response must be divided into four time regimes and using a Duhamel integral approach similar to that presented in section 3 the normalized displacement may be shown to be [14]

$$\frac{x(t)}{x_s} = \frac{t}{r\tau} - \frac{\sin \omega t}{\omega r\tau}, \quad (0 \leqslant t \leqslant r\tau), \tag{17}$$

$$\frac{x(t)}{x_s} = 1 + r - \frac{\sin \omega t}{\omega r\tau} - (r+1)\frac{\sin[\omega(r\tau - t)]}{\omega r\tau} - \frac{t}{\tau}, \quad (r\tau \leqslant t \leqslant (s+r)\tau), \tag{18}$$

$$\frac{x(t)}{x_s} = \frac{t - 2\tau(r+1)}{r\tau} + (r+1)\frac{\sin\omega[(r+2)\tau - t] - \sin[\omega(r\tau - t)]}{\omega r\tau} - \frac{\sin \omega t}{\omega r\tau}, \tag{19}$$

$$[(s+r)\tau \leqslant t \leqslant (s+2r)\tau],$$

$$\frac{x(t)}{x_s} = (r+1)\frac{\sin\omega[(r+2)\tau - t] - \sin[\omega(r\tau - t)]}{\omega r\tau} - \frac{\sin\omega[2(r+1)\tau - t] + \sin \omega t}{\omega r\tau}, \tag{20}$$

$$[(s+2r)\tau \leqslant t \leqslant \infty].$$

The dynamic magnification factor was calculated [14] for forced motion [equations (17), (18) and (19)] and for free motion [equation (20)] using a digital computer program. The program calculated the displacement time history for different values of the parameters r and $\omega\tau$ and also selected the dynamic magnification factors. Typical results are given in Figures 7 through 10.

It is seen that the dynamic magnification factor is plotted against $f\tau'$. This non-dimensionalization ensures that the positive impulse imparted by the N wave as r is varied remains the same. As the rise time ratio r is increased it is seen that the peak in the response during free motion which occurs at $f\tau' \approx 0{\cdot}5$ increases, while the successive peaks decrease in magnitude. When $r = 1{\cdot}0$ the dynamic magnification factor curve begins to look similar to that for a complete cycle sine pulse forcing function (see Figures 4–4 and 4–5 of reference 15). The maximum dynamic magnification factor for the sine pulse is 3·25 at $f\tau \approx 0{\cdot}5$. This magnification factor is larger than the value of 2·68 produced for an N wave with $r = 1{\cdot}0$ (Figure 9) because the impulse for the sine pulse is greater. Since the response is impulse dependent [10] up to values of $f\tau$ of about 0·5, it might be expected that the ratio of these maximum dynamic magnification factors would be very nearly equal to the ratio of the positive impulses for these two forcing functions. This does indeed prove to be the case, since the ratio of impulses is 1·27:1 and the ratio of maximum dynamic magnification factors is 1·22:1.

5. RESPONSE OF A VISCOUSLY DAMPED MASS-SPRING SYSTEM TO A SYMMETRICAL N WAVE

Suppose the damped mass-spring system (shown in Figure 2) is subjected to an N wave [whose force-time history is given by equations (4)].

5.1. FORCED RESPONSE

During excitation, $0 < t < s\tau$ the displacement is given by integrating equation (2) from $\sigma = 0$ to $\sigma = t$ where $p(\sigma)$ is given by the first of equations (4). Thus the normalized displacement may be shown to be [14]

$$\frac{x(t)}{x_s} = 1 - \frac{t}{\tau} + \frac{2\delta}{\omega\tau} - e^{-\omega\delta t}\left\{\left[1 + \frac{2\delta}{\omega\tau}\right]\cos\omega_d t + \left[\omega\delta\tau + \frac{(\omega\delta)^2 - \omega_d^2}{\omega^2}\right]\frac{\sin\omega_d t}{\omega_d\tau}\right\}. \tag{21}$$

Figure 7

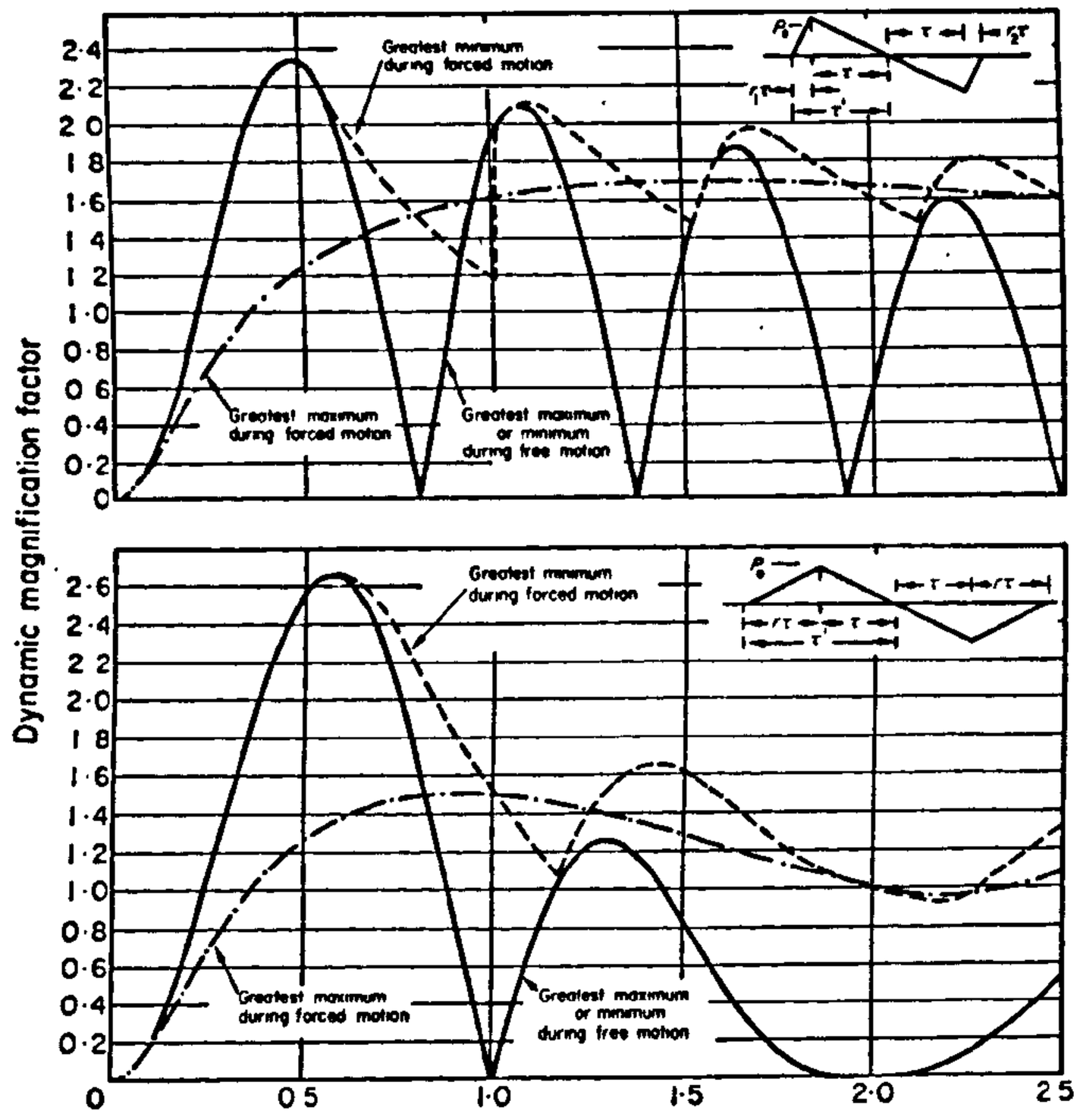

Figure 8

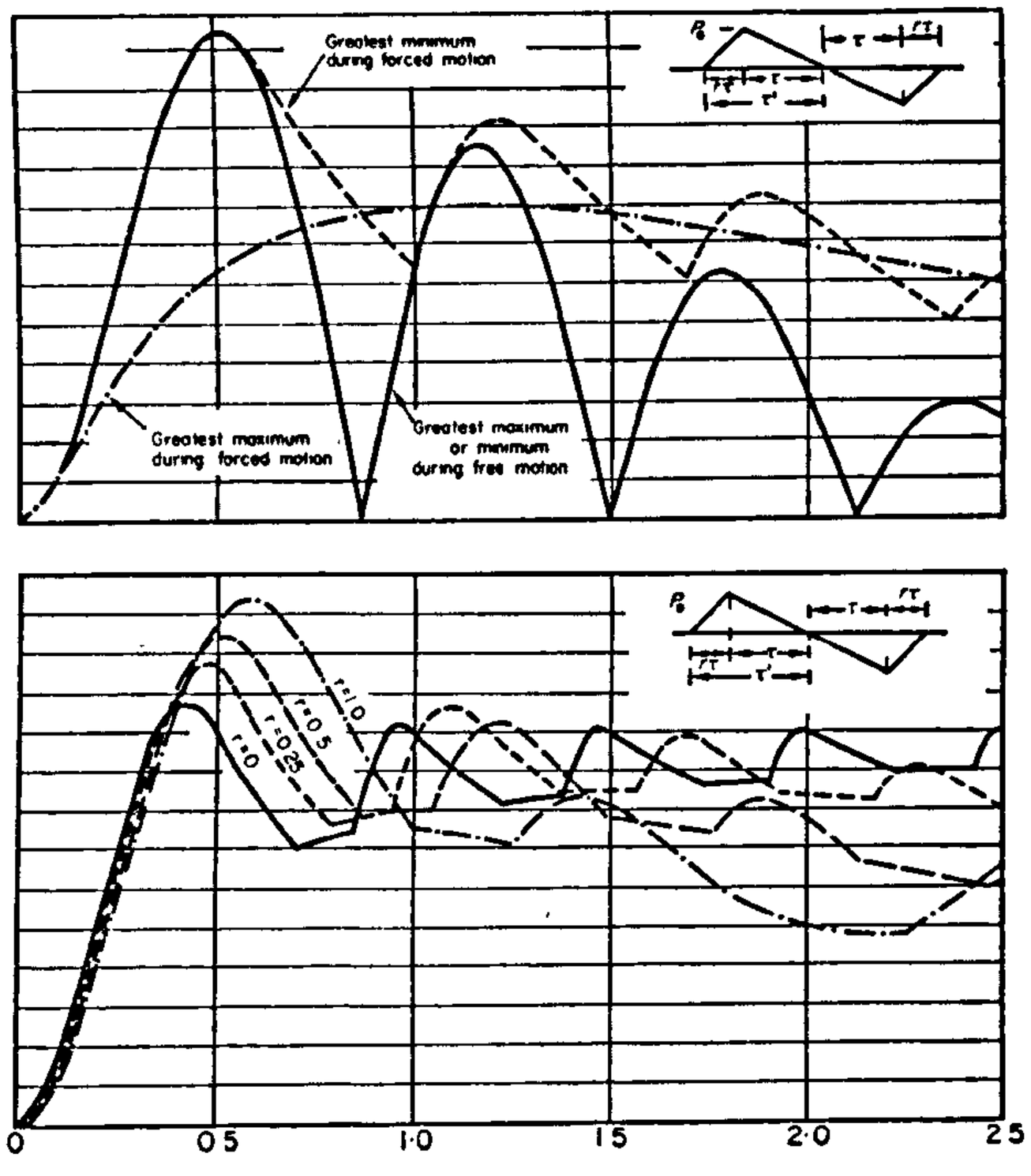

Figure 9

Figure 10

Figure 7. Dynamic magnification factor for response of an undamped simple system to a sonic boom with a finite rise time ($r = 0{\cdot}25$), $r = r_1 = r_2$.
Figure 8. Dynamic magnification factor for response of an undamped simple system to a sonic boom with a finite rise time ($r = 0{\cdot}50$).
Figure 9. Dynamic magnification factor for response of an undamped simple system to a sonic boom with a finite rise time ($r = 1{\cdot}0$).
Figure 10. Variation of dynamic magnification factors for response of undamped simple system to sonic booms as a function of rise time.

5.2. FREE RESPONSE

Similarly after excitation, $s\tau < t < \infty$, the displacement is given by integrating equation (2) from $\sigma = 0$ to $\sigma = s\tau$ where $p(\sigma)$ is again given by the first of equations (4). The normalized displacement is [14]

$$\frac{x(t)}{x_s} = e^{-\omega\delta t}\left\{\left[\left[\tau(s-1)\,\omega\delta - \frac{(\omega\delta)^2 - \omega_d^2}{\omega^2}\right]\frac{\sin[\omega_d(s\tau - t)]}{\omega_d\tau} + \left[(1-s) + \frac{\delta}{\omega\tau}\right]\cos\omega_d(s\tau - t)\right] \times \right.$$
$$\left. e^{\omega\delta s\tau} - \left[\left(1 + \frac{2\delta}{\omega\tau}\right)\cos\omega_d t + \left[\omega\delta\tau + \frac{(\omega\delta)^2 - \omega_d^2}{\omega^2}\right]\frac{\sin\omega_d t}{\omega_d\tau}\right]\right\}. \tag{22}$$

From equation (3) the undamped frequency $\omega = \omega_d/(1-\delta^2)^{1/2}$. Thus, making this substitution in equations (21) and (22), the normalized displacement may be expressed in terms of $\omega_d\tau$ and thus of $f_d\tau$. The dynamic magnification factor was calculated [14] for forced and free vibration using a numerical digital computer program for a symmetric N wave. The program

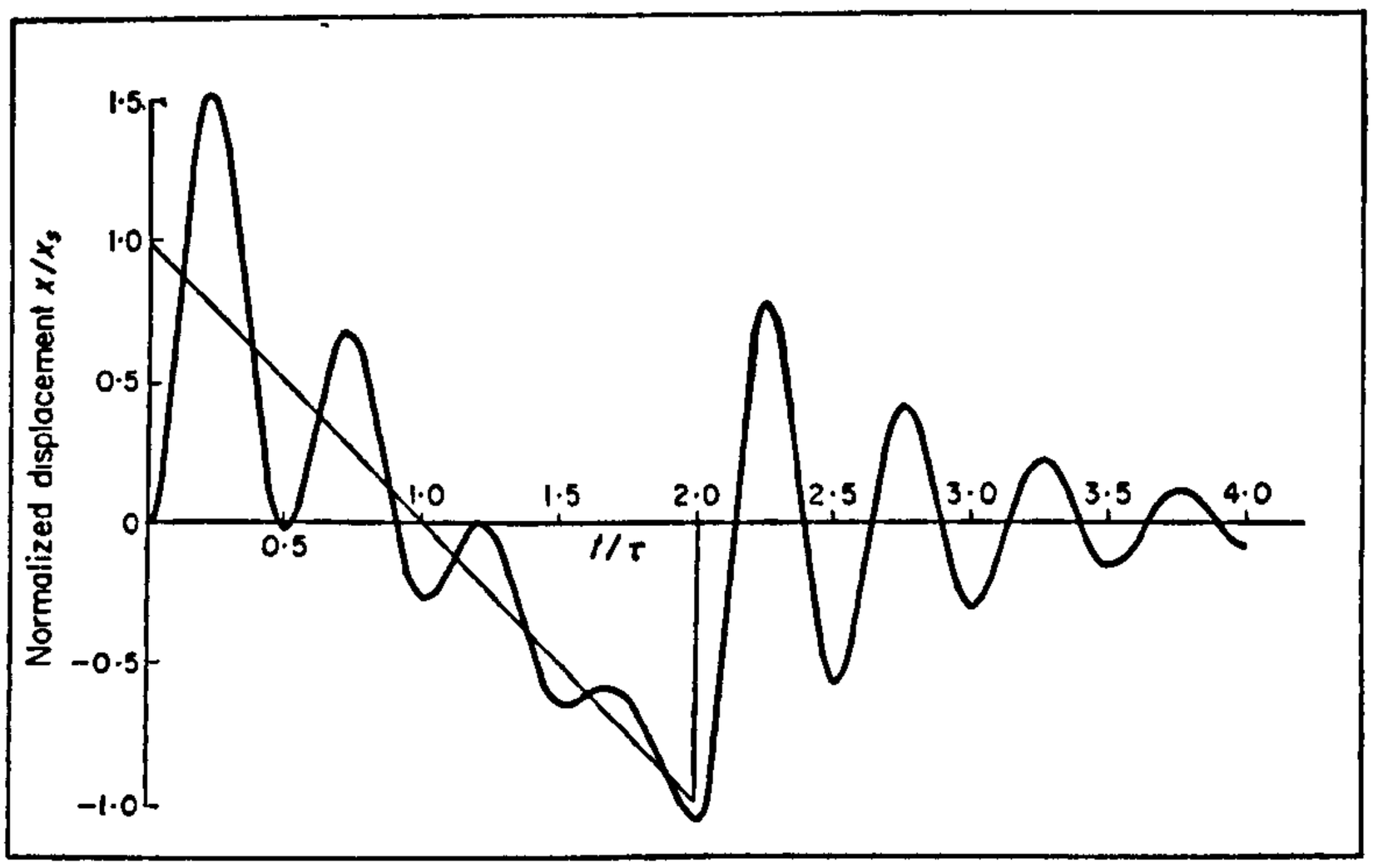

Figure 11. Typical time history of the response of a damped mass-spring system to a symmetrical sonic boom. Critical damping ratio $\delta = 0{\cdot}1$. $Q = 5$; frequency $f_d\tau = 2{\cdot}0$; ratio $s = 2{\cdot}0$.

calculated the response time history for different values of the damping ratio δ and selected the dynamic magnification factors as the parameter $f_d\tau$ was varied. A typical time history is given in Figure 11. Typical dynamic magnification factor plots are given in Figures 12 through 15.

The greatest true maxima or minima are plotted against $f_d\tau$ during forced motion, but during free motion the greatest absolute value of the normalized displacement is plotted. It is seen that damping has the effect of reducing the free motion considerably, especially as $f_d\tau$ is increased. However, the greatest maximum during forced motion is not much reduced and as δ is increased the free motion at higher values of $f_d\tau$ falls further below the forced motion curve. The damping also has the effect of decoupling the system during free motion and smoothing out the nulls and peaks. However, the nulls and peaks still occur at the same values of $f_d\tau$ as for a symmetric N wave (see Figure 4).

6. RESPONSE OF A MASS-SPRING SYSTEM TO AN N WAVE WITH SHOCK REFLECTIONS

When a sonic boom is reflected by the ground or by the wall of a building, shock reflections will occur. Typical measured N waves with reflections are shown in Figure 1(c). A suitable mathematical representation for the force-time history of such a pulse is given by equations

Figure 12

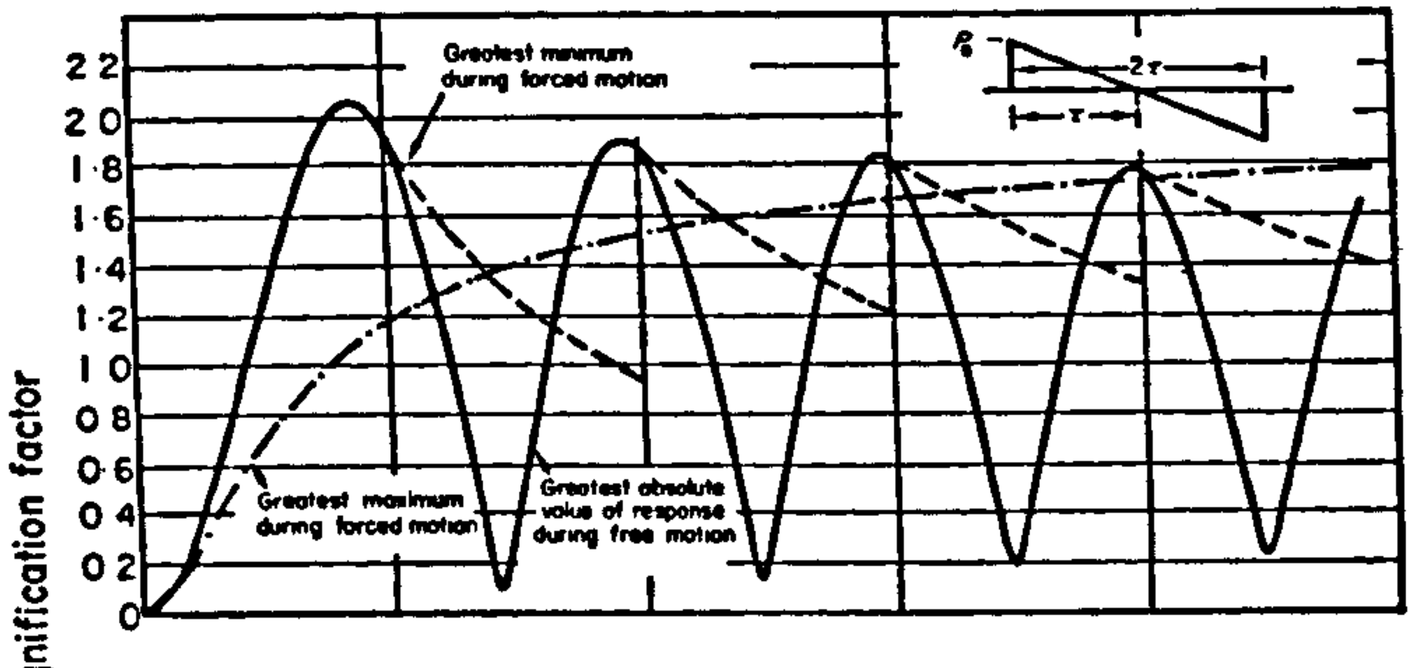

Figure 13

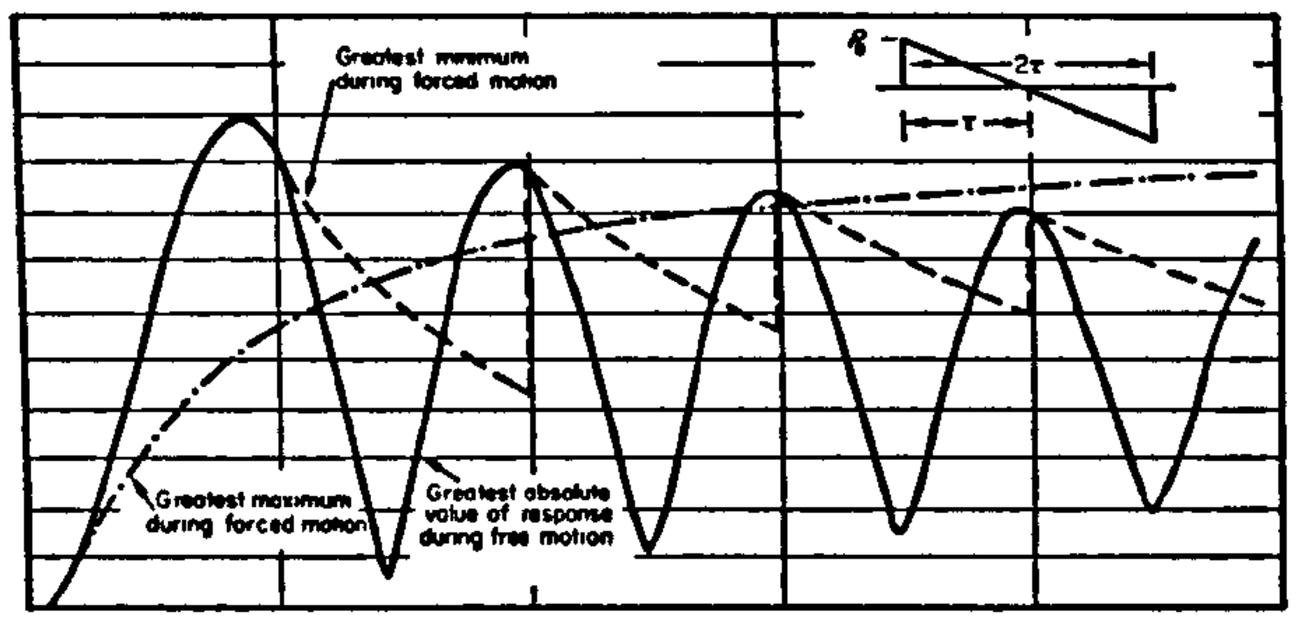

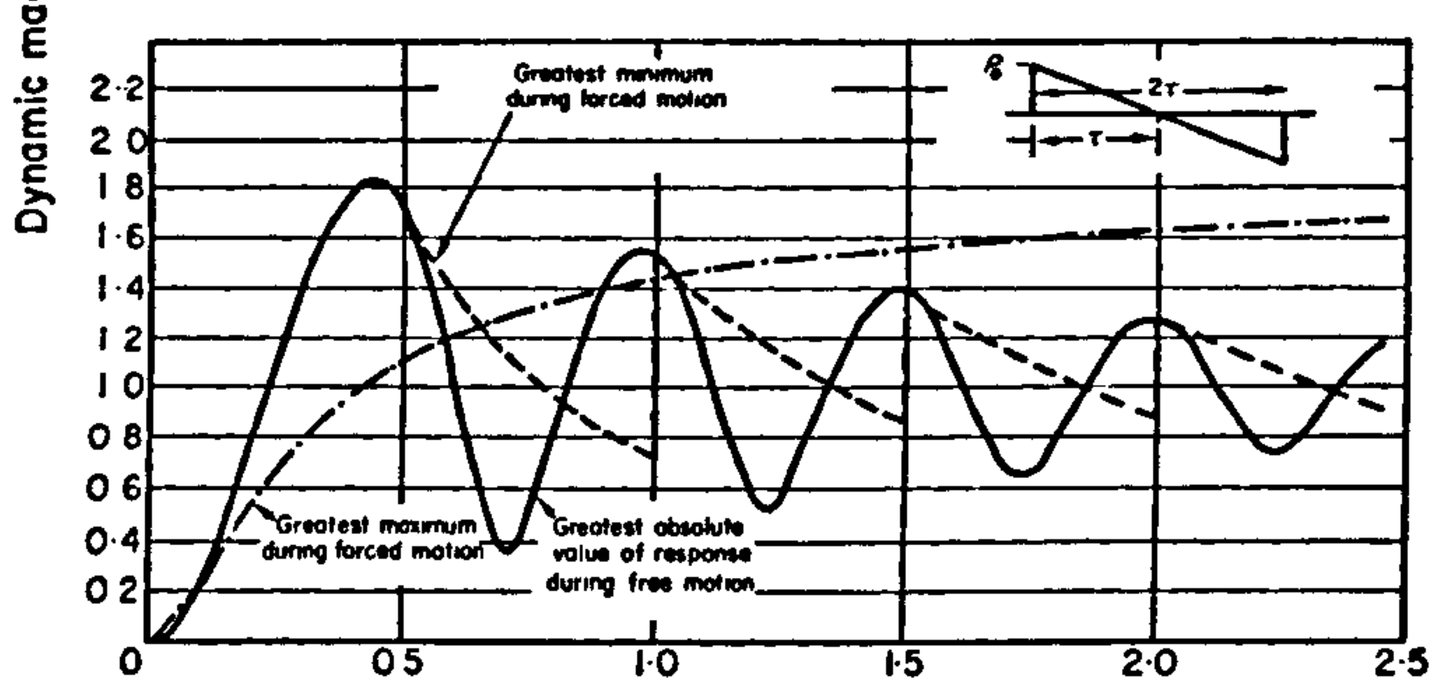

Figure 14

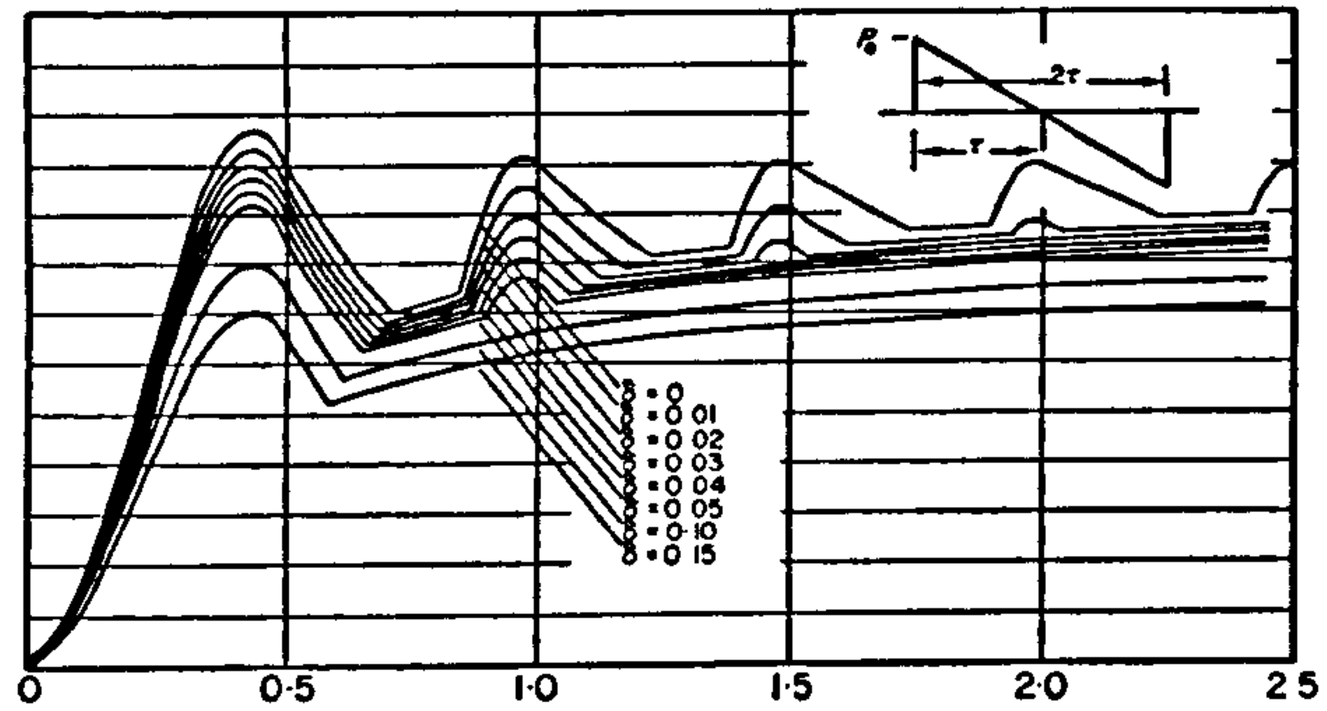

Figure 15

$f_0\tau$ = (Damped frequency) x (positive duration of *N*-wave)

Figure 12. Dynamic magnification factor for response of a damped mass-spring system to a symmetrical sonic boom. Critical damping ratio $\delta = 0{\cdot}01$; $Q = 50$.

Figure 13. Dynamic magnification factor for response of a damped mass-spring system to a symmetrical sonic boom. Critical damping ratio $\delta = 0{\cdot}02$; $Q = 25$.

Figure 14. Dynamic magnification factor for response of a damped mass-spring system to a symmetrical sonic boom. Critical damping ratio $\delta = 0{\cdot}05$; $Q = 10$.

Figure 15. Variation of dynamic magnification factors for response of a damped mass-spring system to a symmetrical sonic boom as a function of damping.

(23) (see Figure 10 of reference 2 or the inset to Figure 16). Using the notation of the inset to Figure 16, the force-time history of this idealized pulse is

$$\left.\begin{aligned} &p = 0, \quad (-\infty < \sigma < 0, \quad (2+u)\tau < \sigma < \infty), \\ &p = p_0\left[1 - \frac{\sigma(1+u)}{2u\tau}\right], \quad (0 < \sigma < u\tau), \\ &p = \tfrac{1}{2}p_0[1 - \sigma/\tau], \quad (u\tau < \sigma < 2\tau), \\ &p = \tfrac{1}{2}p_0\left[1 - \frac{\sigma - 2\tau}{u\tau}\right], \quad (2\tau < \sigma < (2+u)\tau). \end{aligned}\right\} \tag{23}$$

Suppose an undamped mass-spring system is subjected to a shock pulse with a pressure-time history given by equations (23). Again as in section 4, the response must be divided into four time regimes. Using a Duhamel integral approach similar to that presented in section 3, the normalized displacement may be shown to be [14]

$$\frac{x(t)}{x_s} = 1 - \left(\frac{1+u}{2u}\right)T - \cos\Omega T + \left(\frac{1+u}{2u}\right)\frac{\sin\Omega T}{\Omega}, \quad (0 \leqslant T \leqslant u), \tag{24}$$

$$\frac{x(t)}{x_s} = \tfrac{1}{2}\left[1 - T + \frac{1}{\Omega u}\sin[\Omega(u-T)] - 2\cos\Omega T + \left(\frac{1+u}{u}\right)\frac{\sin\Omega T}{\Omega}\right], \quad (u \leqslant T \leqslant 2), \tag{25}$$

$$\begin{aligned} \frac{x(t)}{x_s} = \tfrac{1}{2}\Bigg[1 + (2-T)/u + \frac{1}{\Omega u}\sin[\Omega(u-T)] - 2\cos\Omega T + \left(\frac{1+u}{u}\right)\frac{\sin\Omega T}{\Omega} - \\ - 2\cos[\Omega(2-T)] - \left(\frac{1-u}{u}\right)\frac{\sin[\Omega(2-T)]}{\Omega}\Bigg], \quad (2 \leqslant T \leqslant 2+u), \end{aligned} \tag{26}$$

$$\begin{aligned} \frac{x(t)}{x_s} = \tfrac{1}{2}\Bigg[\frac{1}{\Omega u}\sin[\Omega(2+u-T)] + \frac{1}{\Omega u}\sin[\Omega(u-T)] - 2\cos\Omega T + \left(\frac{1+u}{u}\right)\frac{\sin\Omega T}{\Omega} - \\ - 2\cos[\Omega(2-T)] - \left(\frac{1-u}{u}\right)\frac{\sin[\Omega(2-T)]}{\Omega}\Bigg], \quad (2+u \leqslant T \leqslant \infty), \end{aligned} \tag{27}$$

where $T = t/\tau$ and $\Omega = \omega\tau$.

The dynamic magnification factor was calculated [14] for forced motion [equations (24), (25) and (26)] and for free motion [equation (27)] using a digital computer program. The program calculated the displacement-time history for different values of the parameters u and $\omega\tau$ and selected the dynamic magnification factors. Typical results for the reflection shock pulse ratio $u = 0{\cdot}1$, $0{\cdot}2$ and $0{\cdot}3$ are given in Figures 16, 17 and 18, respectively. Figure 19 shows a comparison of the envelopes for curves with increasing values of u.

It is observed that as the reflection shock pulse ratio u is increased, both the forced and free motion dynamic magnification factors increase although the effect is greater for increasing $f\tau$. One very interesting feature is that the nulls which were observed for free motion for a symmetric N wave (see Figure 4) remain almost unchanged independent of the value of u. The reason for this is that the force-time history [equations (23)] may be regarded as an N wave with the addition of two triangular pulses separated in time by 2τ (see reference 2).

Since the equation of motion is a linear differential equation, the response to these separate pulses may be found by superposition. However, there will be nulls in the free motion due to the N wave when $f\tau \approx (2n+1)/4$, $(n = 1, 2, 3 \ldots)$ (see section 3.5 or reference 5). However, there will also be zero free motion due to the repeated triangular pulses when $2\tau = (2n-1)/(2f)$ or $f\tau = (2n-1)/4$, $(n = 1, 2, 3 \ldots)$ (see section 7). Since the values of $f\tau$ are not quite identical for the N wave and the repeated triangular pulses, absolute nulls will not be produced. Also, since $f\tau \approx (2n+1)/4$ becomes a better solution as n increases, the nulls will become more nearly absolute as $f\tau$ increases. Both these facts are confirmed by Figures 16 to 18.

Figure 16

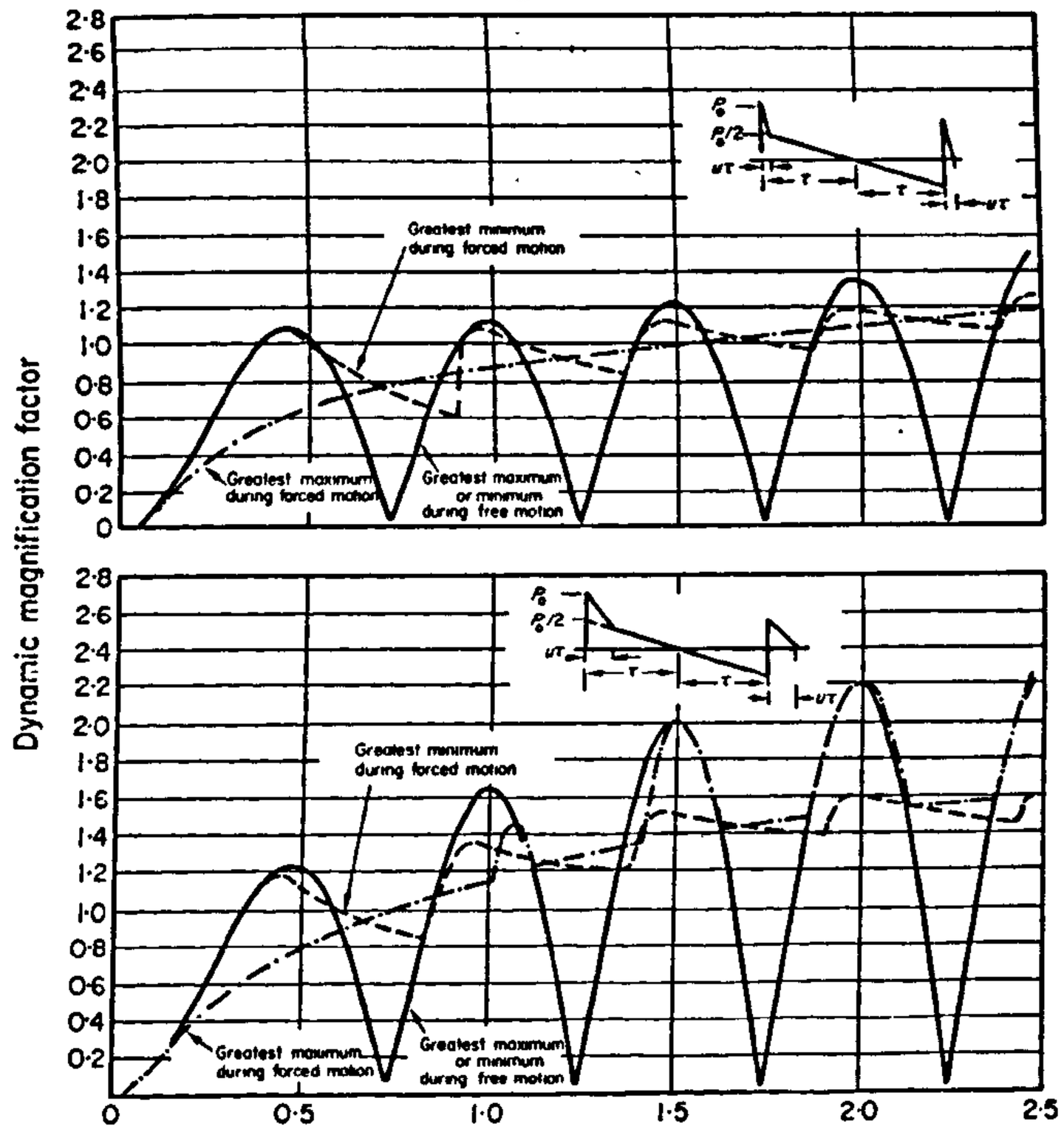

Figure 18

Figure 17

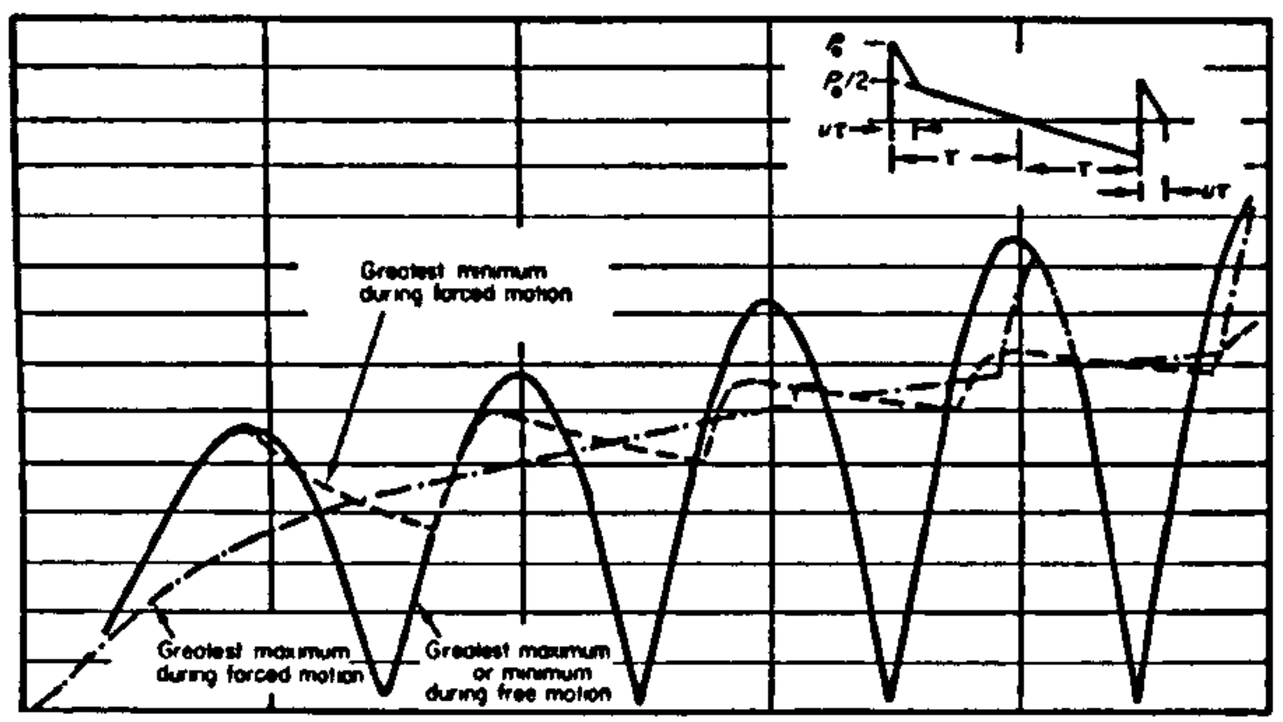

Figure 19

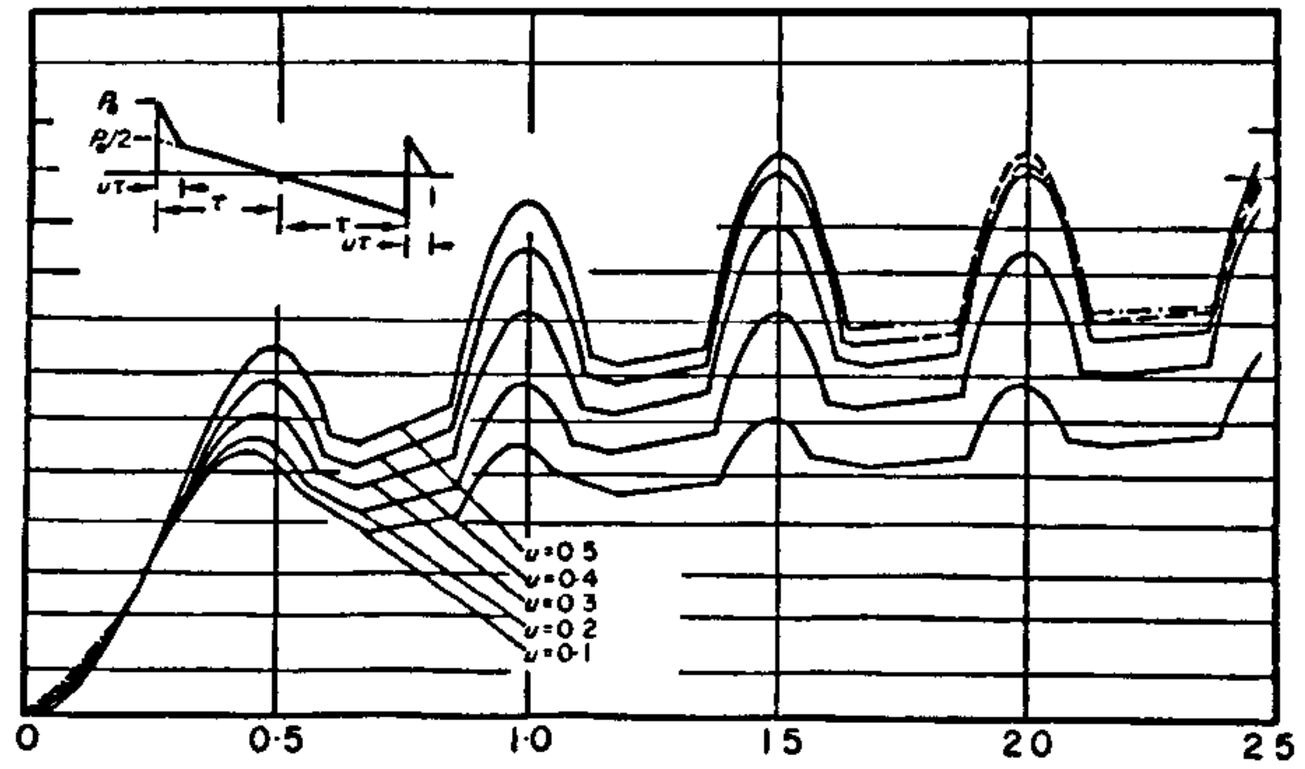

fτ = (Natural frequency) x (positive duration of *N*-wave)

Figure 16. Dynamic magnification factor for response of an undamped simple system to a sonic boom with reflection shocks ($u = 0{\cdot}1$).

Figure 17. Dynamic magnification factor for response of an undamped simple system to a sonic boom with reflection shocks ($u = 0{\cdot}2$).

Figure 18. Dynamic magnification factor for response of an undamped simple system to a sonic boom with reflection shocks ($u = 0{\cdot}3$).

Figure 19. Variation of dynamic magnification factor for response of an undamped simple system to a sonic boom with reflection shocks as a function of the reflection shock pulse ratio u.

7. REPEATED *N* WAVES

In some cases it is found that more than one *N* wave is experienced at a point in space. This may be due to a variety of reasons. The first *N* wave may travel direct while the second is reflected from the ground. Acceleration of the aircraft can also cause two *N* waves. A window in a building may also experience a sonic boom directly on its outside face and then receive on its inside face a sonic boom which is delayed and diffracted through an opening such as a doorway.

These sonic booms may be separated or they may overlap. The analysis for the response of a simple system to repeated *N* waves proves complex since there are four time regimes for the overlapping case and four for the non-overlapping case. However, this problem has been examined in detail in reference 14.

For the case of the free motion, the results are very simple and tractable. It may be shown [14] that the displacement due to each shock pulse during free motion may be expressed as a sine wave.

Let the free response due to the first shock pulse be

$$\frac{x(t)}{x_s} = \sin(\omega t'). \tag{28}$$

Then the free motion displacement due to the second shock pulse is

$$\frac{x(t)}{x_s} = A\sin[\omega(t' - \bar{t})], \tag{29}$$

where t' is the time measured from a displaced origin, $\bar{t}$ is the time difference between the pulses and A is the relative magnitude of the second pulse. Thus the total free motion displacement is [summing equations (28) and (29)]

$$\frac{x(t)}{x_s} = B\sin(\omega t' - \phi), \tag{30}$$

where

$$B = \sqrt{1 + A^2 \quad + 2A\cos\omega\bar{t}} \quad \text{and} \quad \tan\phi = \frac{A\sin\omega\bar{t}}{1 + A\cos\omega\bar{t}},$$

when $A = +1$, $B = 2$, for $\omega\bar{t} = 0, 2\pi, 4\pi, \ldots$, and $B = 0$ for $\omega\bar{t} = \pi, 3\pi, 5\pi, \ldots$. Thus, as might be expected, in free motion for two *N* waves the dynamic magnification factor can be increased by a value up to twice that for the single *N* wave.

The results for forced motion are more complicated although somewhat similar results are found. Again the dynamic magnification factor can be increased to twice the value for a single *N* wave.

8. DISCUSSION AND CONCLUSIONS

Building components will be subjected to a variety of *N* wave shapes during overflights of a supersonic transport (see Figure 1). It is thus desirable to determine an upper limit to the dynamic magnification factor curve against non-dimensionalized frequency $f\tau$ which will encompass the effects of these sonic boom variations. Such a curve (Figure 20) was produced by studying Figures 6, 10, 15 and 19. It is seen that increasing the values of s, r and u tends to produce higher dynamic magnification factors and to cause some shift in the non-dimensionalized frequency $f\tau$ at which peak responses occur. However, increasing values of structural damping ratio δ cause a marked decrease in response particularly for free motion as $f\tau$ increases. Thus, it was necessary to choose upper values of s, r and u and a representative value of δ before Figure 20 could be drawn. With the supersonic transport and with windows

particularly in mind, these upper values were chosen to be $s = 2{\cdot}2$, $r = 0{\cdot}5$ and $u = 0{\cdot}2$. A representative value of $\delta = 0{\cdot}02$ was chosen for the critical damping ratio for a window.

It is seen that the envelope given in Figure 20 rises to a maximum value of 2·5 at $f\tau = 0{\cdot}5$ and then at high values of $f\tau$ assumes a value of 2·0. The assumption is made that increases in the dynamic magnification factor at higher values of $f\tau$ due to the values of s, r and u chosen, are reduced by the damping so that an asymptotic value of the dynamic magnification factor of 2·0 is reached at high values of $f\tau$.

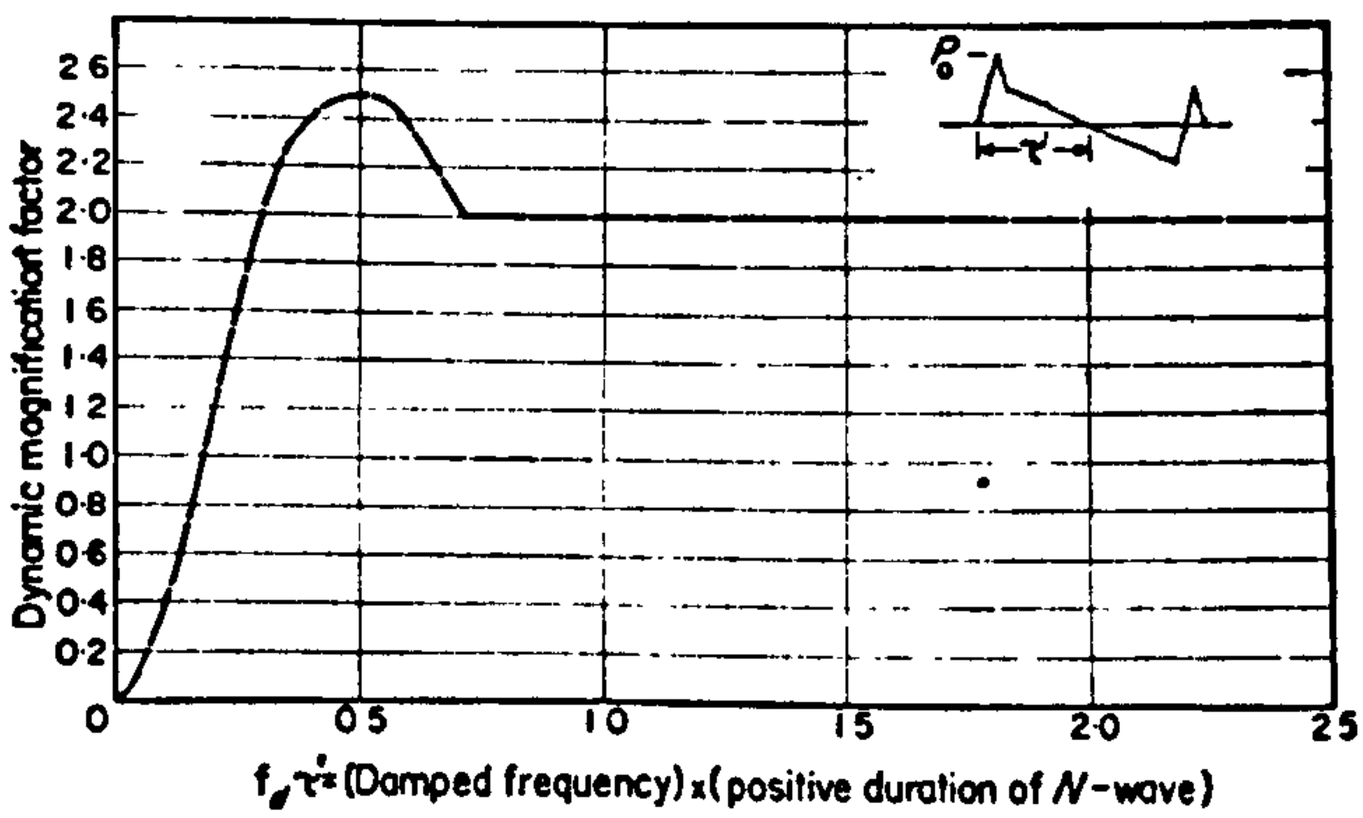

Figure 20. Envelope of dynamic magnification factor curves for use in assessing possibility of damage due to supersonic transport overflight.

Figure 20 should be useful in a study of the possibility of damage to windows and other building structural members due to overflights by a supersonic transport. It is foreseen that the curve in Figure 20 is dependent upon the maximum values of s, r and u chosen and the assumed value of δ. However, it is also seen that the resultant curve is not too sensitive to small changes in the values of these parameters.

One interesting result shown in Figures 11 to 15 is that increasing structural damping causes a considerable reduction in response in all regimes with the exception of the first maximum during forced motion. It would seem very worthwhile if the internal damping ratio of a window could be raised to about 0·05 or 0·10. This might be achieved by lamination or by the attachment of a transparent layer of "damping tape." This should at the very least reduce the free vibration considerably, hence reducing the psychologically bad effect of rattling or vibration of a window when it is excited by a sonic boom.

REFERENCES

1. D. J. Maglieri 1967 *Sonic Boom Research NASA SP*-147 (Ed. A. R. Seebass). Sonic boom flight research—some effects of airplane operations and the atmosphere on sonic boom signatures.
2. M. J. Crocker 1967 *J. acoust. Soc. Am.* **42**, 1070. Multimode response of panels to normal and to travelling sonic booms.
3. M. J. Crocker 1967 *J. Sound Vib.* **6**, 38. Response of panels to oscillating and to moving shock waves.
4. M. J. Crocker 1968 *Proceedings AIAA/ASME 9th Structures, Structural Dynamics and Materials Conference, Palm Springs, California.* Paper 68–287. Response of aerospace vehicle skin panels to oscillating shock waves.
5. M. J. Crocker 1967 *University of Liverpool, Department of Building Science, Report BS/A/67-2.* Dynamic magnification factor produced in a single degree of freedom system by an ideal sonic bang.
6. Wyle Laboratories Research Staff 1965 *Progress Report on Contract* NASA; NAS8-11217. Dynamic magnification factor for response of undamped system to an ideal N-wave.

7. D. H. CHENG and J. E. BENEVISTE 1966 *Int. J. mech. Sci.* 8, 607. Transient response of structural elements to travelling pressure waves of arbitrary shape.
8. Arde Associates 1959 *WADC US Air Force Tech. Rep.* 58–169. Response of structures to aircraft generated shock waves.
9. D. H. CHENG 1964 *LWP-25 NASA Langley Research Center, U.S.A.* Some dynamic effects of sonic booms on building structural elements.
10. W. H. MAYES and J. W. NEWMAN 1966 *LWP-154 NASA Langley Research Center U.S.A.* An analytical study of the response of a single degree-of-freedom system to sonic-boom-type loadings.
11. M. J. CROCKER 1966 *Wyle Lab. Res. Staff Rep. WR66-1.* Multimode response of panels to sonic boom.
12. M. J. CROCKER 1966 *Wyle Lab. Res. Staff Rep. WR66-2.* Theoretical and experimental response of panels to travelling sonic boom and blast waves.
13. M. J. CROCKER and L. C. SUTHERLAND 1968 *J. Sound Vib.* 7, 351. Instrumentation requirements for measurement of sonic boom and blast waves—a theoretical study.
14. M. J. CROCKER and R. R. HUDSON 1968 *University of Liverpool, Department of Building Science, Report BS/A/68-3.* Response of a simple system to a sonic boom.
15. L. S. JACOBSEN and R. S. AYRE 1958 *Engineering Vibrations.* New York: McGraw-Hill.

APPENDIX: LIST OF SYMBOLS

A constant
B constant
C damping coefficient of system
f undamped resonance frequency of system
f_d damped resonance frequency of system
K stiffness of system
M mass of system
n integer
p force
p_0 initial force
r rise time ratio of N wave
s pulse length ratio of N wave
t time
t' time
$\bar{t}$ time delay between N waves
T non-dimensionalized time t/τ
u reflection shock pulse ratio
x displacement
x_s displacement due to static force
δ viscous damping ratio
σ dummy time variable
τ duration of positive phase of N wave
τ' duration $(1 + r)\tau$
ϕ phase angle
ω undamped angular resonance frequency of system
ω_d damped angular resonance frequency of system
Ω non-dimensionalized frequency $\omega\tau$

J. Sound Vib. (1969) **9** (3), 469–486

SOUND TRANSMISSION USING STATISTICAL ENERGY ANALYSIS

M. J. Crocker and A. J. Price

Department of Building Science, University of Liverpool, Liverpool 3, England

(*Received* 31 *July* 1968)

Statistical energy analysis is used to predict the sound transmission loss, the radiation resistance and the vibration amplitude of a partition. Agreement between theory and experiment is shown to be good. The "mass-law" sound transmission is seen to be due to non-resonant modal vibration while the increased transmission in the coincidence region is seen to be due to resonant modal vibration. The observed vibration amplitude is also shown to be due to resonant modes. The previously observed discrepancy between the values of vibration amplitude derived from the mass law and those observed experimentally which has been described in the literature [1] is thus satisfactorily explained.

1. INTRODUCTION

In recent years new techniques have been developed for predicting the acoustic response and radiation properties of complicated structures [2–6]. These techniques sometimes known as "statistical energy methods" have been primarily applied to predicting the noise and vibration levels in aircraft and spacecraft structures. In the past, the classical architectural sound transmission problem has normally been approached theoretically with so-called "mass-law theories" [7–11]. Often these theories neglect damping and stiffness in the partition, which is assumed to be infinite in extent and to respond as a limp membrane. In this paper the classical sound transmission problem is approached using statistical energy methods. This approach includes panel stiffness and damping and the effects of finite panel size and successfully predicts the panel vibration amplitude and the dip in the transmission loss curve at the coincidence frequency.

Theory developed by Lyon [12, 13] and Ungar [14] is used to predict the partition transmission loss and vibration amplitude in section 5 of the paper. The present authors have extended this theory in sections 4.2 and 4.4 of the paper to enable the partition radiation resistance and its coupling with the transmission rooms to be determined. In order to predict the partition transmission loss and vibration amplitude it is necessary to know the radiation resistance of the partition. Both theoretical values (due to Maidanik [4]) and experimental values (determined using the analysis developed in section 4.2) were used in the predictions.

Utley and Mulholland [1] have recently shown that the vibration amplitude of a partition is very much greater than that predicted by mass law. This discrepancy is easily explained by the present approach. As is shown in this paper, the vibration amplitude at any frequency is due to the response of resonant modes. The vibration amplitude is thus governed by the total resistance and by the radiation resistance of the panel at any particular frequency. It is found that using a measured value of the partition total resistance, it is possible to predict the vibration amplitude to within 1 or 2 dB throughout the frequency range 400 to 10,000 Hz.

2. MODAL BEHAVIOUR OF PANEL

The resonant modes of a panel can be divided into two classes. Modes with resonance frequencies above the critical or coincidence frequency and thus having bending velocities

greater than the speed of sound in air are termed acoustically fast (A.F.). Modes with resonance frequencies below the critical frequency and thus having bending velocities less than the speed of sound are termed acoustically slow (A.S.).

It can be shown theoretically [4, 6] that the A.F. modes have a high radiation efficiency, whilst the A.S. modes have a low radiation efficiency. The A.S. modes may be further subdivided into two groups. A.S. modes which have bending phase speeds in one edge direction greater than the speed of sound and bending phase speeds in the other edge direction less than the speed of sound are termed "edge" or "strip" modes. A.S. modes which have bending phase speeds in both edge directions less than the speed of sound are termed "corner" or "piston" modes. Corner modes have lower radiation efficiencies than edge modes.

The theoretical results for the radiation efficiency and classification of modes can also be given a simple physical explanation. Figure 1 shows a typical modal pattern in a simply-supported panel. The dotted lines represent panel nodes.

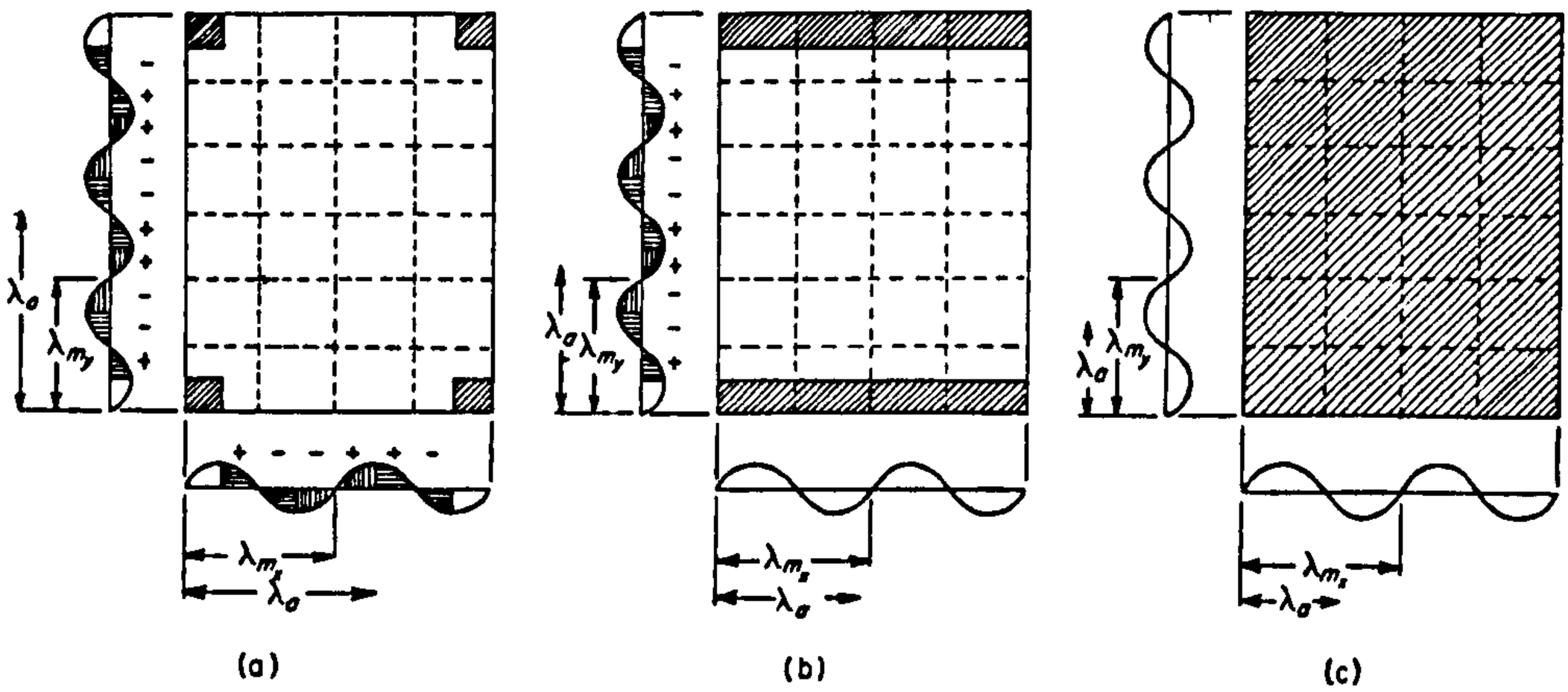

Figure 1. Wavelength relations and effective radiating areas for corner, edge and surface modes. (a) Corner mode; (b) *X*-edge mode; (c) surface mode. ■, Effective radiating area.

The modal vibration of a finite panel consists of standing waves. Each standing wave may be considered to consist of two pairs of bending waves, the waves of each pair travelling in opposite directions. Consider a mode which has bending wave phase speeds which are subsonic in directions parallel to both of its pairs of edges. In this case the fluid will produce pressure waves which will travel faster than the panel bending waves and the acoustic pressures created by the quarter wave cells [as shown in Figure 1(a)] will be cancelled everywhere except at the corners as shown. If a mode has a bending wave phase speed which is subsonic in a direction parallel to one pair of edges and supersonic in a direction parallel to the other pair, then cancellation can only occur in one edge direction and for the mode shown in Figure 1(b), the quarter wave cells shown will cancel everywhere except at the x edges. Acoustically fast modes have bending waves which are supersonic in directions parallel to both pairs of edges. Then the fluid cannot produce pressure waves which will move fast enough to cause any cancellation and the result is shown in Figure 1(c).

Since A.F. modes radiate from the whole surface area of a panel, they are sometimes known as "surface" modes. With surface modes the panel bending wavelength will always match the acoustic wavelength traced on to the panel surface by acoustic waves at some particular angle of incidence to the panel; consequently, surface modes have high radiation efficiency. This phenomenon does not happen for A.S. modes, the acoustic trace wavelength always being greater than the bending wavelength; A.S. modes have a low radiation efficiency.

At the critical frequency (when the panel bending wavelength equals the trace wavelength of grazing acoustic waves), the panel vibration amplitude is high (Figure 17). The radiation efficiency which is proportional to the radiation resistance is also high (Figure 12). Thus at the critical frequency the sound transmission is high and is due to modes resonant in a band centred at this frequency. Since the modes are resonant the transmission can be reduced effectively in this region by increasing the internal damping of the panel.

Well below coincidence the vibration amplitude of resonant modes is low and the radiation efficiency is also low. In this region it is usually found that more sound is transmitted by modes which are not resonant in the frequency band under consideration. Since these modes are not excited at their resonance frequencies they are little affected by internal damping. The contribution due to the non-resonant modes gives rise to the well-known "mass law" transmission. Just above coincidence the panel vibration amplitude and the radiation efficiency are high and the transmission is still resonant. However, as the frequency is increased further, the internal damping increases rapidly, the non-resonant transmission becomes more important, and the transmission again approaches mass law [15].

The relative importance of resonant and non-resonant transmission of course depends upon the practical structure under consideration and upon the variation of internal and radiation resistance with frequency. The radiation resistance is normally increased with the addition of stiffeners which will usually increase resonant transmission. An increase of internal damping which may be achieved in several ways including the use of rivetted structures or damping material will decrease resonant transmission and increase the importance of "mass law" transmission.

3. POWER FLOW BETWEEN COUPLED SYSTEMS

The power flow between coupled oscillator systems has been studied by several authors [3, 12, 16–18]. It is assumed that the power flow from one system to another is proportional to the difference in modal energies of the systems [3].

3.1. TWO COUPLED SYSTEMS

Consider the panel suspended in a reverberant room. The room may be considered as system 1 and the panel as system 2 as shown schematically in Figure 2. Following Lyon and

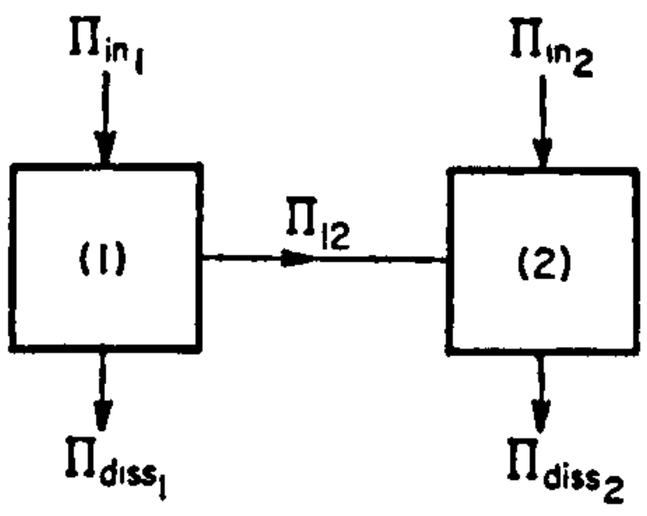

Figure 2. Block diagram representing energy flows between panel and reverberant room.

Scharton [12] the power flow balance for the two systems may be written [equations (1) to (4)]

$$\Pi_{in_1} = \Pi_{diss_1} + \Pi_{12}, \tag{1}$$

$$\Pi_{in_1} = \omega\eta_1 E_1 + \omega\eta_{12} n_1 \left(\frac{E_1}{n_1} - \frac{E_2}{n_2}\right), \tag{2}$$

$$\Pi_{in_2} = \Pi_{diss_2} - \Pi_{12}, \tag{3}$$

$$\Pi_{in_2} = \omega\eta_2 E_2 - \omega\eta_{12} n_1 \left(\frac{E_1}{n_1} - \frac{E_2}{n_2}\right), \tag{4}$$

where Π_{in_1} and Π_{in_2} are the rates of energy flow (in a frequency bandwidth of 1 rad/sec, centred on ω) into systems 1 and 2, respectively, supplied by a loudspeaker or shaker; Π_{diss_1} and Π_{diss_2} are the rates of internal dissipation of energy in systems 1 and 2 (in a bandwidth of 1 rad/sec); E_1 and E_2 are the total energies of systems 1 and 2 (in a bandwidth of 1 rad/sec). It should be noted that the coupling loss factor η_{12} strictly is only defined for zero energy in the second system [19], $E_2/n_2 = 0$, otherwise equations (2) and (4) do not balance. However, in most practical situations $E_2/n_2 \ll E_1/n_1$ and $\eta_{12} \approx \eta_{12}|_{E_2=0}$.

3.2. THREE COUPLED SYSTEMS

Consider the transmission suite shown in Figure 3. This may be considered to consist of three coupled systems as shown schematically in Figure 4. In a similar manner the power flow balance for the three systems may be written

$$\Pi_{in_1} = \Pi_{diss_1} + \Pi_{12} + \Pi_{13}, \tag{5}$$

$$\Pi_{in_1} = \omega\eta_1 E_1 + \omega\eta_{12} n_1 \left(\frac{E_1}{n_1} - \frac{E_2}{n_2}\right) + \omega\eta_{13} n_1 \left(\frac{E_1}{n_1} - \frac{E_3}{n_3}\right); \tag{6}$$

$$\Pi_{in_2} = \Pi_{diss_2} - \Pi_{12} + \Pi_{23}, \tag{7}$$

$$\Pi_{in_2} = \omega\eta_2 E_2 - \omega\eta_{12} n_1 \left(\frac{E_1}{n_1} - \frac{E_2}{n_2}\right) + \omega\eta_{23} n_2 \left(\frac{E_2}{n_2} - \frac{E_3}{n_3}\right); \tag{8}$$

$$\Pi_{in_3} = \Pi_{diss_3} - \Pi_{13} - \Pi_{23}, \tag{9}$$

$$\Pi_{in_3} = \omega\eta_3 E_3 - \omega\eta_{13} n_1 \left(\frac{E_1}{n_1} - \frac{E_3}{n_3}\right) - \omega\eta_{23} n_2 \left(\frac{E_2}{n_2} - \frac{E_3}{n_3}\right). \tag{10}$$

The Π_{13} term represents power flow from system 1 to system 3 when there are no modes excited in system 2 in the frequency band under consideration. Thus the power flow Π_{13} must

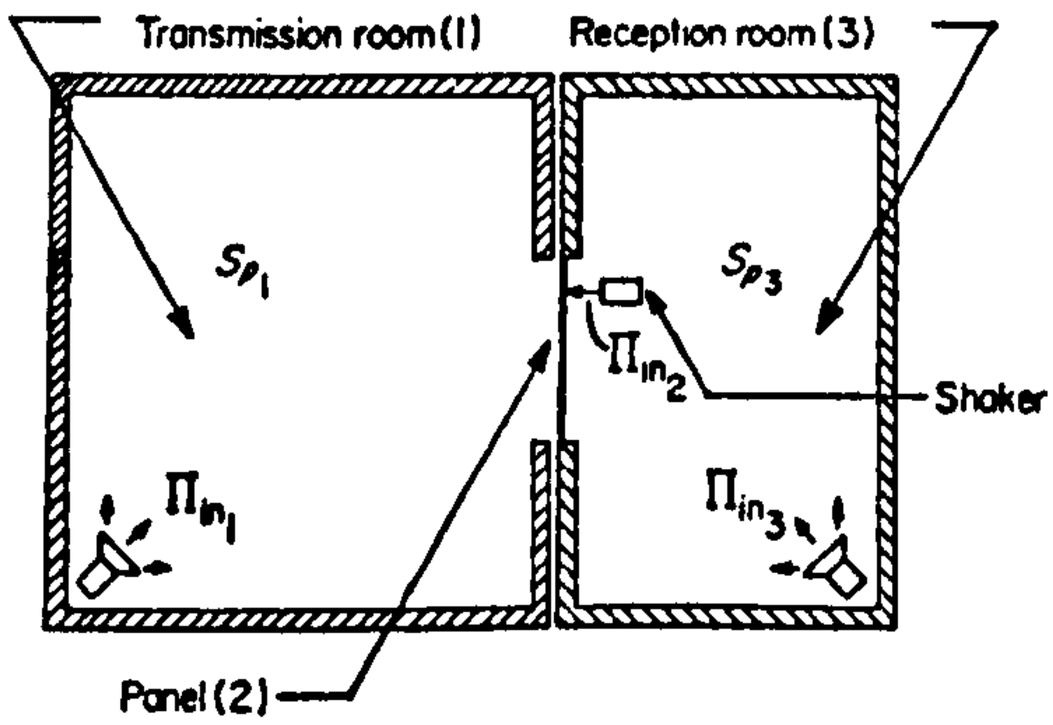

Figure 3. The transmission suite.

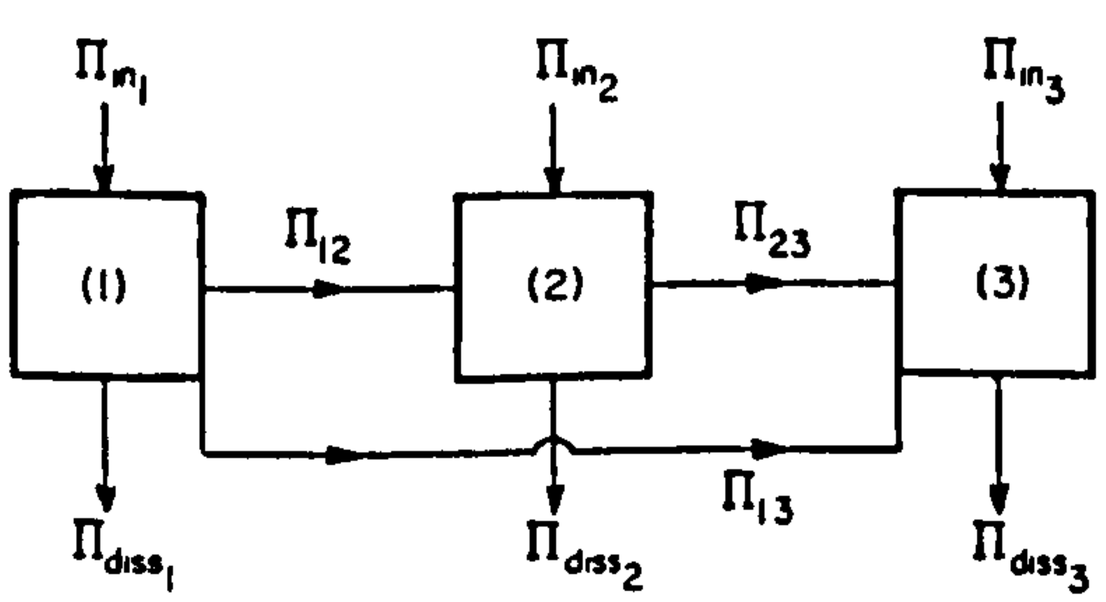

Figure 4. Block diagram representing energy flows between coupled systems of transmission suite.

be due to modes which are resonant outside of the frequency band under consideration. In this situation system 2 is non-resonant and acts only as a coupling element between systems 1 and 3. Providing the coupling factor is defined (i.e. a limp mass giving "mass law" power flow) this non-resonant power flow can be calculated. Since "mass law" transmission is derived assuming zero stiffness and damping in the partition and off resonance, these parameters are unimportant to the response; then Π_{13} can be derived from "mass law" transmission [13, 20].

4. PANEL RADIATION RESISTANCE AND COUPLING WITH ROOMS

4.1. RADIATION RESISTANCE OF PANEL IN REVERBERANT ROOM

Suppose a panel is suspended in a reverberant room and is excited by a shaker. The power flow is given by equations (1) to (4) with $\Pi_{in_1} = 0$. Making this substitution, equations (1) and (3) become equations (11) and (12), respectively:

$$0 = \Pi_{diss_1} + \Pi_{12}, \tag{11}$$

$$\Pi_{in_2} = \Pi_{diss_2} - \Pi_{12}. \tag{12}$$

Thus, combining equations (11) and (12),

$$\Pi_{in_2} = \Pi_{diss_2} + \Pi_{diss_1}. \tag{13}$$

The total power supplied to the panel by the shaker is

$$\Pi_{in_2} = E_2(R_{tot}/M_p) = M_p S_v(R_{tot}/M_p) = (S_a/\omega^2) R_{tot},$$

where

$$R_{tot} = R_{int} + R_{rad}.$$

The rate of energy dissipation by the panel in internal friction is

$$\Pi_{diss_2} = E_2(R_{int}/M_p) = (S_a/\omega^2) R_{int},$$

and the rate of internal energy dissipation by the room is

$$\Pi_{diss_1} = E_1 \beta_1 = [V_1 S_{p_1}/(\rho c^2)] \beta_1.$$

Substituting these expressions in equations (13) gives

$$(S_a/\omega^2) R_{tot} = (S_a/\omega^2) R_{int} + [V_1 S_{p_1}/(\rho c^2)] \beta_1,$$

and, on rearranging,

$$R_{rad} = \frac{\omega^2}{S_a \rho c^2} [S_{p_1} V_1 \beta_1]. \tag{14}$$

Equation (14) was used in the measurement of the radiation resistance described in section 6.3.1. of this paper. But $n_1 = (\omega^2 V_1)/(2\pi^2 c^3)$, thus equation (14) may be rewritten

$$R_{rad} = \frac{2\pi^2 c}{S_a \rho} [S_{p_1} n_1 \beta_1]. \tag{15}$$

Equation (15) is the result obtained by Lyon and Maidanik [3].

4.2. RADIATION RESISTANCE OF PANEL BETWEEN ROOMS

Suppose a panel is clamped between two reverberant rooms (Figure 3) and is excited by a shaker. The power flow is given by equations (5) to (10) with $\Pi_{in_1} = 0$ and $\Pi_{in_3} = 0$. Thus, with this substitution, equations (5) and (9) become equations (16) and (17), respectively:

$$0 = \Pi_{diss_1} + \Pi_{12} + \Pi_{13}, \tag{16}$$

$$0 = \Pi_{diss_3} - \Pi_{13} - \Pi_{23}. \tag{17}$$

Combining equations (16) and (17) and noting that since power flow must be directional, $\Pi_{21} = -\Pi_{12}$, gives equation (18):

$$\Pi_{\text{diss}_1} + \Pi_{\text{diss}_2} = \Pi_{21} + \Pi_{23}. \tag{18}$$

In this instance equation (7) is rewritten as

$$\Pi_{\text{in}_2} = \Pi_{\text{diss}_2} + \Pi_{21} + \Pi_{23}, \tag{19}$$

which becomes, on substituting equation (18),

$$\Pi_{\text{in}_2} = \Pi_{\text{diss}_2} + \Pi_{\text{diss}_1} + \Pi_{\text{diss}_3}. \tag{20}$$

Thus in a similar manner to section 4.1, equation (20) may be rewritten:

$$(S_a/\omega^2)\, R_{\text{tot}} = (S_a/\omega^2)\, R_{\text{int}} + [V_1\, S_{p_1}/(\rho c^2)]\,\beta_1 + [V_3\, S_{p_3}/(\rho c^2)]\,\beta_3.$$

$$R_{\text{rad}} = \frac{\omega^2}{S_a \rho c^2}\,[S_{p_1} V_1 \beta_1 + S_{p_3} V_3 \beta_3], \tag{21}$$

$$R_{\text{rad}} = \frac{2\pi^2 c}{S_a \rho}\,[S_{p_1} n_1 \beta_1 + S_{p_3} n_3 \beta_3]. \tag{22}$$

It is seen that equation (22) reduces to equation (15) if one of the rooms (system 3) is eliminated. Equation (21) was used in the measurement of radiation resistance described in section 6.3.2.

4.3. COUPLING FACTOR FOR PANEL IN REVERBERANT ROOM

If a panel is suspended in a reverberant room and a loudspeaker is driven in the room, the power flow is given by equations (1) to (4) with $\Pi_{\text{in}_2} = 0$. Thus equation (3) becomes

$$0 = \Pi_{\text{diss}_2} - \Pi_{12}, \tag{23}$$

$$\eta_2 E_2 = \eta_{12} n_1 \left(\frac{E_1}{n_1} - \frac{E_2}{n_2}\right). \tag{24}$$

Now Lyon and Scharton [12] and Ungar and Scharton [14] have shown that under most conditions encountered in practice

$$\eta_{12} n_1 = \eta_{21} n_2. \tag{25}$$

But $\eta_{21} = \eta_{\text{rad}}^{4\pi}$ and $\eta_2 = \eta_{\text{int}}$, thus equation (24) may be rewritten:

$$\mu = \frac{\eta_{\text{rad}}^{4\pi}}{\eta_{\text{int}} + \eta_{\text{rad}}^{4\pi}} = \left(\frac{E_2}{n_2}\right) \Big/ \left(\frac{E_1}{n_1}\right), \tag{26}$$

which may be rewritten using the expressions given for E_1, E_2 and n_1 in section 4.1.:

$$\mu = [S_a/S_{p_1}]\, \Gamma^{-1}, \tag{27}$$

where

$$\Gamma = 2\pi^2 [n_p(\omega)/M_p](c/\rho). \tag{28}$$

Equations (27) and (28) give the result obtained by Lyon and Maidanik [3].

4.4. COUPLING FACTOR FOR PANEL BETWEEN ROOMS

If the panel is excited by driving a loudspeaker in each room, then the power flow is given by equations (5) to (10) with $\Pi_{\text{in}_2} = 0$. Thus equation (7) becomes

$$0 = \Pi_{\text{diss}_2} - \Pi_{12} - \Pi_{32}, \tag{29}$$

$$\eta_2 E_2 = \eta_{12} n_1 \left(\frac{E_1}{n_1} - \frac{E_2}{n_2}\right) + \eta_{32} n_3 \left(\frac{E_3}{n_3} - \frac{E_2}{n_2}\right). \tag{30}$$

Thus in a similar manner to section 4.3, equation (30) may be rewritten:

$$\mu = \frac{\eta_{\text{rad}}}{\eta_{\text{int}} + 2\eta_{\text{rad}}} = \frac{E_2}{n_2} \Big/ \left[\frac{E_1}{n_1} + \frac{E_3}{n_3}\right]; \tag{31}$$

$$\mu = [S_a/(S_{p_1} + S_{p_3})]\, \Gamma^{-1}, \tag{32}$$

where Γ is given by equation (28). Equation (32) reduces to equation (27) if one of the rooms is eliminated.

5. SOUND TRANSMISSION AND PANEL RESPONSE

It is assumed that the panel is clamped between the transmission room and the reception room of the transmission suite. Reverberant sound is produced in the transmission room by a loudspeaker. In this case the noise reduction, E_1/E_3, and consequently the sound transmission loss produced by the panel and also the panel vibration amplitude may be determined from equations (5) to (10) with $\Pi_{\text{in}_2} = 0$ and $\Pi_{\text{in}_3} = 0$.

5.1. PANEL TRANSMISSION LOSS

Putting $\Pi_{\text{in}_2} = 0$ in equation (8) and using equation (25), equation (33) is obtained:

$$\frac{E_2}{n_2} = \frac{\left(\frac{E_1}{n_1}\right)\eta_{21} - \left(\frac{E_3}{n_3}\right)\eta_{23}}{\eta_2 + \eta_{21} + \eta_{23}}; \tag{33}$$

but $\eta_{21} = \eta_{23} = \eta_{\text{rad}}$ and, except at low frequency where the present theory does not apply, $E_1/n_1 \gg E_3/n_3$, thus equation (33) becomes

$$\frac{E_2}{n_2} = \frac{E_1}{n_1}\left[\frac{\eta_{\text{rad}}}{\eta_{\text{int}} + 2\eta_{\text{rad}}}\right]. \tag{34}$$

Putting $\Pi_{\text{in}_3} = 0$ in equation (10) yields

$$E_3 = \frac{E_1\,\eta_{13} + E_2\,\eta_{23}}{\eta_3 + \eta_{31} + \eta_{32}}. \tag{35}$$

This is a similar result to that found by Lyon [13], except that no terms are neglected in the present analysis. The term $E_1\,\eta_{13}$ represents the mass law or non-resonant transmission since it occurs without the modes resonant in the frequency band under consideration being excited. The term $E_2\,\eta_{23}$ represents the resonant transmission.

Substituting equation (34) in equation (35) gives

$$\frac{E_3}{E_1} = \frac{\eta_{13} + \eta_{\text{rad}}^2(n_2/n_1)/(\eta_{\text{int}} + 2\eta_{\text{rad}})}{\eta_3 + (n_1/n_3)\,\eta_{13} + (n_2/n_3)\,\eta_{\text{rad}}}. \tag{36}$$

Equation (36) gives the noise reduction from the transmission to the reception room. The parameters η_{13}, η_{rad} and η_3 can be evaluated from the following equations:

$$\eta_{\text{rad}} = \frac{R_{\text{rad}}^{2\pi}}{\omega M_p}, \tag{37}$$

where the panel radiation resistance to half space $R_{\text{rad}}^{2\pi}$ is given by Maidanik [4] as

$$R_{\text{rad}}^{2\pi} = A_p \rho c \cdot \begin{cases} (\lambda_c \lambda_a / A_p)\, 2(f/f_c)\, g_1(f/f_c) + (P\lambda_c/A_p)\, g_2(f/f_c), & f < f_c; \\ (l_1/\lambda_c)^{-1/2} + (l_2/\lambda_c)^{1/2}, & f = f_c; \\ (1 - f_c/f)^{-1/2}, & f > f_c, \end{cases} \tag{38}$$

where

$$g_1(f/f_c) = \begin{cases} (4/\pi^4)(1-2\alpha^2)/\alpha(1-\alpha^2)^{1/2}, & f < \tfrac{1}{2} f_c, \\ 0, & f > \tfrac{1}{2} f_c, \end{cases}$$

$$g_2(f/f_c) = (2\pi)^{-2}\{(1-\alpha^2)\ln[(1+\alpha)/(1-\alpha)] + 2\alpha\}/(1-\alpha^2)^{3/2},$$

$$\alpha = (f/f_c)^{1/2}.$$

It should be noted that the expression for $f < f_c$ given in reference 4 was in error, but the correct expression [21] (communicated by Maidanik), is given in equation (38). The expression for $f > f_c$ given in reference 4 was also incorrect and this has been corrected above.

The coupling loss factor η_{13} due to non-resonant mass-law transmission is obtained from [13]:

$$10\log_{10}\eta_{13} = -\text{T.L.} + 10\log_{10}\left(\frac{A_p c}{4V_1\omega}\right), \tag{39}$$

where T.L. is the random incidence mass law transmission loss value for the second system (the panel). Finally,

$$\eta_3 = \frac{2\cdot 2}{f T_3}. \tag{40}$$

If equations (37), (38), (39) and (40) are evaluated and a value for η_{int} is chosen, or else measured by experiment, then the noise reduction N.R. (in dB) can be evaluated by taking logs of equation (36):

$$\text{N.R.} = 10\log_{10}[\eta_{13} + \eta_{\text{rad}}^2(n_2/n_1)/(\eta_{\text{int}} + 2\eta_{\text{rad}})] - \\ -10\log_{10}[\eta_3 + (n_1/n_3)\eta_{13} + (n_2/n_3)\eta_{\text{rad}}], \tag{41}$$

where the room modal densities are

$$\left.\begin{aligned} n_1 &= \frac{V_1\omega^2}{2\pi^2 c^3}, \\ n_3 &= \frac{V_3\omega^2}{2\pi^2 c^3}. \end{aligned}\right\} \tag{42}$$

The transmission loss is then

$$\text{T.L.} = \text{N.R.} + 10\log_{10}\left[\frac{A_p c T_3}{24 V_3 \ln(10)}\right]. \tag{43}$$

5.2. RESPONSE OF PANEL

The panel vibration amplitude is given by equation (34). For a reverberant field the total energy in a 1 Hz bandwidth $E_1 = S_{p_1} V_1/(\rho c^2)$, and the total panel energy in a 1 Hz bandwidth $E_2 = M_p S_a/\omega^2$; hence equation (34) becomes

$$\frac{M_p S_a}{n_2\omega^2} = \frac{S_{p_1}}{\rho c^2}\frac{V_1}{n_1}\frac{\eta_{\text{rad}}}{\eta_{\text{int}} + 2\eta_{\text{rad}}}. \tag{44}$$

The modal density of the transmission room $n_1(\omega) = V_1\omega^2/(2\pi^2 c^3)$, while the modal density of the panel $n_2(\omega) = \sqrt{3}A_p/(2\pi h c_l)$, and the critical frequency $f_c = \sqrt{3}c^2/(\pi h c_l)$, thus

$$\frac{S_a}{S_{p_1}} = \frac{\eta_{\text{rad}}}{\eta_{\text{int}} + 2\eta_{\text{rad}}}\frac{\pi^2 f_c}{\rho_s \rho c}. \tag{45}$$

If the panel responded as a limp mass, the response would be

$$\frac{S_{a_{\text{m.l.}}}}{S_{p_w}} = \frac{1}{\rho_s^2}, \tag{46}$$

where S_{p_w} is the pressure spectral density at the panel surface. Neglecting panel motion, $S_{p_w} = 2S_{p_1}$, since there is pressure doubling for each wave arriving at the panel surface, although at any instant only half the waves are travelling towards the panel. Thus,

$$\frac{S_{a_{\text{m.l.}}}}{S_{p_1}} = \frac{2}{\rho_s^2}. \tag{47}$$

Dividing equation (45) by equation (47) gives the panel response relative to mass law:

$$\frac{S_a}{S_{a_{\text{m.l.}}}} = \frac{\eta_{\text{rad}}}{\eta_{\text{int}} + 2\eta_{\text{rad}}} \frac{\pi^2 f_c \rho_s}{2\rho c}. \tag{48}$$

6. EXPERIMENTAL MEASUREMENTS

Experiments were made to measure the radiation resistance, the total resistance, the coupling factor, the modal density, the transmission loss and the vibration response of an aluminium panel. The panel was $\frac{1}{8}$ in. thick and measured 77·5 by 61·0 in. when clamped in a frame. In some of the following experiments the panel was suspended from two corners in an anechoic room or in a 4500 ft^3 reverberant room. In these experiments the panel was surrounded by a 2 ft wide baffle and the narrow gap between the panel and baffle was sealed

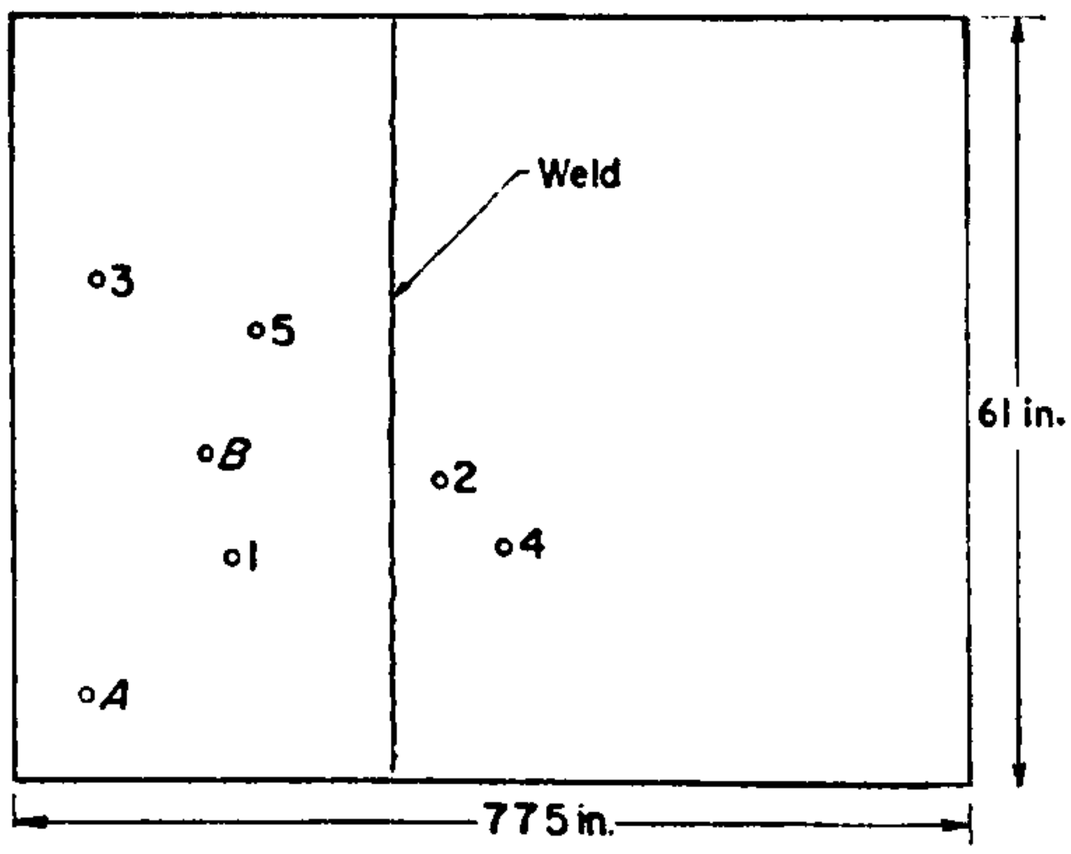

Figure 5. Positions on panel.

with a plastic tape. In the other experiments described here the panel was clamped in a frame between the transmission and reception rooms. The panel edge conditions were intended to be fully fixed and the frame was attached to the reception room (Figure 3) which was vibration-isolated from the transmission room with glass fibre. Unless otherwise stated the experiments in section 6 were conducted by supplying $\frac{1}{3}$-octave bands of white noise to the loudspeakers or shakers in use. Panel measurement positions are shown in Figure 5.

6.1. MEASUREMENTS OF PANEL MODAL DENSITY

The panel was suspended in an anechoic room and excited by a loudspeaker producing acoustic waves at grazing incidence and in a direction diagonally across the panel. The experimental arrangement is shown in Figure 6, where the sine-wave generator was driven at a very low speed from the level recorder. The output from an accelerometer was fed into the level recorder. A typical result is shown in Figure 7. The modal density was computed by counting the number of modes in a given frequency band and dividing by the bandwidth.

For a simply-supported panel the modal density is

$$n_p(f) = \frac{\sqrt{3} A_p}{c_l h}. \tag{49}$$

For aluminium, the speed of longitudinal waves is $c_l \approx 17{,}000$ ft/sec, and for the panel, $A_p = 37{\cdot}6\ \text{ft}^2$, $h = 1/96$ ft. Hence the modal density is

$$n_p(f) = 0{\cdot}36 \text{ modes/Hz}.$$

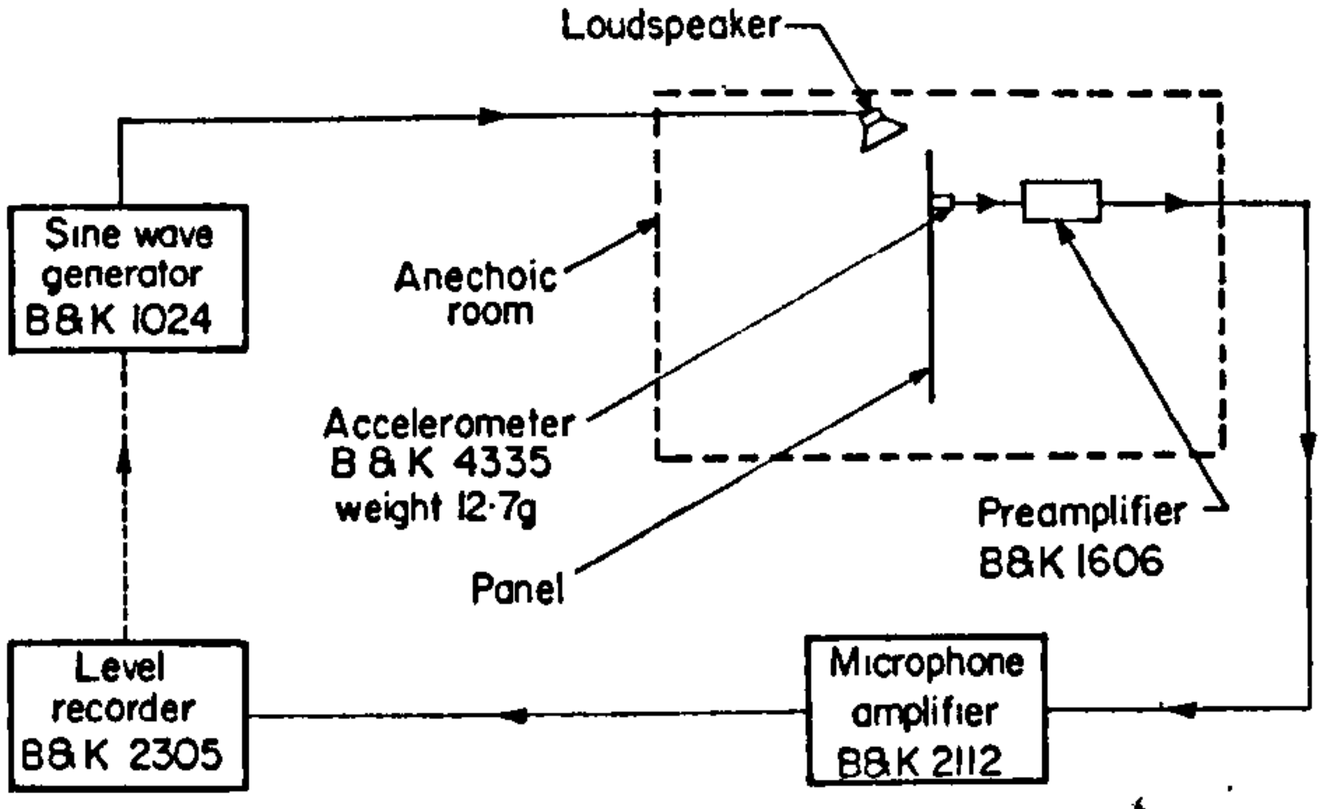

Figure 6. Experimental apparatus to measure panel modal density.

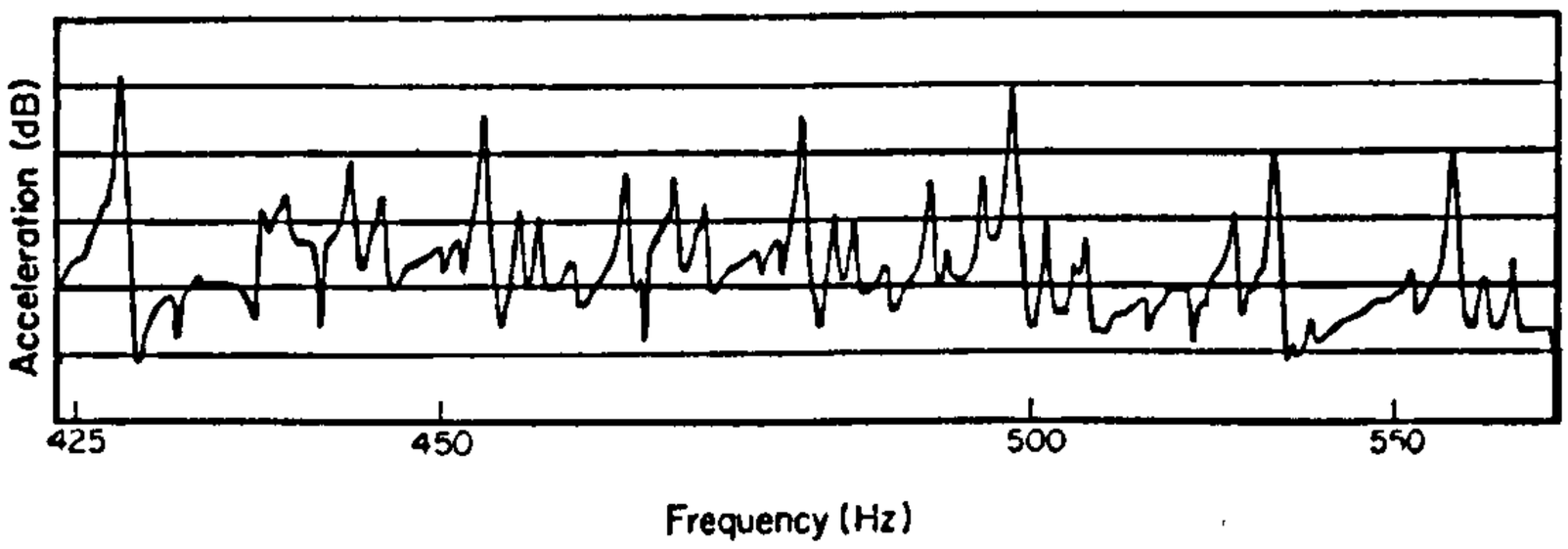

Figure 7. Modal resonances in panel.

Figure 8 shows that except at very low frequency (<20 Hz) the agreement between theory and experiment is good. The experiment was repeated with the panel clamped between the rooms.

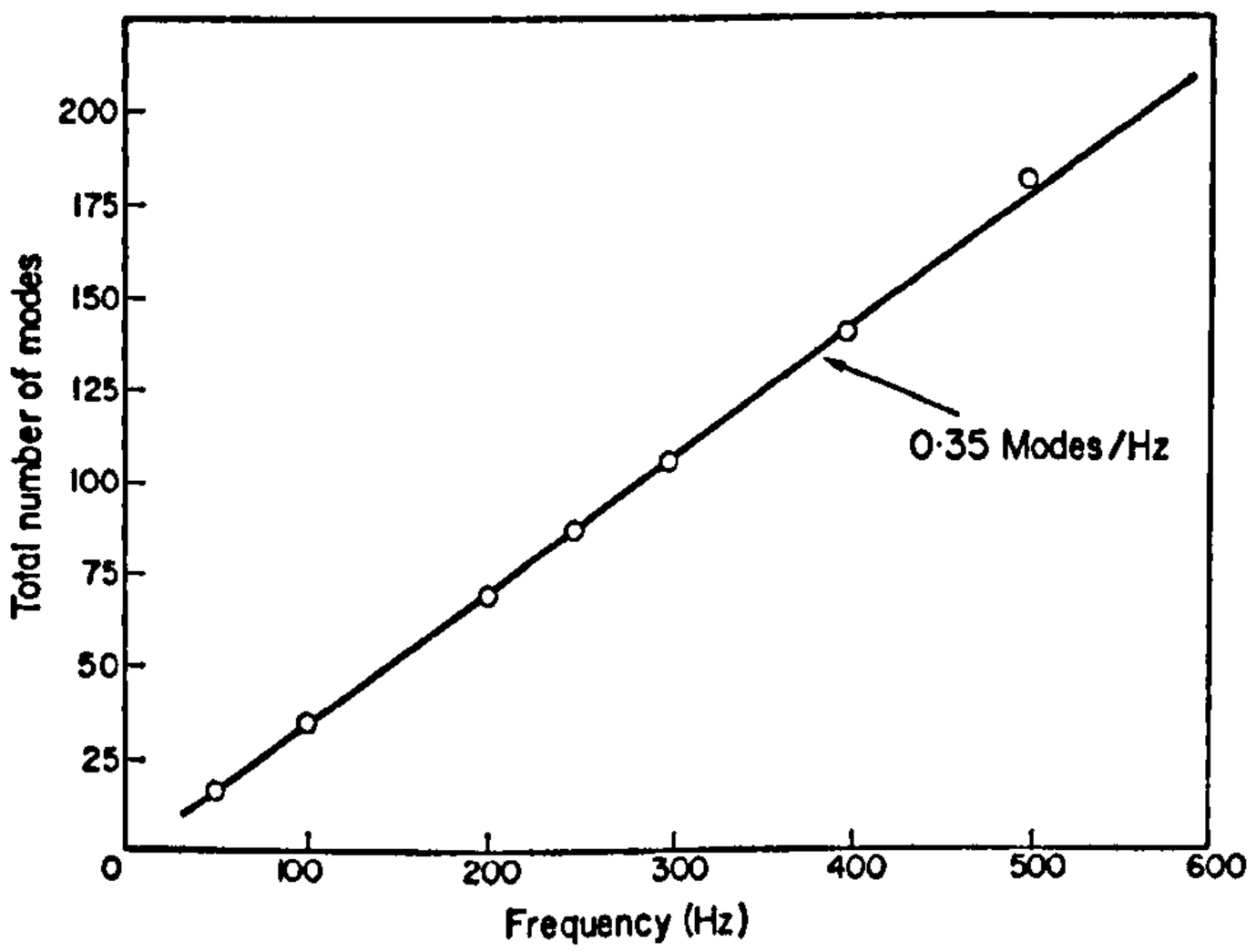

Figure 8. Modal density of panel.

The clamping reduced the area to 32·9 ft² and hence the theoretical modal density to 0·315 modes/Hz. This compared with a measured value of 0·303 in the mid-frequency range (about 500 Hz).

6.2. MEASUREMENT OF TOTAL RESISTANCE

The apparatus used is shown schematically in Figure 9. The panel was clamped at its edges between the two rooms and excited with a shaker near to one corner (Figure 5, position A). The panel damping was determined from decay measurements when excitation was abruptly terminated. Use of discrete tone excitation instead of $\frac{1}{3}$-octave bands of white noise ap-

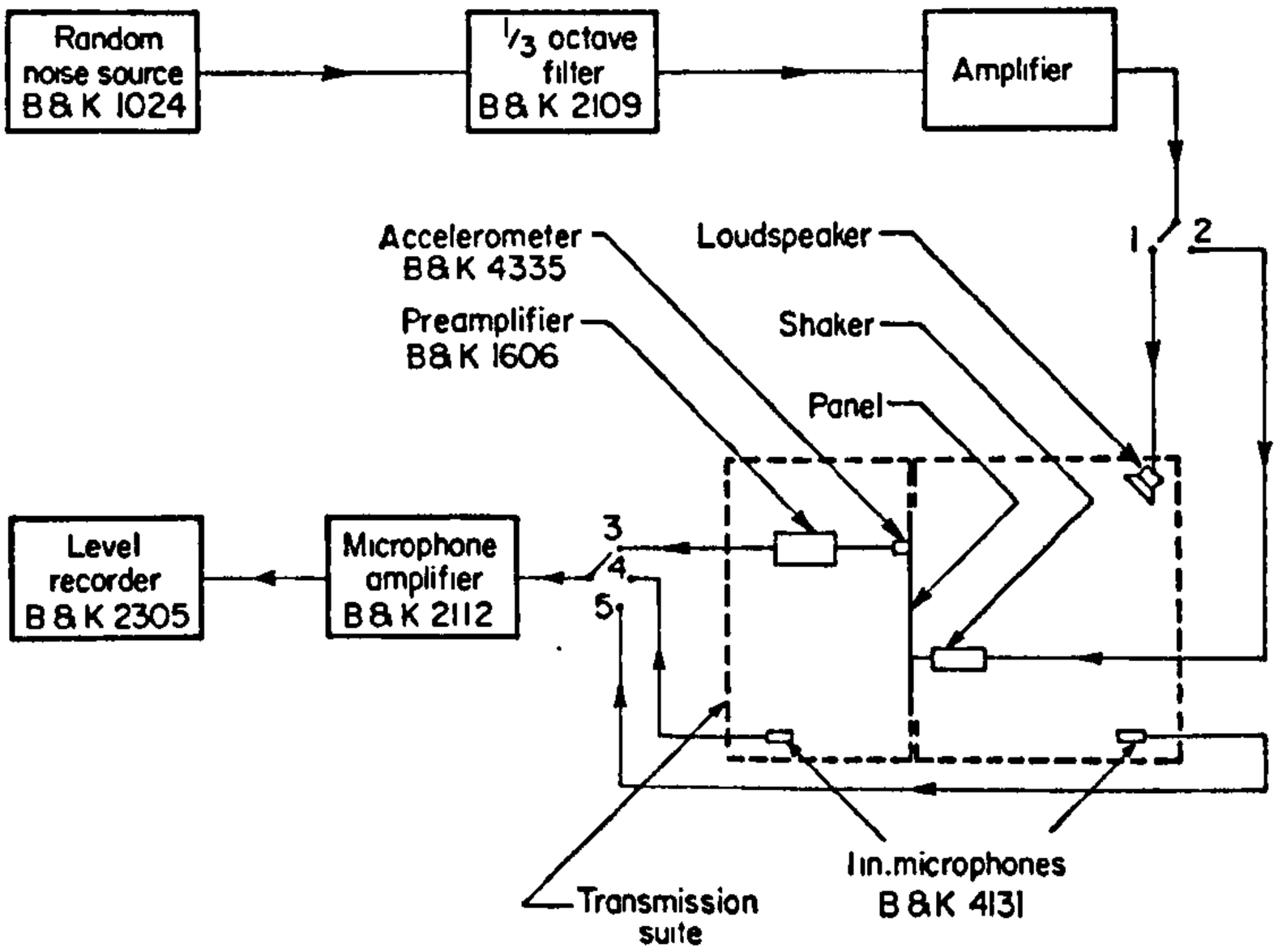

TABLE

Measurement	Switch positions
Total resistance	2, 3
Radiation resistance	2, 4 and 5
Noise transmission	1, 4 and 5
Vibration response	1, 3

Figure 9. Apparatus used to measure panel total resistance, radiation resistance, noise transmission and vibration response.

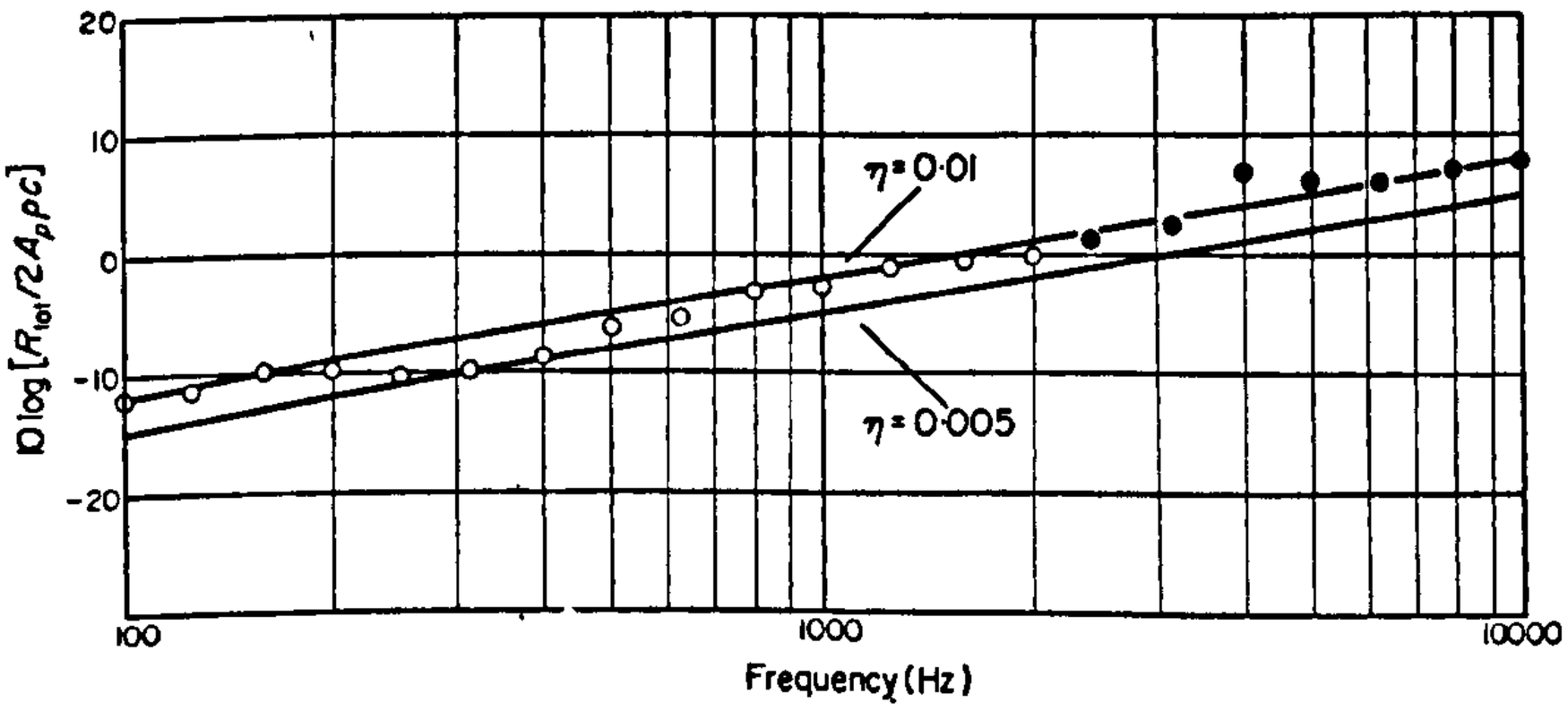

Figure 10. Normalized total resistance of panel: direct measurement (○); measured using reduced playback speed on tape-recorder (●).

peared to give rather inconsistent results, depending upon whether or not the frequency coincided with a modal resonance [22]. Due to limitations in the writing speed of the level

corder it was only possible to measure directly the total resistance of the panel up to 2000 Hz. Above this frequency it was necessary to use a tape-recorder and play back the signal at a slower speed. The plot of normalized total radiation resistance is given in Figure 10. The total resistance† was determined from

$$R_{tot} = (13{\cdot}8/T_2)\, M_p.$$

6.3. MEASUREMENT OF RADIATION RESISTANCE

6.3.1. *Baffled panel in reverberant room*

The panel was excited by a shaker attached at position B. The pressure levels were measured at two points in the room and the acceleration was measured at positions 2 and 3 on the panel

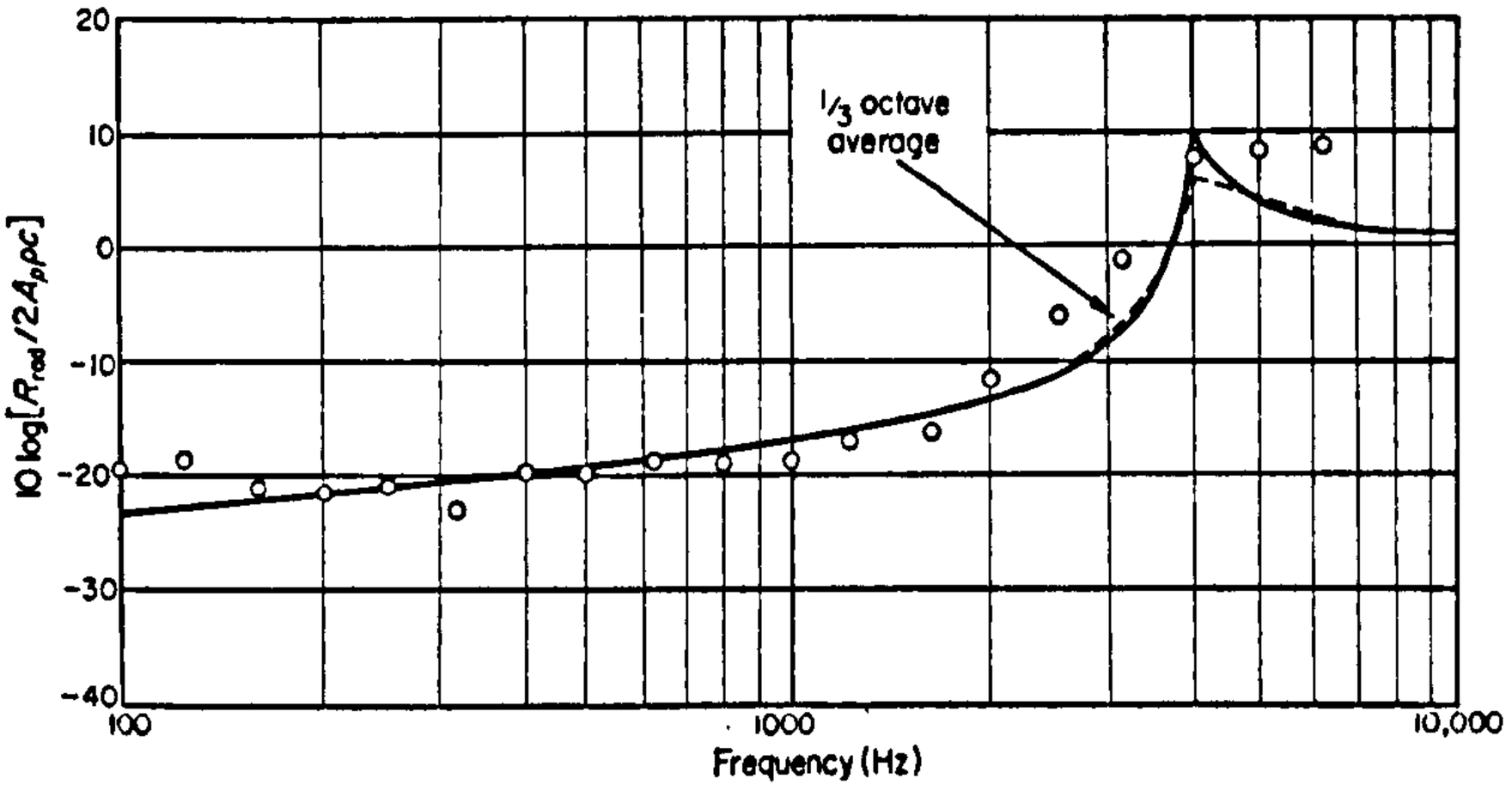

Figure 11. Normalized radiation resistance—baffled panel.

(see Figure 5). The reverberation time of the room against frequency was measured. The radiation resistance was calculated using equation (14) and averaged values of S_{p_1} and S_a. The results are plotted in Figure 11.

6.3.2. *Panel between rooms*

The radiation resistance was measured in a similar manner to section 6.3.1. The panel was excited by a shaker attached at position *A*. The pressure levels were measured at five positions

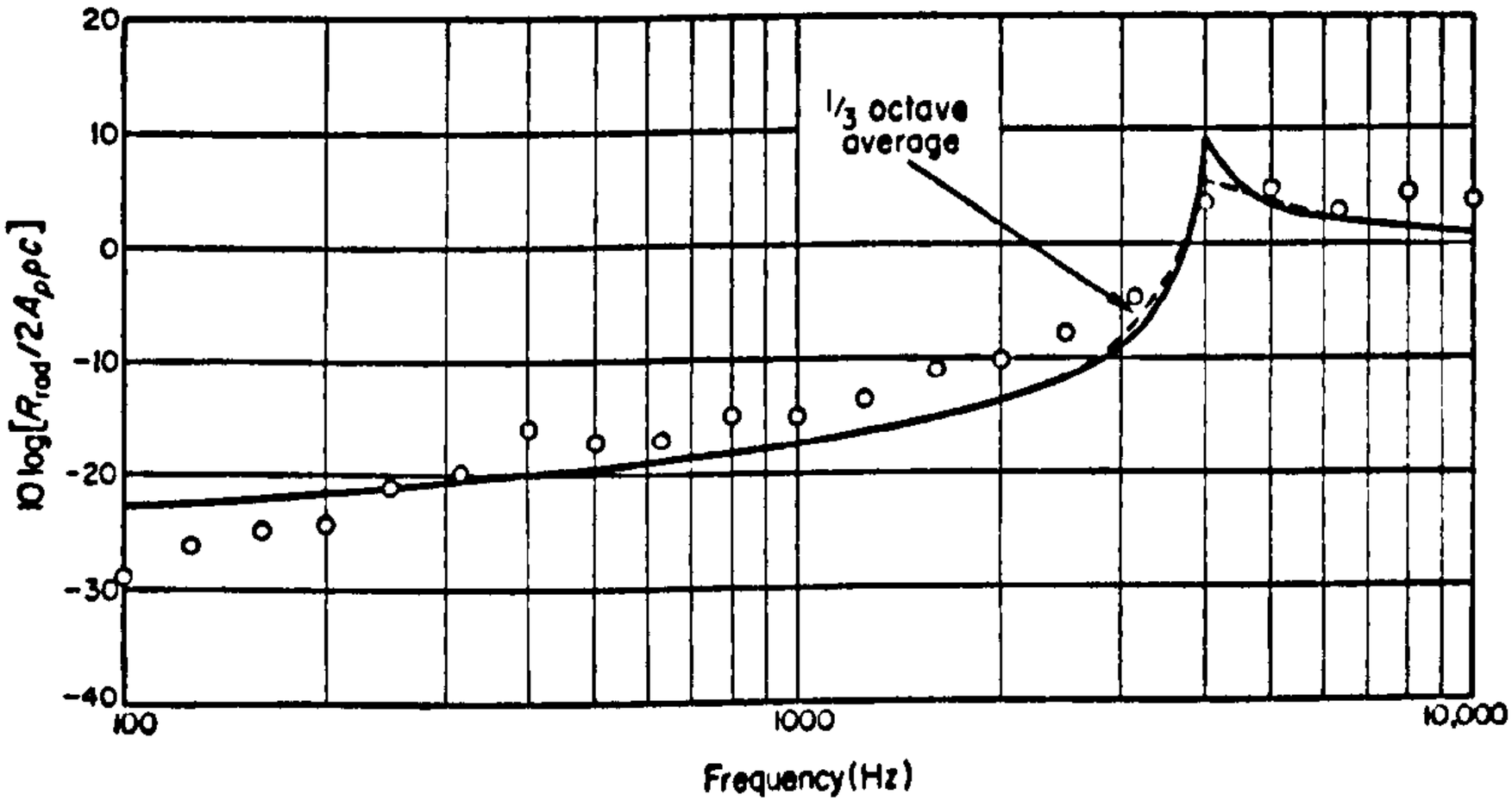

Figure 12. Normalized radiation resistance—panel between two rooms.

† It should be noted that the total resistance $R_{tot} = \beta M_p = \eta\omega M_p = 2\delta\omega M_p$.

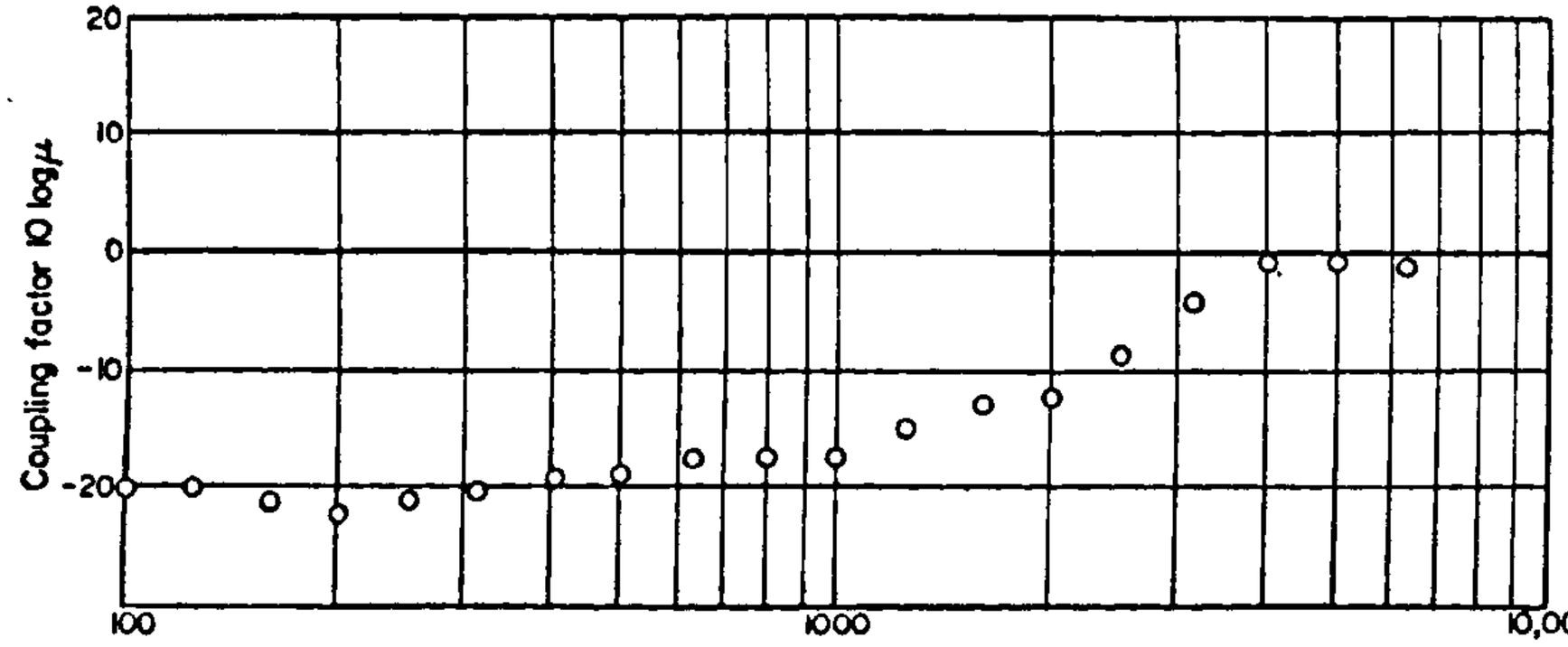

Figure 13. Coupling factor for baffled panel.

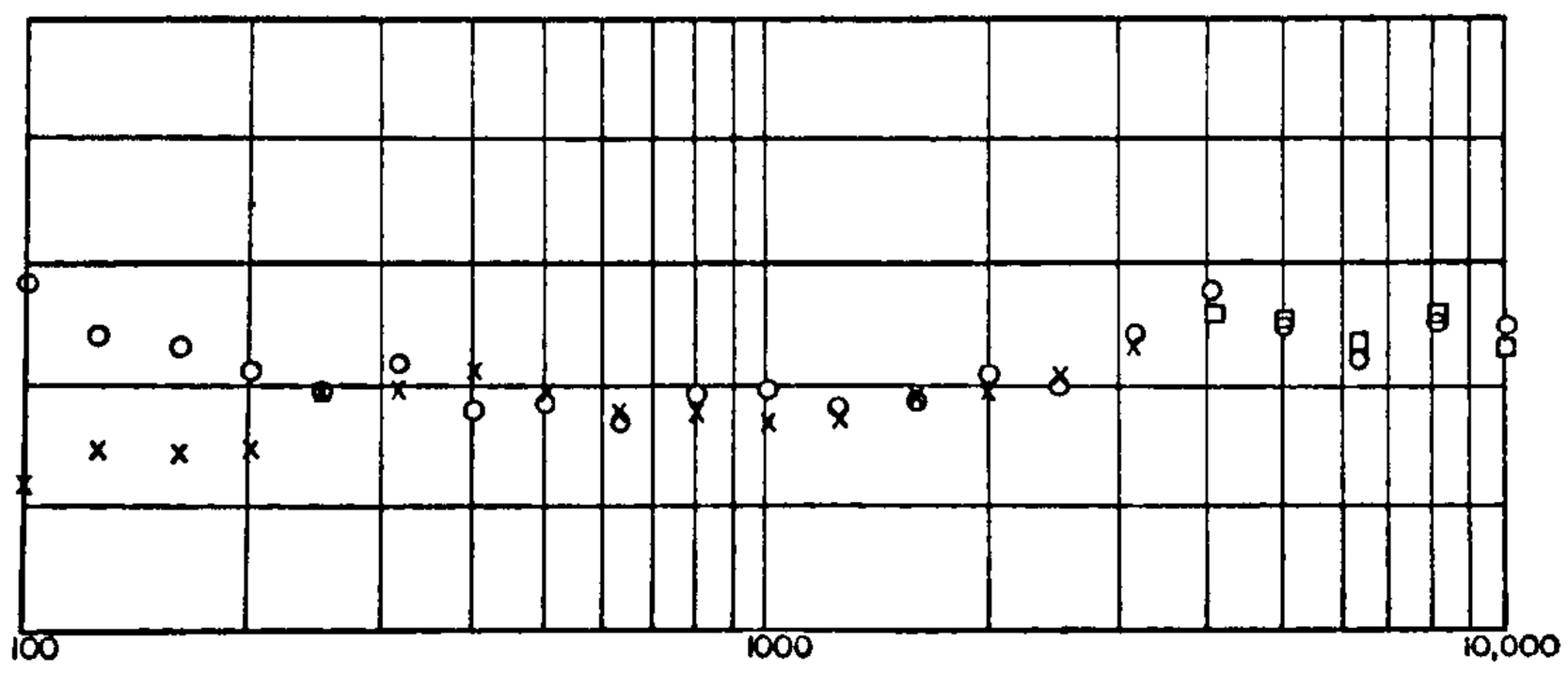

Figure 14. Coupling factor for panel between rooms. ○, Experiment; ×, deduced from measured $R_{rad}^{2\pi}$ and R_{tot}; □, deduced from measured $R_{rad}^{2\pi}$ and $\eta_{int} = 0{\cdot}01$.

in each room and the acceleration at five points on the panel (see Figure 5). The reverberation times of each room were measured (as a function of frequency) and the radiation resistance was calculated from equation (21) using averaged values of S_{p_1}, S_{p_3} and S_a. The result is plotted in Figure 12.

6.4. MEASUREMENT OF PANEL COUPLING FACTOR

6.4.1. *Baffled panel in reverberant room*

The panel was excited with reverberant white noise in $\frac{1}{3}$-octave bands from a loudspeaker at one corner in the room. The acceleration level was measured at five points on the panel and the pressure level at five points in the room. The coupling factor was calculated using equations (27) and (28) and arithmetically averaged values of S_{p_1} and S_a. The result is plotted in Figure 13.

6.4.2. *Panel between rooms*

The panel was again excited with reverberant white noise in $\frac{1}{3}$-octave bands. The noise was produced by feeding the same signal through different amplifiers to a loudspeaker in each room. At the beginning of the experiment the amplifier gains were adjusted until the levels in each room were approximately the same throughout the frequency range. The gains were then kept constant throughout the experiment. The acceleration level was measured at five points on the panel and the pressure level at five points in the room. The coupling factor was calculated using equations (32) and (28). The result is shown in Figure 14.

6.5. MEASUREMENT OF TRANSMISSION LOSS AND PANEL RESPONSE

6.5.1. *Transmission loss*

The panel was placed between the two large reverberant rooms (Figure 3). $\frac{1}{3}$-octave bands of white noise were made in the transmission room with a loudspeaker (Figure 9) and the levels recorded in each room. This was repeated at five positions of the microphone in each room. The reverberation time of the reception room was measured as a function of frequency. A plot of transmission loss calculated by the theory of section 5.1 is given in Figure 15.

6.5.2. *Panel response*

At the same time as the transmission loss experiment described above was performed, the acceleration of the panel was measured for five different panel positions (Figure 5). The panel response compared with mass law was calculated from equation (48) and is plotted in Figure 17.

7. DISCUSSION OF EXPERIMENTAL RESULTS

The total resistance of a panel R_{tot} is the sum of the internal resistance R_{int} and the radiation resistance R_{rad}. At low frequency, where the radiation resistance is small, the resistance of the panel is mostly due to the internal resistance. At the critical frequency the resistance is mostly due to the radiation resistance, but well above coincidence the total resistance again normally becomes dominated by the internal resistance. The measured values of total resistance, in general, tended to confirm the above hypotheses. Figure 10 shows that the total resistance lies between $\eta_{tot} = 0{\cdot}005$ and $0{\cdot}01$, below coincidence. This value agrees fairly closely with the value measured by Lyon for a similar sized aluminium panel of $\frac{1}{16}$ in. thickness [12].

The measurements of radiation resistance appear to agree well with the theory (Figures 11 and 12). The panel in Figure 11 was freely supported and baffled, while the panel in Figure 12 had clamped edges. The panel assumed in the theoretical comparison had simply-supported

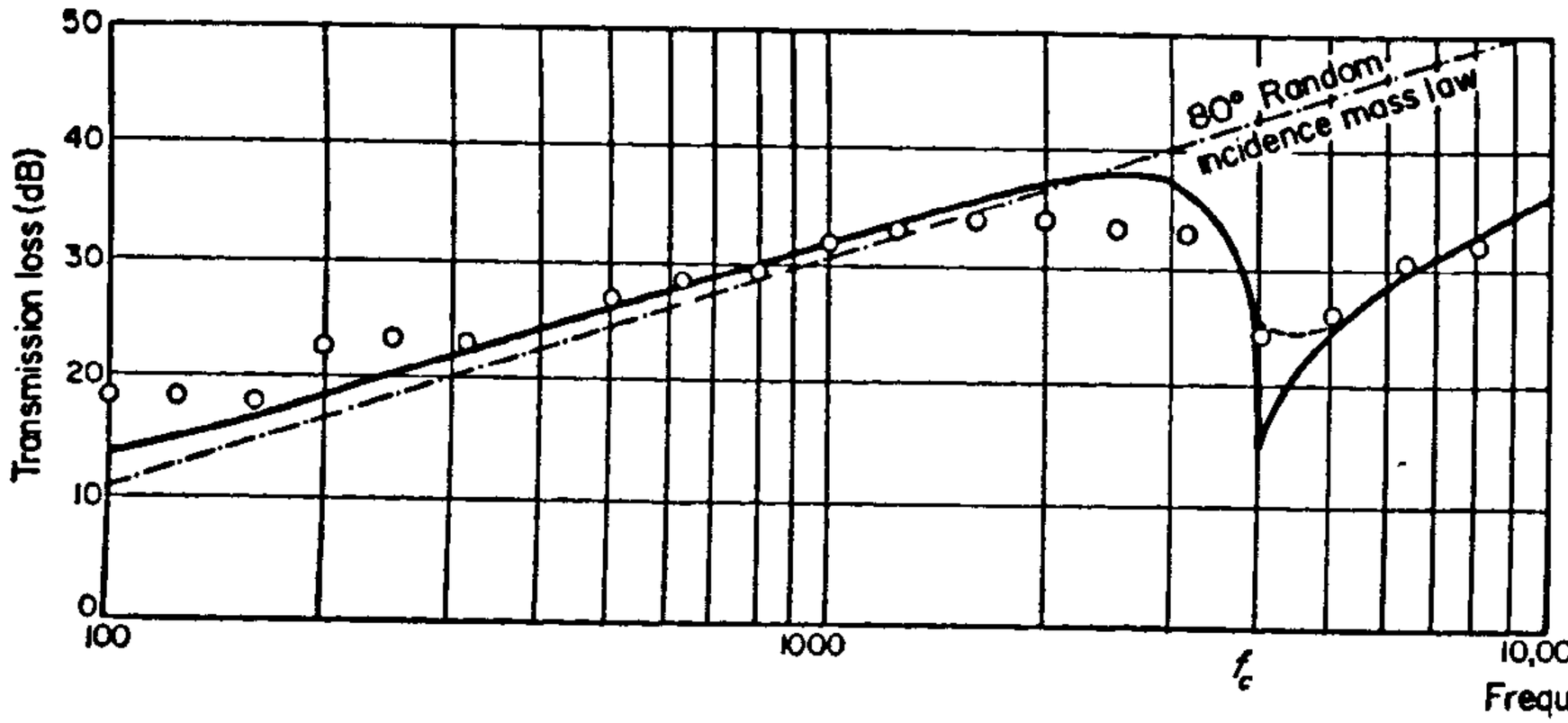

Figure 15. Experimental values of panel transmission loss compared with theoretical prediction. ---, $\frac{1}{3}$-octave average; ——, $\eta_{int} = 0{\cdot}005$.

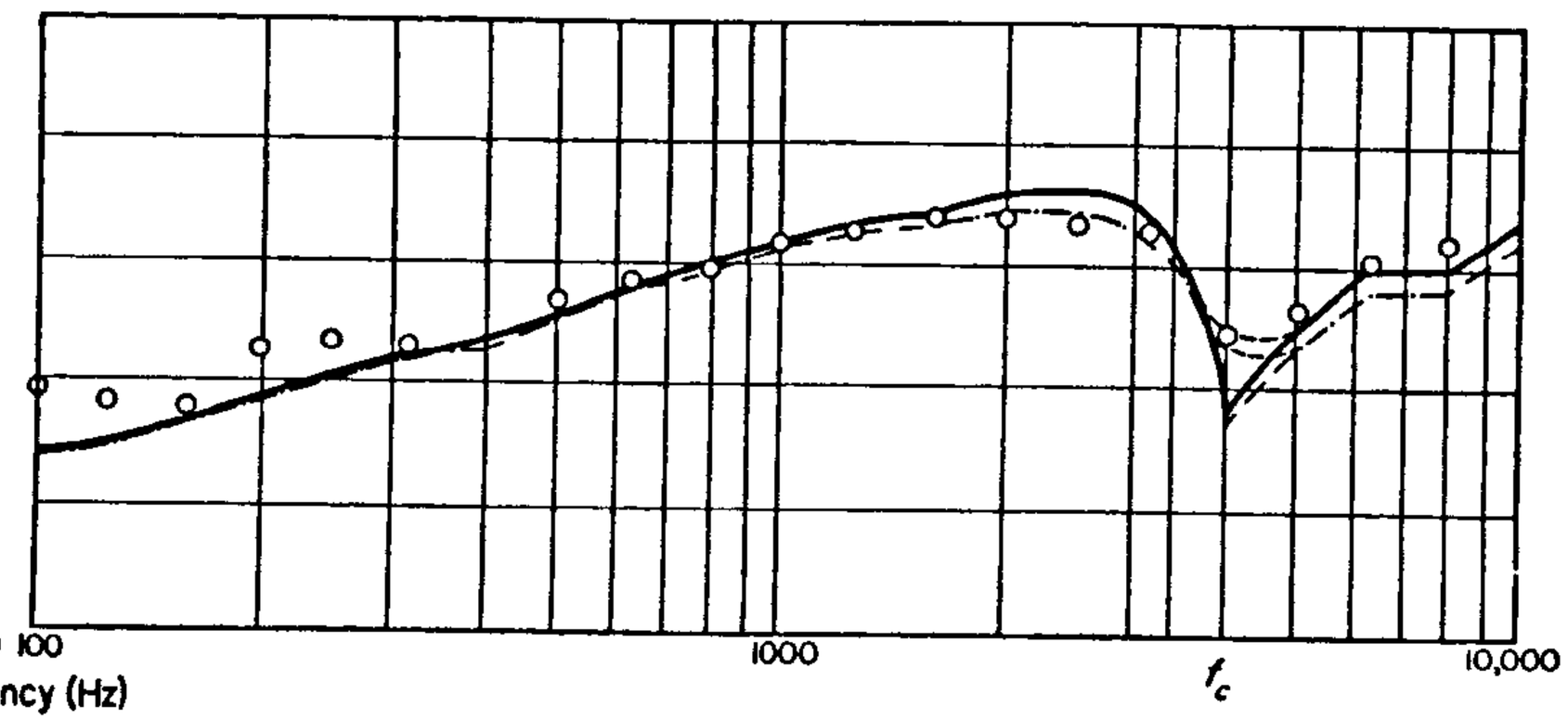

Figure 16. Comparison of experimental panel transmission loss with prediction using experimental values of R_{rad} for two values of η_{int}. ---, $\frac{1}{3}$-octave average; ——, $\eta_{int} = 0{\cdot}01$; —·—, $\eta_{int} = 0{\cdot}005$.

edges and the weld was assumed to act as a rib. It is probable that the difference in the mid-frequency range between Figures 11 and 12 is due to the different edge conditions. Maidanik states [4] that at low frequencies the radiation resistance of a clamped panel should be twice that of a simply-supported panel. The difference between the theoretical and experimental results in Figure 11 may be due to the inefficiency of the baffle at low frequencies.

The coupling of the panel with the rooms is shown in Figures 13 and 14. In the first case the coupling factor $\mu = R_{rad}/[R_{int} + R_{rad}]$. As expected the coupling factor $\mu \to 1$ above coincidence because $R_{rad} \gg R_{int}$ at and just above coincidence when the panel was freely-supported. However, when the panel was clamped between the two rooms, the coupling factor became $\mu = \frac{1}{2}R_{rad}/[R_{int} + R_{rad}]$ and the internal resistance was increased considerably. Thus, as expected, at and just above coincidence $\mu \to 0{\cdot}5$; also as the frequency increases above

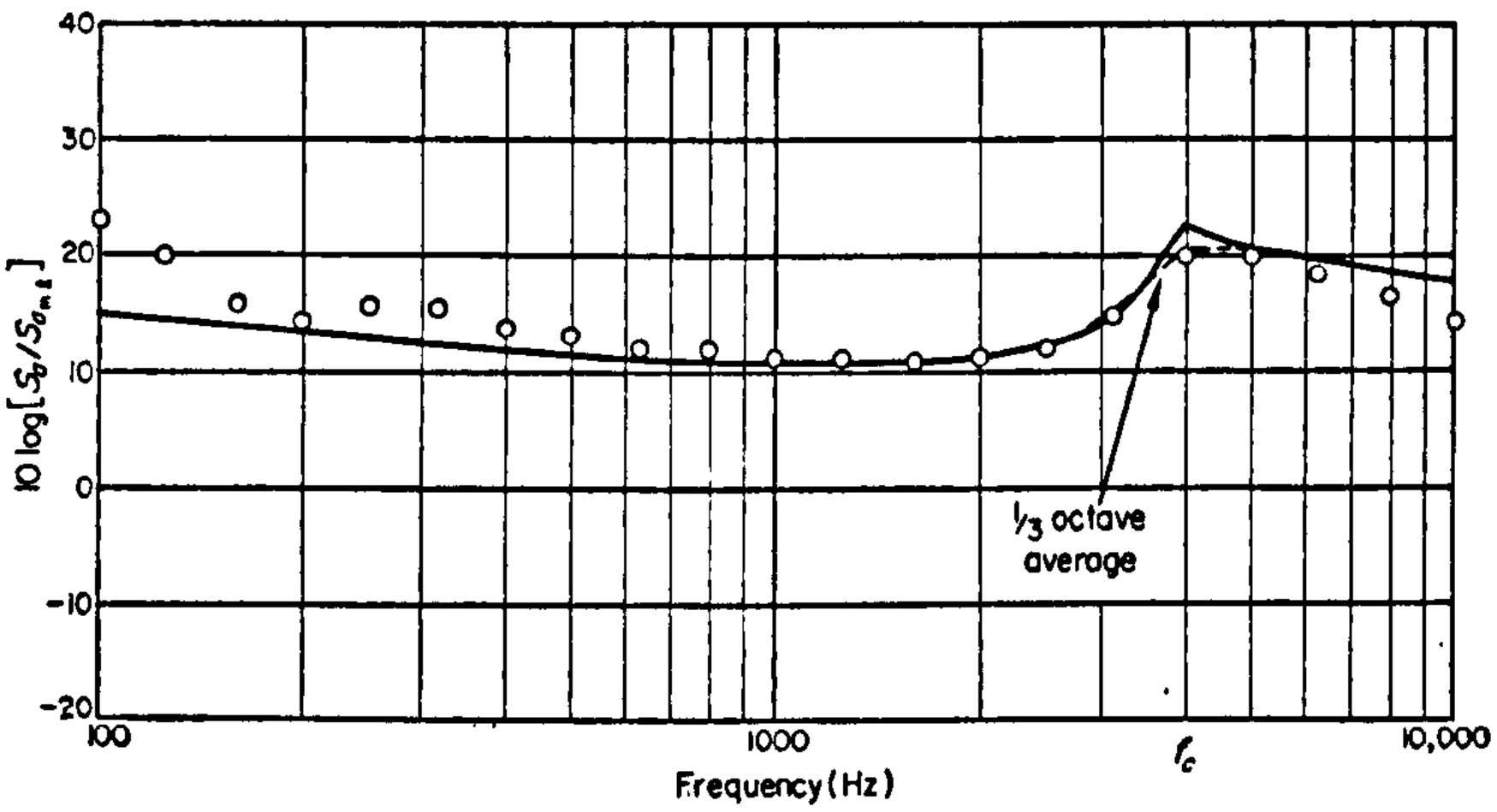

Figure 17. Panel response relative to mass law. $\eta_{int} = 0{\cdot}005$.

coincidence μ decreases again, due to the rapid relative increase in R_{int}. The agreement between the values of μ given in Figure 14 found from experiment (section 6.4.2) and those determined from experimental values of R_{rad} and R_{tot} is satisfactory, except at low frequency (<400 Hz). It is thought that the low-frequency disagreement, which is considerable, is due to the low-frequency panel/room modal interaction. At low-frequencies there are insufficient panel modes to make a correct average, a fact which is not included in the present theory.

Figure 15 shows a comparison between the transmission loss of the panel measured experimentally and that calculated using the theory of section 5.1. The value of η_{int} used in the theoretical calculation was 0·005 and the theoretical values of η_{rad} used were determined from Maidanik's expressions for a simply-supported panel [equation (38)]. It is seen that agreement between experiment and theory is good, with two exceptions. These are at low frequency (<400 Hz) and just below coincidence. The low-frequency disagreement is again thought to be due to room mode/panel mode coupling as also observed in the coupling factor experiment and discussed above. The apparent discrepancy just below coincidence is removed if experimental values of η_{rad} are used in the calculations (see Figure 16).

The measured acceleration level of the panel above mass law as compared with that predicted by the theory is given in Figure 17. For the theoretical prediction a value of $\eta_{int} = 0{\cdot}005$, and η_{rad} determined from Maidanik's expressions were again used. A similar low-frequency discrepancy to that observed in the other experiments was again apparent. The agreement is otherwise remarkably good. Above coincidence the experimental values start to fall below the theoretical curve; part of this disagreement above coincidence is probably

due to mass loading of the panel by the accelerometer. No correction was made for mass loading which was expected to be of the order of 1 or 2 dB in this frequency region.

8. CONCLUSIONS

"Statistical energy analysis" has been shown to provide a useful way of predicting the transmission loss of a panel. This analysis obviously has its uses in classical architectural transmission loss problems as well as in aerospace transmission loss predictions. The vibration amplitude of a partition has also been satisfactorily predicted thus explaining the previously observed discrepancy [1] between the experimental partition response and that predicted by mass law.

ACKNOWLEDGMENTS

The authors would like to thank Dr R. H. Lyon and Dr G. Maidanik for discussions and helpful comments and suggestions. The authors are indebted to Professor H. D. Parbrook for his encouragement. The research was supported by the Science Research Council.

REFERENCES AND BIBLIOGRAPHY

1. W. A. Utley and K. A. Mulholland 1967 *J. Sound Vib.* **6**, 419. Measurement of transmission loss using vibration transducers.
2. P. W. Smith 1962 *J. acoust. Soc. Am.* **34**, 640. Response and radiation of structural modes excited by sound.
3. R. H. Lyon and G. Maidanik 1962 *J. acoust. Soc. Am.* **34**, 623. Power flow between linearly coupled oscillators.
4. G. Maidanik 1962 *J. acoust. Soc. Am.* **34**, 809. Response of ribbed panels to reverberant acoustic fields.
5. R. H. Lyon 1962 *J. acoust. Soc. Am.* **35**, 1265. Sound radiation from a beam attached to a plate.
6. P. W. Smith and R. H. Lyon 1965 *NASA CR*-160. Sound and structural vibration.
7. E. Buckingham 1925 *Scientific Papers of the Bureau of Standards No.* 506. Theory and interpretation of experiments on the transmission of sound through partition walls.
8. A. L. Kimball 1936 *J. acoust. Soc. Am.* **7**, 222. Theory of transmission of plane sound waves through multiple partitions.
9. L. L. Beranek and G. A. Work 1949 *J. acoust. Soc. Am.* **21**, 419. Sound transmission through multiple structures containing flexible blankets.
10. A. London 1949 *J. Research Nat. Bur. of Stand.* **42**, RP 1998, 605. Transmission of reverberant sound through single walls.
11. A. London 1950 *J. acoust. Soc. Am.* **22**, 270. Transmission of reverberant sound through double walls.
12. R. H. Lyon and T. D. Scharton 1965 *J. acoust. Soc. Am.* **38**, 253. Vibrational-energy transmission in a three-element structure.
13. R. H. Lyon 1966–67 Lecture notes from *Bolt, Beranek and Newman Inc. Program for Advanced Study—Aerospace Noise and Vibration, Los Angeles.* Ch. IX.
14. E. E. Ungar and T. D. Scharton 1967 *Shock Vibr. Bull.* **36**, Pt. 5, 41. Analysis of vibration distributions in complex structures.
15. R. H. Lyon, C. W. Dietrich, E. E. Ungar, R. W. Pyle and R. E. Apfel 1966 *NASA CR*-589. Low-frequency noise reduction of spacecraft structures.
16. R. H. Lyon and E. Eichler 1964 *J. acoust. Soc. Am.* **36**, 1344. Random vibration of connected structures.
17. E. Eichler 1965 *J. acoust. Soc. Am.* **37**, 995. Thermal circuit approach to vibrations in coupled systems and the noise reduction of a rectangular box.
18. D. E. Newland 1968 *J. acoust. Soc. Am.* **43**, 553. Power flow between a class of coupled oscillators.
19. E. E. Ungar 1966 *AFFDL-TR*-66-52. Fundamentals of statistical energy analysis of vibrating systems.
20. R. H. Lyon 1967 *Shock and Vibration Information Center, United States Department of Defence, Monograph SVM*-1. Random noise and vibration in space vehicles.
21. G. Maidanik 1968 Private Communication.
22. A. J. Price and M. J. Crocker 1968 *University of Liverpool, Department of Building Science Report BS/A*/68-2. The theory and measurement of radiation from panels.

APPENDIX: LIST OF SYMBOLS

A_p panel surface area
c speed of sound in air
c_l speed of longitudinal panel waves
E_i total energy in ith system
f frequency
f_c critical or coincidence frequency
g_1, g_2 functions of f/f_c
h panel thickness
i, j integer subscripts representing system numbers ($i = 1, 2, 3$ and $j = 1, 2, 3$)
l_1, l_2 length, breadth of panel
M_p total panel mass modal density of ith system in radian frequency
n_i model density of the ith system in radian frequency
n_p modal density of panel
P perimeter of panel (including twice length of weld)
R_{int} internal resistance of panel
R_{rad} radiation resistance of panel to whole space
$R_{rad}^{2\pi}$ radiation resistance of panel to half space
R_{tot} total resistance of panel
S_a spectral density of panel acceleration
$S_{a_{m.l.}}$ spectral density of panel acceleration predicted by mass law
S_{p_1} spectral density of pressure in transmission room or reverberant room
S_{p_2} spectral density of pressure in reception room
S_v spectral density of panel velocity
T_i reverberation time of ith system
V_1 volume of transmission room or reverberant room
V_3 volume of reception room
β_1 energy decay constant for transmission room or reverberant room
β_3 energy decay constant for reception room
η_i internal loss factor for ith system
η_{ij} coupling loss factor from ith to jth system
η_{int} internal loss factor for panel
η_{rad} radiation loss factor for panel (to half space)
$\eta_{rad}^{4\pi}$ radiation loss factor for panel (to whole space)
η_{tot} total loss factor for panel
λ_a acoustic wavelength
λ_c coincidence wavelength of panel
μ coupling factor between acoustic field and panel
Π_{ij} power flow from ith to jth system
Π_{diss_i} power dissipated internally by ith system
Π_{in_i} power supplied to ith system
ρ air density
ρ_s panel surface density
ω angular frequency

J. Sound Vib. (1969) 9 (3), 501–508

LETTERS TO THE EDITOR

DAMPING IN PLATES

In a recent paper [1], measured total loss factors for plain and stiffened panels were presented. These factors were determined by recording the decay of strain following impulsive excitation. In previous experiments at Liverpool University the present authors had already attempted to make similar measurements of panel damping and were forced to reject impulsive excitation as unsatisfactory for determining total loss factors in $\frac{1}{3}$ octave bandwidths. There were two reasons for this decision. The first was that the value of loss factor deduced seemed to depend upon size and hardness of the hammer used to produce the impulsive excitation. The second was that the loss factors deduced from this method did not agree throughout most of the frequency range under examination with those determined from the decay of vibration produced by a mechanical shaker, or by a loudspeaker, supplied with $\frac{1}{3}$ octave bands of white noise. The authors have subsequently studied this interesting phenomenon further and give the results of some experiments and their conclusions below.

The total loss factor for an aluminium panel measuring 61 × 77·5 × $\frac{1}{8}$ in. thick was deduced both from the decay of acceleration following the decay of steady-state vibration produced by a mechanical shaker and from the decay of acceleration following impulsive excitation. The panel boundary conditions at the edges were intended to be clamped. The panel was plain with the exception of a vertical weld near the panel centre.

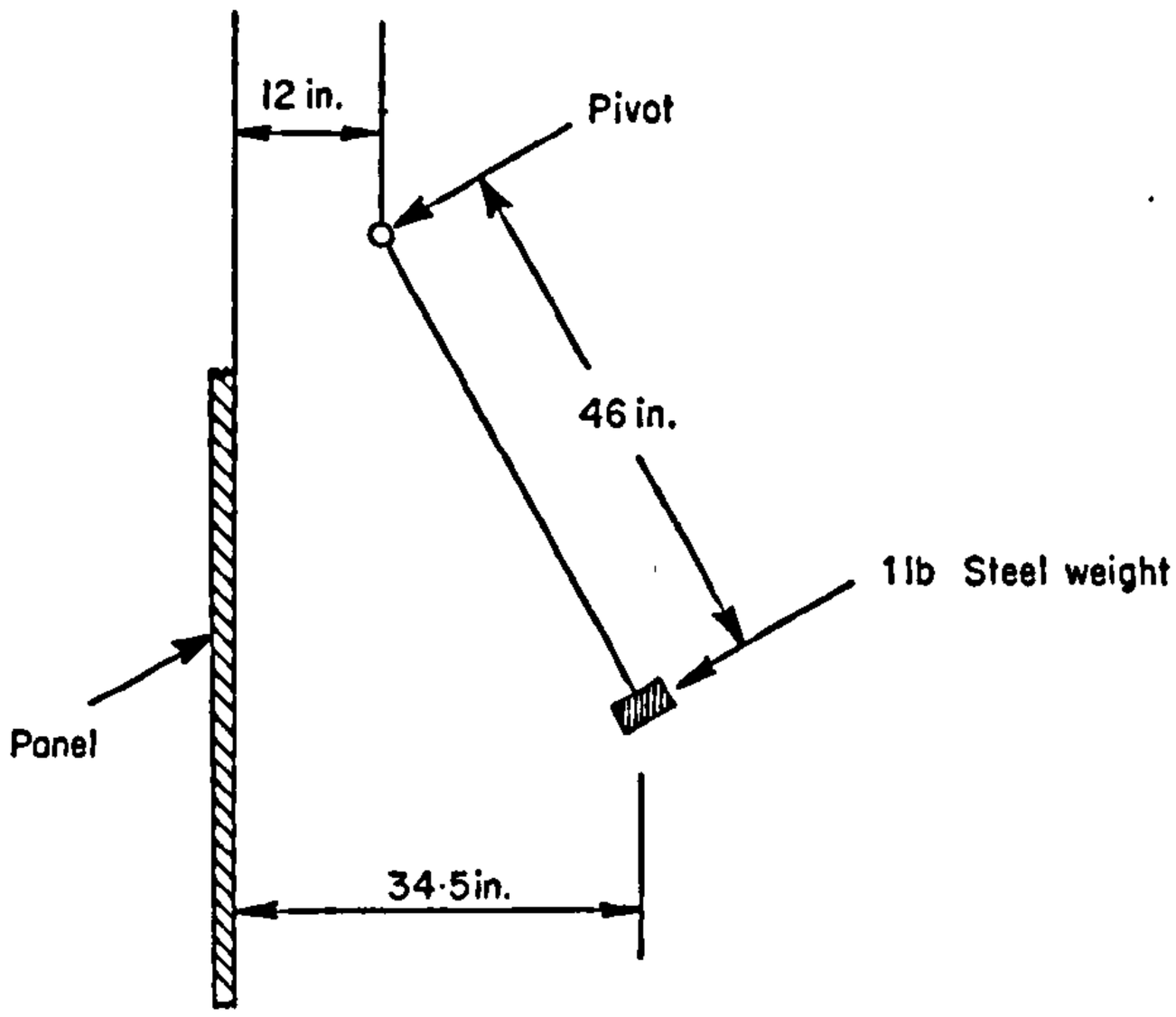

Figure 1. Sketch of mechanism for producing impulsive excitation.

The impulsive excitation was repeatedly produced by allowing a 1 lb steel weight to swing against the panel as shown in Figure 1. Records of the decay of the acceleration were made by recording the output from a Brüel and Kjær 4335 accelerometer on a B & K 2305 level recorder. The signal from the accelerometer was fed through a $\frac{1}{3}$ octave filter and traces were obtained for decays for each $\frac{1}{3}$ octave centre frequency from 100 to 1000 Hz. Typical records of 400 and 800 Hz are shown in Figure 2. The records are characterized by fluctuations about a mean decay of roughly constant slope at low frequency. At higher frequency the fluctuations

decrease in magnitude but the slope steadily decreases in value with time. For comparison a total loss factor was calculated by determining the mean slope of the first 5, 15 and 25 dB decay

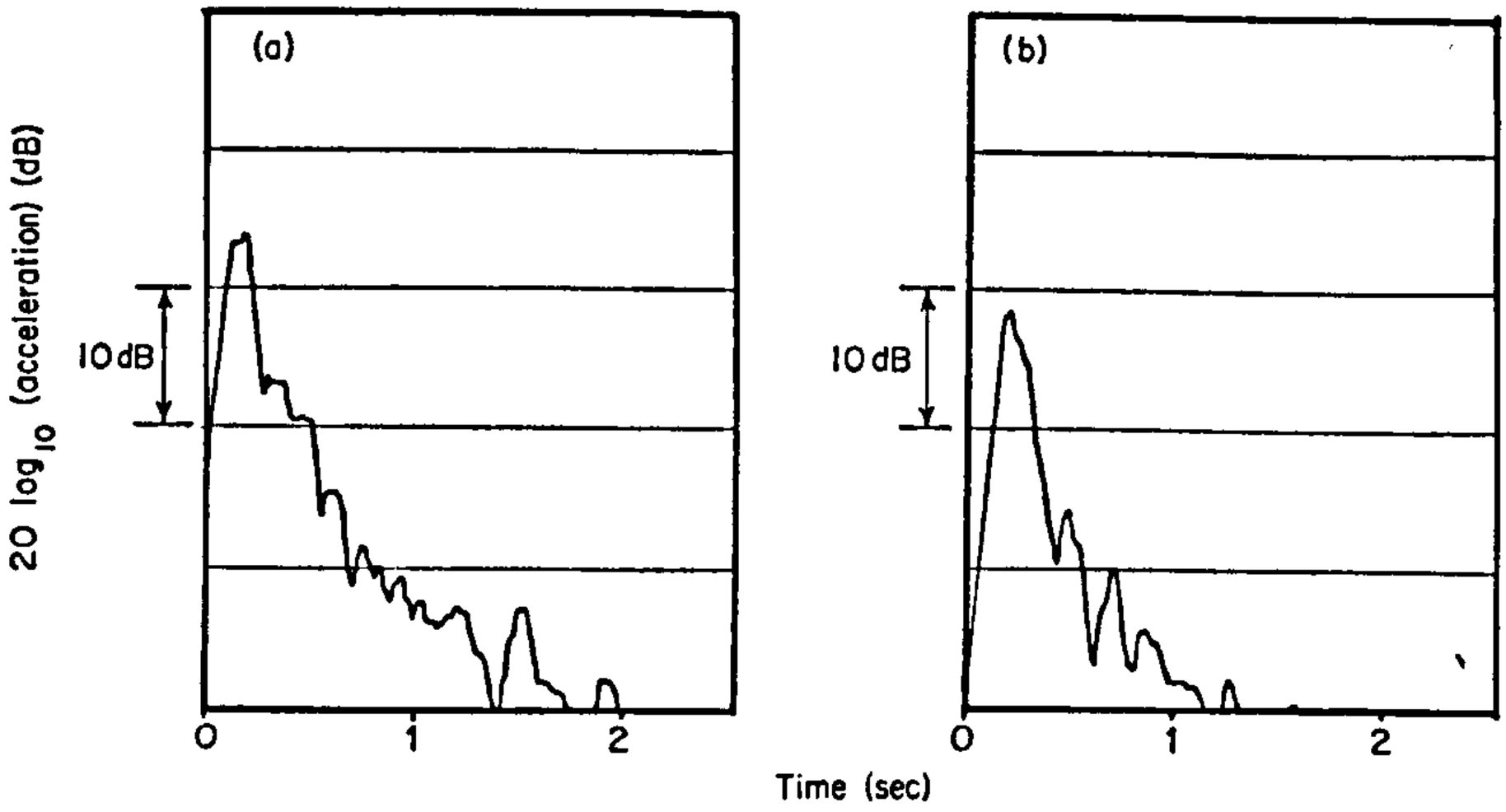

Figure 2. Typical ⅓ octave band filtered records of acceleration decay produced after impulsive excitation. (a) Centre frequency 400 Hz; (b) centre frequency 800 Hz.

of each record. The results are plotted in Figure 3. The records were also used to determine the approximate amplitude–frequency response of the panel to the impulse by measuring the peak acceleration level of each ⅓ octave record. These levels are plotted in Figure 4.

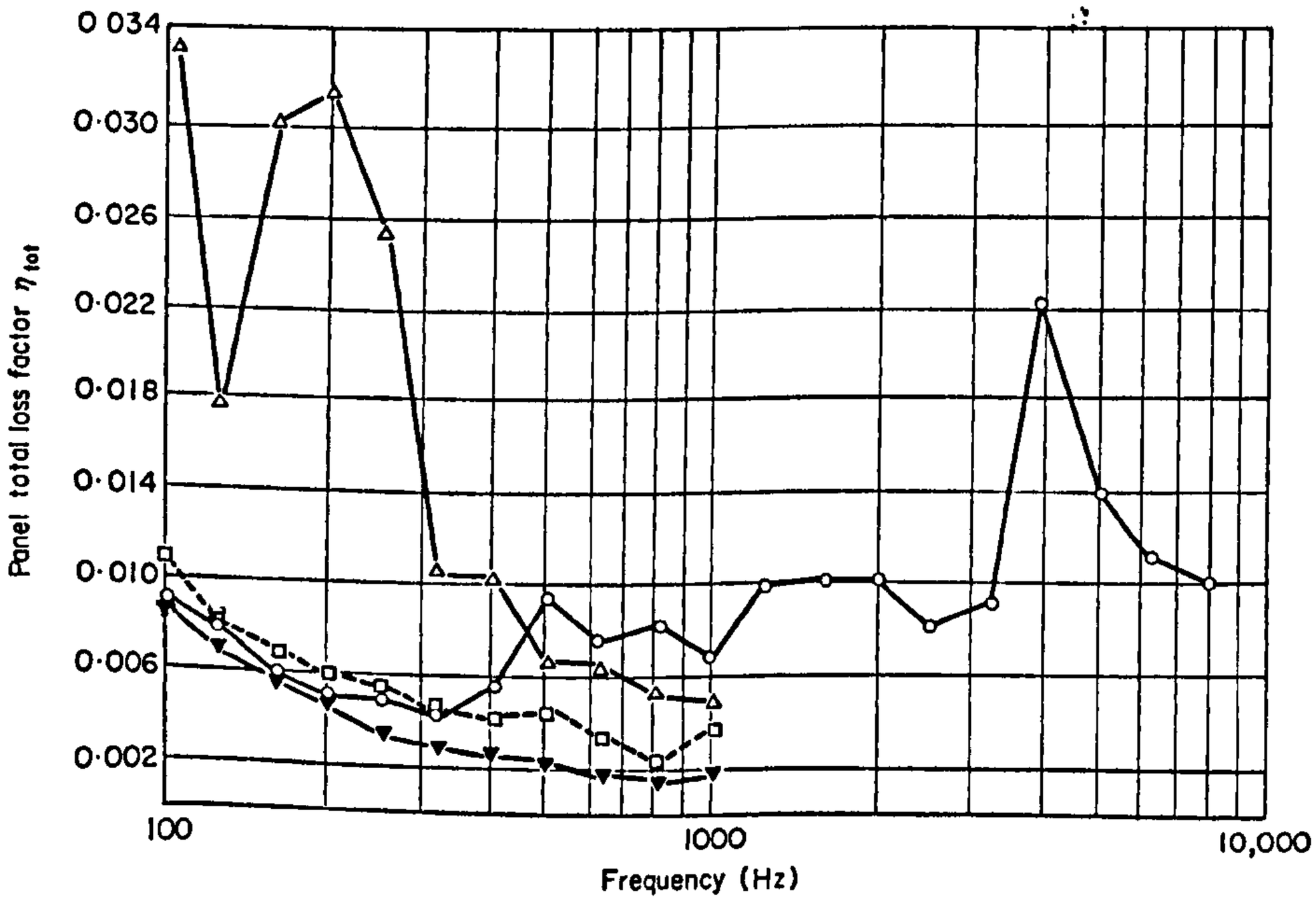

Figure 3. Total loss factor of panel. —▼—, Impulsive exitation, first 25 dB of record; — — □ — —, impulsive excitation, first 15 dB of record; —Δ—, impulsive exitation, first 5 dB of record; —○—, white noise excitation first 15 dB of record.

The panel was also excited by supplying with "white noise" a Goodmans shaker attached near to a corner. The signal from an accelerometer filtered through a ⅓ octave filter was recorded on a level recorder at frequencies up to 1000 Hz as before. Typical records of 400 and

800 Hz are shown in Figure 5. The recorder traces had a very different appearance from those obtained from the decay of impulsive excitation.

In this instance they were characterized by fluctuations about a mean decay whose slope remained constant for a greater duration at each frequency than for impulsive excitation. At higher frequencies this was particularly noticeable. It is also interesting to note the appearance of very lightly damped modes at the end of the higher frequency traces. Values of total loss factor were deduced from the mean slope of the first 15 dB decay of each record and the results are plotted in Figure 3. Using this method of excitation the most consistent results

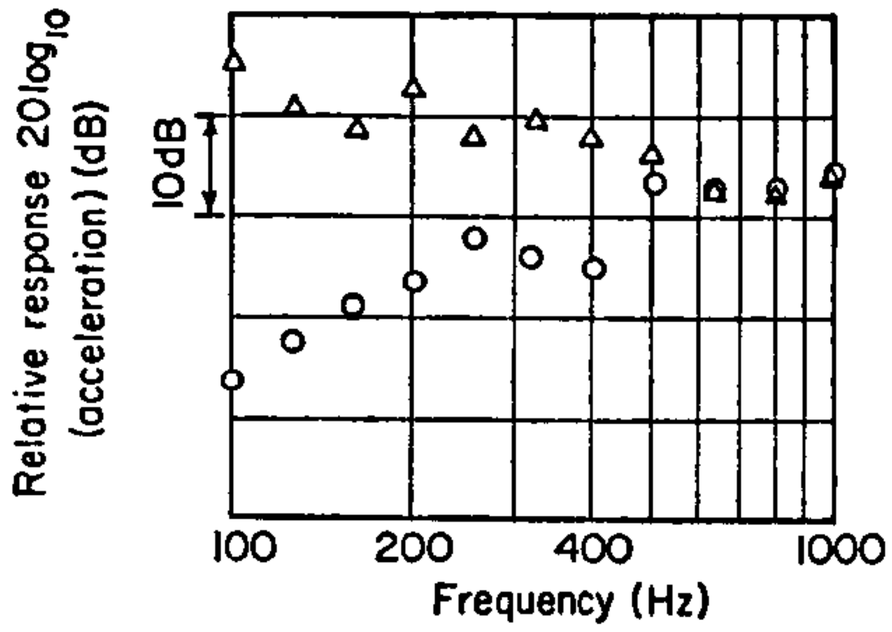

Figure 4. Panel acceleration response against frequency for two types of excitation; ○, white noise excitation, △, impulsive excitation.

were obtained and so this method was chosen to measure η_{tot} at higher frequencies. Since the decay times of the panel response at frequencies above 1000 Hz were so small, the decay was recorded on a tape recorder at a high tape speed, and then played back at a lower tape speed, the ratio of the speeds being chosen so that a measurable decay could be obtained.

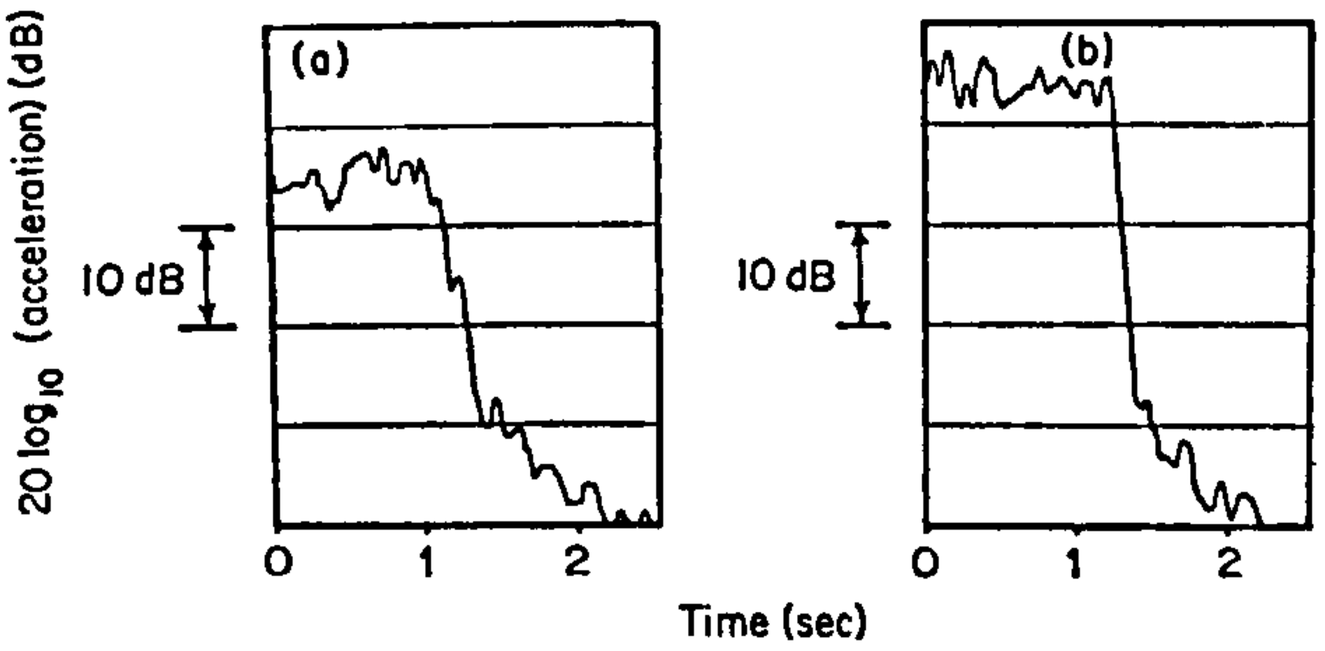

Figure 5. Typical ⅓ octave band filtered records of acceleration decay produced after excitation by shaker fed with white noise. (a) Centre frequency 400 Hz; (b) centre frequency 800 Hz.

The steady-state acceleration response of the panel against frequency was also determined by supplying the shaker with "white noise" and filtering the output in ⅓ octave bands. The result is plotted in Figure 4.

A study of all the shaker-excited and impulse-excited decay records (of which Figures 2 and 5 are examples) reveals that the decays due to the two types of excitation are very different, particularly at higher frequency. In the impulsive case the mean slope decreased much sooner than in the shaker-excited case, particularly for the higher frequencies.

The authors offer the following explanation which appears to fit all the observed phenomena. As Figure 4 demonstrates, the impulse tends to produce a higher acceleration

level in the lower-order modes than the higher-order modes. The opposite occurs with "white noise" excitation by the shaker which produces a higher acceleration level in the higher-order modes than in the lower-order modes. The low-frequency difference in levels between the two types of excitation is of the order of 30 dB. Since the low-frequency modes are much less damped, they decay more slowly and it is proposed that energy is transferred to higher-order modes. This is supposed to happen to a greater extent with impulsive excitation than with excitation by a mechanical shaker, because the impulse excites the lower-order modes very much better. Thus it is proposed that with the impulsive decays, particularly with the higher frequency records, that only the first part of the trace (say about 5 dB) represents a true decay. The latter part of the trace is artificially extended by energy transferred from the lower-order modes. It is indeed observed in Figure 3 that only at higher frequency does the initial part of the impulsive curve give a value of η_{tot} which roughly agrees with that deduced from the shaker traces, and even then the value is lower.

The authors have not been able to prove conclusively that the change in slope in the higher frequency impulsive traces is due to appreciable coupling with lower-order modes; however, they point out that this does appear to be plausible and to fit the facts. Nevertheless, it has been demonstrated that the decay curves derived from impulsive decay differ markedly from those produced from decay of vibration produced by a shaker. Also it appears that it is necessary to use more interpretive judgment with the impulsive decay curves and thus they are less satisfactory. Perhaps this points to the necessity for the use of a completely different method of determining the total loss factor in a plate. It should be noted that the phenomenon of a change of slope in a decay record has already been discussed in the literature [2, 3]; however, in most of these instances the explanation is due to the presence of some modes in each band with very low damping.

The authors thus suggest that there may be some doubt in the values of η_{tot} presented for the higher frequency range in Figure 4 of reference 1. Other researchers [4, 5] seem to find that for similar plain plates η_{tot} does not decrease with frequency as shown in this Figure, but remains roughly constant at about 0·01, or even increases a little. For stiffened plates η_{tot} should be considerably larger. It is interesting to note the rise in η_{tot} in Figure 3 at the coincidence frequency, since this is exactly what is to be expected due to the increase in η_{rad}. Since $\eta_{tot} = \eta_{int} + \eta_{rad}$ and at coincidence $\eta_{rad} \geqslant \eta_{int}$ then $\eta_{tot} \approx \eta_{rad}$. It is indeed found that the value for η_{tot} at 4000 Hz is in good agreement with the experimental value of η_{rad} measured at coincidence [5] and with the theoretical value of η_{rad} [6].

Errors in η_{tot} may also partly explain the large discrepancies between experimental and theoretical values of the radiation resistance for different panels reported in Figure 3 of reference 1. A considerable increase in the value of η_{tot}, for a particular measured value of $\mu(\omega)$ will necessitate an increased value of η_{rad}. At the lower frequencies some of the scatter observed may be due to cavity-panel mode coupling. Radiation resistance is normally better measured by directly exciting the panel under examination and measuring the reverberant pressure level produced [6]. An indirect method such as that used in reference 1 has the danger of additional inaccuracy due to the necessity of also measuring η_{tot} with consequent further experimental error.

Department of Building Science,
The University of Liverpool,
P.O. Box 147,
Liverpool, England

M. J. CROCKER
A. J. PRICE

Received 29 *November* 1968

REFERENCES

1. F. J. FAHY and R. B. S. WEE 1968 *J. Sound Vib.* 7, 431. Some experiments with stiffened plates under acoustic excitation.
2. P. M. MORSE 1948 *Vibration and Sound* p. 406. New York; McGraw-Hill.
3. L. L. BERANEK 1954 *Acoustics* p. 294. London: McGraw-Hill.
4. R. H. LYON and T. D. SCHARTON 1965 *J. acoust. Soc. Am.* 38, 253. Vibrational-energy trans- in a three-element structure.
5. M. J. CROCKER and A. J. PRICE 1969 *J. Sound Vib.* 9, 469. Sound transmission using statistical energy analysis.
6. G. MAIDANIK 1962 *J. acoust. Soc. Am.* 34, 809. Response of ribbed panels to reverberent acoustic fields.

Reprinted from

APPLIED ACOUSTICS

THE EFFECT OF SURFACE TREATMENT ON SOUND-ABSORBING MATERIALS

A. J. PRICE and K. A. MULHOLLAND

ELSEVIER PUBLISHING CO LTD

THE EFFECT OF SURFACE TREATMENT ON SOUND-ABSORBING MATERIALS

A. J. PRICE and K. A. MULHOLLAND

Department of Building Science, The University of Liverpool, Great Britain

(Received: 10 July, 1967)

SUMMARY

Measurements of the effect of paint finishes on the acoustic absorption properties of a number of surfaces suitable for use as sound absorbers are reported. It is shown that in no case does the paint fail to alter the absorption characteristics of the surface. In the case of materials having open pores on their surfaces the effect is particularly harmful. In these cases it is recommended that the surfaces be first covered with perforated board which can enhance the acoustic properties and which provides a surface which will take paint without the acoustic properties being affected.

INTRODUCTION

The fundamental purpose of employing sound-absorbing materials in architecture is to control the average sound pressure level (S.P.L.) in an enclosure or the reverberation time or both. It is easy to show[1] that each doubling of the total amount of absorption in an enclosure results in the reverberation time being halved and the S.P.L. being reduced by 3 dB. Hence, by a suitable selection of absorbing materials, the acoustic properties of an enclosure may be adapted to suit one's requirements. In practice, however, this does not merely mean choosing a material with the desired absorption coefficient, but the following points must also be considered.

(i) Can the material be mounted easily or even integrated into the structural design?

(ii) Does the material conform with the prescribed fire precautions?

(iii) Is the lighting in the enclosure reduced to an undesirable level by the presence of the absorbing material?

(iv) Is the visual effect of the material desirable?

Applied Acoustics—Elsevier Publishing Company Ltd., England—Printed in Great Britain

When all these points have been considered it seems that the absorption coefficient is only of secondary importance. Perhaps the most important point is that the desired visual impact must, on most occasions, dictate the surface finish of the material, *i.e.*, we must consider the paintability of the chosen absorbing materials.

It is clearly of primary importance that the acoustic properties be maintained and be essentially unaltered following painting.[2] In the case of porous materials, the mechanism by which sound is absorbed depends upon air particles excited by the incident sound wave being able to enter the material wherein dissipation of energy by turbulence, etc., takes place. Thus, clearly, if this access is completely or even partially blocked then either a loss in sound absorbing efficiency or a shift in the absorption frequency curve will occur. Either of these will alter the room acoustics from the original design. It would appear, therefore, that an investigation into the effect of painting the surface of porous materials upon their acoustic properties is necessary.

Of the other two mechanisms whereby sound may be absorbed, the first, the resonant panel, is not affected by paint and the second, the Helmholtz resonator, is unaffected provided that the entrance to the resonator is not obstructed by the paint.

EXPERIMENTAL WORK

The absorption coefficient of a material can be measured by either the *reverberation room* method or by using a *standing wave tube*. The latter method was chosen for this work, and hence all the results quoted for the absorption coefficient apply only to a normal incidence field. It is known[3] that this value is about one-half the random incidence value at low frequencies, while at high frequencies the values are approximately equal.

Samples of various types of acoustic materials were tested and an absorption coefficient/frequency curve measured for the untreated surface and for the surface treated with paint.

The effect of paint applied by brush and by spray was also studied.

EXPERIMENTAL RESULTS

Results for the following four materials are given, these being considered as representative of their type of sound absorbing material:

(i) wood-wool with $\frac{1}{4}$-in plaster facing
(ii) felt
(iii) polyurethane foam
(iv) polystyrene tiles.

(*i*) *Wood-wool*

The absorption coefficient *vs.* frequency curve for a 2-in-thick wood-wool sample alone and with $\frac{1}{4}$-in plaster facing, is shown in Fig. 1.

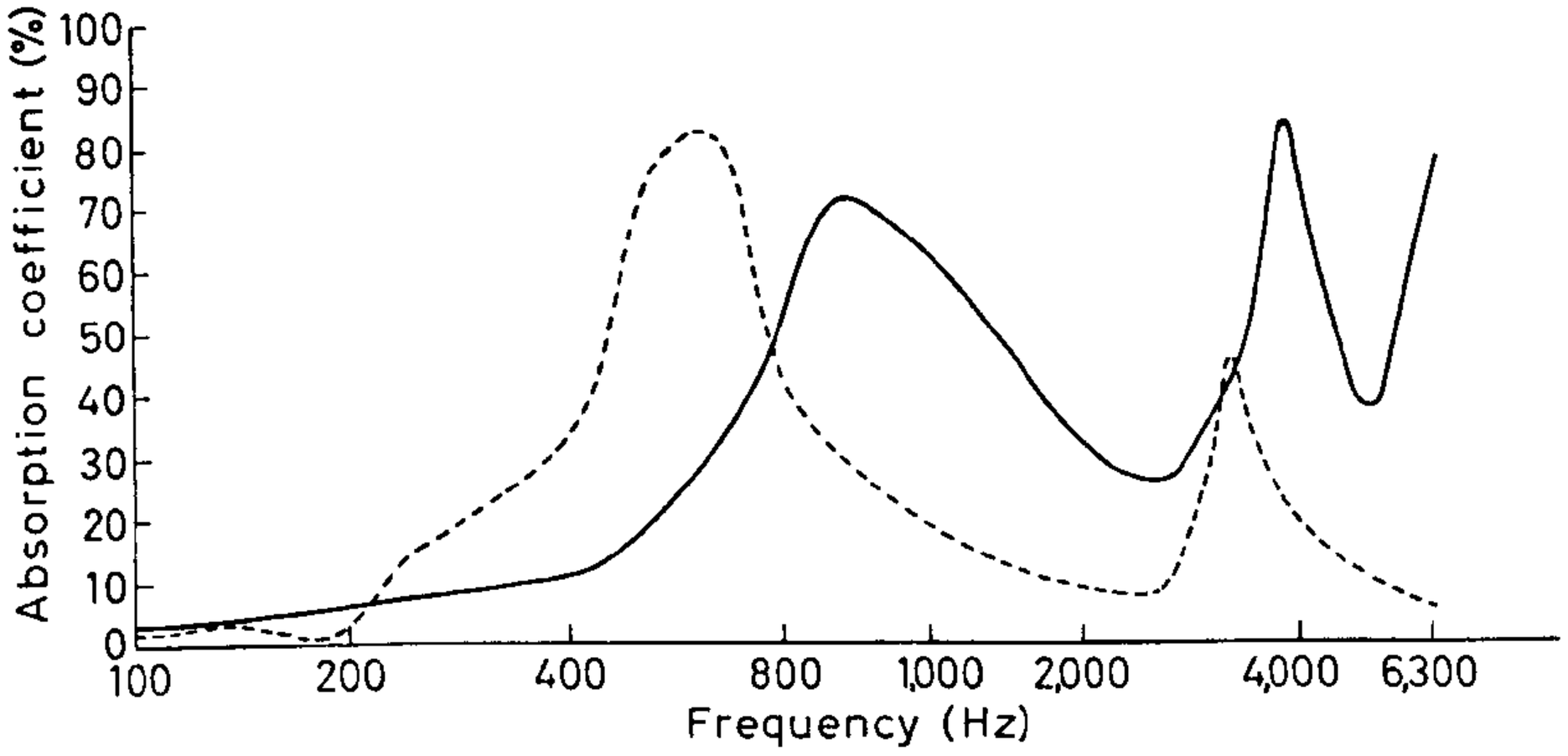

Fig. 1. Effect of $\frac{1}{4}$-inch plaster coating on 2-inch wood-wool. ———, untreated; – – – –, with $\frac{1}{4}$-inch plaster coating.

Clearly, the effect of plastering the surface is to shift the curve towards the low-frequency end so that the low-frequency absorption coefficient is increased while at the high frequencies it is decreased. This type of shift behaviour can be explained qualitatively.

The effect of painting the plaster surface with domestic paint is shown in Fig. 2. Painting decreases the absorption coefficient while keeping the general pattern of the original curve. As more layers of paint are added the absorption coefficient de-

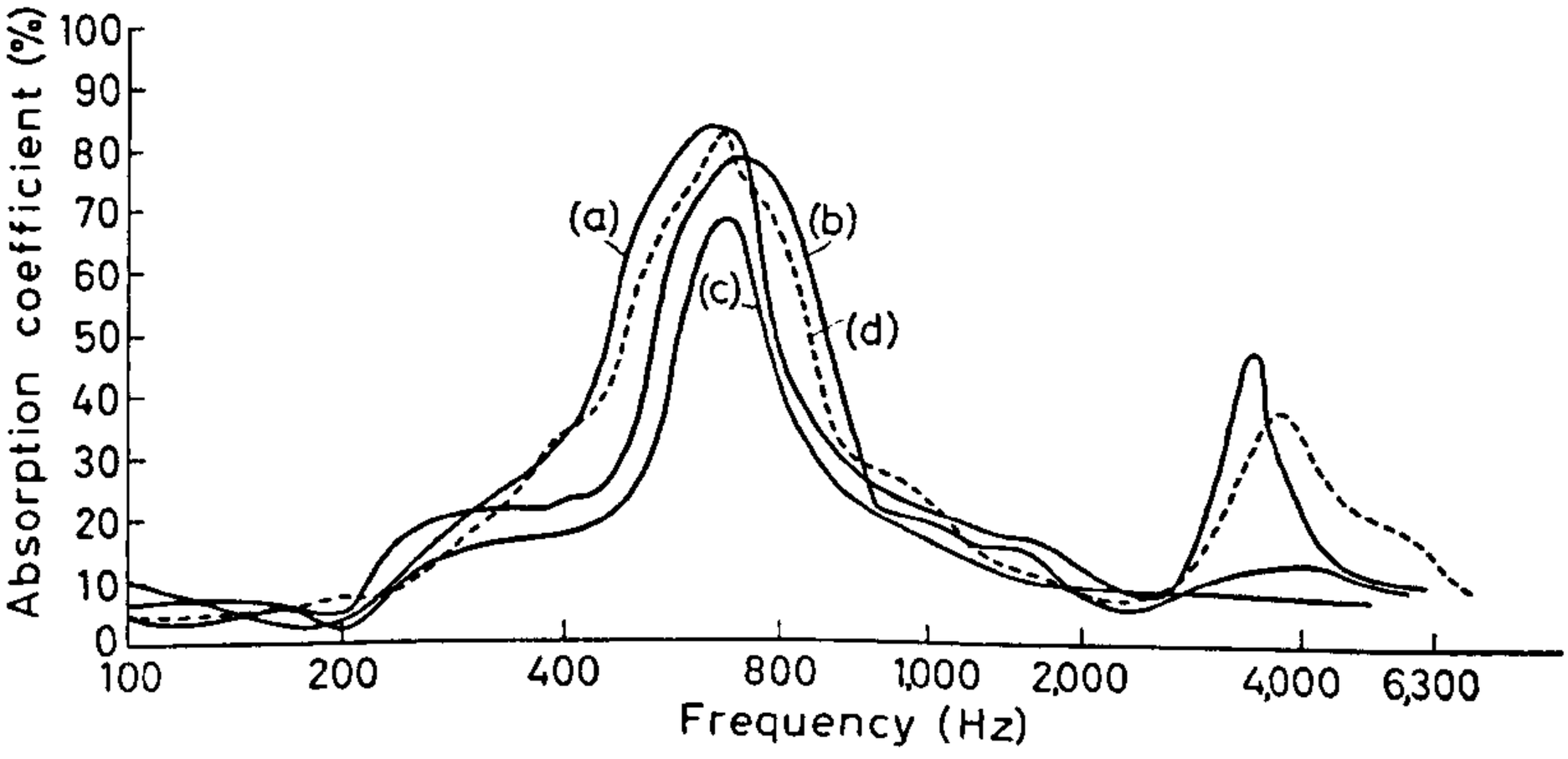

Fig. 2. Effect of paint upon absorption coefficient when applied by brush to $\frac{1}{4}$-inch plaster coating on 2-inch wood-wool. (a) Untreated plaster surface; (b) one coat of paint applied by brush; (c) two coats of paint applied by brush; (d) spray-gun application.

creases. It can also be seen from Fig. 2 that the original acoustic properties are changed less when the paint is sprayed on than when applied by brush.

(*ii*) *Acoustic felt*

The application of paint by brush is seen (Fig. 3) in this case to shift the curve towards the low frequencies but at the same time a considerable (15%) overall

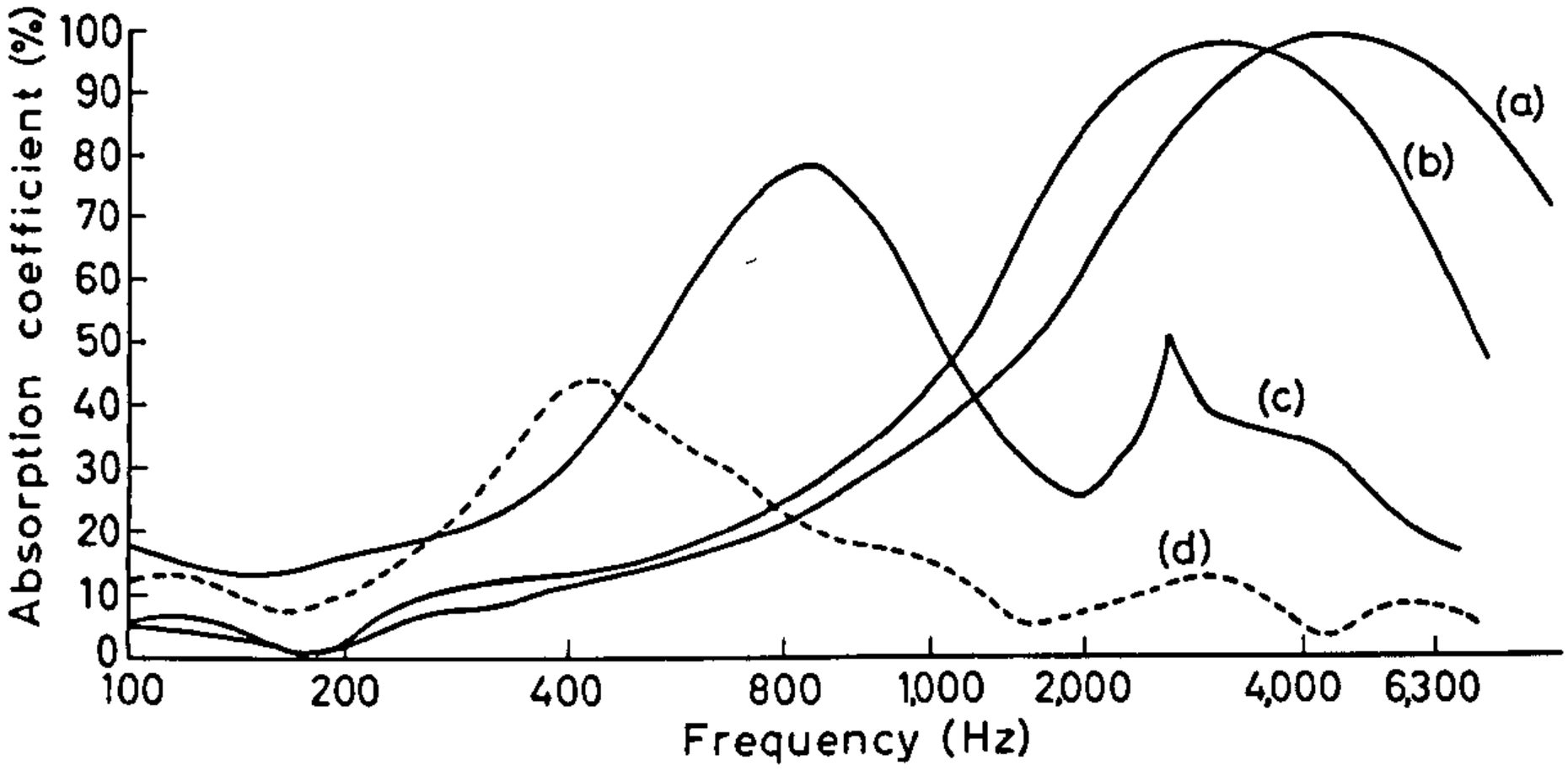

Fig. 3. Paint applied by brush and spray-gun to acoustic felt. (a) Untreated surface; (b) one coat of paint, sprayed; (c) one coat of paint, applied by brush; (d) two coats of paint, applied by brush.

decrease in the absorption coefficient, α, is noted. Applications of further coats decrease α considerably and still shift the original unpainted curve towards the low frequencies. Spraying is again seen to reduce the absorption coefficient less drastically than by brush painting.

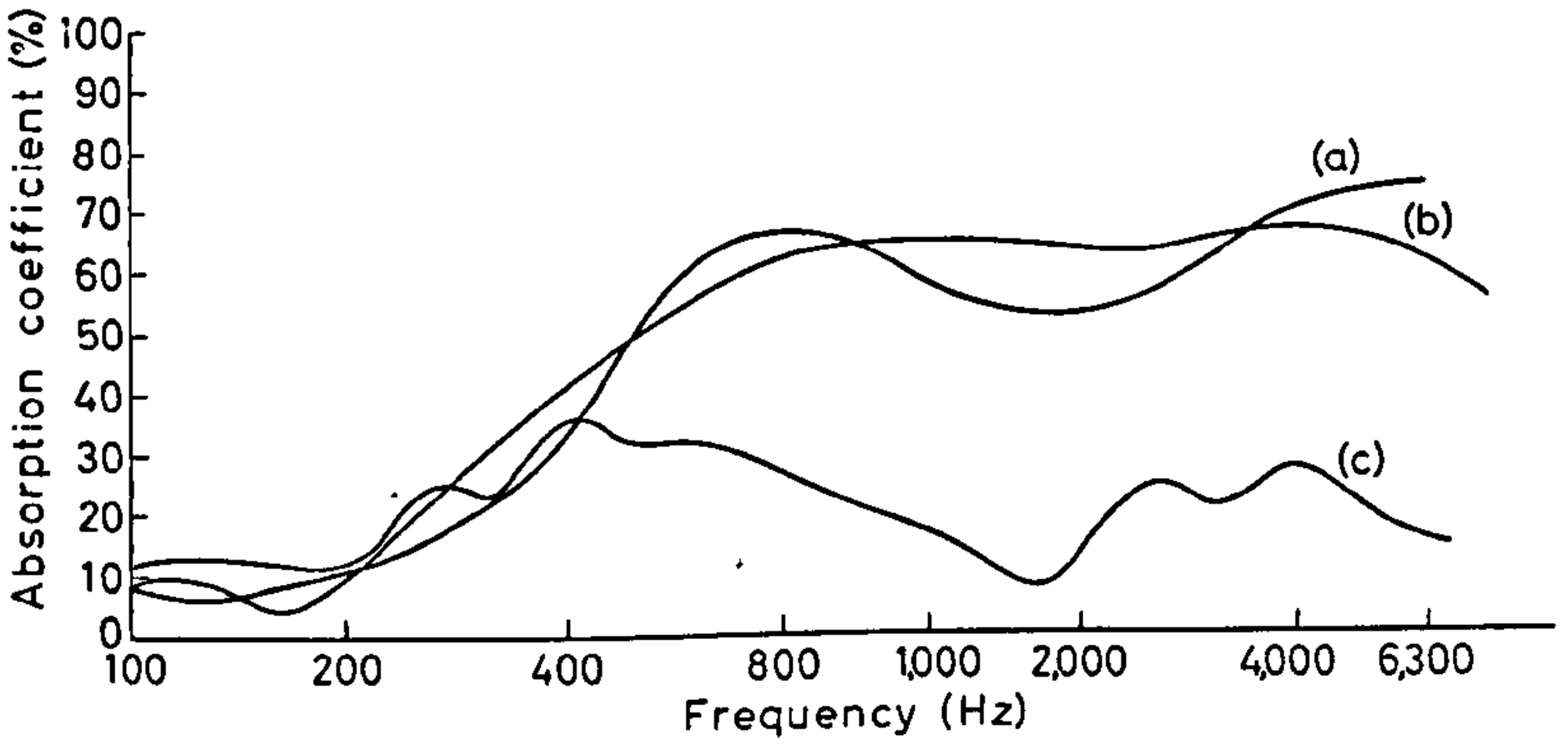

Fig. 4. Effect of paint applied by brush and spray-gun to polyurethane foam. (a) Untreated; (b) one coat of paint, sprayed; (c) one coat of paint, applied by brush.

(*iii*) *Polyurethane foam*

Application of paint by brush is now seen (Fig. 4) to be drastic in its effect upon

the acoustic properties while spraying seems to alter only slightly the absorption coefficient curve.

(*iv*) *Polystyrene* (*acoustic tile*)

The high absorption in the 1000–4000 Hz range (Fig. 5) is seen to be considerably reduced by the application of paint both when applied by brush and by spray-gun. Once again spraying appears to be less drastic than brush painting.

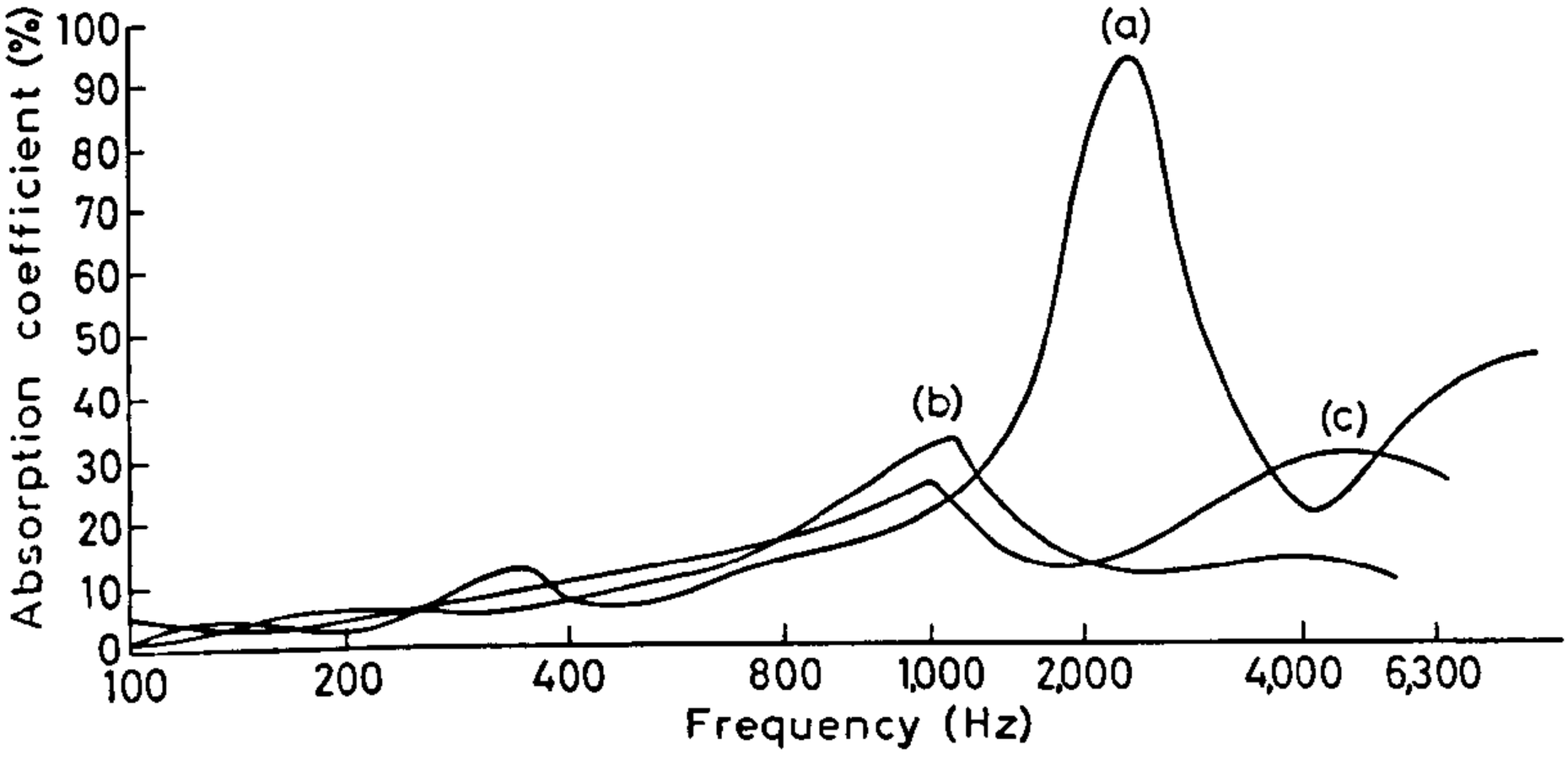

Fig. 5. 1½-inch polystyrene (acoustic tiles) when painted by brush and by spray-gun. (a) Untreated material; (b) two coats of paint, applied by brush; (c) paint applied by spray-gun.

QUANTITATIVE EXPLANATION OF RESULTS

As suggested by Kosten[4] the paint layer may be thought of as a very thin layer of relatively great air resistance backed by the impedance of the unpainted layer. Hence, the impedance curve of the total layer, giving the impedance in its complex plane as a function of frequency, is approximately the same as that of the untreated layer except for a shift in the positive direction of the real axis through a distance determined by the air resistance of the coating. This means an improvement in the low frequencies and a reduction in the mid and high frequencies.

This type of behaviour was seen in all three types of acoustic material tested.

The more porous the surface of the material the more drastic the effect of paint becomes simply due to the blocking of the "access passages" into the material. Hence, paints of minimum solid material should be used. Oil paint would appear to be catastrophic if used on very porous materials (*i.e.* foam). Hence, for porous materials, spray-gun applications of well-thinned (water-base) paints are recommended.

CONCLUSION

The paintability of architectural acoustic materials is of primary importance and must be considered when choosing an acoustic material for use in buildings. It

appears that the more open-surface type materials suffer most from the application of paint, and if the painting of the surface is absolutely essential then only very thin paints should be used and these should be applied by means of a spray-gun.

In the case of materials like felt and polyurethane foam it would appear that the only way to obtain a desirable surface finish is to cover the surface with a perforated panelling of the Helmholtz resonator type. By choosing the spacing and diameter of the holes in a panel of given thickness the resonant frequency can be made to fall in the range 100–500 Hz thereby increasing the absorption in the low frequency. For example, Fig. 6 shows the effect of adding a $\frac{1}{4}$-in-thick perforated panel with

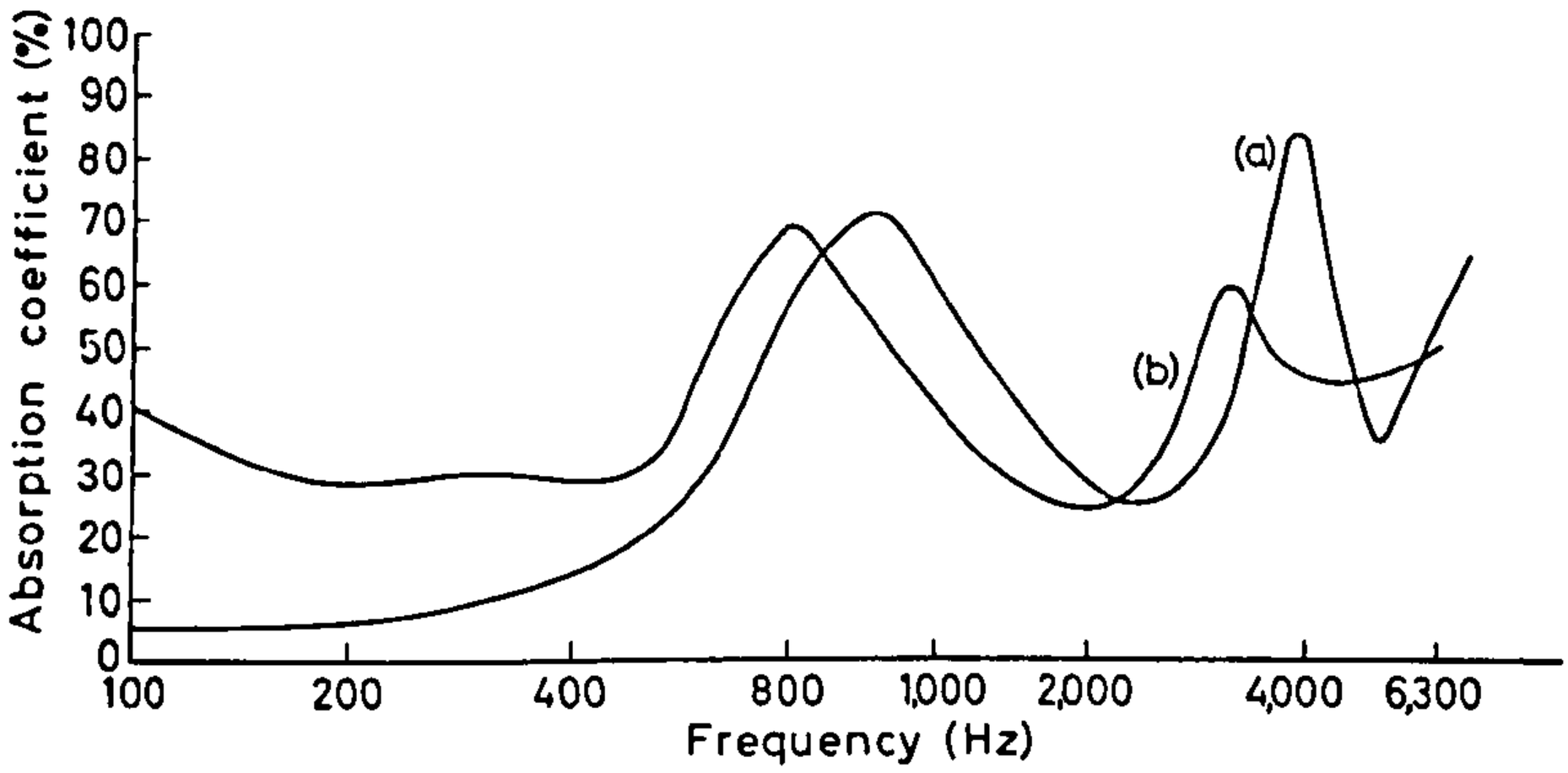

Fig. 6. 2-inch wood-wool covered by a $\frac{1}{4}$-in-thick perforated panel with $\frac{1}{4}$-in-diameter holes spaced at a distance of $\frac{1}{2}$ inch. (a) Wood-wool; (b) wood-wool plus perforated panel.

$\frac{1}{4}$-in-diameter holes at $\frac{1}{2}$-in centres to a layer of wood-wool 2 in thick. It can be seen that the low-frequency absorption coefficient is increased without substantially reducing the high-frequency performance. This panel can now be painted any number of times, and, provided the holes are not blocked, it will not be affected by the paint.

REFERENCES

1. L. L. BERANEK, *Noise Reduction*, McGraw-Hill, N.Y., 1960, p. 409.
2. Research Paper RP 1298, *J. Res. Natl. Bur. Stand.*, **24** (May 1940).
3. L. L. BERANEK, *Noise Reduction*, McGraw-Hill, N.Y., 1960, p. 391.
4. A. B. RICHARDSON (editor), *Technical Aspects of Sound*, Elsevier, Amsterdam, 1953, Ch. 4.